EXPERIMENTAL ANALYSIS OF FLOW STRUCTURE ON MODERATE SWEEP DELTA WING

A THESIS SUBMITTED TO
THE GRADUATE SCHOOL OF NATURAL AND APPLIED SCIENCES
OF
MIDDLE EAST TECHNICAL UNIVERSITY

BY

İLHAN ÖZTÜRK

IN PARTIAL FULFILLMENT OF THE REQUIREMENTS
FOR
THE DEGREE OF MASTER OF SCIENCE
IN
MECHANICAL ENGINEERING

JANUARY 2014

Approval of the thesis:

EXPERIMENTAL ANALYSIS OF FLOW STRUCTURE ON MODERATE SWEEP DELTA WING

submitted by **İLHAN ÖZTÜRK** in partial fulfillment of the requirements for the degree of **Master of Science in Mechanical Engineering Department, Middle East Technical University** by,

Prof. Dr. Canan Özgen ____________________
Dean, Graduate School of **Natural and Applied Sciences**

Prof. Dr. Suha Oral ____________________
Head of Department, **Mechanical Engineering**

Assoc. Prof. Dr. Mehmet Metin Yavuz ____________________
Supervisor, **Mechanical Engineering Dept., METU**

Examining Committee Members:

Prof. Dr. Kahraman Albayrak ____________________
Mechanical Engineering Dept., METU

Assoc. Prof. Dr. Mehmet Metin Yavuz ____________________
Mechanical Engineering Dept., METU

Assoc. Prof. Dr. Ahmet Yozgatlıgil ____________________
Mechanical Engineering Dept., METU

Asst. Prof. Dr. Yiğit Yazıcıoğlu ____________________
Mechanical Engineering Dept., METU

Assoc. Prof. Dr. Oğuz Uzol ____________________
Aerospace Engineering Dept., METU

Date: 30.01.2014

I hereby declare that all information in this document has been obtained and presented in accordance with academic rules and ethical conduct. I also declare that, as required by these rules and conduct, I have fully cited and referenced all material and results that are not original to this work.

Name, Last name : İlhan ÖZTÜRK

Signature :

ABSTRACT

EXPERIMENTAL ANALYSIS OF FLOW STRUCTURE ON MODERATE SWEEP DELTA WING

Öztürk, İlhan
M.Sc., Department of Mechanical Engineering
Supervisor: Assoc. Prof. Dr. Mehmet Metin Yavuz

January 2014, 182 pages

Experimental investigation of flow over a 45° moderate swept delta wing is performed using laser illuminated smoke visualization, surface pressure measurements, and Laser Doppler Anemometry (LDA) techniques in low-speed wind tunnel. The formation of leading-edge vortices and their breakdown, and three-dimensional separation from the surface of the wing are studied at broad range of attack angles and Reynolds numbers. Smoke visualizations are performed at three different cross flow planes along with vortex axis plane. The footprint of flow regimes on the surface of the planform is captured by the surface pressure measurements from the pressure taps located at the corresponding three stations along the wing cord in spanwise direction. In addition, velocity measurements at vortex core and locations close to the surface of the planform are utilized. Using statistics and spectral density analysis, the unsteadiness of flow is studied in detail and the amplitude and the frequency of the pressure and velocity fluctuations at different locations are compared. The results of the study indicate that the surface pressure measurements are quite in line with the flow visualization results where the vortex cores correspond to the largest suction pressures at the surface of the planform. The vortex breakdown and three-dimensional surface separation cause significant loss in suction pressure of the vortex core and reattachment pressure at the wing surface. Considering the attack angles of $\alpha = 4°$, $7°$ and $10°$, the highest velocity fluctuations take place at the regions around the vortex core axis. However, the highest velocity fluctuations occur at locations close to the reattachment region at 13-degree angle of attack and high Reynolds numbers, when the vortex breakdown location reached to the apex of the wing.

Keywords: Moderate sweep delta wing, Leading edge vortex, Vortex breakdown, Laser illuminated flow visualization, Laser Doppler Anemometry (LDA)

ÖZ

ORTA SÜPÜRME AÇILI DELTA KANAT ÜZERİNDEKİ AKIŞ YAPISININ DENEYSEL OLARAK İNCELENMESİ

Öztürk, İlhan
Yüksek Lisans, Makina Mühendisliği Bölümü
Tez Yöneticisi: Doç. Dr. Mehmet Metin Yavuz

Ocak 2014, 182 sayfa

45 derecelik orta süpürme açılı bir delta kanadın etrafında oluşan akış, lazer aydınlatmalı akış görüntüleme, yüzey basınç ölçümleri ve Lazer Doppler Anemometre yöntemi kullanılarak düşük hızlı bir rüzgâr tünelinde deneysel olarak incelenmiştir. Kanat ucu girdabının oluşum ve kırınımı ve kanat yüzeyinden üç boyutlu akış ayrılması geniş bir hücum açısı ve Reynolds sayısı aralığında çalışılmıştır. Akış görüntüleme deneyleri akışa dik üç farklı düzlemde ve kanat ucu girdabı ekseni üzerinde alınan bir düzlemde gerçekleştirilmiştir. Planform üzerindeki akış rejimlerinin izleri, kanat yüzeyinde bir uçtan diğer uca gidecek şekilde kanat veteri boyunca üç farklı istasyonda sıralanmış olan basınç ölçüm deliklerinden alınan yüzey basınç ölçümleri ile elde edilme çalışılmış, hız ölçümlerinde ise girdap merkezi ve planform yüzeyine yakın konumlar kullanılmıştır. İstatistiki ve spektral analiz yöntemleri kullanılarak akışın düzensizliği detaylı olarak araştırılmış ve farklı noktalardaki basınç ve hız çalkantılarının büyüklük ve frekansları karşılaştırılmıştır. Yapılan çalışmalar, girdap merkezlerinin konumlarının kanat yüzeyindeki en yüksek emme basınçlarının görüldüğü yerler ile örtüşmesi neticesinde, yüzey basınç ölçüm sonuçları ile akış görüntüleme sonuçlarının birbiriyle oldukça uyumlu olduğunu ortaya çıkarmıştır. Girdap kırınımı ve kanat yüzeyinden üç boyutlu akış ayrılmasının,

kanat yüzeyi üzerinde girdap merkezinin emme basıncı ve akışın yeninden yüzeye bağlanma basıncında önemli kayıplara neden olduğu görülmüştür. Hızdaki çalkantılar incelendiğinde; $\alpha = 4^\circ,\ 7^\circ$ ve10° hücum açılarında en yüksek çalkantı değerlerinin girdap ekseni civarında ölçüldüğü, girdap kırınım noktasının kanat ucuna eriştiği $\alpha = 13^\circ$ hücum açısı ve yüksek Reynolds sayıları durumlarında ise en yüksek çalkantı değerlerinin akışın yüzeye yeniden bağlandığı bölge civarında elde edildiği görülmüştür.

Anahtar kelimeler: Orta süpürme açılı delta kanat, Kanat ucu girdabı, Girdap kırınımı, Lazer aydınlatmalı akış görüntüleme, Lazer Doppler Anemometri (LDA)

To my parents and my youth…

ACKNOWLEDGEMENTS

I would like to express my sincerest appreciation to all those people who has supported me either physically or morally throughout this study.

I am fully grateful to my supervisor Assoc. Prof. Dr. M. Metin Yavuz for his unmatched guidance, encouragement, support, criticism and invaluable supervision. I am also thankful to him for sharing his experiences and advices about real life with me. It was an honor for me to study with him throughout my graduate education.

I need to express my sincere thanks to my colleagues Mohammad Reza Zharfa, Gökay Günacar, Alper Çelik, İsa Kavas, Osman Akdağ, Berat Çelik and Berksu Erkal for their support in experiments and data processing, and to Gülsüm Çaylan, Mehmet Yalılı, Kadir Ali Gürsoy and for their moral support. I have been very lucky to share unforgettable moments in Fluid Mechanics Lab with these good friends of mine.

I would like to show my gratitude to the lab technicians Rahmi Ercan and Mehmet Özçiftçi for their invaluable help.

I would also like to express my sincere thanks to TÜBİTAK (The Scientific and Technological Research Council of Turkey) for the graduate scholarship I received during my study.

Last but the most, I owe my deepest gratitude to my parent İbrahim and Gülbiye Öztürk, my sister Aylin Bektaş and my brother in law Gökhan Bektaş for their unconditional love, full support and encouragement, which made possible all the years spent here.

TABLE OF CONTENTS

CHAPTERS

APPENDICES

LIST OF TABLES

TABLES

LIST OF FIGURES

FIGURES

NOMENCLATURE

Λ = sweep angle

c = chord length

s = semispan

$\tilde{s}$ = local semispan at pressure stations

α = angle of attack

Re = Reynolds number based on chord length

u_∞ = freestream velocity

u = streamwise velocity

ω = vertical velocity

x = chordwise distance from wing apex

y = spanwise distance from wing root

f = frequency

St = dimensionless frequency

p = static pressure

$\bar{p}$ = average of the static pressure

p_∞ = static pressure of the flow

p_{dyn} = dynamic pressure of the flow

$p_{R.M.S.}$ = rms value of the static pressure

C_p = pressure coefficient

$C_{p,\ R.M.S.}$ = rms value of pressure coefficient

ρ = density of the fluid

N = number of samples in a measurement

CHAPTER 1

INTRODUCTION

Micro Air Vehicles (MAVs) and Unmanned Combat Air Vehicles (UCAVs) have drawn a considerable interest in recent years due to their increased use in both civilian and military tasks. Non-traditional wing planforms, such as delta wings having low to moderate sweep ($35 - 55°$) have been used extensively on these types of vehicles in cases where high levels of lift are essential to ensure high maneuverability over a wide range of angles of attack. Figure 1.1 illustrates some conceptual UCAV designs having blended delta wing-body configurations and some MAV configurations which use low sweep angle delta wings. Gursul [1] stated that vortex-dominated flows exhibit on all these configurations. It is recognized at the Workshop on Aerodynamic Issues of Unmanned Air Vehicles [2] that serious aerodynamic, stability and control issues may exist for these aforementioned configurations. Laminar-transitional flows are mostly dominant and flow structures such as separation, transition and vertical flow have a significant role on these delta wing planforms.

Delta wings are generally classified into two groups such as slender and nonslender wings. Gursul et al. [3, 4] defined the nonslender wings as one with a leading-edge sweep equal to or less than 55°, and slender wings, which have a leading edge sweep more then 55°.

When a flow pasts a delta wing at an angle of attack, two counter rotating leading-edge vortices (LEV) form as the flow separates into a pair of curved free shear layers along the leading edges as it is stated by Yavuz [5] and Yayla [6]. These LEV’s dominate the flow on slender wings at considerably high angles of attack [4]. Figure 1.2 shows the sketch of vortical flow around a delta wing taken from Taylor and Gursul [4]. Gursul [3] stated that a boundary layer separation caused by the interaction of the primary vortex with the boundary layer developing on the wing surface forms a secondary vortex of opposite sign vorticity compared to the primary vortex. This vortex type has been shown by many investigators, including Doligalski et al. [7] and Andreopoulos et al. [8]. Ol and Gharib [9] stated that for nonslender delta wings, LEV's have a similar formation at angles of attack as low as 2.5° although at these low angles the flow field behaves as wake-like flow. The size of these vortices increases as they are convected downstream by the streamwise velocity of the outer flow [8]. One of the advantages of these organized structures is stabilizing the flow on the wing and generating additional lift force, which is an important criterion for design of an unmanned combat air vehicle [5]. Yayla [6] stated that as much as 40% of the total lift of a delta wing is attributed by these LEV's at high angles of attack, and these vortices remains stationary on the wing surface because the vorticity originating from the leading edge is transported along the cores of the separation vortices. Earnshaw and Lawford [10] stated that the lift coefficient of a delta wing decreases as the sweep angle decreases. Figure 1.3 shows the variation of lift coefficient with wing sweep, adapted from Earnshaw and Lawford's data. Stall angles and the maximum lift coefficients of nonslender wings are lower than more slender planforms as it is stated by Earnshaw and Lawford [10].

LEV's are desired flow structures for delta wing since they have some advantages as mentioned above. However, these structures cannot be maintained above the wing at all angles of attack. At sufficiently high angles of attack, the flow along the vortex core stagnates and the vortices go a sudden expansion, which is called as vortex breakdown, (also referred as vortex bursting in some studies) first witnessed by Werle in a water tunnel facility [11]. Main drawback of this behavior is a dramatic drop both in lift and moments. However, Williams [12] stated that unlike slender delta wings, vortex breakdown is not a limiting factor in the lift generation for nonslender delta wings. Yavuz [5] stated that this behavior also causes large amplitude unsteady loading (buffeting) of the surface of the wing, which may lead to structural damage of the wing, as well as loss in control and stability. The vortex breakdown observed in nonslender wings is much less abrupt than the breakdown over slender wings, which makes the precise determination of the breakdown location more challenging [3]. An example illustrating leading edge vortices and vortex breakdown, taken from Delery [13] is shown in Figure 1.4. Also, another example depicting main delta wing flow and vortex breakdown characteristics, taken from Breitsamter [14] is given in Figure 1.5.

One of the distinct features of the flows over nonslender wings is the dual vortex structure that exists over the wing at low incidence. This vortex structure was first calculated numerically by Gordnier and Visbal in 2003 [15]. This structure arises from the interaction between the surface boundary layer and the proximity of the vortex formation to the wing surface, and has been demonstrated both experimentally and computationally at recent studies. An illustration showing the dual vortex structure and the vortex breakdown on a $\Lambda = 50°$ moderate-swept delta wing, taken from Taylor and Gursul [4], is given in Figure 1.6. The formation of dual vortex structure, taken from Wang and Zhang [16] is shown in Figure 1.7.

Another important difference between slender and nonslender wings is the reattachment of the flow to the wing surface on nonslender wings, whereas for slender wings the shear layer rolls up into a discrete vortex [12]. Gursul et al. [17] stated that reattachment is possible for nonslender wings even after vortex breakdown reaches the apex of the wing. However, there is no clear reattachment of the flow when the stall is witnessed.

1.1 Motivation of the Study

A great deal of effort has been spent on the studies of high sweep delta wing. It is possible to say the flow structure over these kinds of wings is well-understood. However the researches in the field of low and moderate sweep angle delta wings are quite limited compared to high sweep wings and further studies are a required in order to understand the flow structure and aerodynamics of these wings in detail. Low and moderate sweep delta wings, which are generic planforms of MAVs and UCAVs, have serious control and stability problems due to not having conventional aerodynamic control surfaces.

For these wings,

- interaction between leading edge vortex and boundary layer,

- leading edge vortex and its breakdown,
- localized surface flow separation,
- the effects of these on surface vibration and buffeting, and flow

are among the fundamental research topics. It is possible to find a solution to the control and stability problems by making further investigations on these topics and understanding the phenomena better.

1.2 Aim of the Study

In this thesis project, the flow structure on 45-degree swept delta wing is investigated in detail. Specifically, the following are studied:

- Mean and unsteady surface pressure measurements
- Analyzing the formation of leading edge vortex by smoke visualization
- Mean and unsteady velocity measurements
- The effects of attack angle and Reynolds number on flow structure
- Spectra analysis of unsteady pressure and velocity measurements
- Dominant frequencies in the flow and their relations with flow instabilities

Figure 1.1 Current and future unmanned combat air vehicles and micro air vehicles [2]

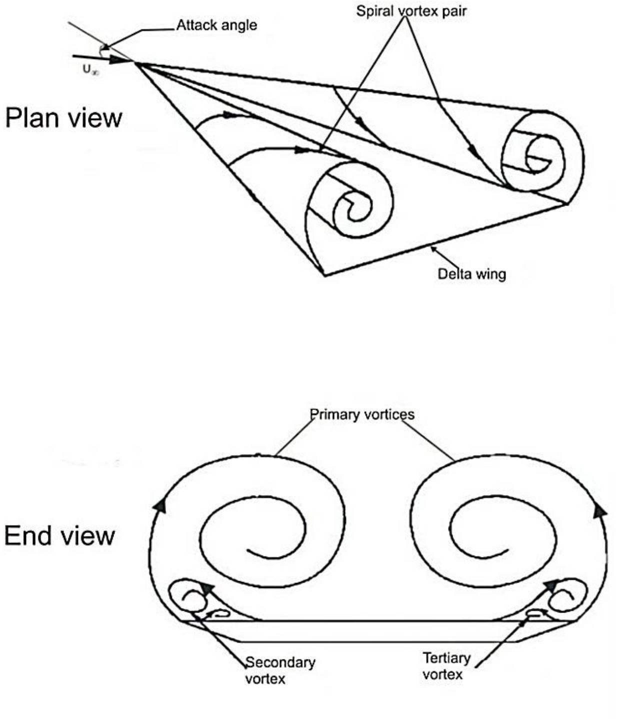

Figure 1.2 Sketch of vertical flows around a delta wing [4]

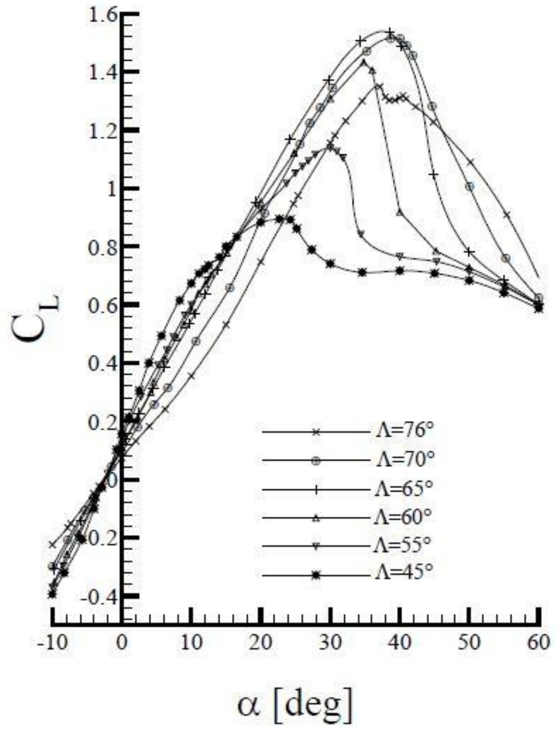

Figure 1.3 Variation of lift coefficient with angle of attack, adapted from [10]

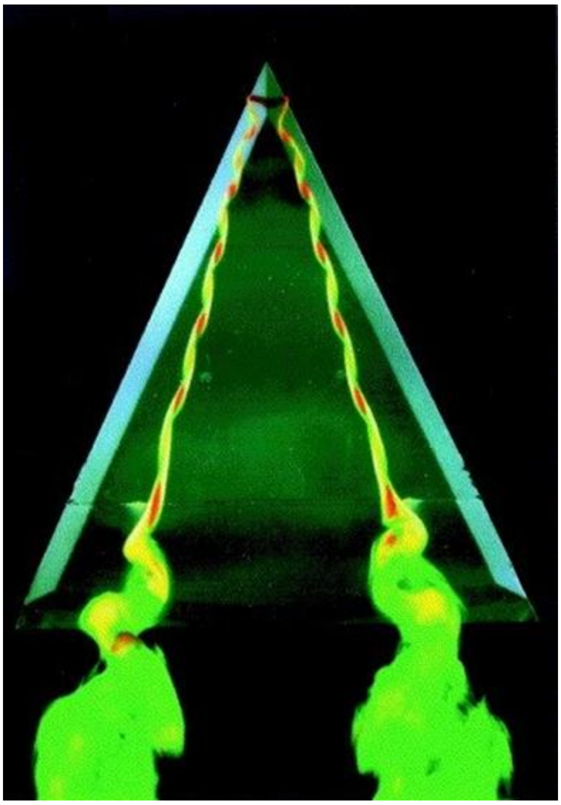

Figure 1.4 Leading-edge vortices and vortex breakdown over 65°-sweep wing [13]

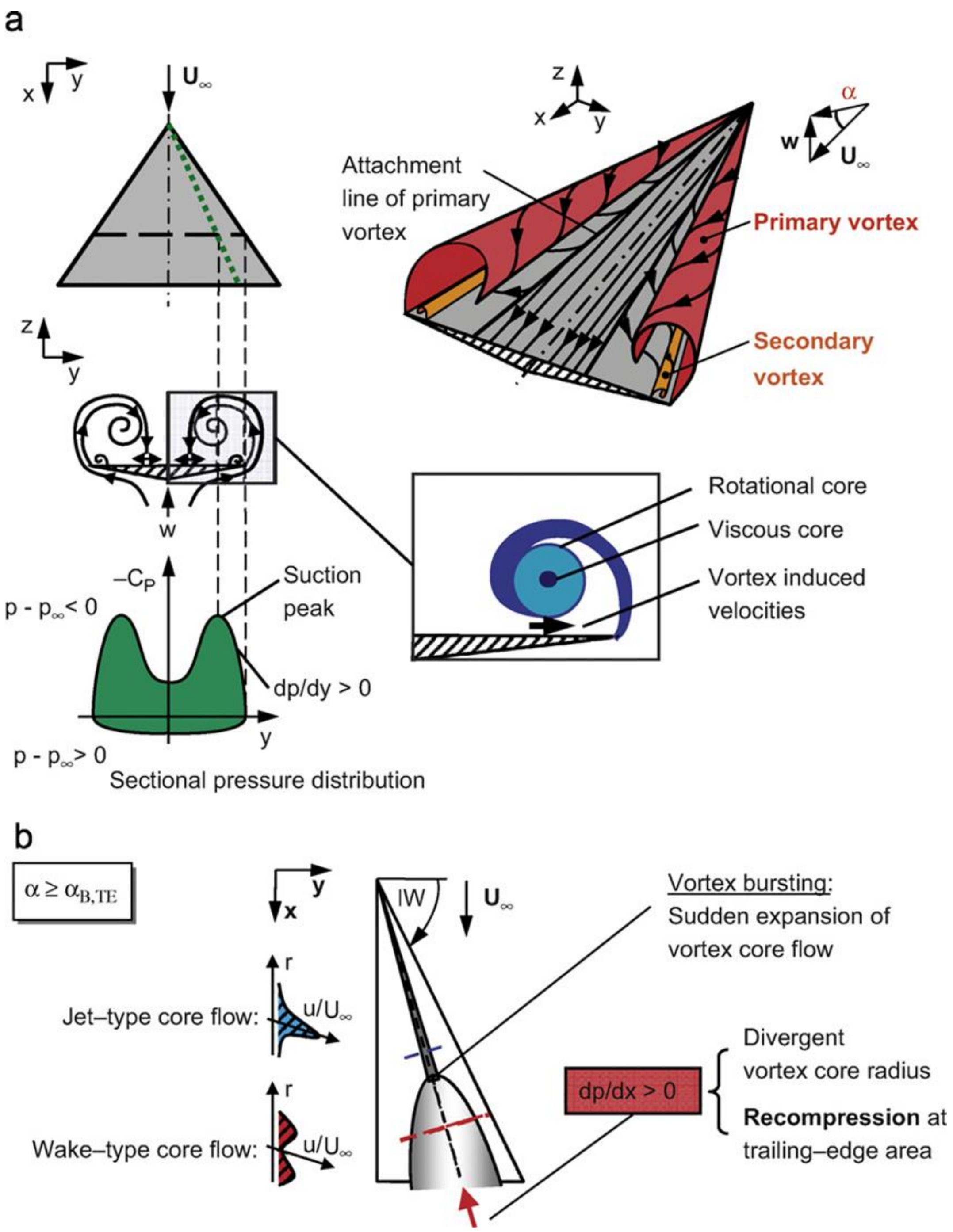

Figure 1.5 Delta wing vortex formation [14]: main delta wing flow features (a) and vortex bursting characteristics (b)

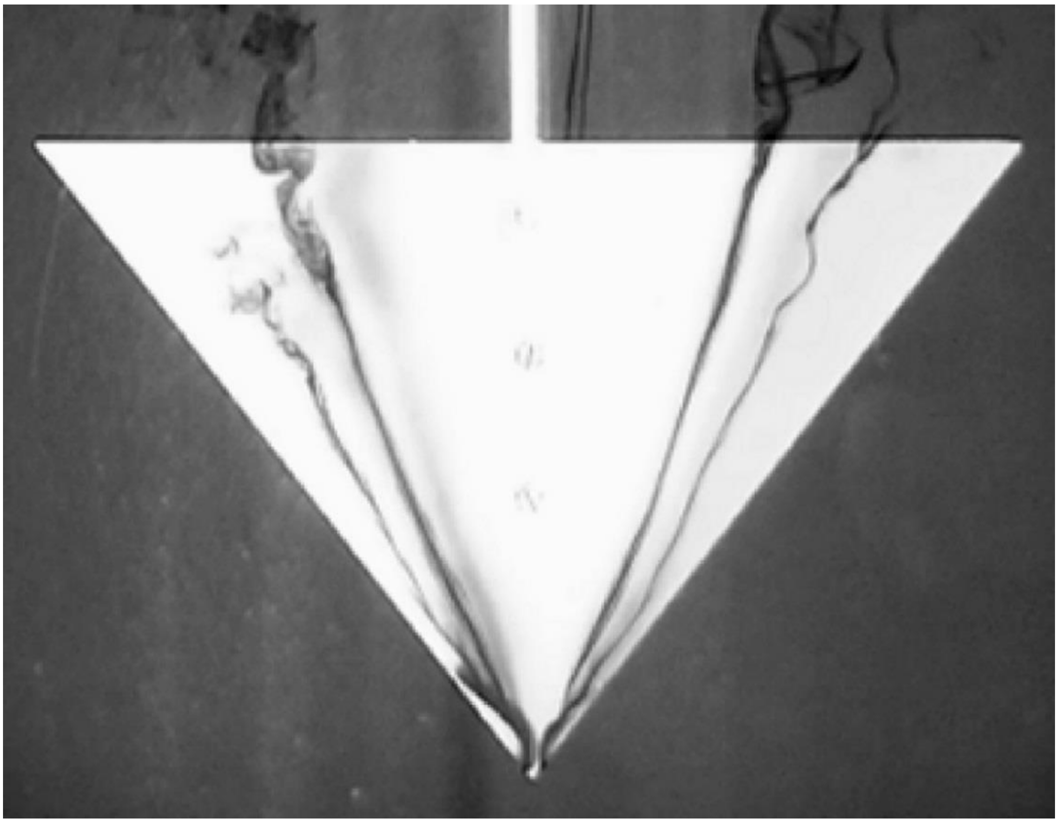

Figure 1.6 Dye flow visualization for vortex flow for $\alpha = 5°$ at Re = $8.7x10^3$ in water tunnel experiments [4]

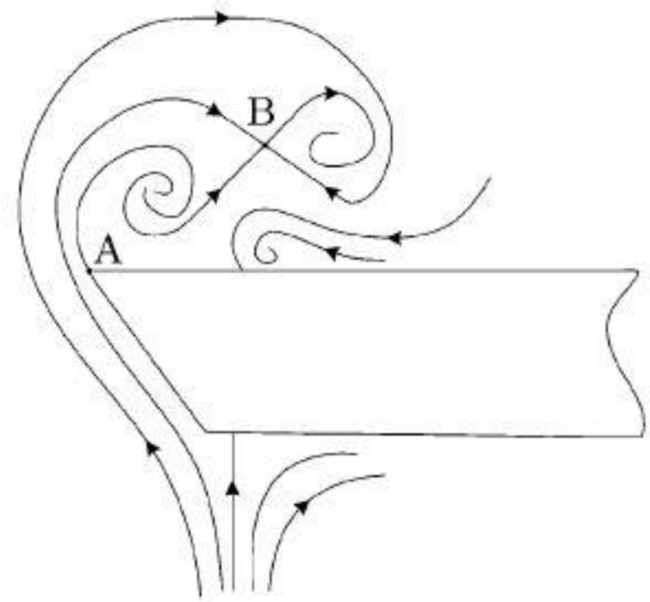

Figure 1.7 Sketch of the dual-vortex structure formation [16]

CHAPTER 2

PREVIOUS STUDIES

2.1 Flow Structure on High Sweep Delta Wings

The number of studies have been conducted on delta wings are numerous since it is a hot topic for researchers for a long time. Much of these studies have been carried out on slender delta wings and brought substantial knowledge about the flow structure on these types of wings. Several researchers including Earnshaw and Lawford [10], Wentz and Kohlman [18], Erickson [19], Barlett and Vidal [20], Benjamin [21,22], Sarpkaya [23,24,25], Leibovich [26,27], Wedemeyer [28], Polhamus [29], Escudier [30], Lee and Ho [31], Brown and [32] and Delery [33] focused on the aerodynamic characteristics of delta wings, vortices and vortex breakdown in their studies while some of them including Rockwell [34], Gordnier and Visbal [35], Menke, Yang and Gursul [36], Ashley, Katz, Jarrah and Vaneck [37], Gursul [38, 39, 40], Lowson [41] and Redinoitis, Stapountzis and Telionis [42] worked on the unsteady phenomena of these flows. It is found in these studies that there are some unsteady flow phenomena exist in high sweep delta wings, such as oscillations of vortex breakdown location [41], vortex shedding [42], vortex wandering [43], helical mode instability [40,44] and shear layer instabilities [35]. The importance of these instabilities arises from their impact on buffeting at aircraft structures such as wings and fins and aircraft stability, which has been well documented by the aforementioned authors. Although the unsteady flow structure over high sweep wings are well understood, there is still lack of knowledge about these phenomena over low and moderate sweep wings which require further studies on these planforms [3]. Illustration of some of these unsteady phenomena as a function of dimensionless reduced frequency is documented by Menke et al. [36], which is given in Figure 2.1. It can be seen from the figure that all the unsteady phenomena shown in the plot has a unique frequency band compared to each other.

2.1.1 Oscillations of vortex breakdown location

Unsteadiness of the vortex breakdown location over delta wings and oscillations of these locations along the axis of the vortex were observed in the experiments which were conducted by Lowson [41] and Fisher et al. [45]. A low frequency peak has been indicated by the pressure and velocity spectra of the wake of vortex breakdown, which is related with the fluctuations of vortex breakdown location throughout the wing in streamwise direction. Ayoub and McLachan's study [46] has revealed that the oscillations of breakdown location have an antisymmetric motion for left and right leading edge vortices. It is shown in Fig. 2.1 that when these oscillations compared to the other instabilities such as the helical mode and Kelvin-Helmholtz instabilities, they have very low dominant frequencies. It was also stated by Ayoub and McLachan [46], Menke and Gursul [47], Gursul and Yang [48], Menke, Yang and Gursul [36], and Portnoy [49] that oscillations of vortex breakdown location are quasi-periodic. Moreover, it was found that an increase in the angle of attack or sweep angle causes a decrease between the time-averaged breakdown locations which results in larger and more coherent oscillations.

It was stated by Yavuz [5] and Gursul [39] that these oscillations cause unsteady loading which may cause substantial consequences for wing and tail buffeting, and might play an important role on the control and stability of highly maneuverable aircraft. Menke and Gursul [50] investigated the spectra of difference and average of breakdown locations of a slender wing at high incidences and they have discovered a dominant peak which corresponds to the quasi-periodic antisymmetric oscillations of breakdown location. Same studies were conducted by several researchers in water tunnels and low speed wind tunnels at low and high Reynolds numbers, and they all observed a similar range of dominant frequencies of quasi-periodic oscillations of vortex breakdown location which indicates that this phenomenon exist at both low and high Reynolds numbers.[39].

2.1.2 Vortex shedding

Two point velocity measurement experiments in the wake of a delta wing was conducted by Rediniotis, Stapountzis and Telionis [42, 51] and it was shown that vortex shedding exists at high incidences. They found that both symmetric and antisymmetric modes of vortex shedding existed (Fig. 2.2.). Occurrence of this quasi-periodic phenomenon was found to be over wide range of angles of attack without any substantial effect of Reynolds number. They stated that for a delta wing of sweep angle $\Lambda = 76°$, only symmetric mode of vortex shedding occur up to $\alpha = 70$ deg. angle of attack. At larger angles of attack, both symmetric and antisymmetric modes of vortex shedding exist simultaneously despite the fact that the symmetric mode is more dominant. Gursul and Xie [44] worked on the transition between vortex shedding and helical mode instability. They observed the disappearance of the helical mode instability of swirling flow after the vortex breakdown reaches the apex of the wing, and the appearance of the dominant frequency of vortex shedding in the spectra. They encountered with a rapid transition from helical mode instability to vortex shedding which was occurred at the angle of attack that vortex breakdown reached the apex (Fig 2.3). It was also stated that the frequency of vortex shedding is nearly constant in the near wake.

2.1.3 Vortex wandering

Vortex wandering is an unsteady phenomenon which can be defined as the random displacement of the vortex core [52]. A great deal of effort has been spent on the study of vortices by many researchers, including Schmucker et al. [53], Degani et al. [54], Gursul et al. [52], Kommallein et al. [55], Cornelius [56] and Menke et. al [43], who have revealed the existence of large velocity fluctuations in the vortex core. These fluctuations, which are because of the random displacements of the vortex core, take place over delta wings at upstream of vortex breakdown as well as in the cases without a breakdown, regardless of the Reynolds number and wing geometry. Free stream turbulence was stated as one of the potential sources of vortex wondering, however Menke et al. [43] showed that the vortex core displacements caused by free stream turbulence were much smaller than the considered displacements. The other possibilities that may play a noteworthy role in the occurrence of this phenomenon were stated as the nonlinear interactions between the small scale vortices, mainly due to the Kelvin-Helmholtz instability of the separated shear layer, unsteady turbulent flow in the wake of the wing, and the leading edge vortex over the wing.

2.1.4 Helical mode instability

It is well-accepted that helical mode instability is a well-documented instability which exists downstream of vortex breakdown. Several researchers, including Cassidy et. al [57], Mabey et al. [58], Gursul et. al, [40], Lee et al., [58], and Klute et al.[59] observed these periodic oscillations after breakdown in various swirling flows. The association between downstream convection of wave pattern with vortex breakdown was found in the unsteady pressure measurement experiments conducted on delta wings and fins. The periodic pressure/velocity oscillations that were observed in the experiments correspond to the most unstable modes of the time-averaged velocity profiles of the vortex, which is determined from linearized, inviscid stability analysis. It is stated that these instabilities can be represented as $e^{i(kx+n\emptyset-\omega t)}$, where k is the number of the wave propagating in axial direction, and ω the rotation frequency of the structure. First and second helical mode instability was corresponded by integers n=1 and n=2, respectively. When the first helical mode (n=1) at constant phase surfaces at a given instant is considered, sense of the helix is opposite to the direction of rotation of the vortex, although the rotation direction of the whole structure is same as the vortex. It was also stated that the frequency of the helical mode instability decreases in the streamwise direction, which implies that the wavelength of the helix increases in the streamwise direction.

Knowledge of the dominant frequency of helical mode instability can be useful on buffeting problems. The information in the literature on the dominant frequency of helical mode instability for vortex breakdown naturally occurring over slender delta wings is quite sufficient, and can be used by researchers for rapid calculations. However, these data are not valid for vortex breakdown types induced by other structures of the wing, such as fins, at smaller angles of attack, and there are no available data related to this type of premature breakdown. Variation of the dimensionless frequency fx/U_∞ as a function of angle of attack for delta wings having different sweep angles is given in Figure 2.4 [40].

2.1.5 Shear layer instabilities

The shear layers separated from leading edge roll up periodically into discrete vertical substructures that form leading edge vortices. This instability type occurs on both slender and nonslender wings and was first reported by Gad-el-Hak and Blackwelder [60]. They also stated that two different wings having sweep angles of $\Lambda = 45°$ and $\Lambda = 60°$, had the same frequency at which vortices developed in the shear layer. Cross sectional view of this type instability is given in Figure 2.5 (taken from Riley and Lowson [61]). Instantaneous flow structure of a delta showing the shear layer instabilities is illustrated in Figure 2.6, which is take from Gordnier and Visbal's [15] numerical study.

Both experimental and numerical studies were conducted by several researchers to enlighten how this instability originates, but still there is no universally accepted definition, yet. Researchers have two main arguments on this issue; some of them, including Gad-el-Hak et al. [60], Payne et al. [62], Lowson [63] and Gordnier [64] attributed this instability to two dimensional Kelvin-Helmholtz type instability, whereas Reynolds et al. [65], Ng et al. [66] and Visbal et al. [67, 68] suggested another hypothesis that the interaction between secondary vortex from the wing surface and the shear layer emanating from the windward side of the wing predominantly induce the transverse perturbation of these substructures along the leading edge of the wing. Moreover, Gad-el-Hak et al. [60], Reynolds et al. [65], and Gordnier [64] observed temporal substructures, regarding the vertical substructures of the shear layer, rotating around the leading edge vortex, whereas Squire [69], Payne et al. [62], Lowson [63], Verhagen et al. [70], Washburn et al. [71], Ng et al. [66], Riley et al. [61], Mitchell et al. [72], Morton [73], and Newsome [74] revealed the existence of spatially stationary substructures around the leading edge vortex. In the view of such information, Visbal and Gordnier claimed that these temporal and stationary substructures are not necessarily two distinctly different phenomena, rather representation of the same transition process in different manners. The shear layer and the transition process need to be investigated further. However, providing a complete unsteady data set of the flow field is not feasible due to the spatial and temporal limitations of PIV and Global Doppler techniques, whilst LDA and Hot Wire Anemometry techniques do not provide whole flow field data instantaneously [75]. Therefore, further studies in numerical simulations seem essential in order to characterize this instability.

2.2 Flow Structure on Low and Moderate Sweep Delta Wings

The worldwide need for highly maneuverable and flexible next generation air vehicles is increased the interest to the nonslender delta wings, which are generic planforms of MAVs and UCAVs, and made them a hot topic for the researchers in recent years. Nonslender delta wings have substantially different types of flow patterns when they compared to the slender ones [3]. When it is compared to the extensive studies about the flow structure of slender wings, the knowledge in the literature about this distinctive flow patterns is relatively limited due to the recent interest of this type of wings.

Taylor and Gursul [4] and Ol and Gharib [9] conducted experimental studies to seek the existence of leading edge vortices at low angles of attack. Taylor and Gursul used surface oil flow visualization technique on a $\Lambda = 50°$ wing, whereas Ol and Gharib used flow visualization via dye injection and stereoscopic PIV on $\Lambda = 50°$ and $\Lambda = 65°$ wings. They both revealed the existence of coherent leading edge vortex structure on these wing at angles of attack as low as $2.5°$. A plot from Ol and Gharib's study, showing the spanwise locations of leading edge vortex cores at low angles of attack is given at Figure 2.7. It is stated in the experimental studies of Ol et al. [9], Taylor et al. [4], Yaniktepe et al. [76] and Canpolat [77], and numerical simulation of Gornier et al. [15] that an elongated separated flow region exists at low angles of attack, and very close to surface of the wing. Numerical calculations of Gornier et al. [15] also gave detailed information about the characteristics of averaged and instantaneous flow structure. The Experimental studies of Ol [78], and Ol et al. [79] shows a wake-like velocity profile at low angles of attack, which in line with Gordnier and Visbal's numerical computations [15] that indicates wake-like velocity profile. It was concluded that even at conditions without any discernable vortex breakdown, $\Lambda = 50°$ wing fails to show a significant axial velocity peak, whereas slender wings exhibit a jet-like velocity profile with increasing angle of attack. However, it is found that at higher angles of attack and more typical Reynolds number, a jet-like velocity profile can be recovered.

Taylor, Schnorbus and Gursul [80], and Taylor and Gursul [4] performed dye visualization to visualize the leading edge vortex cores of a flow over a $\Lambda = 50°$ delta wing at low angles of attack and at relatively low Reynolds numbers. They experimentally showed the existence of dual vortex structure, which was observed in the numerical calculations of Gordnier and Visbal [15], for the first time in the literature. The existence of this structure was also confirmed by experimental PIV measurements of Taylor et al. [80] and Yaniktepe et al. [76]. It was found that at low angles of attack and at relatively low Reynolds numbers, flow over a $\Lambda = 50°$ wing exhibits a dual primary vortex system, whereas a transition from this structure to a single and large-scale vortex, which is a basic feature of leading edge vortices of slender wings, occurs at higher angles of attack. Surprisingly, Ol and Gharib conducted flow visualization experiments on the same planform at quite similar range of angles of attack and Reynolds numbers in the same year with Taylor et al. [80]'s study, however they did not observe the dual vortex structure in their study. Wang and Zhang [16] took the studies on dual vortex structure a step further, and they investigated this phenomenon on various delta wings with $\Lambda = 45° - 65°$. They used dye injection and hydrogen bubble visualization techniques to seek the existence of dual vortex structure at various angles of attack and at different Reynolds numbers. They found that this phenomenon is not a distinctive feature of nonslender delta wings, and this structure can exist for slender wings under some certain conditions. They showed the range of angles of attack that dual vortex structure can be observed for each of the wing, which is given in Figure 2.8. They stated that the vortex breakdown location moves upstream towards the apex with increasing angle of attack, and downstream with the increase of sweep angle. Moreover, they reported that for any given angle of attack, a decrease in the sweep angle of a delta wing causes a vortex breakdown location that is closer to the apex of the wing.

Flow visualization studies of Taylor et al. [80], and Taylor and Gursul [4] on a $\Lambda = 50°$ wing, revealed the sensitivity of the vortex structure to Reynolds number. They stated that the trajectory of the vortex core moved inboard towards the centerline, and the onset of breakdown was discernibly delayed when the Reynolds number is reduced. It is also reported that the flow approaches an asymptotic state at high Reynolds number (on the order of $3x10^4$), and only small variations in the location of vortex core and breakdown occur with a further increases in the Reynolds number. Wang and Zhang [19] investigated the Reynolds number effect on flow over various delta wings with $\Lambda = 45° - 65°$. They found that Reynolds number has a significant influence on the generation of dual vortex structure. It is stated that at low Reynolds numbers, the high shear forces on the separated flow prevents the generation of dual vortex structure, thus, the Reynolds number should be greater than a critical value in order to have a dual vortex structure on the flow at certain ranges of angles of attack. They also reported the influence of Reynolds number on the breakdown locations of the dual vortex structure.

Honkan and Andreopoulos [81] performed an experimental study on a nonslender delta wing of sweep angle $\Lambda = 45°$ with novel triple orthogonal hot wire probes. They observed patterns of instantaneous vorticity and showed the existence of discrete stationary vortices in the feeding shear layer in addition to the primary vortex. Taylor and Gursul [4] investigated the reattachment process, near surface topology and buffeting of a flow over a delta wing of sweep angle $\Lambda = 50°$ via PIV technique. They found that the region of large velocity fluctuations occurred at the same location as the reattachment line of the shear layer which was in good agreement with Honkan et al. [81]'s study. It was noted that the primary reattachment line moves inboard, toward the wing centerline, with increasing the angle of attack. A figure from Taylor and Gursul's study, showing the inboard progression of the primary attachment line is given in Figure 2.9. Taylor and Gursul stated that the reattachment of the shear layer induces the main source of buffeting on the surface of the wing as opposed to vortex breakdown. They also reported the existence of spectral peaks in the velocity fluctuations just before the stall in the field of reattached shear layer. Gursul et al. [3] stated that the attachment of shear layer that is separated from the leading edge of a low sweep delta wing is one of the distinct features of a nonslender wing flow structure.

Yaniktepe and Rockwell [76] performed PIV experiments at different angles of attack over a delta wing of sweep angle $\Lambda = 38.7°$. They observed the formation of an elongated vorticity layer that tends to reattach the surface of the wing. They also found high vorticity concentrations enclosed with the shear layer which concurred with fields of high unsteadiness in the flow. Yavuz et al. [82] investigated the flow structure immediately adjacent to the surface of a delta wing of sweep angle $\Lambda = 38.7°$ via near surface technique of PIV. A PIV result from their study, which shows the shear layer substructures, is given in figure 2.10. They showed the distributions of time averaged flow data are symmetric with respect to the centerline of the wing, and exhibiting well-defined vorticity concentrations of like sign along the leading edges of the wing. They stated that the mentioned results indicate the existence of small scale vorticity concentrations having a co-rotating pattern.

McClain [84], Kawazoe et al. [85], Miau et al. [83], and Kegelman et al. [86] investigated the influence of the leading edge profile on the flow structures of various delta wings. It is stated that leading edge shape can affect the basic flow features of delta wings, especially the nonslender ones. McClain used delta wings of sweep angle $\Lambda = 50°$ that have different leading edge profiles. They observed the region of reattachment more outboard, which means a delay in the stall, for all the wings having rounded edges. Figure 2.11 shows the location of reattachment line for various leading edge profiles as a function of angle of attack [84]. They also reported that the wings with rounded edges showed significant delays on measured lift coefficients. Kawazoe et al. studied the effect of leading edge profile on a delta wing of sweep angle $\Lambda = 45°$, and they came up with results in agreement with McClain's results, which indicate a delay in the stall for rounded leading edge shape due to reaching of primary reattachment line to wing centerline at larger angles of attack. Miau et al. used delta wings of sweep angle $\Lambda = 50°$ that having different leading edge profiles. Based on the experiment that were conducted at low Reynolds number (Re=7000) where the viscous forces are dominant, they reported a strong influence of leading edge profiles on the separation and formation of the leading edge vortices. They observed that at this low Reynolds numbers, the flow over wings with leeward beveling greater than $60°$ was devoid of strong leading edge vortices at $\alpha = 10°$. They also performed force measurements at higher Reynolds numbers and observed the effect of leading edge profile is small in the pre-stall region. Kegelman reported that the vortex breakdown location is strongly affected by the leading edge profile for slender wings, although no change in stall angle was detected. Moreover, the influence of leading edge shape in lift is weak for slender wings. It was also stated that wings with rounded leading edges generally have a milder stall. In a recent study, Verhaagen [87] investigated the effect of leading edge radius on the flow over delta wing of sweep angle $\Lambda = 50°$. It is stated that a larger a larger leading edge radius results in a reduction in both size and strength of the primary vortex, and a movement of this vortex outboard and closer to the wing surface.

Canpolat et al. [88] investigated the yaw angle effect on the flow structure of a delta wing with a sweep angle of $\Lambda = 45°$. They observed a symmetrical flow structure on the wing when the yaw angle is $\theta = 0°,$ as it was expected. When they increased the yaw angle, it was observed deterioration in the symmetric flow structure. They stated that the vortex breakdown that occurs on the windward side of the delta wing is earlier than the one on leeward side. They also reported that the main rotating vortices in crossflow planes occur in the inner side, close to the centerline of the wing.

Air vehicles, which have complex geometries, can have delta wings as part of these complex structures. Diamond and lambda type wings, which have low sweep delta wing on their geometry, are good examples to those structures. Yayla [89] investigated the flow structure via dye visualization and PIV measurements at near surface and various cross sections on these types of wings. X-45, which is an actual UCAV, has a very complex geometry, and both the fuselage and wing extensions have low sweep delta wings. Elkhoury et al. [90, 91] conducted dye visualization and complementary PIV measurements on crossflow and near surface planes on an X-45 planform in order to investigate the mean and unsteady flow structure and flow topology. A figure from their study, which compares the patterns of dye visualization and near surface patterns of streamline topology, is given in Figure 2.12.

2.3 Control of Flow Structure on Delta Wings

Control of the flow on various air vehicle planforms was emerged from the need for an increase in flight performance and stability of air vehicles, as well as to reduce the effects of the unsteady loading on structures such as wing and fins. The main objectives of flow control on wings are elimination of three-dimensional separation, delaying or preventing vortex breakdown and increasing the lift.

Control of flow generally classified into two groups, active and passive control of the flow structure. Passive flow control do not require any energy input and any feedback mechanism, and can be applied by adding control surfaces to the wing such as canards, strakes, flaps and leading edge fences. Passive control can also be applied by using variable-sweep or flexible delta wings. On the other hand, active flow control requires an energy input in order to manipulate the flow structure over the wing. There are various applications of active control such as continuous or oscillating blowing and suction from different regions of wing, piezoelectric and acoustic excitation, and small and large scale perturbations.

2.3.1 Passive Control

The flow structures of slender and nonslender wings are quite different than each other, as a result the passive flow control method that would be used to manipulate the flow over a delta wing is highly depend the type of the wing.

Mitchell and Delery [92] stated that the passive control of a flow over nonslender wings can only be achieved either by increasing the wing flexibility or using additional flow control surfaces on the wings. Gursul et al. [17] stated that the methods that aim reattachment of the flow to the wing surface are the most effective ones on nonslender delta wing, and the only possible method by means of passive control on nonslender wings for this purpose is the increase of wing flexibility. Taylor et al. [93, 94] investigated the effect of wing flexibility on various delta wings having sweep angles of $\Lambda = 40°, 45°, 50°, 55°, 60°$. They found that the stall was delayed and the lift force was increased only in wings having low sweep angle. Vardaki et al. [95] performed a similar study on delta wings of sweep angles $\Lambda = 50°$ and $60°$, and they obtained the same results with Taylor et al. They also stated that the excitation of shear layer instabilities and promotion of reattachment of the shear layer is the main mechanism for lift enhancement.

For slender delta wing, flow control techniques that aim to control breakdown of a vortex are have a significant place among the other techniques. Gursul et al. [17], and Mitchell et al. [92] stated that various passive control techniques, such as canards, apex flaps, leading edge flaps and extensions and Gurney flaps, can be used on slender wings in order to control the breakdown of a vortex. Myose et al. [96] showed that a canard that attached on a 60-degree sweep delta wing delayed both the vortex breakdown and three-dimensional surface flow separation. Spedding et al. [97]'s study showed that the strength of leading edge vortices of a delta wing having leading edge flaps is twice of the other one without these flaps. Lamar and Campbell [98] found that the leading edge flaps that bended upwards decreased the drag on the wing, whereas the ones that bended downwards increased the lift force and drag. Klute et al. [99] investigated the effect of apex flap on the flow structure over a delta wing flow. They found that breakdown of the vortex was delayed on both cases, where the flap was stationary and was bended. They also reported that the longest delay was occurred when the apex flap bended with an angle toward negative direction. Bucholz et al. [100] investigated the effects of leading edge fences and Gurney flaps on a flow over a 60-degree sweep delta wing, and they found that both method resulted in high lift gain.

2.3.2 Active Control

Active flow control can be applied in various ways. Control of the flow by suction and blowing have been performed by many researchers and can be categorized into different groups such as leading edge suction and blowing, trailing edge blowing, tangential blowing and leeward surface suction. This method can also be applied in different manners such as symmetric, asymmetric, periodic and steady suction and blowing. Wood et al. [101], Greenwell et al. [102], Bean et al. [103], and McCormick et al. [104] et al. employed steady suction and blowing, whereas Gad-el-Hak et al. [105] and Gu et al. [106] performed periodic tangential blowing and suction along the leading edge. Ferman et al. [107] studied the effect of tangential blowing on a model of F-15 aircraft by blowing from three different points chosen upstream of vortex breakdown. Chui et al. [108, 109] investigated the effect symmetric and differential blowing from forebody slots in their studies. A figure from their work, which shows the effects of both passive (canard) and active (blowing) flow control, is given in Figure 2.12. Vorobieff et al. [110] employed intermittent trailing-edge blowing to prevent vortex breakdown in their study. Johari et al. [111, 112] implemented a new method of blowing called "recessed angled spanwise blowing" at different angles from surface port located below the vortex core. Maines et al. [113] investigated the effectiveness of leading-edge suction through a line of holes on both sides of a delta wing. Badran et al. [114] tried both leading edge suction and suction from the upper surface of a wing, whereas Hummel [115] employed suction at the trailing-edge. Owens et al. [116] applied a suction boundary layer from the suction side surface of a wing in order to manipulate the breakdown location. Helin et al. [117], Shih et al. [118], Mitchell et al. [119] and Phillips et al. [120] studied blowing from trailing-edge and showed its' effectiveness on the flow characteristics and onset of vortex breakdown. Nawrocki [121] and Wang et al. [122] took the research on trailing-edge blowing one step further by investigating jet vectoring. Deng et al. [123] focused on another active flow control method, and they investigated the effects of oscillating leading-edge flaps on flow structure of a slender delta wing and showed a strong dependence between oscillation amplitude and vortex breakdown.

The effort that has been devoted to control of the flow structure on low sweep wings is very little compared to the studies on high sweep wings. However, active flow control studies on nonslender slender delta wings have shown an increase in recent years. Yavuz et al. [124, 125] prevented three-dimensional separation from the surface by using steady trailing-edge blowing on a 35-degree sweep delta wing. Williams et al. [126] studied on the same planform and investigated the effects of oscillatory blowing from the leading-edge. Wang et al. [127] and Jiang et al. [128] employed trailing-edge blowing on 50-and-65-degree sweep delta wings. Wang et al. studied the interaction of thrust vectoring jets with leading edge vortices and its effects, whereas Jiang et al. sought the effects of blowing on wing aerodynamics. Vardaki et al. [129] and Yaniktepe et. al. [76] studied the effects of small amplitude wing oscillations on delta wings at post-stall regime and they showed that the totally separated flow can be reattached on oscillating low and moderate sweep delta wings, which was illustrated in Figure 2.13. Ozgoren et al. [130] and Yilmaz et al. [131] performed similar flow control studies and they investigated the flow structure of delta wings subjected to small amplitude perturbations.

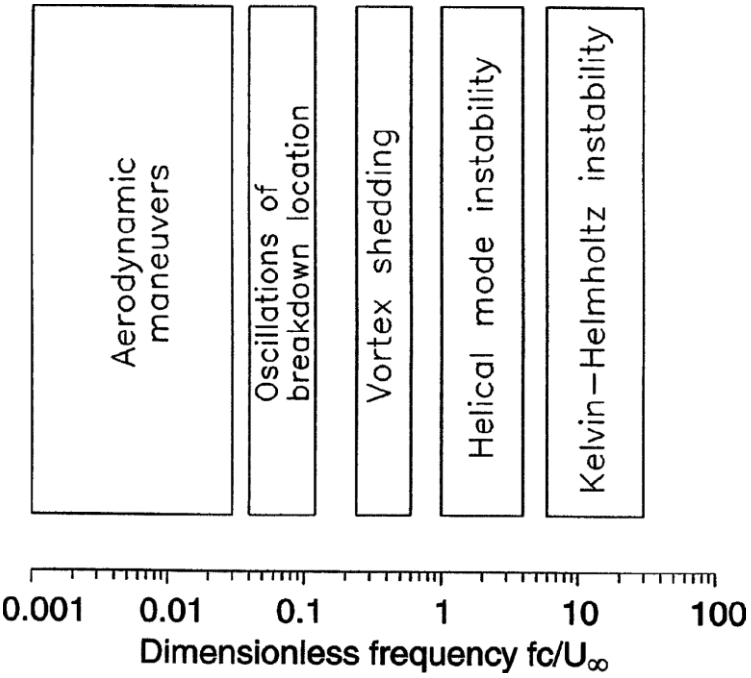

Figure 2.1 Spectrum of unsteady flow phenomena over delta wings as a function of dimensionless frequency [36]

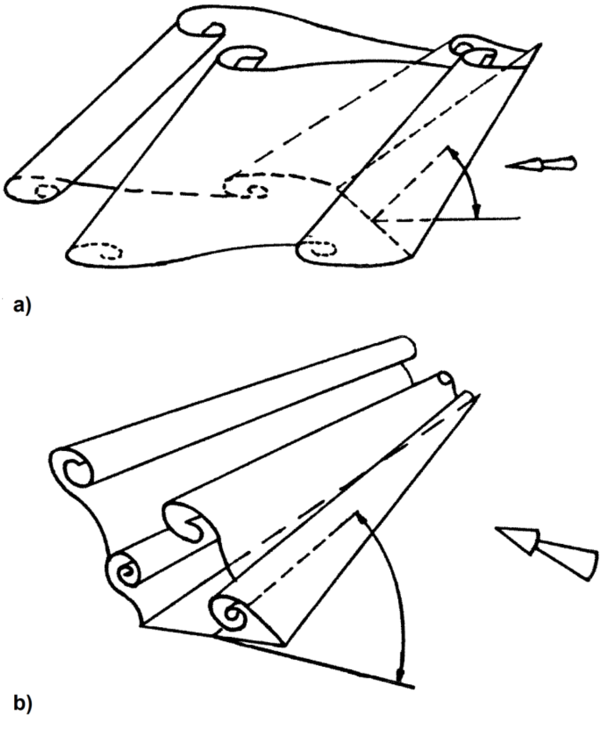

Figure 2.2 Vortex shedding from a slender delta wing [51] a) symmetric and b) antisymmetric modes

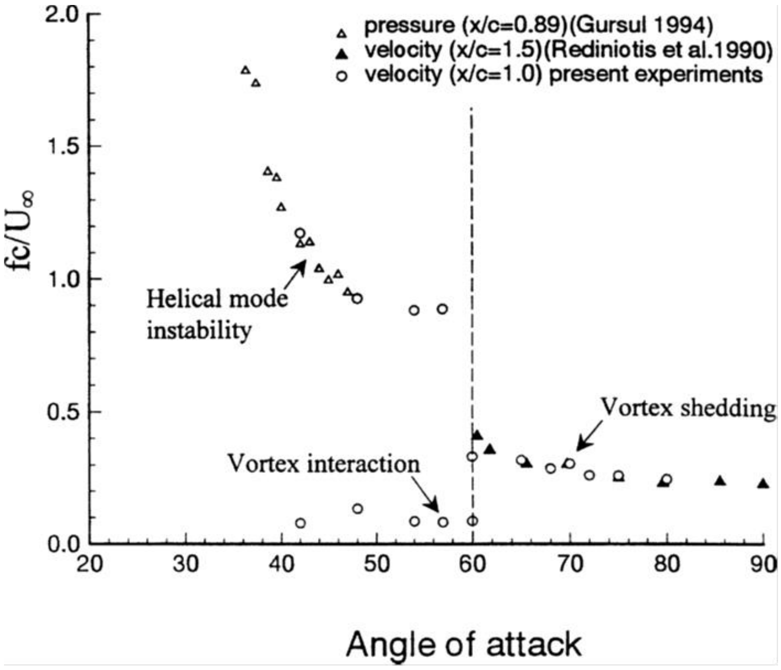

Figure 2.3 Variation of dimensionless frequency for unsteady phenomena as a function of angle of attack [44]

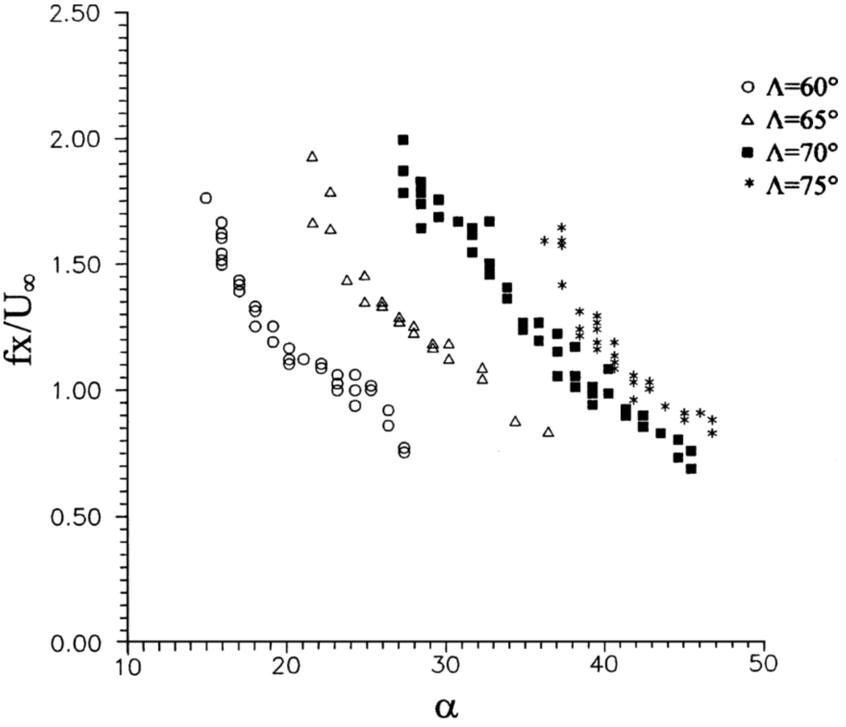

Figure 2.4 Variation of dimensionless frequency as a function of angle of attack for different sweep angles [40]

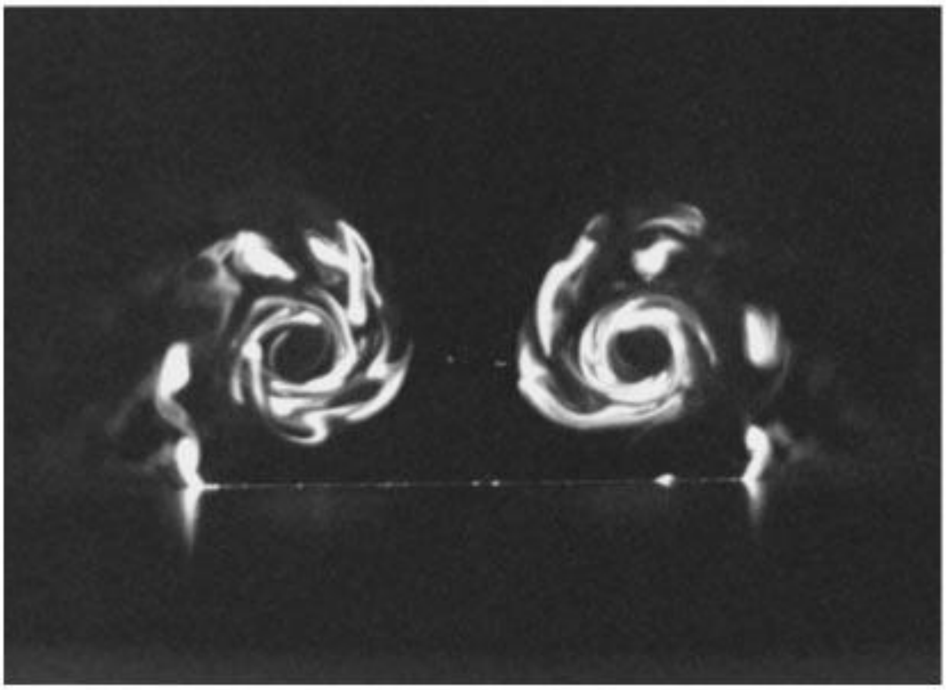

Figure 2.5 Cross-sectional view of the unsteady instability [61]: $\Lambda = 85°$, $\alpha = 12.5°$, *x/c* = 0.6, Re_c = 164900

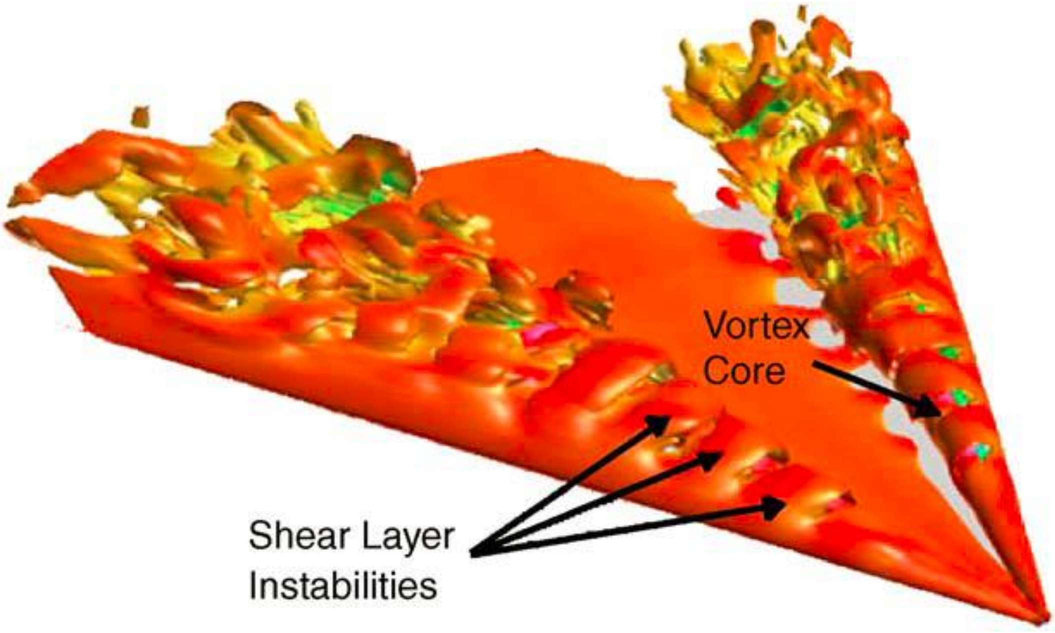

Figure 2.6 Instantaneous vortex structure over a $\Lambda = 50°$ wing at $\alpha = 15°$[15]

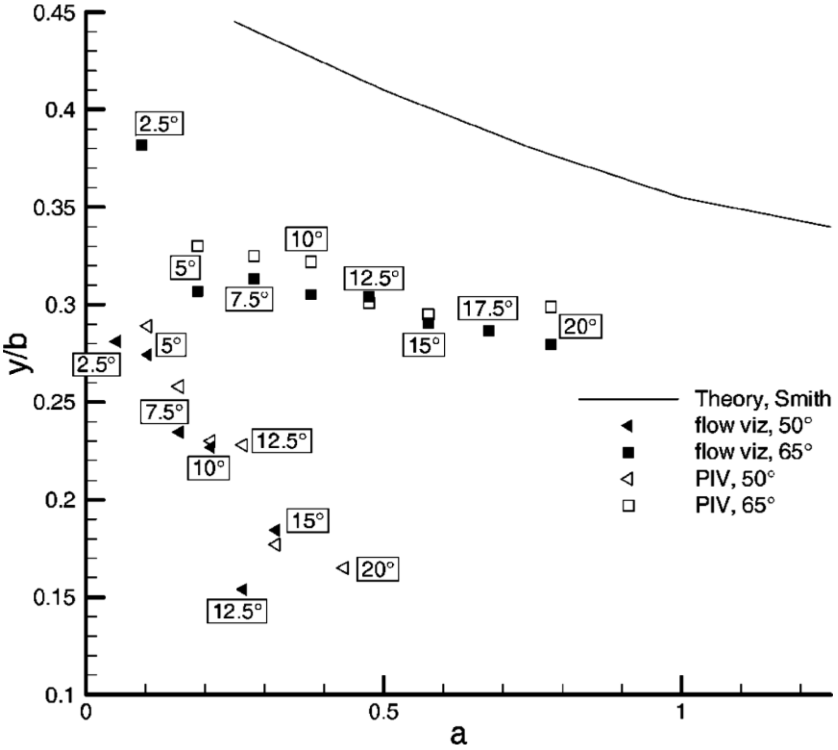

Figure 2.7 LEV core spanwise location [9] for 50-and 65-degree wings measured at *x*/*c* = 0.296

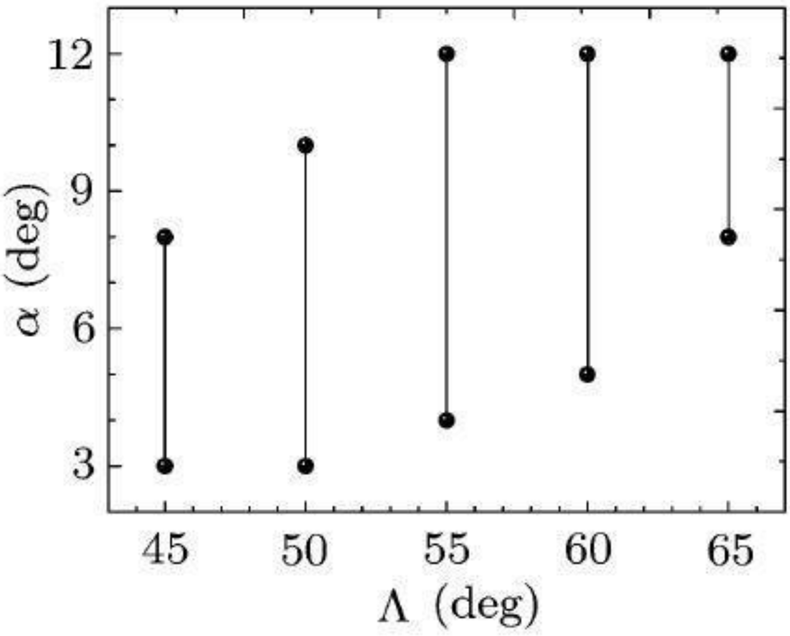

Figure 2.8 Range of α for the existence of dual vortex structure [19]

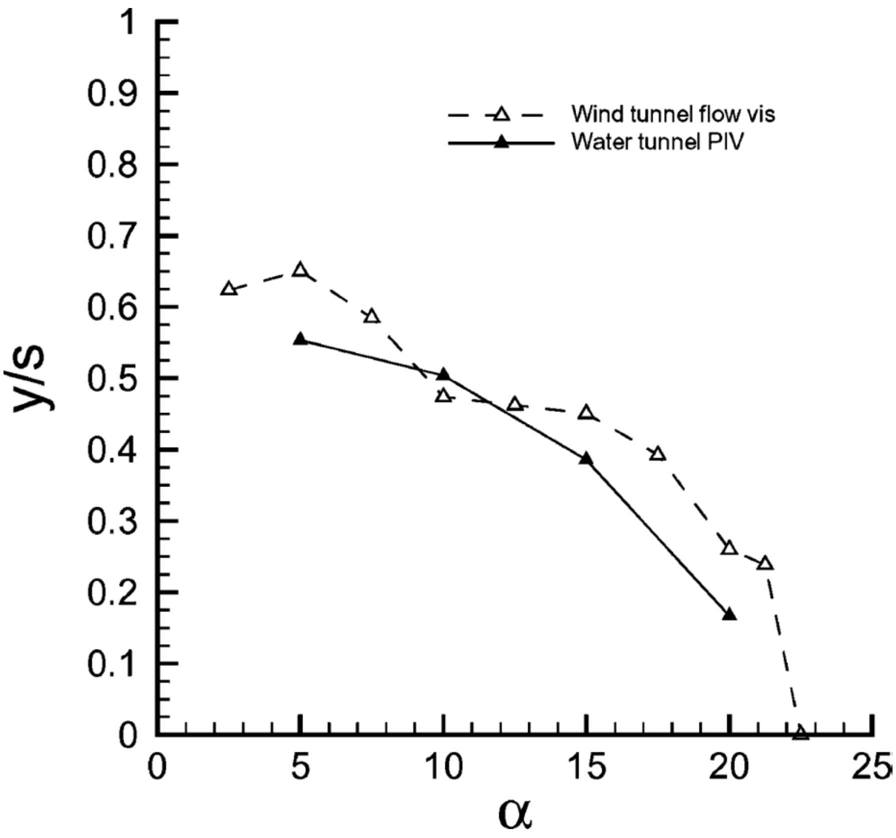

Figure 2.9 Variation of spanwise location of reattachment line with incidence for water-tunnel and wind-tunnel models [4]

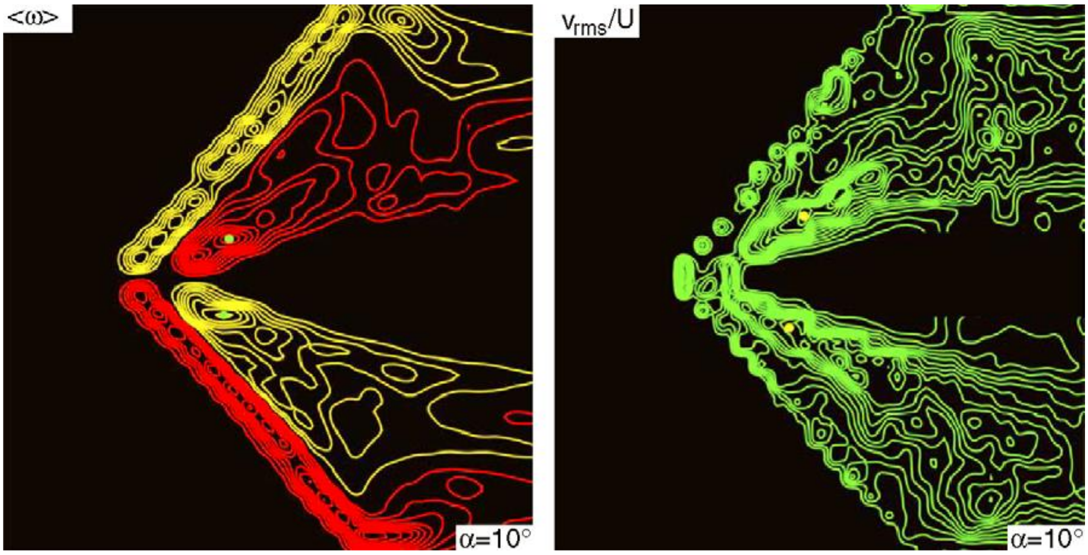

Figure 2.10 Shear layer substructures visible in the PIV measurements of Yavuz et al. [82] for a $\Lambda = 38.7°$ sweep wing on a plane parallel and immediately adjacent to the surface of the wing

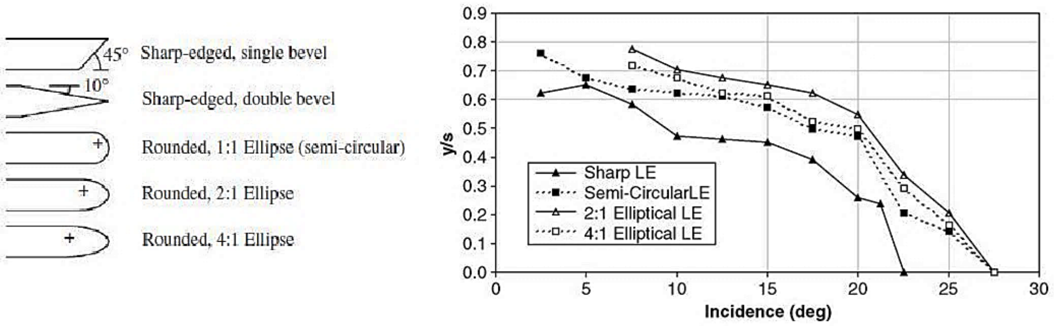

Figure 2.11 Location of reattachment line as a function of angle of attack [83] for various leading-edge shapes, having thickness to chord ratio of 4%

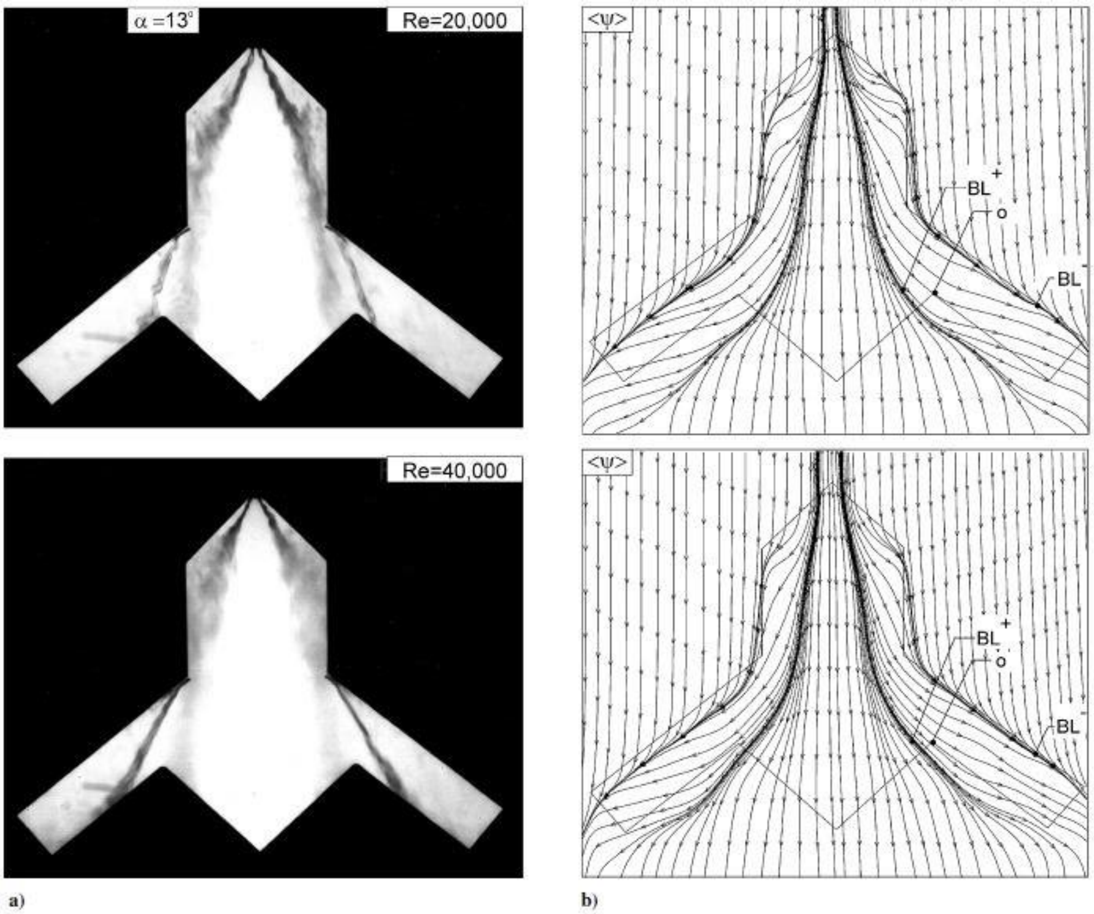

Figure2.12 Comparison of patterns of dye visualization with near-surface patterns of streamline topology (Ψ), moderate angle of attack α=13 deg over range $Re=2\times10^4$–4×10^4

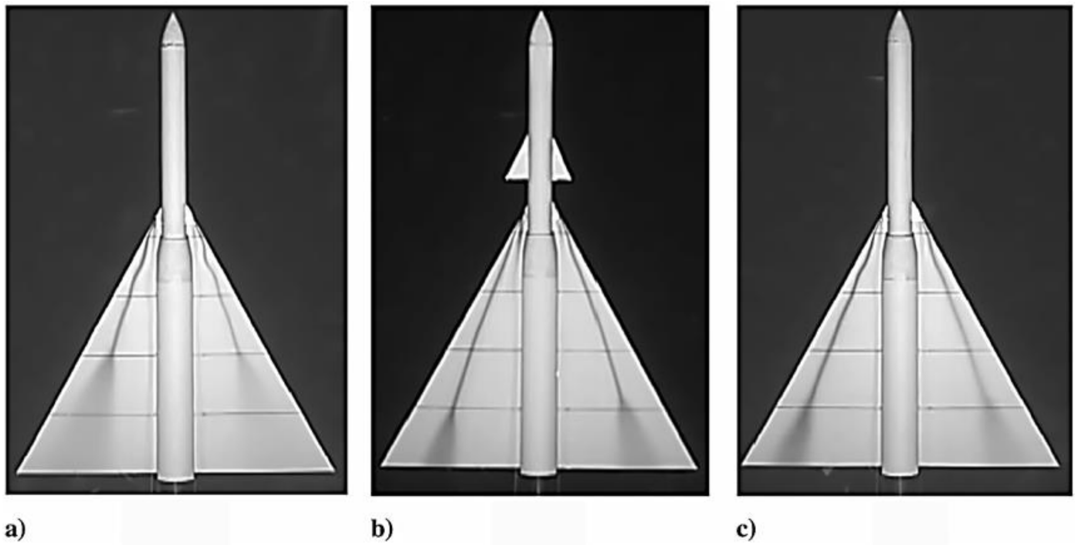

Figure 2.13 Effects of canards and double-sided forebody slot blowing [109] on the vortex breakdown location at $\alpha = 20°$ and Re = 6.8 x 10^4 for a) basic configuration, b) basic configuration with canards, and c) basic configuration with double-sided slot blowing at Cμ = 0.2

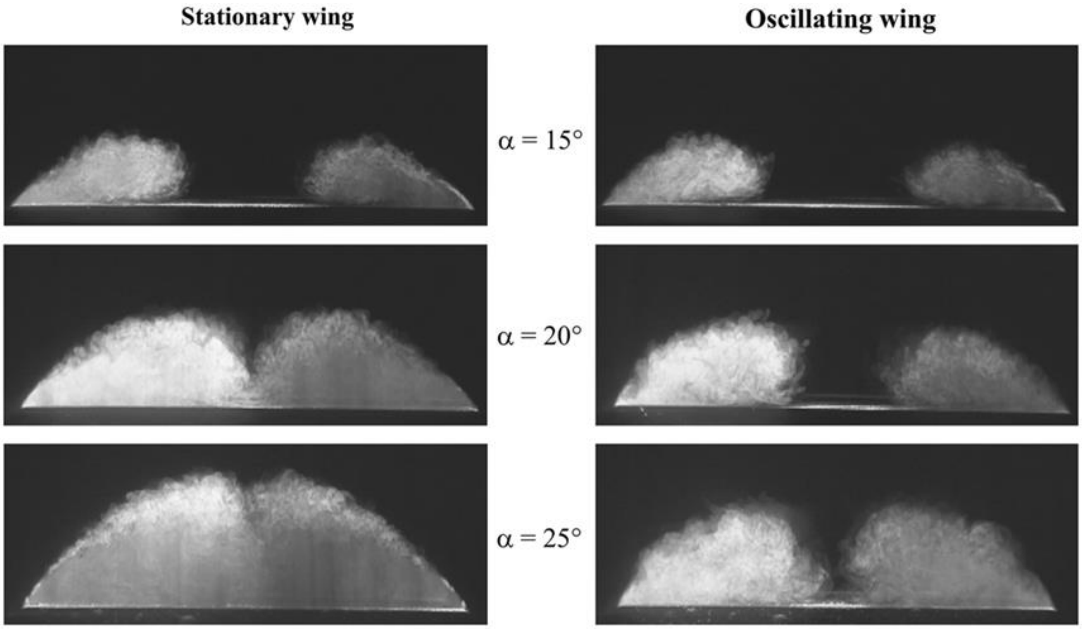

Figure 2.14 Time-averaged laser fluorescence flow visualization [129] for stationary (Sr = 0) and oscillating wings (Sr = 1.0, $\Delta\emptyset = 1$ deg), $\Lambda = 50$ deg

CHAPTER 3

EXPERIMENTAL SYSTEM AND TECHNIQUES

3.1 Tunnel Facility

All the experiments were conducted in a low speed, suction type, and open-circuit wind tunnel set in Fluid Mechanics Laboratory of the Mechanical Engineering Department at Middle East Technical University. The tunnel consists of five parts; namely, settling chamber, contraction cone, test section, diffuser and drive section. The whole tunnel facility is illustrated in Figure 3.1.

There are two inlet sections at sides of the tunnel entrance for air inlet. Fine mesh screens are installed at both inlets in order to prevent the entrance of any foreign objects and increasing the air uniformity. The total length of the entrance section is 2700 mm. A honeycomb and three fine mesh screens are used in this section for maintaining the turbulence intensity in low levels and increasing the uniformity of the flow.

A contraction cone takes part between the settling chamber and test section of the tunnel. The purpose of the contraction cone is turning the large volume of air into a small volume, and increasing the flow speed before it enters to test section part. The one that used in the wind tunnel facility has a total length of 2000 mm and a contraction ratio of 8:1.

A fully transparent test section of dimensions 750 *x* 510 *x* 2.000 mm is designed and fabricated for the experiments. The former one was semi-transparent and was not suitable for image capturing in flow visualization studies on a plane parallel to vortex core. Figure 3.2 illustrates the fabricated test section which was used in this research study. Although up to 30 m/s velocities can be reached in the test section area of the tunnel, the tunnel was run on between 0.85 – 15.85 m/s velocities because these values were enough to reach the desired Reynolds numbers based on the chord length of the wing. Experiments are conducted in the test section of the wind tunnel at different angles of attack and at a wide range of Reynolds number as it is illustrated in the experimental matrix given in Figure 3.3.

Diffuser is a gradually-expanding passage for the high speed air coming out of the test section. The main purpose of this part is increasing the pressure of the flow by decreasing its velocity, which yields a reduction on the power needed to drive the tunnel facility. The cone angle of the current diffuser is 3°, and its total length is 7300 mm.

An axial fan assembled at the exit part of the diffuser was used via a remote control unit to power up the wind tunnel.

3.1.1 Wind tunnel characterization

The velocity measurements in the test section of the tunnel were employed at different fan powers, both directly by Laser Doppler Anemometry (LDA) technique at a point located indirectly by Pitot - static tube pressure measurements using both inclined manometer and pressure scanner in order to obtain the calibration curve of the tunnel before the experiments commence. Velocities are calculated indirectly from the dynamic pressures obtained from Pitot - static tube taking the ambient temperature and humidity, and the elevation of the lab into account. The velocities calculated from the inclined manometer measurements are found to be the same with the ones that calculated from pressure scanner measurements. However, the velocities that were directly measured using LDA technique are found to be slightly higher than the velocities calculated from the Pitot – static tube measurements. Therefore, the average of the aforementioned velocities are calculated and assumed to be the exact velocities in the test section for corresponding fan powers. The expected error in these velocities is found to be around 3% according to the differences in the velocity measurement results. The average velocities are tabulated in Table 3.1, and the calibration curve of the tunnel is calculated from these velocities by curve fitting method in Excel as it is seen in Figure 3.4. It was noticed that the calibration curve well fits to a linear curve for fan power values greater than 6%, however the remaining curve for the fan power values less than 6% fits to a polynomial curve which was caused by the high losses on the fan at the low power values. Moreover, a necessity to seek the uniformity of the flow in the test section at very low velocities is came up due to some of the experiments, which are planned to be conducted at very low velocities. Thus, the flow in the test section was traced by Laser Doppler Anemometry (LDA) method at two different low velocities where the higher one corresponds to a Reynolds number close to the minimum Reynolds numbers of the planned experiments. Results of the measurements, which are given in Figure 3.5, shows that the maximum difference in the velocities at various points in the test section do not exceed 5.7% at these low velocities. LDA method is also used to determine the turbulence intensities in the test section at wide range of velocities. It is found that the turbulence intensities in the test section, which are tabulated in Table 3.2, do not exceed 1%.

Table 0.1 Results of velocity measurements and their average inside the test section at different fan powers.

	Fan Power (%)														
	4.5	10	15	20	25	30	35	40	45	50	55	60	65	70	75
Average velocities in the test section (m/s)	0.798	2.220	3.622	5.101	6.561	8.072	9.518	11.117	12.674	14.100	15.777	17.253	18.588	20.096	21.491

Table 0.2 Turbulence intensities that were measured via LDA in the test section at different velocities.

Velocity (m/s)	Turbulence Intensity (%)
1.06	0.783
3.47	0.928
6.36	0.754
9.12	0.807
12.20	0.865
16.70	0.931
20.72	0.862

3.2 Wing Model and Mount

The delta wing that was used in this study has a sweep angle of $\Lambda = 45°$, a chord of 150 mm and a span of 300 mm. The wing was made of fine polyamide PA2200 and its thickness is 15 mm. The leading-edges were beveled on the windward side at an angle of $45°$. A two-dimensional sketch that shows the lower surface of the wing at plan-view is given in Figure 3.6.

Wing dimensions are determined considering the test section dimensions of the wind tunnel and the blockage ratio of the prospective wing. The maximum blockage is calculated to be 1.32% at 13 degrees angle of attack which was the highest degree used in this study.

The number of pressure taps and their locations at each station on the wing are determined so as to have as much as possible taps on the wing surface to have high resolutions at the experiments. Limitations of fabrication techniques were also considered in order not to encounter with any problem during the manufacture process. Furthermore, the diameter of pressure taps on the wing surface are selected as to have 0.5 mm diameter so as not to have a significant disturbances in the flow structure on the wing surface. The designed wing model has 74 pressure taps on the lower surface of the wing, which were symmetrically distributed to three spanwise stations located at chordwise distances of $x/c = 0.32,\ 0.56$ and 0.80 at both left and right halves of the wing as it is seen in Figure 3.6.

Smoke visualization process requires smoke injection holes on the wing in order to successfully introduce the smoke to the flow. The aim of these holes is to generate streaklines to trace the leading edge vortices, to provide the visibility of flow structures over the wing, and to provide seeding particles for LDA measurements. Four small smoke visualization holes near the apex of the wing are designed and combined with a bigger hole, which is supposed to transform the smoke from the smoke generator to the smoke holes, drilled in the wing from the tail to the tip in chordwise direction.

The designed wing has a very complex structure as shown in Figure 3.7; therefore it could not be manufactured in a single piece by traditional methods and materials. As a result, a non-traditional fabrication method, rapid prototyping (stereolithography) is selected for the fabrication of the wing. The fabricated wing is illustrated in Figure 3.8 from different views.

Rapid prototyping is a computer aided manufacturing method which is used to fabricate the desired parts or assemblies rapidly. This method has also been referred to as layered manufacturing since it divides the part into layers than fabricate one layer at a time and moves to the next layer at the next step. Hence, the part grows layer by layer. The manufacturing process ends when the last layer is fabricated. There are various commercially available Rapid Prototyping techniques such as Stereolithography, Laser Sintering, Fused Deposition Modeling and Solid Ground Curing. These techniques differ from each other by the materials that were used in fabrication and the manufacturing methods. The wing that was used in this study was made of fine polyamide PA2200, and manufactured by laser sintering based rapid prototyping machine, branded EOSINT P380. The build volume of the machine is 320x320x600 mm^3. The working principle of the machine is layer-wise solidification of the thermoplastics (i.e. polyamide, polystyrene) by means of a CO_2 laser. The powdered thermoplastic absorbs the energy supplied by the laser which leads to a local solidification of the material. The strength of the part is increased by the compress applied by the blade of the recoating system which is used to apply powder to the process chamber. The layer thickness that was processed at each step is 0.15 mm, and the minimum diameter of the zone that can be traced by the laser head is 0.6 mm.

A specific mount was designed and manufactured in order to keep the wing stable in the test section without inducing a significant disturbance in the flow field of the delta wing. The manufactured mount is capable of giving angle of attack, yaw and roll angles to the wing at the same time. In order not to disturb the flow downstream of the wing and decreasing the support effect on the flow, a thin steel rod with a 10 mm diameter was used as a support. The wing, mount and test section assembly is shown in Figure 3.9.

3.3 Qualitative Measurement

Laser illuminated flow visualization was employed as a qualitative measurement technique.

3.3.1 Laser illuminated flow visualization using smoke

Flow visualization is a simple and cheap technique to observe the flow structure and direction. The necessity of using smoke with this technique arises from the invisibility of the most fluid flows to the human eye. Introducing smoke to a flow field makes the flow observable and traceable. One important point is the term smoke does not always limited to combustion products but can also be vapor, steam and mist. As stated by Merzkirch [132], these substances are not neutrally buoyant tracers due to having densities significantly larger than the density of air, but the buoyancy effects can be considered as negligible since the particles have diameters less than 1 μm.

Although there are various methods to generate smoke, vaporizing mineral oils is a common method used in laboratory experiments and there are commercially available smoke generators for this purpose. The one used in this study is based on the vaporization of kerosene (paraffin) mist and it consists of a heating element and a device that mixes the mist with pressurized carbon dioxide (illustrated in Figure 3.10). The flow rate of the smoke introduced to the flow field was adjusted by increasing or decreasing the pressure of the carbon dioxide gas flowing into the smoke generator.

Introducing smoke into the fluid flow does not always enough to visualize a flow if flow structures like wakes, vortices and separation are of interest. One should use an illuminated plane sheet in order to make that particular flow structures visible, and this can be done by a laser light sheet created by a laser source and some optics. In this study, a Diode-pumped solid-state (DPSS) green laser with 532 nm wavelength and 400 mW power output and a cylindrical lens were used to create light sheets at planes normal to the wing surface and a plane parallel to the leading edge vortices. The locations of the planes normal to wing surface are x/c=0.32, x/c=0.56 and x/c=0.80 which are also the locations of three pressure tap stations respectively. A Canon 50D Digital SLR camera was used to capture images at all planes. The aperture size set to the values which provided clear views of flow structures, and the shutter speed was varied in the range of $1/30$ and $1/200$ second with the same purpose. A mirror having $45°$ angle with flow direction was mounted into the test section at far downstream of the wing for taking the cross-flow images from the side window of the test section as illustrated in Figure 3.11. The images showing the flow structure near the wing surface (parallel to leading edge vortices) were taken from the bottom side of the fully transparent test section as illustrated in Figure 3.12.

3.4 Quantitative Measurements

Quantitative pressure and velocity measurements were done using a 16-channel pressure scanner and Laser Doppler Anemometry.

3.4.1 Pressure measurements

Pressure measurements were conducted using a Netscanner 9116 Intelligent Pressure Scanner (illustrated in Figure 3.113), which integrates 16 silicon piezoresistive pressure sensors with a range of 0 – 2.5 kPa. Each sensor incorporates with a temperature sensor. The system is factory-calibrated over the specified pressure and temperature spans and the calibration data is stored in the EEPROM's of each transducer. Before the pressure data is transferred to the host computer, microprocessor of the system compensates transducer outputs for offset, nonlinearity, sensitivity, and thermal effects utilizing the calibration data and the temperature data obtained from the temperature sensors. By this way, the system guarantees a measurement resolution of $\pm 0.003\%$, a static accuracy (includes the combined errors due to non-linearity, hysteresis, and non-repeatability) of ± 0.15, and a total thermal error of ± 0.0015 on full scale.

There were 74 pressure taps of 0.5 mm diameter on the windward side of the wing. The first 37 taps were located on the left half of the wing, and the other 37 are located on the right half of the wing. The taps on the both sides of the wing are divided into three groups in such a way that all the groups are positioned at three different chordwise locations corresponding to x/c=0.32 (first station), x/c=0.56 (second station) and x/c=0.80 (third station). Figure 3.6 shows the locations of the pressure taps on the schematic of the wing. Preliminary measurements are performed on all stations at both half of the wing at different angles of attack and Reynolds numbers. Results of these preliminary measurements showed a symmetrical structure in pressure distributions on the full wing. For simplicity, all the pressure measurements that were illustrated in this study are employed on the pressure taps located on left half the wing due to the existence of symmetrical flow structure below the wing at various angles of attack and Reynolds numbers.

Each tap is connected to the pressure scanner and the samples were taken at 500 Hz and each tap was measured for 10 seconds. However, due to the limited number of pressure channels of the measurement system, all the pressure taps on the wing surface could not scanned at the same time. Therefore, all the taps of first station and first nine taps of the second station were scanned first, and then the last three taps of second station which are closest to the leading edge of the wing, and some taps of third station, which are illustrated in Figure 3.8, were connected to the pressure scanner and scanned under the same experimental conditions.

Dimensionless pressure coefficients are calculated from Equation 3.1 using the measurement data of each pressure tap in order to demonstrate the relative pressure distribution on the wing surface at three different spanwise stations. Root mean square (RMS) calculations are performed from Equation 3.2 to obtain the unsteady fluctuations in the pressure, and using Equation 3.3 the results are converted into fluctuations in pressure coefficient and added to unsteady pressure distribution charts as error bars at respective spanwise points. All the calculated C_p values and their fluctuations are plotted as $-C_p$ distribution on the surface of the wing at the results section.

$$C_p = \frac{p - p_\infty}{\frac{1}{2}\rho u_\infty^2} = \frac{p - p_\infty}{p_{dyn.}} \tag{3.1}$$

p : Measured static pressure at an instant

p_∞ : Static pressure of the flow

$p_{dyn.}$: Dynamic pressure of the flow

ρ : Density of the fluid

u_∞ : Freestream velocity of the fluid in streamwise direction

$$p_{R.M.S.} = \sqrt{\frac{\sum_{i=1}^{N}[(p_i - \bar{p})^2]}{N}} \tag{3.2}$$

N : Number of samples in the measurement

p : Measured static pressure at an instant

$\bar{p}$: Average of the static pressure at the end of the measurement

$$C_{p,\ R.M.S.} = \frac{p - p_\infty \pm p_{R.M.S.}}{p_{dyn.}} = C_p \ \pm \frac{p_{R.M.S.}}{p_{dyn.}} = C_p \ \pm \frac{\sqrt{\frac{\sum_{i=1}^{N}[(p_i - \bar{p})^2]}{N}}}{p_{dyn.}} \tag{3.3}$$

3.4.2 Velocity measurements via Laser Doppler Anemometry

Laser doppler anemometry (LDA) is a non-intrusive, pointwise velocity measurement technique that has widespread applications such as laminar and turbulent flows, subsonic and supersonic flows, combustion, aerodynamic and hydrodynamic investigations, turbines, mixing phenomena, velocity and vibration measurements on a surface, etc. Name of the technique comes from the Doppler Effect (or Doppler shift), which is known as the change in the frequency of a wave when an observer moves relative to the source of the wave. Major drawback of the technique is the necessity of seeding tracer particles that scatter light into the flow in order to utilize from the Doppler Effect for measuring the velocity of the flow.

The basic working principle of the system is sending a pair of laser beams intersecting on the point to be measured, and seeding tracer particles to the flow which are expected to pass from the measurement location, and then collecting the laser light scattered back from those illuminated particles and converting it to an electrical signal using a photodetector. The light scattered back from the particles when they pass through the control volume has components from both laser beams, and produces a pulsating light intensity which is proportional to the velocity of the particles seeded into the flow. Therefore, the velocity of the particles can be obtained by calculating these shifted frequencies collected on the photodetector, and converting them to velocities using the Doppler shift theorem. One should note that the system requires a pair of laser beams in order to obtain each component of the velocity. Thus, three pairs of laser beam intersected on the same control volume are needed for measuring the three components of the velocity. Basic working principle of an ordinary LDA system and its optical units are shown in Figures 3.14 and 3.15, respectively.

An Argon-ion laser having 750 mW power output was used to create a continuous laser beam. An optical unit (beam splitter) connected the exit of the laser is capable of splitting the laser beam into three different wavelengths at 514.5 nm, 488 nm and 476.5 nm, and creating two laser beam from each of those wavelengths. However, one pair of fiber manipulators must have been installed on this optical unit for each pair of laser beams that would be used in measurements since these manipulators transmit the light from the optical unit to the laser probe throughout fiber cables. The system used in this study has only one pair of fiber manipulators, thus measures only one component of the velocity at a time. However, by rotating the laser probe 90 degrees, the system was capable of measuring the second component of the velocity. Therefore, the system is used to measure the two components of the velocity. Steady and unsteady velocity measurements were done for the first component of the velocity, and then repeated for obtaining the second one. The components of the LDA system except the laser probe are shown in Figure 3.16. Both the laser source and optical unit of the current system are illustrated in Figure 3.17.

Seeding tracer particles into the flow plays a vital role in velocity measurements by a LDA system, as mention before. A commercial fog generator, which use Glycerin based smoke liquids, is used to generate the necessary fog for seeding into the flow when the velocities in the test section were measured. Two types of liquids, medium and high density, were tested on this generator and it was observed that the fog generated from the high density fluid yields better data acquisition rates at the same laser power due to higher refractivity caused by bigger particle sizes. On the other hand, another smoke generator, which is used to generate smoke for flow visualization and explained in “Laser Illuminated Flow Visualization Using Smoke” part of this chapter, was used in the velocity measurements in the leading edge vortex core. Both of the smoke generated by the aforementioned smoke generators have the advantage of being neutrally buoyant and following the flow.

The current LDA system is equipped with a Dantec BSA F60 signal processor. The optics and the laser of the LDA system are connected to this specific processor. The processor itself is connected to a workstation computer, which has a BSA Flow Software running on, via a local area network. The BSA processor is for analyzing the signal coming from the photodetector for corresponding light scatters from the seeding particles passing from the control volume, and applying a 40 MHz frequency shift to the wavelength of one of the laser beams in order to prevent directional ambiguity on the measured velocities. The BSA processor is also able to make True FFT signal processing for high accuracy.

The velocity measurements by the LDA system were done using BSA Flow Software which controls the system and acquires data. The basic outputs of the acquired data are the “time” that a burst is detected, and the “velocity” of the particle which caused that burst. Since the data rate depends on the burst detection, this method is not able work with constant data rate, thus gives the output of velocity data with unequally spaced time intervals. The software also calculates the mean value and root mean square (RMS) of the velocity components and their corresponding turbulence intensity. Another visually appealing feedback of the software is the validation of the results which is calculated using statistically confidence levels, distribution functions and curve fitting routines. The BSA Flow Software is also capable of making post processing to the acquired data such as 2-D or 3-D plotting, spectral analysis, filtering, calculating an object, etc.

The velocity measurements was first employed at the core of the leading-edge vortex at angles of attack $\alpha = 4°$ and $\alpha = 7°$ and Reynolds number $Re = 10^4$ on three different planes corresponding to the pressure measurement sections as shown in Figure 3.18. Each point was measured for 5 seconds with a data rate around 1000 Hz for both streamwise and vertical velocity components.

After completing the velocity measurements at the vortex core, near surface velocity measurements were performed at points 5 mm close to the wing surface. Locations of the points that were used in near surface velocity measurements are shown in Figure 3.19. The lines of “Section a” and “Section b” illustrated in the figure are simply divide the semispan of the wing into three equally spaced regions. Measurements were conducted at angles of attack $\alpha = 4°,\ 7°, 10°$ and 13°, and at Reynolds numbers $Re = 10^4,\ 3.5x10^4$ and 10^5. Each point was measured for 5 seconds with a data rate around 1000 Hz for both streamwise and vertical velocity components.

3.5 Power Spectral Density Analysis

3.5.1 Spectral Analysis of the Velocity Data

Power Spectral Densities of all the velocity data obtained from the LDA measurements are calculated via Lomb-Scargle Normalized Periodogram code that runs on MATLAB software. Calculations were also performed via MATLAB’s built in FFT function and the Spectrum Add-on of the LDA software. It is important to note that Matlab’s FFT function is not able to work with measurement data that were taken at not equally-spaced time intervals such as LDA data. Thus, the LDA data is linearly interpolated using an in-house interpolation code before it is exported to Matlab’s FFT function. This process is not used for Lomb-Scargle method due to its ability of working with not equally-spaced data. When the results of the each method is compared, it was seen that the Lomb Scargle method and the method used by LDA software were quite similar, although the results of MATLAB’s FFT function was also similar but the densities of the peaks were much lower compared to the other methods. As a result, the Lomb-Scargle Normalized Periodogram method was chosen to be used in the computations of spectral densities due to the limited plotting options of the LDA software. The source code of the method that runs on MATLAB is given at Appendix C. The source code for spectral density analysis using Matlab’s FFT function, and the linear interpolation code that was developed to interpolate the LDA data for getting an evenly spaced measurement results are also given at Appendix C.

3.5.2 Spectral Analysis of the Pressure Data

Power Spectral Densities are only computed for the pressure data obtained from the pressure taps lie on the projections of velocity measurement locations, which are shown in Figure 3.20. The lines of "Section a" and "Section b" that were illustrated in the figure are simply divide the semispan of the wing into three equally spaced regions on the pressure measurement sections. The Lomb-Scargle Normalized Periodogram method and MATLAB's built in FFT function was compared with each other using the pressure data. Results of the Lomb-Scargle method was seen to be more coherent compared to the other method. Thus, the Lomb-Scargle Normalized Periodogram method was also used in the computations of pressure spectrums.

Figure 3.1 The low speed wind tunnel facility used in this study

Figure 3.2 Designed and fabricated fully transparent test section

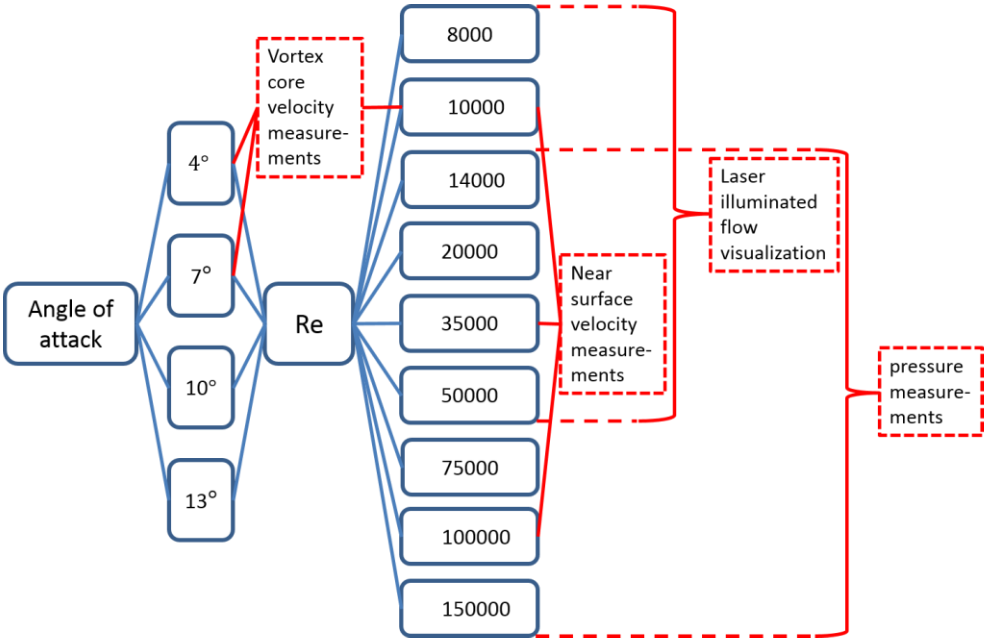

Figure 3.3 Experimental matrix

Tunnel Calibration Curve	
Ave. Velocity (m/s)	Power (%)
0.33	3
0.79	4.5
1.07	6
1.34	7
1.67	8
1.95	9
2.21	10
3.61	15
5.09	20
6.7	25
8.07	30
9.6	35
11.12	40
12.67	45
14.1	50
15.78	55
17.25	60
18.59	65
20.1	70
21.49	75
T=28 °C	

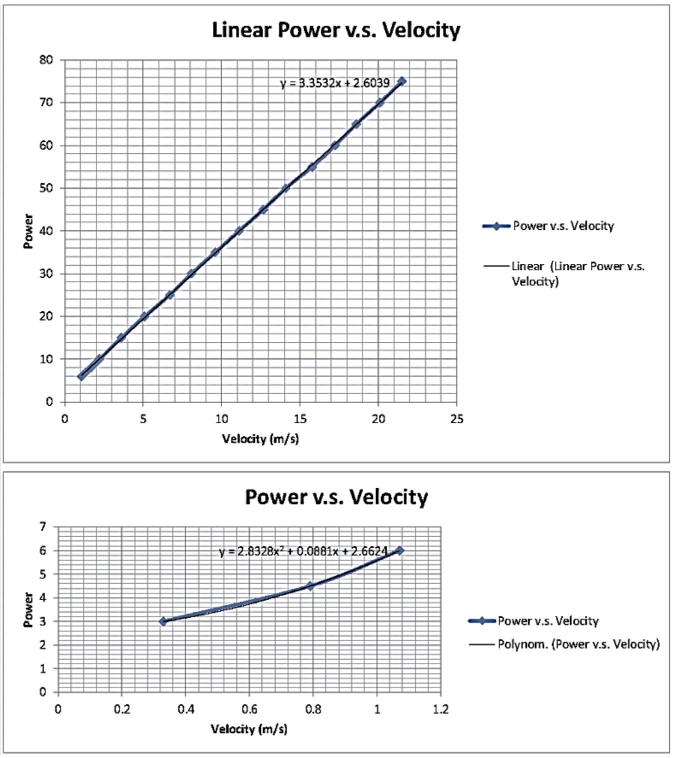

For Power values ≥ 6%; $P = 3.3532x + 2.6039$

For Power values < 6%; $P = 2.8328x^2 + 0.0881x + 2.6624$

Figure 3.4 Calibration curve of the wind tunnel for obtaining the required fan power for a given velocity

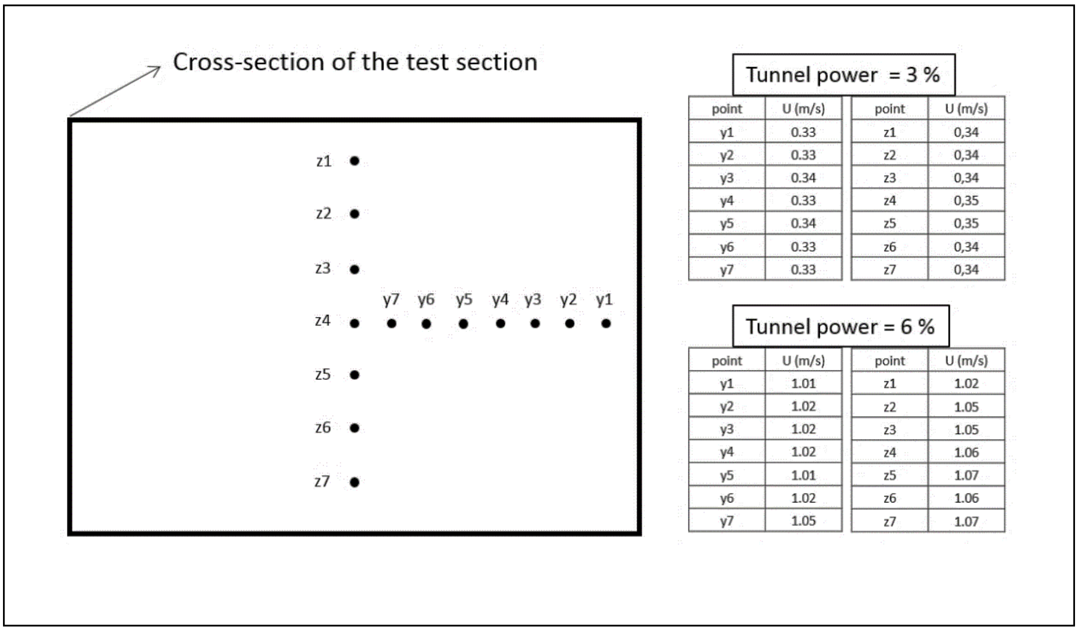

Tunnel power = 3 %

point	U (m/s)	point	U (m/s)
y1	0.33	z1	0,34
y2	0.33	z2	0,34
y3	0.34	z3	0,34
y4	0.33	z4	0,35
y5	0.34	z5	0,35
y6	0.33	z6	0,34
y7	0.33	z7	0,34

Tunnel power = 6 %

point	U (m/s)	point	U (m/s)
y1	1.01	z1	1.02
y2	1.02	z2	1.05
y3	1.02	z3	1.05
y4	1.02	z4	1.06
y5	1.01	z5	1.07
y6	1.02	z6	1.06
y7	1.05	z7	1.07

Figure 3.5 Velocity measurements performed in the test section in order to see the uniformity of the flow at low velocities

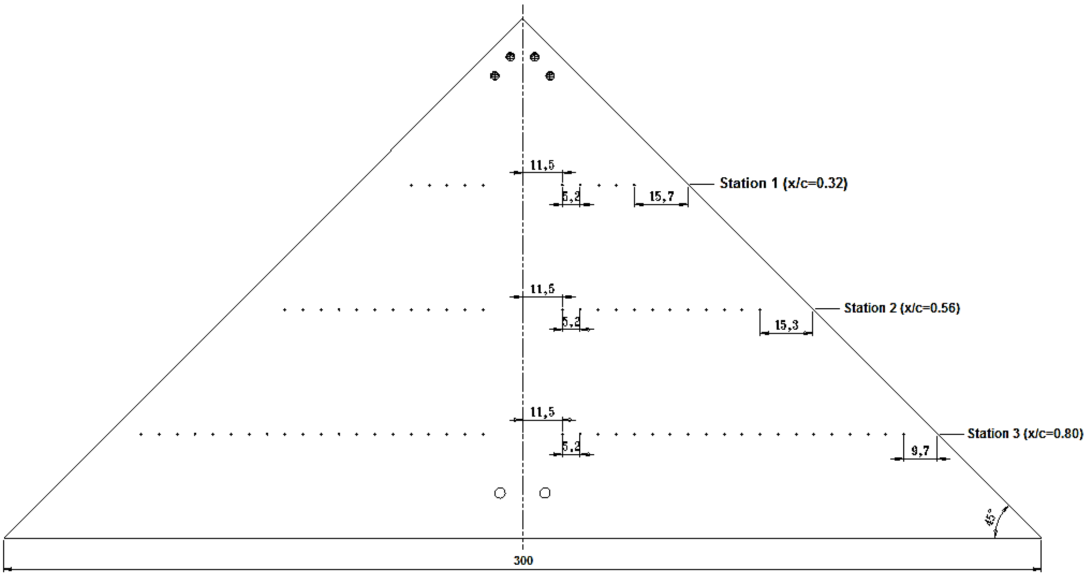

Figure 3.6 Plan view of the delta wing showing pressure tap locations and the three chordwise stations

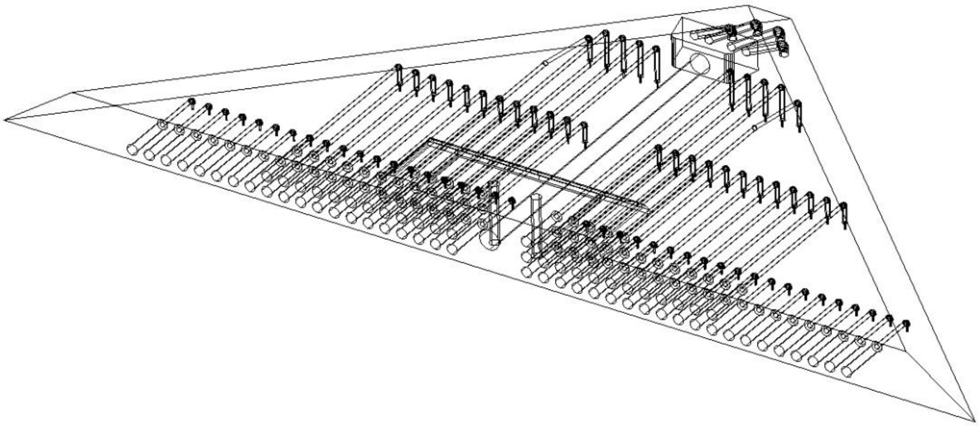

Figure 3.7 Figure 3.7. CAD drawing of the fabricated delta wing

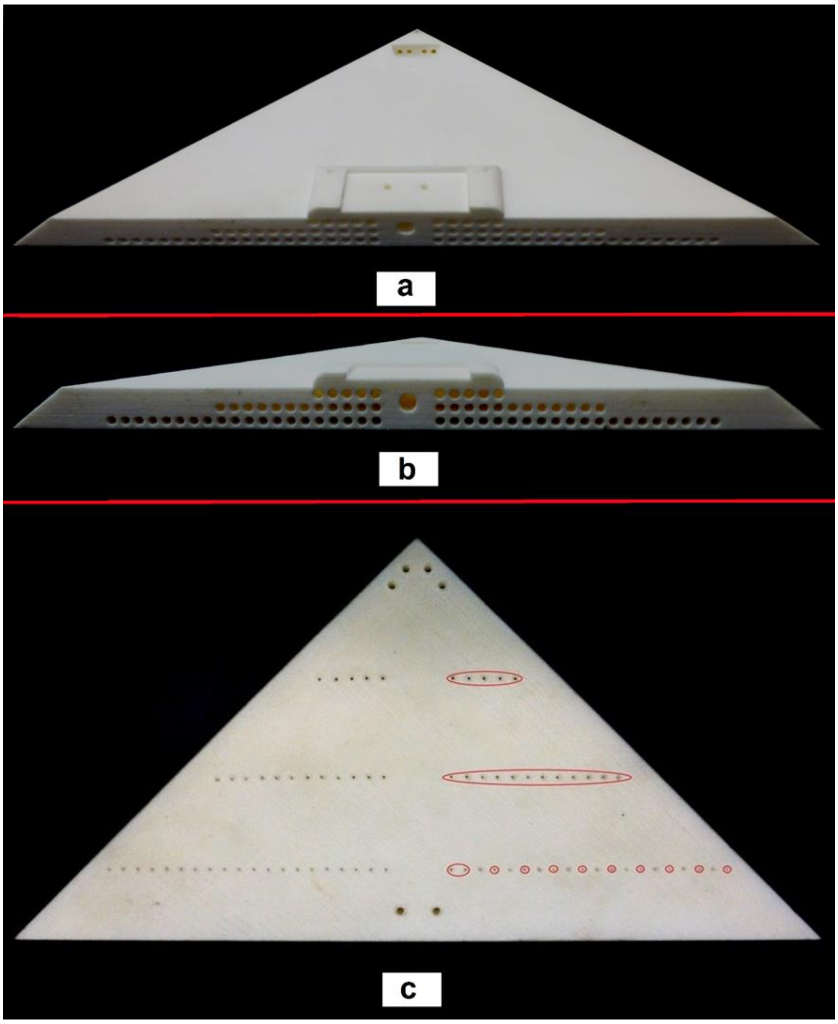

Figure 3.8 Photographs of the fabricated delta wing from different views; a) Top-back view, b) Back view, c) Bottom view, which also shows the pressure taps that were used in pressure measurements

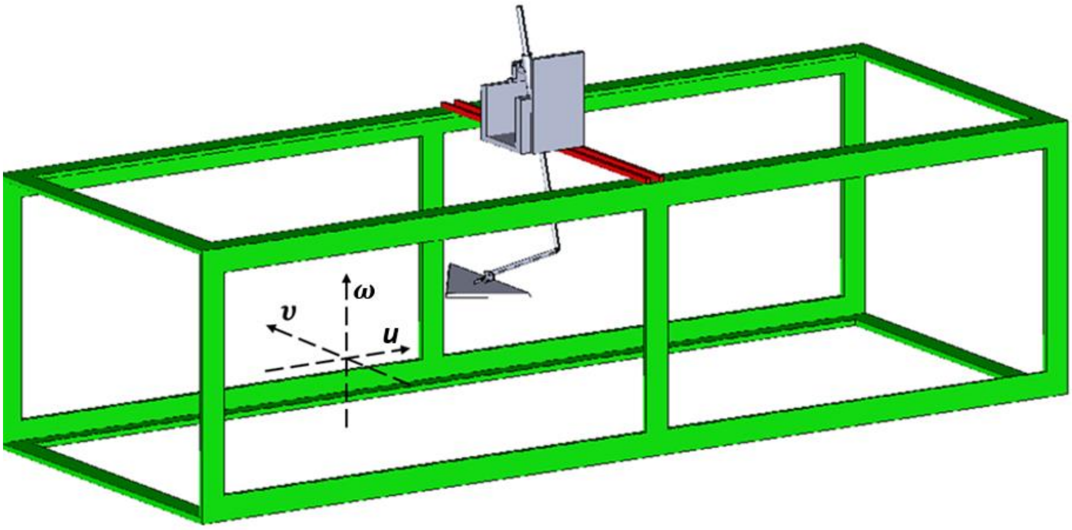

Figure 3.9 Solid model of the wing, mount and test section assembly with directions of velocity components

Figure 3.10 The smoke generator used in experiments

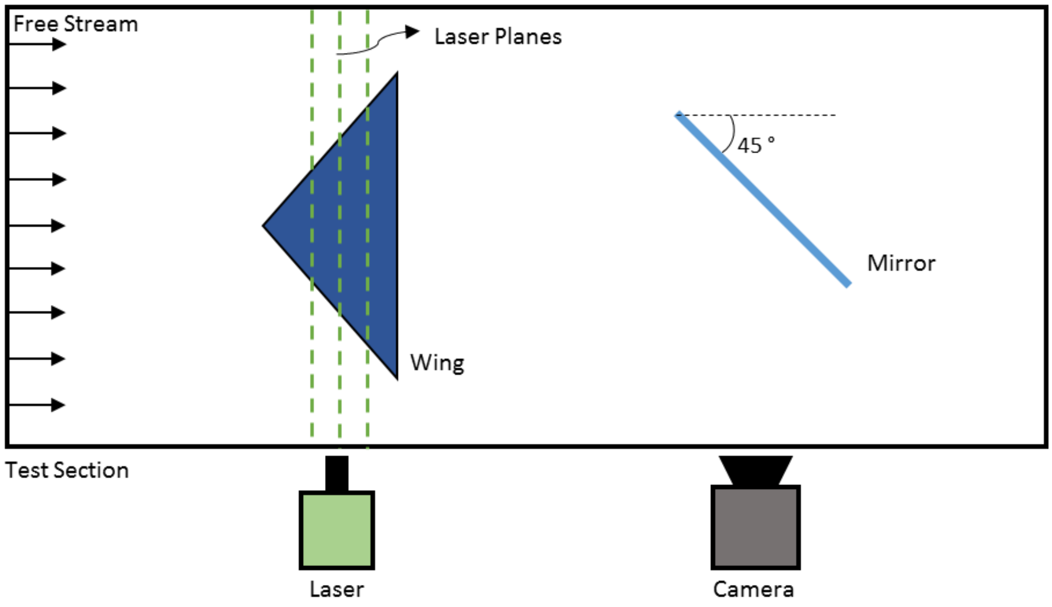

Figure 3.11 Experimental set-up for flow visualization at cross-flow planes x/c=0,32, x/c=0,56 and x/c=0,80 (plan view)

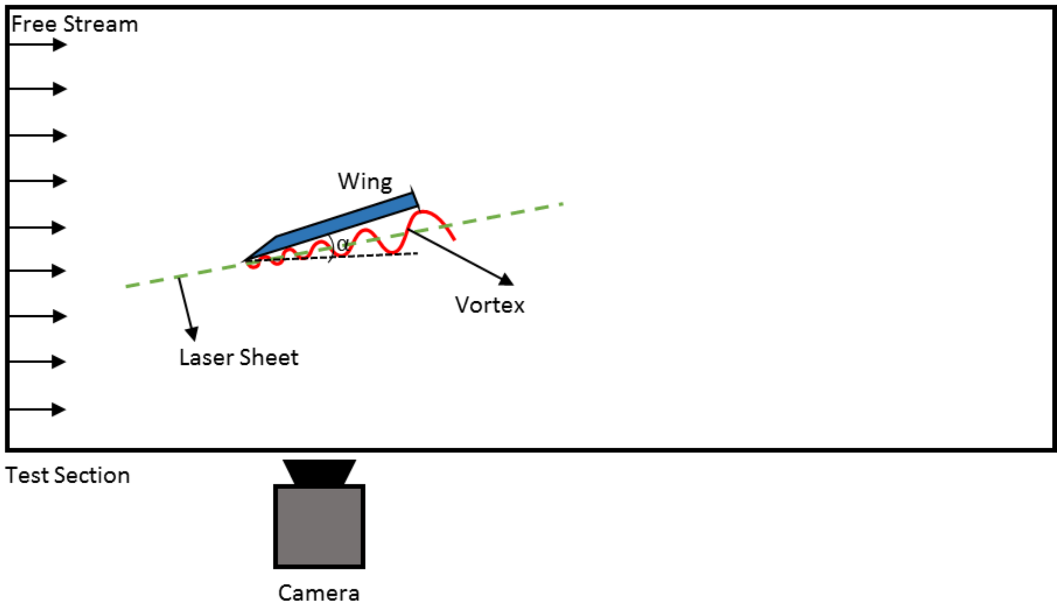

Figure 3.12 Experimental set-up for flow visualization at a plane parallel to the leading edge vortices (side view)

Figure 3.13 The 16-channel pressure scanner system used in the experiments

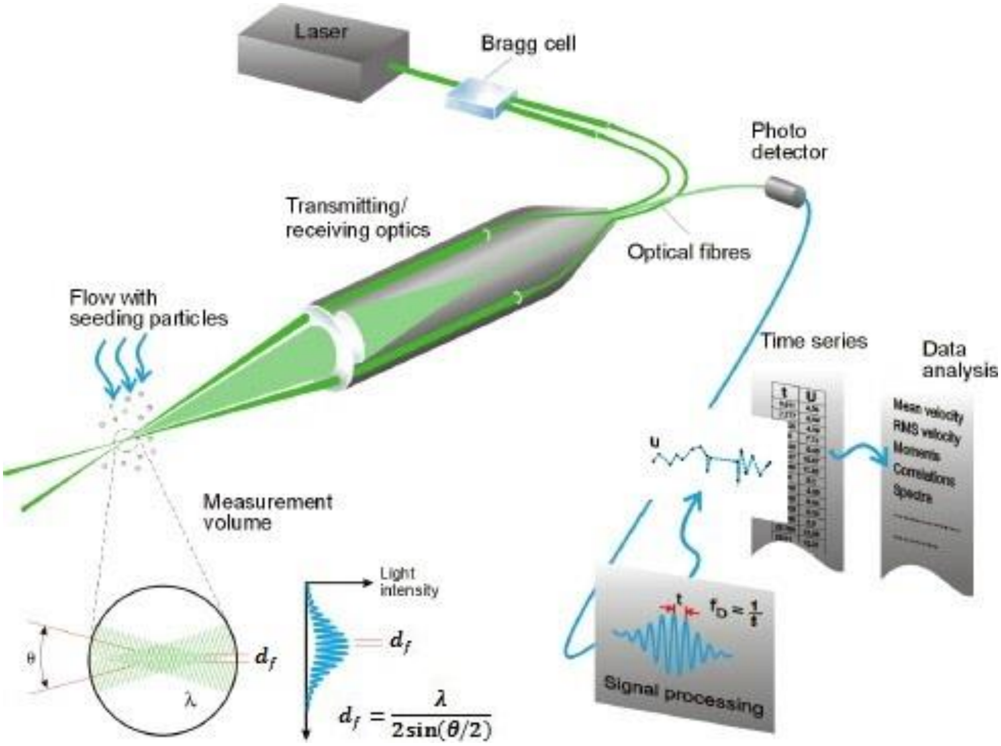

Figure 3.14 Basic working principle of LDA system [133]

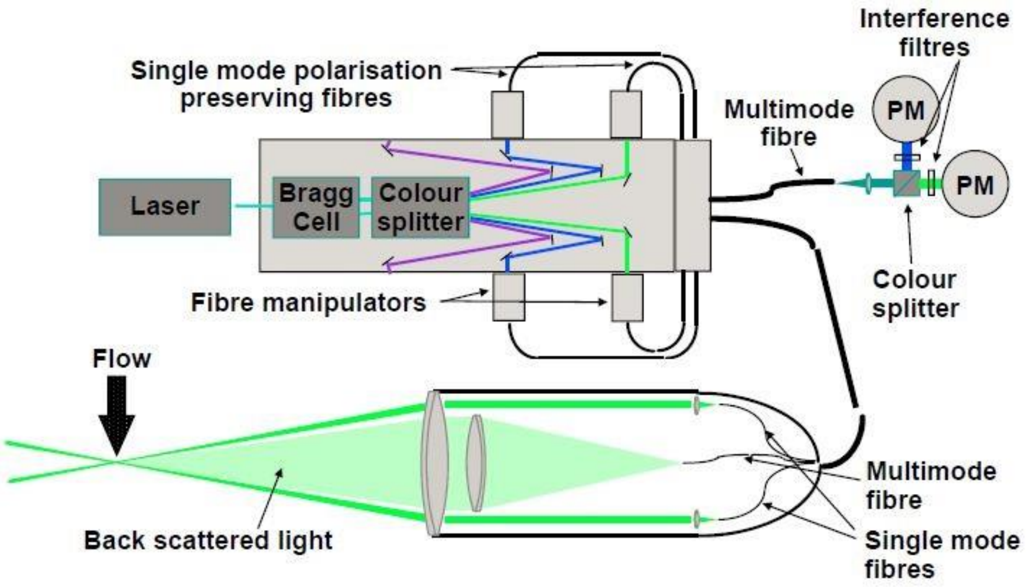

Figure 3.15 Optical units of the LDA system [133]

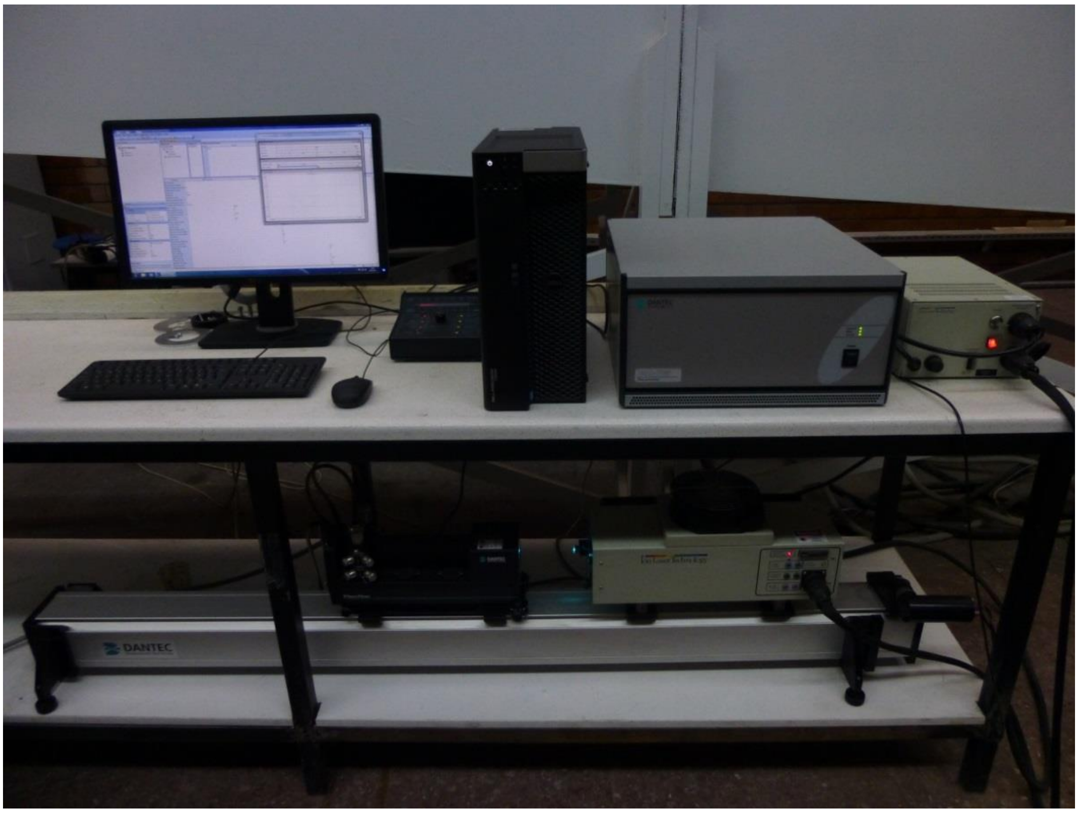

Figure 3.16 The LDA system used in the study

Figure 3.17 The optical and laser units of the LDA system used in the study

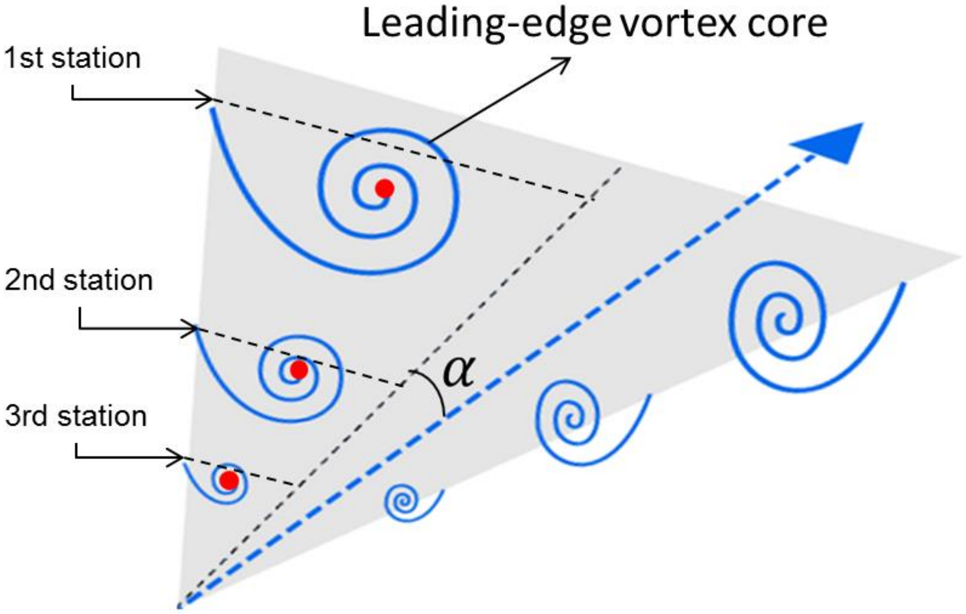

Figure 3.18 Illustration of vortex core velocity measurement points

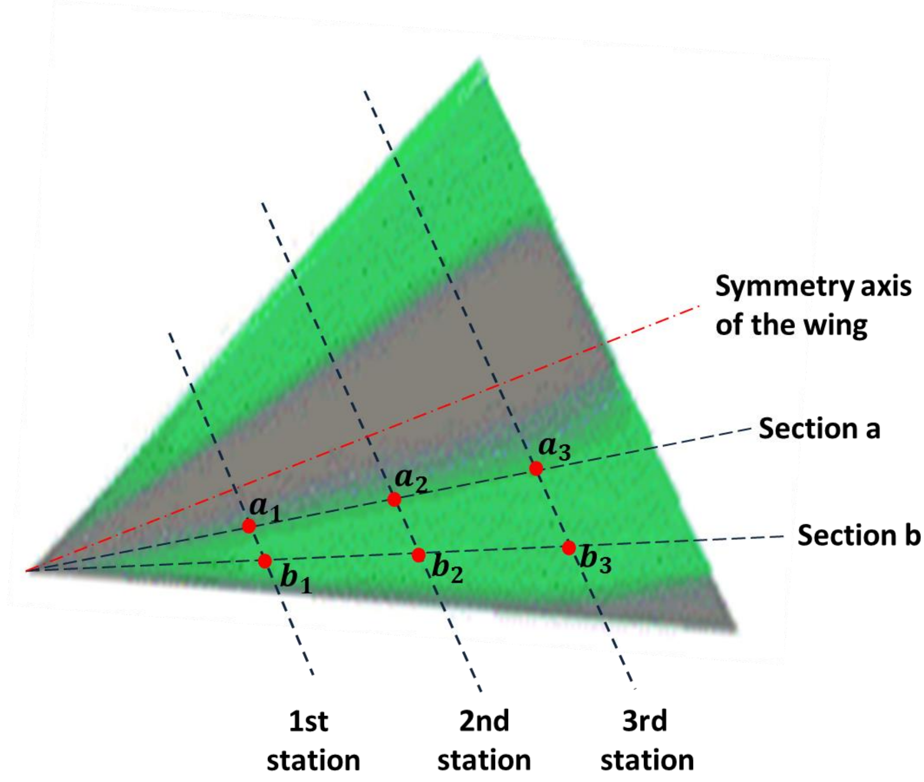

Figure 3.19 Illustration of the locations of velocity measurement points used in near surface LDA measurements

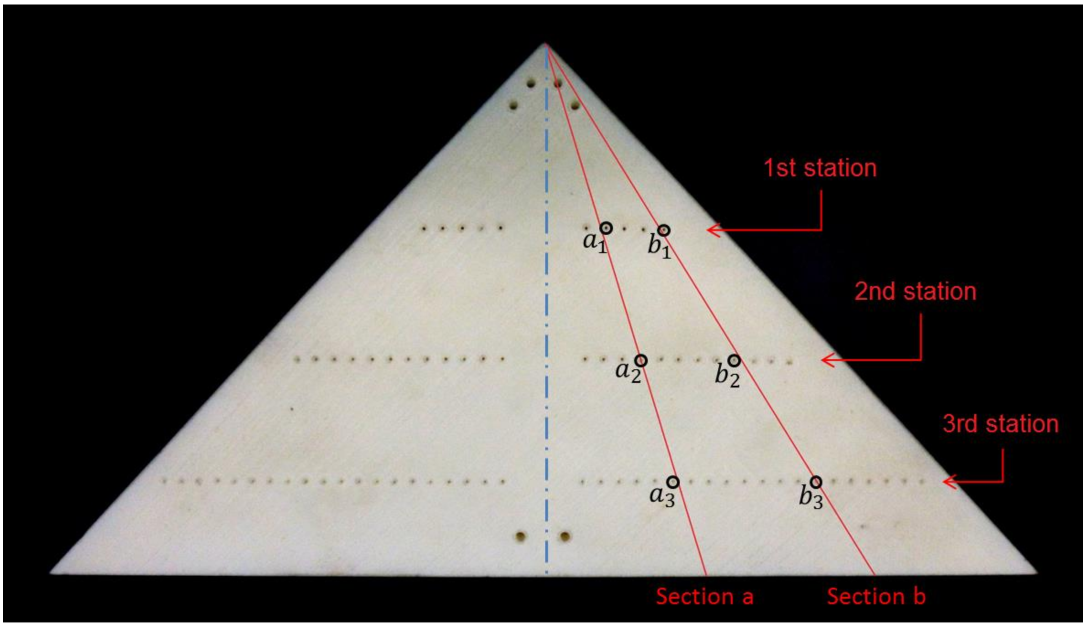

Figure 3.20 Illustration of the locations of pressure taps used in Power Spectral Density computations

CHAPTER 4

RESULTS

4.1 Results of Flow Visualization

Results of the crossflow smoke visualization experiments are given in Figures 4.1 – 4.24 for three different crossflow planes at different angles of attack and Reynolds numbers. A ruler that represents the local spanwise distances on the surface of the wing is added to top of the each crossflow visualization images so as to be able to observe the locations of the critical structures in the flow field.

In order to see the effect of Reynolds number in the flow structure easily, the flow visualization images that were taken on the same crossflow plane are grouped into single figures for same angle of attack and sorted from the lowest Reynolds number to the highest. These figures have been added to Appendix A as Figures A1 – A12, where Figures A1 - A3 correspond 4-degree angle of attack, A4 – A6 correspond 7-degree angle of attack, A7 – A9 correspond 10-degree angle of attack and A10 – A12 correspond 13-degree angle of attack. The first figure from the set of figures for same angle of attack corresponds to the crossflow plane at x/c = 0.32, where the second and third ones correspond to crossflow planes $x/c = 0.56$ and $x/c = 0.80$, respectively.

The flow structure below the wing at a vortex axis plane is given in Figures 4.25 – 4.29 at different angles of attack. Each figure shows the flow structures that were captured at a certain angle of attack at different Reynolds numbers. Thus, the influence of Reynolds number in the flow at a given angle of attack can easily be seen in a single figure.

4.1.1 Results of crossflow planes

Flow visualization images that show the flow structures below the wing on spanwise crossflow planes located at chordwise distances x/c = 0.32, x/c = 0.54 and x/c = 0.80 are illustrated in Figures 4.1, 4.2, 4.3, 4.4, 4.5 and 4.6 for an angle of attack $\alpha = 4°$ and Reynolds numbers, $Re = 8x10^3,\ \ 10^4,\ \ 1.4x10^4,\ \ 2x10^4,\ \ 3.5x10^4$ and $5x10^4$, respectively. The other crossflow visualization images for same Reynolds number range and for angles of attack $\alpha = 7°, 10°$ and $13°$ are shown in the same manner in Figures 4.7 – 4.12, 4.13 – 4.18 and 4.19 – 4.24, respectively. Additionally, dimensionless local spanwise distances are illustrated on top of the each crossflow visualization image.

Figure 4.1 indicates the presence of coherent leading edge vortex cores on all crossflow planes, which shows that vortex breakdown does not take place over the wing at 4-degree angle of attack and Reynolds number $Re = 8x10^3$. Considering the spanwise locations of the vortex cores, the flow structure can be considered as symmetric. Slight deviation from left to right is primarily due to the fact that there is unsteady nature of vortex structure which spatially oscillates in spanwise direction and camera images are representing only one instant in time.

When the Reynolds number is increased to $Re = 10^4$, a transition from primary vortex structure to dual-vortex structure occur, as seen in the first crossflow plane of Figure 4.2. The secondary vortex, which separates the primary vortex into two discrete primary vortices, can be clearly seen in the first crossflow plane of the figure. It can be seen from the second crossflow plane image that the core of the inboard primary vortex is still visible. However the second primary vortex is started to disperse in the flow, which indicates a vortex breakdown. Moreover, the secondary vortex is still visible in the image, but not as clear as it was in the first plane due to a decrease in its intensity with downstream movement. When the flow reaches to the third end-view plane, it is seen from the last image of the figure that no evidence from the secondary vortex remains and the second primary vortex disperse to the whole flow field between the primary vortex, which is not broken down yet, and the leading edge of the delta wing.

A further increase in Reynolds number decreases the strength of the second primary vortex and its proximity to the inboard primary vortex, seen in the first end-view plane of Figure 4.3. When the second end-view planes are examined, it is observed that the inboard primary vortex is conically expanded and started to disperse in the flow, whereas the second primary vortex is already broken down and dispersed into the flow field. The separated flow reattaches to the wing surface at $y/\tilde{s} \cong 0.34$ at the third cross-flow plane as it is seen in the third end-view plane of the figure.

The flow structure at the end-view planes of the wing is shown in Figure 4.4 for 4-degree angle of attack and Reynolds number $Re = 2x10^4$. It can be seen from the top image that the flow structure is similar to the case of $Re = 10^4$, but the strength of the second primary vortex is much weaker and it is started to disperse around, which points to a vortex breakdown. The image in the middle shows that the second primary vortex is totally broken down and dispersed in the flow field, but the relatively higher smoke intensity around the inboard primary vortex indicates that it is broken down after the breakdown of the second primary vortex. Moving further downstream causes an increase in the dispersion of leading edge vortices, which is visible in the bottom image of the figure.

Effect of further increase in Reynolds number at 4-degree angle of attack is illustrated in Figures 4.5 and 4.6 for $Re = 3.5x10^4$ and $Re = 5x10^4$. It is clearly visible at both figures that an increase in Reynolds number moves the breakdown location upstream of the first end-view plane located at chordwise distance $x/c = 0.32$ since a distinctive leading edge vortex is not evident in any of end view planes. Furthermore, the flow structures at both of these relatively high Reynolds numbers are quite similar with each other, which can be the indication of reaching to an asymptotic state in the flow that a further increase in Reynolds number do not change the flow structure significantly, but cause small variations in the location of vortex core and breakdown as it is stated by Taylor and Gursul [4] for a 50-degree sweep delta wing at Reynolds number on the order of $3x10^4$.

It is shown in Figure 4.7 that at 7-degree angle of attack and Reynolds number $Re = 8x10^3$, leading edge vortex cores present on all crossflow planes which indicates a generic delta wing vortex flow structure below the wing without a breakdown for up to the third end-view plane located at $x/c = 0.80$. Unsteadiness of the flow structure is captured in the middle image at second end-view plane located at $x/c = 0.56$, where two primary vortices that were separated by a secondary vortex take place below the surface of right half of the wing, and a single primary vortex structure seems to dominate the flow below the surface of left half of the wing. A possible reason for seeing such an asymmetric flow structure at that end-view plane is oscillations of vortex breakdown locations, hence the vortex below the left half of the wing can be having a breakdown earlier than the one below the other half.

The resultant flow structure for same angle of attack and slightly increased Reynolds number is given in Figure 4.8. There are coherent primary vortex cores on both side of the wing at all end-view planes; however the cores at the third plane are started to expand which points to a start of vortex breakdown in the flow structure.

Increasing the Reynolds number to $Re = 1.4x10^4$ cause a transition from primary vortex structure to dual-vortex structure, as seen in the first end-view plane of Figure 4.9. However, intensities of the second primary vortices are seemed to be less than the inboard primary vortices at the present case, where their intensity was as much as the inboard primary vortices in the case of 4-degree angle of attack at same Reynolds number, seen in Figure 4.3. The secondary vortex that separates the primary vortex into two vortices of different concentrations is also visible at the first end-view plane. When the second end-view plane is examined, it is seen that the second primary vortex is broken down before it reaches to this plane, but the core of inboard primary vortex still exist on both sides of the wing. However, a further downstream movement in the flow causes a breakdown on the primary vortex which can be understood from the conical expansion of its core, seen in the last end-view plane.

When the Reynolds number is increased to $Re = 2x10^4$, the dual vortex structure, which was seen in the preceding case in Figure 4.9, does not take place in any of the end-view planes of Figure 4.10 due to the upstream movement of the vortex breakdown location. It is seen from the first end-view plane of the figure that core of the inboard primary vortex is lost its intensity and it is about to have a breakdown, whereas the second primary vortex is totally dispersed in the flow which indicates that it is broken down much earlier than it reaches to the location of first end-view plane. As it is seen from the second end-view plane that further movement in downstream increases the dispersion of the second primary vortex in the flow field and expands the core of the inboard primary vortex which is the indication of vortex breakdown. When the flow reaches to the third end-view plane, all the vortical structures become dispersed in the flow field, thus a distinctive leading edge vortex is not evident anymore.

The effect of further increase in Reynolds number is shown in Figures 4.11 and 4.12. The flow structures have a similar profile at both cases of Reynolds numbers $Re = 3.5x10^4$ and $Re = 5x10^4$ which can be an indication of reaching to an asymptotic state in the flow. The flow has a similar structure at each end-view plane, but its height increases when it proceeds downstream in the freestream flow direction.

The flow structure below the wing at 10-degree angle of attack and Reynolds number $Re = 8x10^3$ is illustrated at three consecutive end-view planes in Figure 4.13. Surprisingly the flow structure at each plane seems quite different than 4 and 7-angle of attack cases at same Reynolds numbers and this flow structure may be interpreted as three-dimensional separation from the surface. In this case, it is not possible to say the flow is dominated by leading edge vortices, since there is no mark from strong leading edge vortices. The shear layer that were separated from the leading edge and two rotating structures that arise from the apex of the wing and form close to the wing center exist in the flow as it is clearly visible in the first end-view plane. These two rotating structures do not exist at the second end-view plane, but there are some identifiable vortical substructures in the flow field. These instabilities are also identifiable further downstream of the flow, at the third end-view plane. One should also note that another result of the increase in angle of attack is to the movement of the primary reattachment line inboard of the wing centerline, which can be understood from the dimensionless scales over the images.

An increase in Reynolds number from $Re = 8x10^3$ to $Re = 10^4$ does not bring a substantial difference in the flow structure as it can be seen from Figure 4.14. It is seen from the first end-view plane that shear layers separated from each leading edge and two counter rotating weak structures still exist in the flow close to the wing centerline. However, the vortical substructures do not exist in the flow field any more as it can be seen from the second and third end-view planes. The flow structure at these planes is similar to the structure that generally occur at downstream of vortex breakdown.

Figure 4.15 indicates that a further increase in Reynolds number causes a transition from the rotating weak structures to stronger leading edge vortices by increasing their strength. However, the other consequence of the increase in Reynolds number is the movement of the vortex breakdown location towards the apex of the wing. Thus, the leading edge vortices have a breakdown just upstream of the first end-view plane, which can be understood from the conical expansion of the vortex cores in the flow field. The flow structure in the subsequent end-view planes is not much different from an ordinary vortex breakdown flow field without any footprints of leading edge vortices.

It is seen from the first crossflow plane of Figure 4.16 that at $Re = 2x10^4$, the regions that have a higher smoke intensity indicate an occurrence of vortex breakdown before the first end-view plane. However, the breakdown occurs in a location closer to the apex of the wing when it's compared to the previous case of $1.4x10^4$, which can be understood from the smoke intensities of core locations at first end-view planes of Figures 4.15 and 4.16. This is due to the upstream movement of the breakdown location as a result of an increase in Reynolds number.

Increasing the Reynolds number to $Re = 3.5x10^4$ and $Re = 5x10^4$ moves the breakdown location more upstream towards the leading edge, so a flow field with broken and dispersed leading edge vortices become the dominant structure of the flow, seen in each end-view planes of Figures 4.17 and 4.18.

The flow structure for the case of 13-degree angle of attack and Reynolds number $8x10^3$ is shown in Figure 4.19. At this relatively high angles of attack and low Reynolds numbers, an asymmetric flow structure with three-dimensional separation from the wing surface, which might be interpreted as stall for this type of wings, is observed below the wing. When the figure is examined, it is seen that the intensity of the flow below the left half of the wing is much higher than the flow at the other half. Moreover, an identifiable vortical structure that arise from the apex of the wing, which interacts with the flow structure that occur at the other half of the wing at the region of wing centerline, exists in the denser part of the flow. Nonetheless, it is observed in the experiments that the stronger flow and the vortex in it not always take place below the left half of the wing, but time to time they shift to the other half of the wing and the vortex changes its sign. The coherent vortical structure that is seen in the first end-view plane is also identifiable at the second end-view plane, but when the third end-view plane is examined it is seen that this structure is disintegrated into small scale vortical substructures.

As it is seen from Figure 4.20 and Figure 4.21 that a symmetrical flow structure is recovered, but three-dimensional separation from the surface still dominates the flow below the wing at Reynolds numbers $Re = 10^4$ and $Re = 1.4x10^4$ at the same angle of attack. Distinctive leading edge vortex is not evident in any of the end-view planes at these Reynolds numbers as can be seen from the figures. The separated flows reattach to the wing surface at regions in close proximity to the wing centerline as it is seen at the all end-view planes.

The effect of further increase in Reynolds number is shown in Figures 4.22, 4.23 and 4.24 for $Re = 2x10^4$, $3.5x10^4$ and $Re = 5x10^4$, respectively. The resultant flow structure is a separated shear layer from the leading edge of the wing without identifiable vortical structures and it is similar at all these Reynolds number at all crossflow planes. An important difference from the cases with lower Reynolds numbers that the reattachment location moves outboard of the wing centerline with increasing Reynolds number. When the flow structures at Reynolds numbers $Re = 3.5x10^4$ and $Re = 5x10^4$ are compared, it is seen that the resultant flow structures and reattachment regions are quite similar, which may be concluded as a further increase in Reynolds number at high Reynolds numbers do not change the flow structure significantly.

When all the crossflow visualization images including the ones given in Appendix A are examined, it can be stated that an increase in angle of attack moves the flow structure more inboard towards the wing centerline for both vortex dominated flows and flows with a three-dimensional separation from the wing surface. On the other hand, an increase in Reynolds number cause a contrary effect in the flow by moving the flow structure more outboard towards the leading edge. It is also possible to draw a conclusion that an increase in angle of attack can significantly change the flow structure at low Reynolds numbers; however, its influence in the flow structure at high Reynolds numbers, where the flow at different angles of attack have similar structures, is very limited. Moreover, the flow structures at Reynolds numbers $Re = 3.5x10^4$ and $Re = 5x10^4$ are very similar, which can be the indication of reaching to an asymptotic state in the flow. Since the flow visualization experiments are not conducted at Reynolds numbers higher than order of $5x10^4$, a general conclusion cannot be conducted in the light of present flow visualization results, but the pressure measurements on the wing surface at Reynolds numbers higher than order of $5x10^4$ can be used as complementary experimental data to draw a conclusion about reaching to an asymptotic state in the flow structure at certain Reynolds numbers.

4.1.2 Results of vortex core plane

The behavior of flow structure below the wing on a plane at vortex axis is shown in Figure 4.25, Figure 4.26, Figure 4.27 and Figure 4.28, at different Reynolds numbers for angles of attack $\alpha = 4°, 7°, 10°$ and 13°, respectively.

The effect of Reynolds number on the flow structure below the wing at plan-view plane parallel to the leading edge vortices can be seen in Figure 4.25 for 4-degree angle of attack. A pair of spiral primary leading edge vortices dominate the flow without any breakdown below the wing at $Re = 8x10^3$. When the Reynolds number is increased to $Re = 10^4$, secondary vortices separate the primary vortices into two discrete primary vortices, seen from the figure. Moreover, these vortices break down at a region downstream of the wing. Increases in Reynolds number to $Re = 1.4x10^4$ and $Re = 2x10^4$ do not change the dual vortex structure but move the breakdown locations of these vortices towards the apex of the wing. Breakdown locations of the vortices reach the apex of the wing with further increase in Reynolds number, thus the resultant flow structure is similar at Reynolds numbers $Re = 3.5x10^4$ and $Re = 5x10^4$ as it is mentioned in crossflow visualization images.

The trend of the flow structure below the 45-degree sweep delta wing at 7-degree angle of attack is similar to the one that was observed at 4-degree angle of attack as it is seen in Figure 4.26. The only difference is the dual vortex structure start to be arise at Reynolds number $Re = 10^4$, but the second primary vortex is not as dense as the one that was occurred at 4-degree angle of attack at the same Reynolds number, seen in Figure 4.25.

When the angle of attack increased to $\alpha = 10°$, the dominant flow structure below the wing is different than the generic spiral leading edge vortex dominated flow at low Reynolds numbers due to the high viscous forces which results in as three-dimensional flow separation from the surface of the wing, seen in Figure 4.27. An increase in the Reynolds number energizes the separated shears layer and forms the leading edge vortices. The breakdown locations of these vortices reach to the apex of the wing at Reynolds numbers $Re = 3.5x10^4$ and $Re = 5x10^4$, thus the resultant flow is same and have a separated flow region in these cases.

A further increase in angle of attack causes large-scale swirl structures that are related to three-dimensional flow separation from the surface of the wing and oriented toward the apex of the wing at low Reynolds numbers, seen in Figure 4.28. A transition from the swirl structure to a broken down vortex structure occurs when the Reynolds number is increased to $Re = 2x10^4$, and a further increase in Reynolds number increase the distance between the primary reattachment line and wing centerline.

It can be stated that the flow structures explained in crossflow images are verified by the plan view images, which are also clearly showed the progression of the vortex breakdown location upstream of the wing towards the apex with increasing Reynolds number at low angles of attack. When the angle of attack is increased to relatively higher values, a three-dimensional separation from the surface of the wing arises from the apex and progresses downstream of the wing by covering large regions below the wing at low Reynolds numbers. An increase in Reynolds number moves this structure towards the apex and decreases its size at the regions that below the wing. The aforementioned structure reaches to the apex of the wing with further increase in Reynolds number and the resultant flow structure becomes similar to those having vortex breakdown that is reached to the apex at high Reynolds numbers.

4.2 Results of Steady and Unsteady Pressure Measurements

Variation of pressure distribution on wing surface at non-dimensional spanwise locations of three different pressure measurement stations located at chordwise distances x/c = 0.32, 0.56 and 0.80 is given in Figure 4.29 for angle of attack $\alpha = 4°$, for different Reynolds numbers. Variation of pressure distribution for angles of attack

$\alpha = 7°, 10°$ and 13° are shown in the same way in Figures 4.30, Figure 4.31 and Figure 4.32, respectively.

The pressure distributions at different stations are plotted as $-C_p$ versus spanwise locations on the surface of the wing. High $-C_p$ values represent the lowest pressure values where high velocities occur, and stand for high suctions on the wing, whereas the regions with $-C_p$ values close to zero have the highest pressures and mark the regions that the flow reattaches to the wing surface. Footprints of vortex structure as significant suction peaks are clearly visible at all angles of attack in Figures 4.29 – 4.32. These suction peaks mark the axis of leading edge vortex and in line with smoke visualization results. Likewise, when the suction peaks compared to each other at different stations, it is seen that they reduce with downstream movement, which is an expected behavior due to an increase in the proximity of flow structure to the wing surface with downstream progression of the flow at freestream direction, as well as the effects of decreased vortex intensities and possible breakdowns at downstream of the wing. As it is seen from the steady pressure measurement figures that the suction peaks broadens, and the vortex core axis and the reattachment line moves inboard of the wing toward the centerline with increasing the angle of attack. It should also be noted that the suction peaks increase with increasing the Reynolds number and angle of attack except for 10 and 13-degree angles of attack at low Reynolds numbers, where three-dimensional separation from the wing surface is observed. A relatively low and broad $-C_p$ distribution on the wing is witnessed for this condition, instead of high $-C_p$ values that represent the marks of strong vortex structures and low $-C_p$ values that represent the marks of strong reattachment to the wing surface, which is have a negative effect on the wing's lift performance and also explains the stall situation of the wing. The wing recovers its aerodynamic performance with an increase in Reynolds number to relatively higher values. An increase in Reynolds number at high Reynolds numbers does not bring a significant change in -C_p distributions at all angles of attack. However, it causes small increases in the -C_p values, especially at first station, due to the upstream movement of vortex breakdown location and an increase in the velocities of the flow with increasing Reynolds number. These findings are very in line with the possible asymptotic state of the flow structure at high Reynolds numbers that were explained in the results of smoke visualization experiments for

Reynolds numbers $Re = 3.5x10^4$ and $Re = 5x10^4$. The pressure measurements for Reynolds number up to $Re = 1.5x10^5$ provided complementary experimental data, which was made it possible to relate the findings of flow visualization experiments to much higher Reynolds numbers. Therefore, it can be stated that the effect of Reynolds number to the flow structure at high Reynolds numbers and present angles of attack is quite minimal.

When the unsteady pressure measurement figures of first station is examined, it is seen that the highest fluctuations in pressure distribution occur at places where the suction peaks that mark the vortex core are observed for almost all the cases except for 13-degree angle of attack at Reynolds numbers higher than $Re = 2x10^4$. The highest fluctuations in pressure occurs at places around the reattachment region at this relatively high angle of attack and high Reynolds numbers since the vortex breakdown location reaches to the apex of the wing and the result flow structure can be defined as pre-stall for these type of wings. One should also note that the lowest fluctuations are observed in reattachment region at all the cases except pre-stall, seen in Figures 4.33 – 4.36. These results have o good analogy with the study that was conducted by Taylor and Gursul [4]. They measured the highest velocity fluctuations along the reattachment line on a 50-degree sweep delta wing at pre-stall conditions. They also observed that the highest velocity fluctuations occur around the vortex core in the absence of pre-stall and stall conditions.

Unsteady pressure distribution on second station indicates that the points with highest fluctuations are take place at locations that have the suction peak or points just outboard of the location of suction peak towards the leading edge for all the cases except for 13-degree angle of attack at Reynolds numbers higher than $Re = 2x10^4$ as it is seen in Figures 4.37 – 4.40. Similar to the structure that was observed in the first station, the highest fluctuations in pressure distribution occur at places between the reattachment region and the vortex core at 13-degree angle of attack and Reynolds numbers greater than $Re = 2x10^4$, when the wing suffers from pre-stall.

The unsteady behavior of the flow at third station changes with increasing Reynolds number and angle of attack, seen in Figures 4.41 – 4.44. The highest pressure fluctuations on the wing surface along the pressure taps of third station occur at points closest to the leading edge at Reynolds numbers $Re = 1.4x10^4$ and $Re = 2x10^4$ at angles of attack between $\alpha = 4° - 10°$. When the Reynolds number increased, the location of highest fluctuations moves inboard of the wing toward the centerline and takes place at where the suction peak occur for angles of attack up to $\alpha = 13°$. The unsteady behavior of the flow on third station at 13-degree angle of attack is similar to those observed on first and second stations at same angle of attack; highest fluctuation occur at the pressure tap that closest to the leading edge at $Re = 1.4x10^4$, and it takes place between the reattachment region and the vortex core at higher Reynolds numbers, which was described in the observations of previous stations, seen in Figure 4.44.

Power Spectral Densities of the pressure data measured from two different taps, whose locations are illustrated in Chapter 3, at each of the spanwise pressure measurement stations are plotted both as a function of frequency for up to 250 Hz (part “a)” of the figures) and as a function of dimensionless frequency $St = fc/U_\infty$ for up to 4 (part “b)” of the figures) in Figures 4.45 – 4.56. However, due to the high velocities at the case of Reynolds number $Re = 10^5$, aforementioned Power Spectral Densities are plotted for dimensionless frequencies up to $St \cong 3.5$ rather than $St = 4$. Power Spectral Density of the pressure measurements for angle of attack $\alpha = 4°$ are shown in Figures 4.45, 4.46 and 4.47 for Reynolds numbers $Re = 10^4,\ 3.5x10^4$ and 10^5, respectively. The spectral densities that are plotted at foregoing Reynolds numbers for angles of attack $\alpha = 7°,\ 10°$ and $13°$ are shown in Figures 4.48 – 4.50, Figures 4.51 – 4.53 and Figures 4.54 – 4.56, respectively.

The pressure spectrums for $Re = 10^4$ case indicate that instead of existence of a common spectral peak in the spectra, there are broad pressure spectrums with wide range of spectral peaks. This might be related to the influence of vortical structures in the flow at this relatively low Reynolds number.

When the spectral peaks are examined for $Re = 3.5x10^4$ case, it is seen that increasing the Reynolds number decreased the dimensionless frequencies of the spectral peaks and concentrated them between $St = 0$ and 0.5 at both measurement points on each station on the wing surface and at all angles of attack. The pressure spectrums are still broad but the spectral densities of dimensionless frequencies greater than $St = 0.5$ are much smaller compared to the dominant spectral peaks. In addition to these dominant spectral peaks, coherent sub-dominant peaks having lower spectral densities are also witnessed at dimensionless frequencies between $St = 0.5$ and 1.5 for the case of 13 degree angle of attack.

The influence of relatively high Reynolds number in pressure distribution on the wing surface can be seen from the pressure spectra for Reynolds number $Re = 10^5$. The dimensionless frequencies of the spectral peaks decrease more with increasing Reynolds number and become concentrated between $St = 0$ and 0.2 at both measurement points on each station on the wing surface and at all angles of attack.

The foregoing Power Spectral Densities of the pressure data that were measured at same Reynolds numbers are plotted as a function of dimensionless frequency $St = fc/U_\infty$ and sorted with respect to their angle of attack in order the investigate the effect of angle of attack on the pressure spectra. These figures have been added to Appendix B as Figures B.1 – B. 9. Figures B.1 – B.3 show the pressure spectrums at $Re = 10^4$ at angles of attack $\alpha = 4°, 7°, 10°$ and 13°, whereas Figures B.4 – B6 and B.7 – B.9 show the pressure spectrums at same angles of attack but at different Reynolds numbers, $Re = 3.5x10^4$ and $Re = 10^5$, respectively.

4.3 Results of Mean and Unsteady Velocity Measurements

Power Spectral Densities of 2-components (streamwise and vertical) of the velocity measured at the leading edge vortex core at chordwise locations $x/c = 0.32$, $x/c = 0.56$ and $x/c = 0.80$, which are corresponding to pressure measurement stations of the wing, are shown in Figure 4.57 as a function of dimensionless frequency $St = fc/U_\infty$ for up to 25. The measurements shown in this figure are carried out at angles of attack $\alpha = 4°$ (part “a)” of the figure) and $\alpha = 7°$ (part “b)” of the figure), and at Reynolds number $Re = 10^4$, where a coherent pair of leading-edge vortices take place on the whole measurement locations.

As it is seen in Figure 4.57, results of velocity measurements shows that the axial velocities at the vortex core are higher than the freestream velocity at streamwise direction at chordwise distances $x/c = 0.32$ and $x/c = 0.56$ at both angles of attack that measurements employed. However, the velocities decrease with downstream movement below the wing and become very close to the freestream velocity at chordwise distance $x/c = 0.80$ due to an attenuation in vortex strength. The highest axial velocity at vortex core is measured at 4-degree angle of attack at $x/c = 0.32$, and it is found to be 1.77 times greater than the freestream velocity. Moreover, it is seen from the root mean square (RMS) of the velocity measurements that the velocities at the vortex core highly fluctuates at both streamwise and vertical directions.

When the velocity spectra of the vortex core are examined, there is no such a spectral peak that exists at all the cases, instead the peaks generally exist at different dimensionless frequencies as it is seen in Figure 4.57. The spectra of both components of the velocity at 4-degree angle of attack at $x/c = 0.32$ have peaks at same dimensionless frequency $St = 20.8$, and the spectrum at $x/c = 0.56$ at same angle of attack for streamwise direction of velocity have a similar peak at $St = 19.7$, whereas rest of the spectra for 4-degree angle of attack have broadband peaks. It is seen from the velocity spectra for 7-degree angle of attack that u and ω components of velocity that were measured at $x/c = 0.32$ have spectral peaks at $St = 0.7$ and $St = 2.25$, respectively; whereas the spectra at $x/c = 0.56$ and $x/c = 0.80$ have broadband spectral peaks, and have a spectral peak around $St = 5$ at both velocity components.

Figures 4.58 – 4.75 illustrates the Power Spectral Densities of 1-component of velocity measured via Laser Doppler Anemometry (LDA) at two points (locations of the measurement points are described in Chapter 3) as a function of dimensionless frequency $St = fc/U_\infty$ for up to $St = 8$. However, the smoke intensity was inadequate for collecting data with LDA around 1000 Hz at some measurement points at Reynolds number $Re = 10^5$, seen in figures 4.70 – 4.75. The velocity data was collected at a rate between 832 – 980 Hz at these points, which corresponds to dimensionless frequencies in the range of $St = 6 - 8$. Each figure show the spectral analysis of the velocity data that were measured at two different points located at a crossflow plane that corresponds to one of the pressure measurement sections, and at a constant Reynolds number at four different angles of attack, namely $\alpha = 4°$, $7°, 10°$ and $13°$. The odd-numbered figures show the results of streamwise (u) component of the velocity, whereas the even-numbered ones show the vertical (ω) component of the velocity. Figures 4.58 – 4.63 illustrate the spectral densities for $Re = 10^4$, whereas Figures 4.64 – 4.69 and Figures 4.70 – 4.75 illustrate the spectral densities for $Re = 3.5x10^4$ and $Re = 10^5$, respectively. The necessary information about Reynolds number, measurement location and component of the velocity are also shown in each figure.

As it is seen in Figures 4.58 – 4.63 that at 4 and 7-degree angles of attack and at Reynolds number $Re = 10^4$, spectral peaks of dimensionless frequency around $St = 5$ are clearly visible at velocity spectra of the measurement points that were influenced by strong leading edge vortex core, and this influence can be observed better at the spectra of vertical component of the velocity. Downstream movement in streamwise direction reduces the vortex strength which results in as a decrease in the spectral densities of spectral peaks at dimensionless frequencies around $St = 5$, and make the peaks that close to $St = 0$ the dominant peaks in the flow. The measurement points located in a short distance to a strong leading-edge vortex core have dominant peaks around $St = 0$, but they also have sub-dominant peaks around $St = 4$ (i.e. $u-$ component of velocity spectra at 7-degree angle of attack at a point that lie on section b and located beneath the first station), whereas the points which are located at regions in the absence of vortex core have spectral peaks around $St = 0$, although the footprints of the dimensionless frequencies around $St = 5$ still exhibits as subdominant peaks in the spectra of ω component of velocity which have broader spectra compared to the u component of velocity (i.e. u and ω components of velocity spectra at 4 and 7-degree angles of attack at points that lie on section b and located beneath the second station). It is also seen that the flow structure with a three-dimensional separation from the wing surface at this relatively low Reynolds number and high angles of attack shows distinct peaks concentrated between dimensionless frequencies $St = 0 - 1$ in the u component of velocity spectra, whereas the ω component of velocity spectra have broader spectra but its dominant peaks still exist in the range of $\mathrm{S}t = 0 - 1$ $(\mathrm{i.e.}$ u and ω components of velocity spectra at 13-degree angle of attack at all measurement locations).

The velocity spectra calculated at Reynolds numbers $Re = 3.5x10^4$ and $Re = 10^5$ at different angles of attack are similar to each other, seen in Figures 4.64 – 4.75. Vortex breakdown occurs in the flow at this relatively high Reynolds numbers at each measurement planes located at chordwise distances $x/c = 0.32$, $x/c = 0.56$ and $x/c = 0.80$, at all angles of attack. The velocity spectra have peaks scattered in broad dimensionless frequencies and neither a common spectral peak nor dominant peaks concentrated between $St = 0 - 1$ exist in the spectra, except for very few cases, as they were in the case of Reynolds number $Re = 10^4$.

When the unsteady velocity measurement results are examined, it is seen that the fluctuations in velocities that were measured on ‘Section a’ are generally much greater than the ones measured on ‘Section b’ for both velocity components at Reynolds number $Re = 10^4$ and at all angles of attack. These high velocity fluctuations at Section a can be originated from the highly unsteady flow structures of vortex cores that exist at the region of measurement at 4 and 7-degree angles of attack, and the vortical structures, that arising from the apex of the wing exist at the region of measurement at 10 and 13-degree angles of attack, which can be interpreted from the results of smoke visualization experiments. Moreover, when the ω component of the velocity measurements at “Section b” are compared for each angle of attack, it is found that the minimum fluctuations are measured at 13-degree angle of attack, where a three-dimensional separation from the surface of the wing occurs. This was an expected resulted since the stalled flows have very low mean velocities and velocity fluctuations near the surface of the wing as stated by Gursul et al. [3]. In contrast to the previous trend, it is seen that the velocity fluctuations measured on ‘Section b’ are generally much greater than the ones measured on ‘Section a’, due to a transition from a vortex dominated flow to a flow structure with broken down vortices in separated flow field, for both velocity components at Reynolds numbers $Re = 3.5x10^4$ and $Re = 10^5$ and at all angles of attack except $\alpha = 13°$. A possible reason for this situation is the existence of reattachment regions in a close proximity to ‘Section a’, which can be interpreted from the smoke visualization results at angles of attack $\alpha = 4°,\ 7°$ and $\alpha = 10°$, whereas the measurement points on ‘Section a’ is totally covered with broken down vortices at angle of attack $\alpha = 13°$ since the reattachment region is moved inboard toward the wing centerline. Thus, an important conclusion can be drawn from the unsteady velocity measurements at these high Reynolds numbers that the fluctuations at both components of the velocity measured in regions close to the reattachment line are generally far less than the ones measured at vortex breakdown regions at more outboard locations towards the leading edges. The velocity fluctuations measured on ‘Section a’ at 13-degree angle of attack are found to be greater than the ones measured on ‘Section b’, for both velocity components at almost all of the measurement locations. Moreover, it is found that at 13-degree angle of attack and at these relatively high Reynolds numbers, the highest velocity fluctuations at both components of the velocity are measured at ‘Section a’. In spite the fact that the reattachment region moved more inboard and not in a close proximity to ‘Section a’ at this high angle of attack, it might be still have an influence on the measurements since Taylor and Gursul [4] stated that the highest velocity fluctuations near the surface of the wing occur along the reattachment line in the case of pre-stall, when the vortex breakdown is reached to the apex at high angles of attack. It is important to note that the aforementioned unsteady velocity measurement results shows a great analogy with the unsteady pressure measurement results.

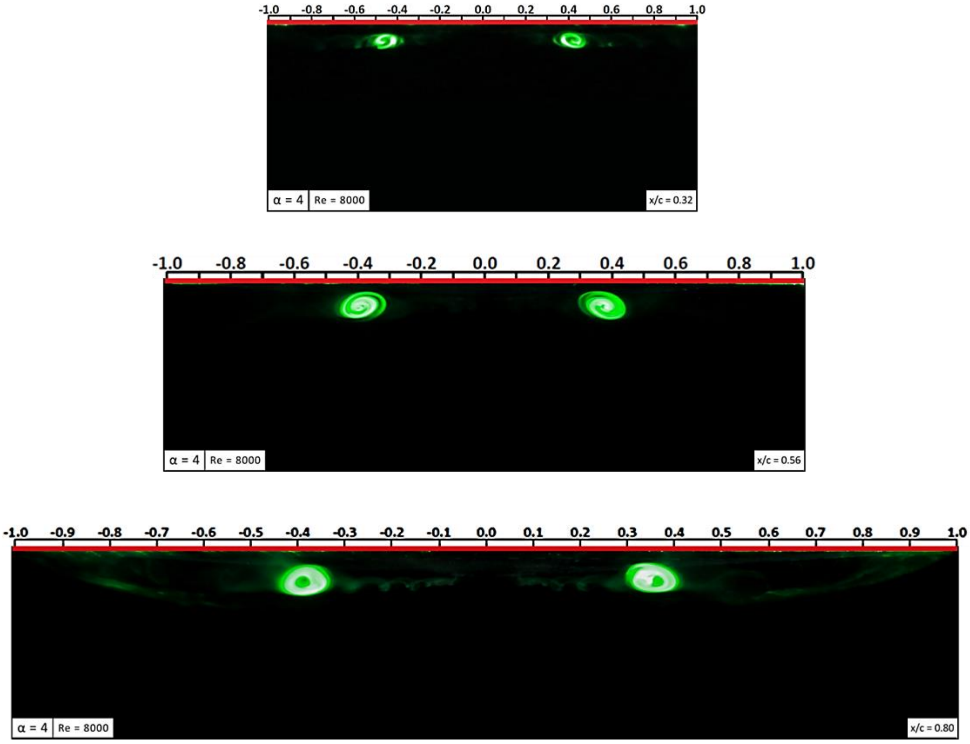

Figure 4.1 Crossflow visualization at 4-degree angle of attack and $Re = 8000$ in end-view planes at x/c = 0.32, x/c = 0.56 and x/c = 0.80

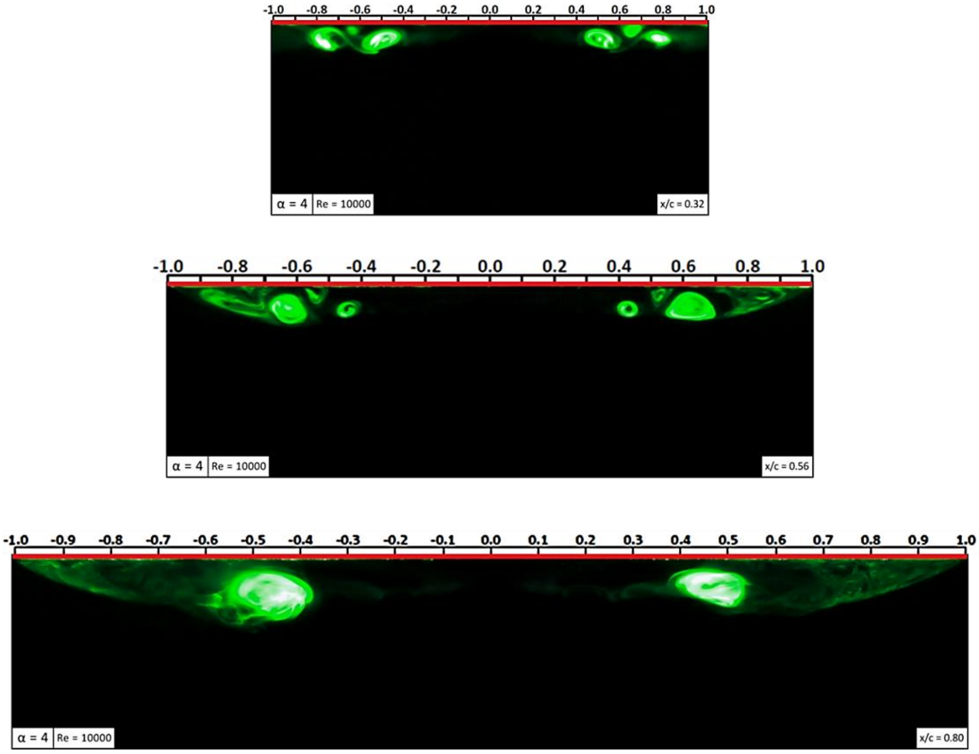

Figure 4.2 Crossflow visualization at 4-degree angle of attack and $Re = 10000$ in end-view planes at x/c = 0.32, x/c = 0.56 and x/c = 0.80

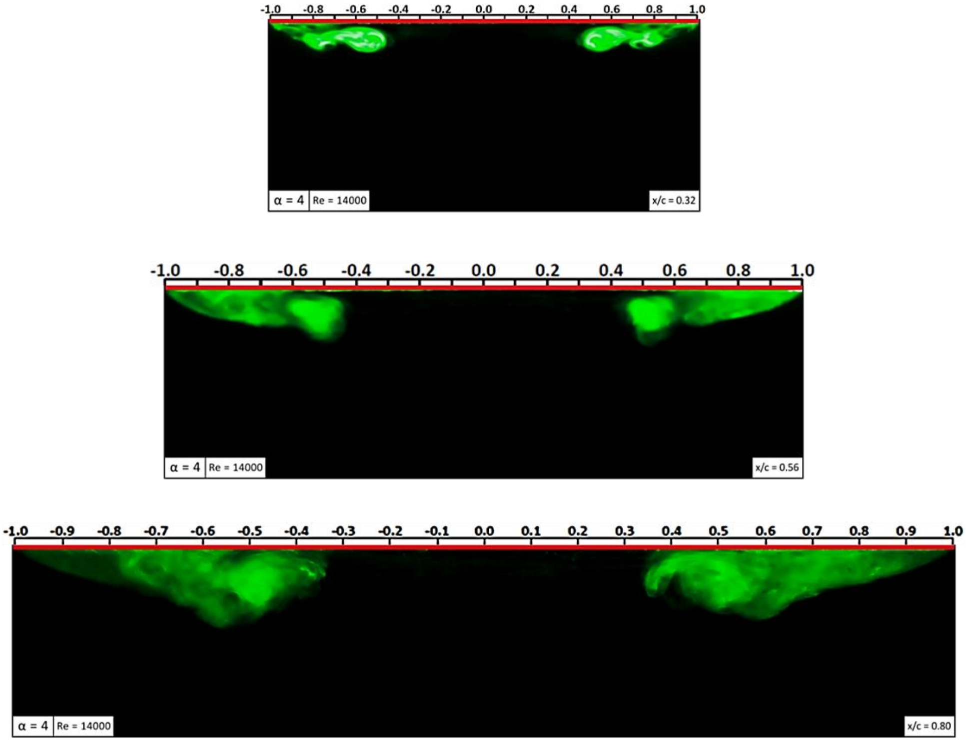

Figure 4.3 **Crossflow visualization at 4-degree angle of attack and $Re = 14000$ in end-view planes at x/c = 0.32, x/c = 0.56 and x/c = 0.80**

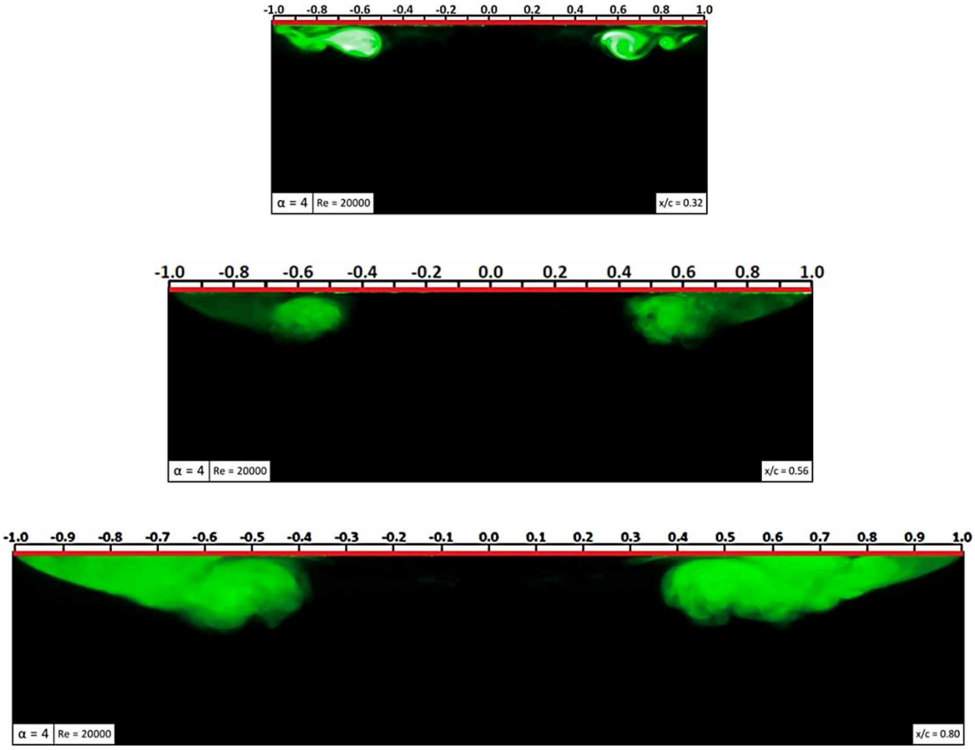

Figure 4.4 **Crossflow visualization at 4-degree angle of attack and $Re = 20000$ in end-view planes at x/c = 0.32, x/c = 0.56 and x/c = 0.80**

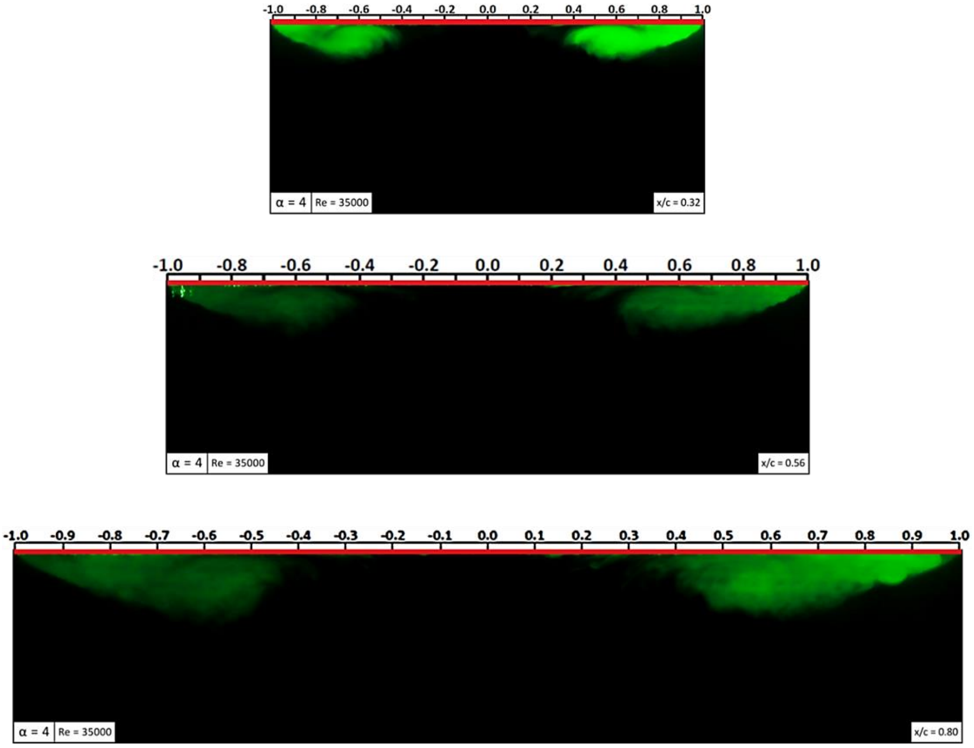

Figure 4.5 Crossflow visualization at 4-degree angle of attack and $Re = 35000$ in end-view planes at x/c = 0.32, x/c = 0.56 and x/c = 0.80

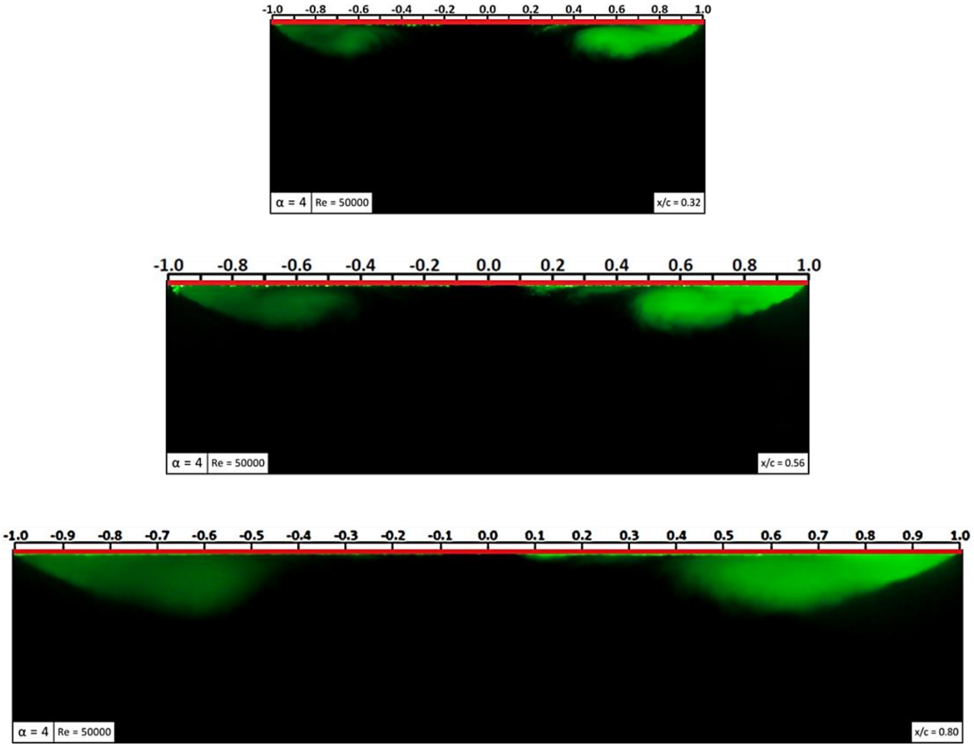

Figure 4.6 Crossflow visualization at 4-degree angle of attack and $Re = 50000$ in end-view planes at x/c = 0.32, x/c = 0.56 and x/c = 0.80

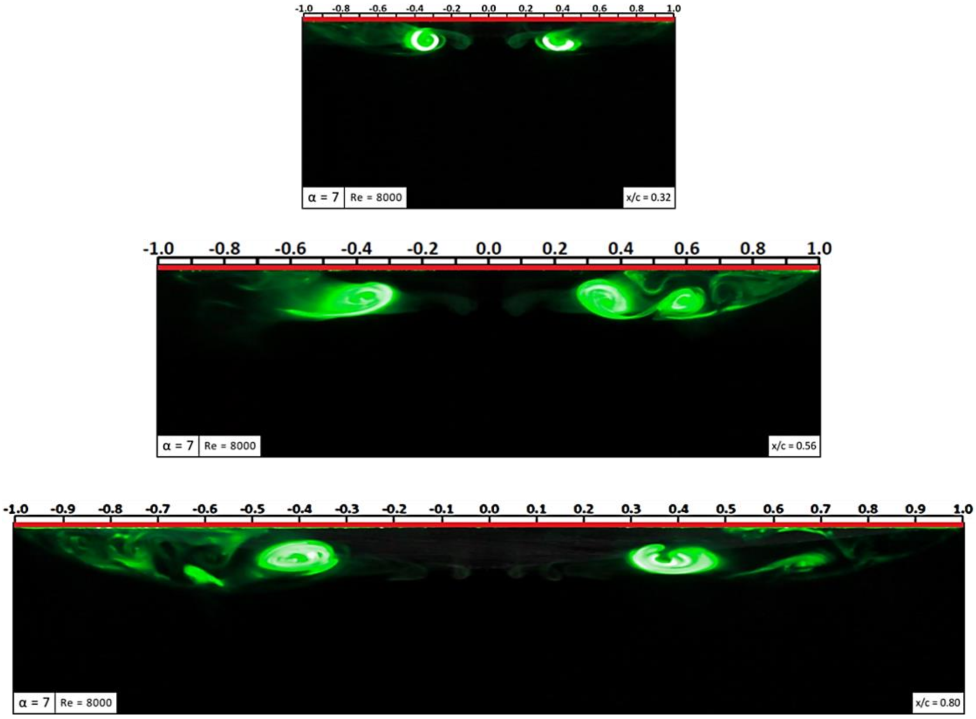

Figure 4.7 Crossflow visualization at 7-degree angle of attack and $Re = 8000$ in end-view planes at x/c = 0.32, x/c = 0.56 and x/c = 0.80

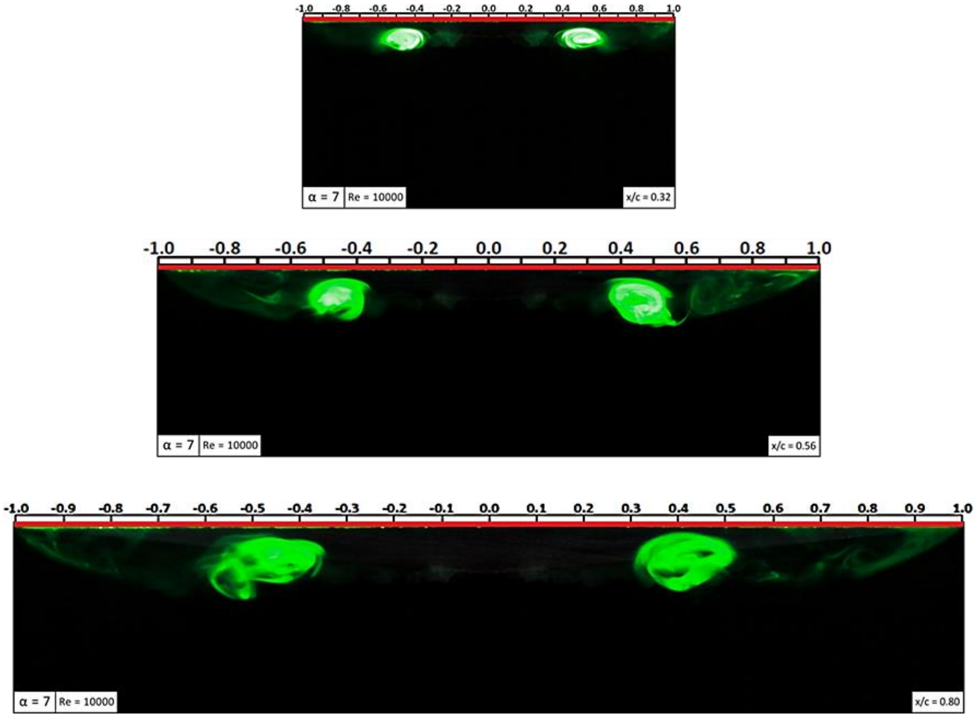

Figure 4.8 Crossflow visualization at 7-degree angle of attack and $Re = 10000$ in end-view planes at x/c = 0.32, x/c = 0.56 and x/c = 0.80

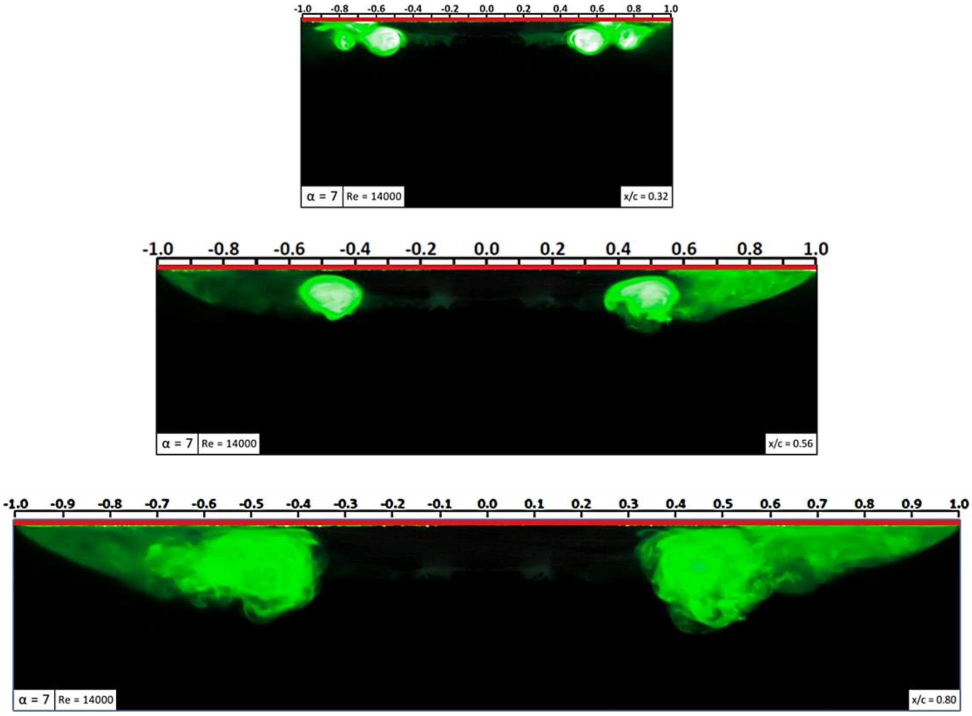

Figure 4.9 Crossflow visualization at 7-degree angle of attack and $Re = 14000$ in end-view planes at x/c = 0.32, x/c = 0.56 and x/c = 0.80

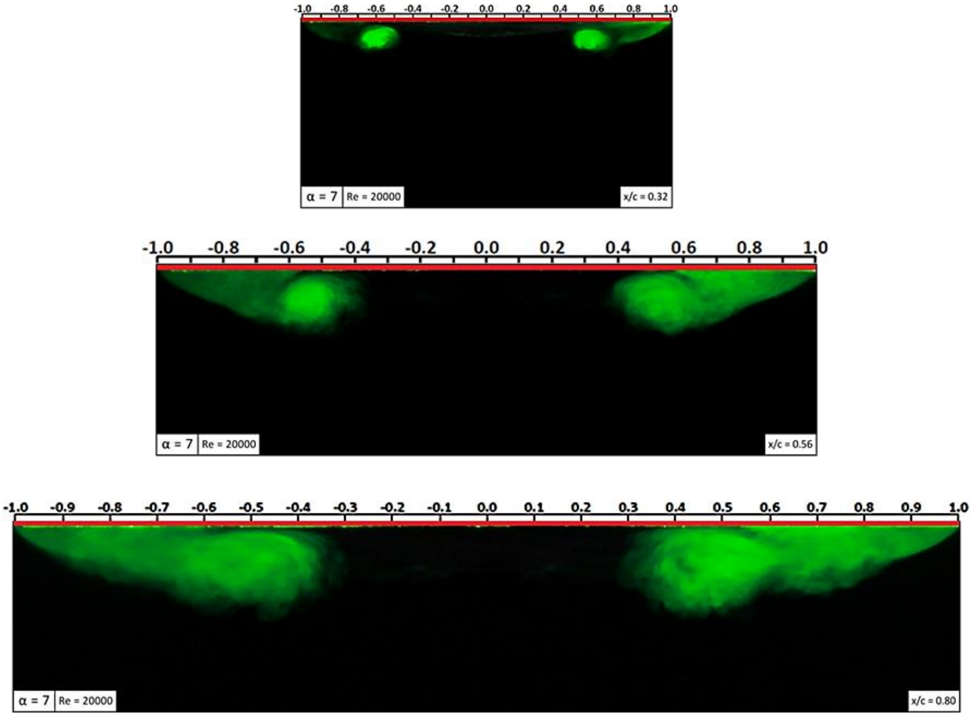

Figure 4.10 Crossflow visualization at 7-degree angle of attack and $Re = 20000$ in end-view planes at x/c = 0.32, x/c = 0.56 and x/c = 0.80

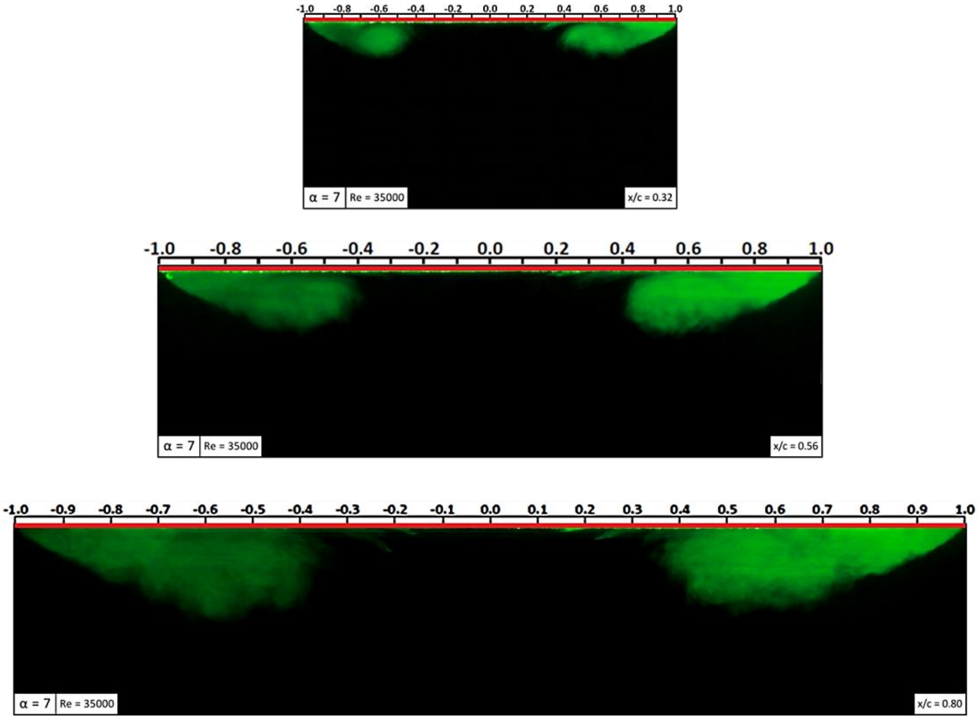

Figure 4.11 Crossflow visualization at 7-degree angle of attack and $Re = 35000$ in end-view planes at x/c = 0.32, x/c = 0.56 and x/c = 0.80

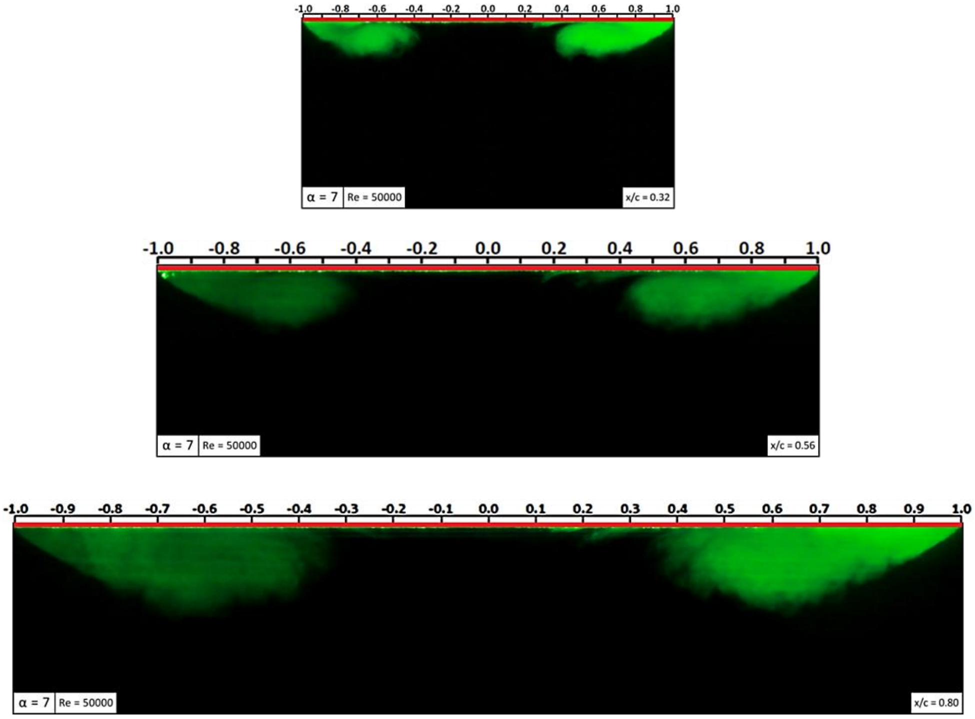

Figure 4.12 Crossflow visualization at 7-degree angle of attack and $Re = 50000$ in end-view planes at x/c = 0.32, x/c = 0.56 and x/c = 0.80

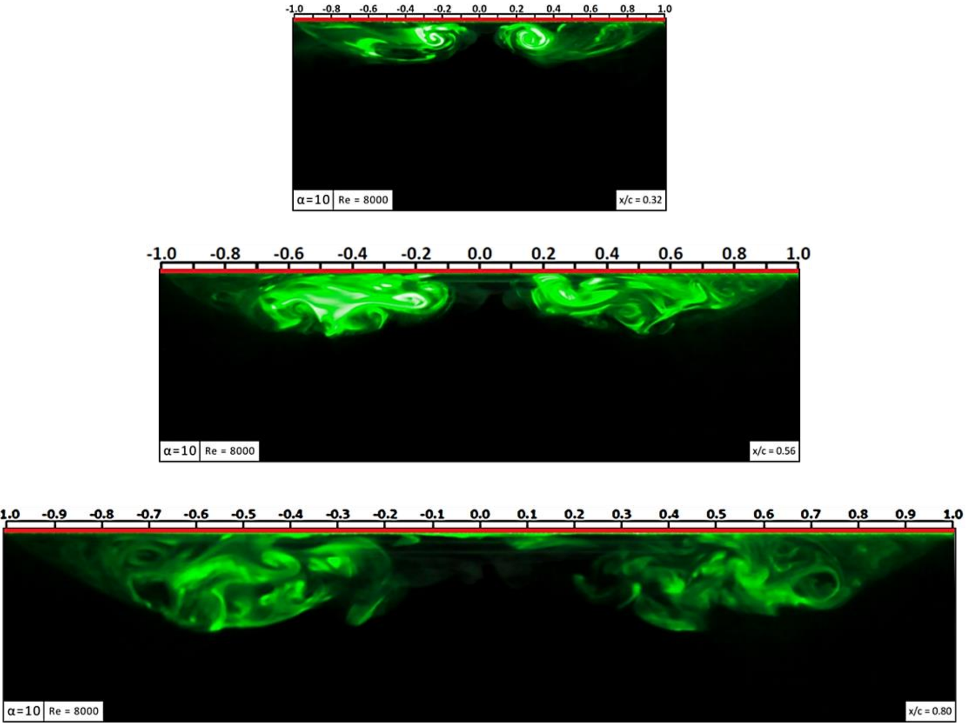

Figure 4.13 Crossflow visualization at 10-degree angle of attack and $Re = 8000$ in end-view planes at x/c = 0.32, x/c = 0.56 and x/c = 0.80

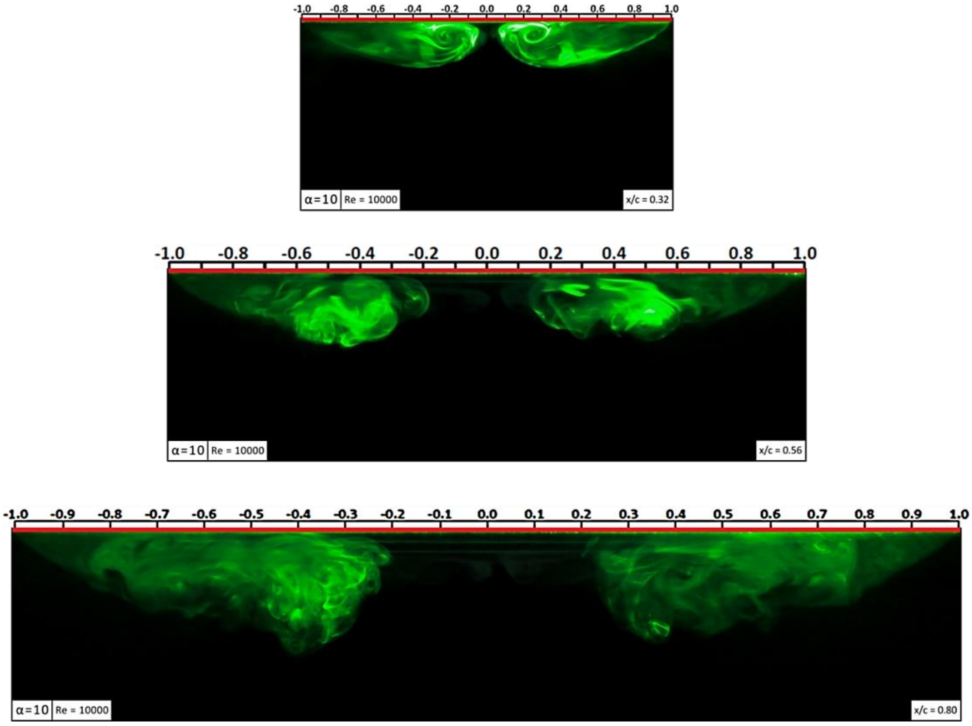

Figure 4.14 Crossflow visualization at 10-degree angle of attack and $Re = 10000$ in end-view planes at x/c = 0.32, x/c = 0.56 and x/c = 0.80

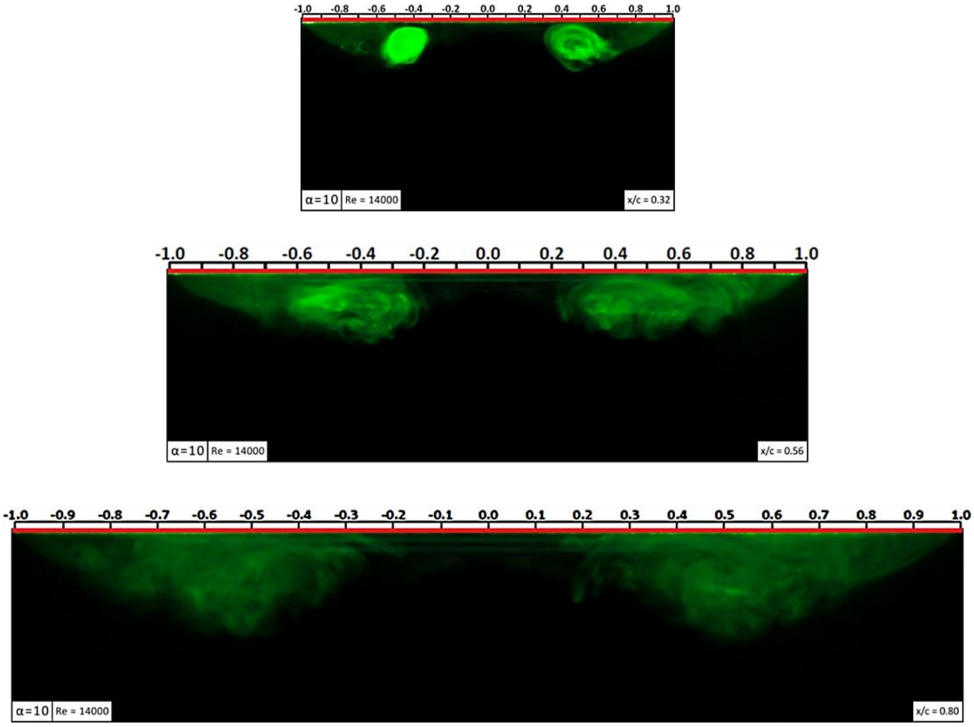

Figure 4.15 Crossflow visualization at 10-degree angle of attack and $Re = 14000$ in end-view planes at x/c = 0.32, x/c = 0.56 and x/c = 0.80

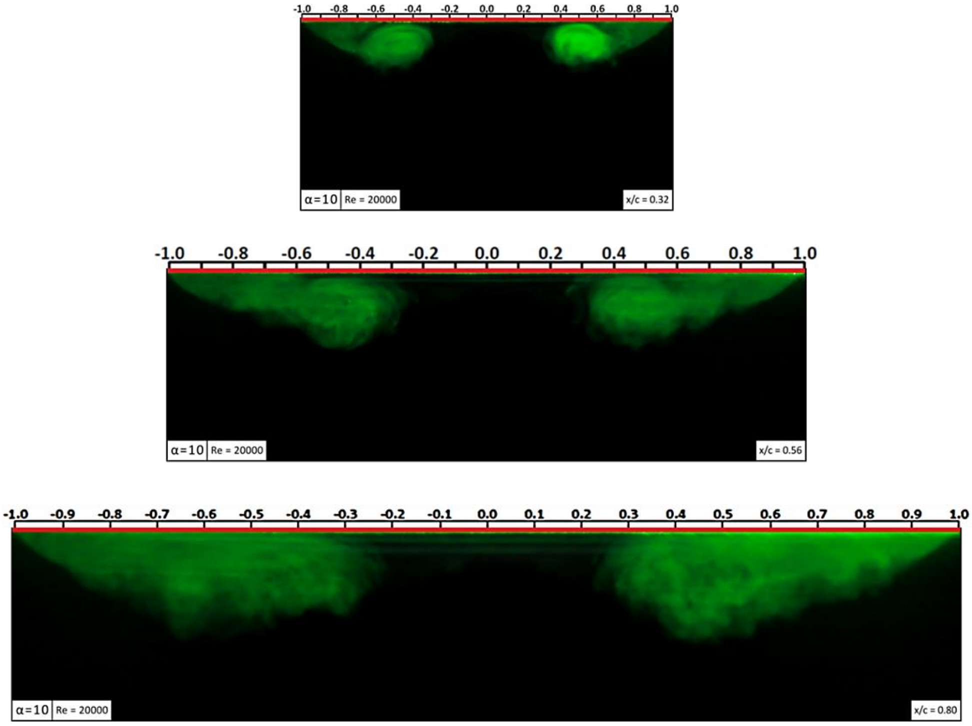

Figure 4.16 Crossflow visualization at 10-degree angle of attack and $Re = 20000$ in end-view planes at x/c = 0.32, x/c = 0.56 and x/c = 0.80

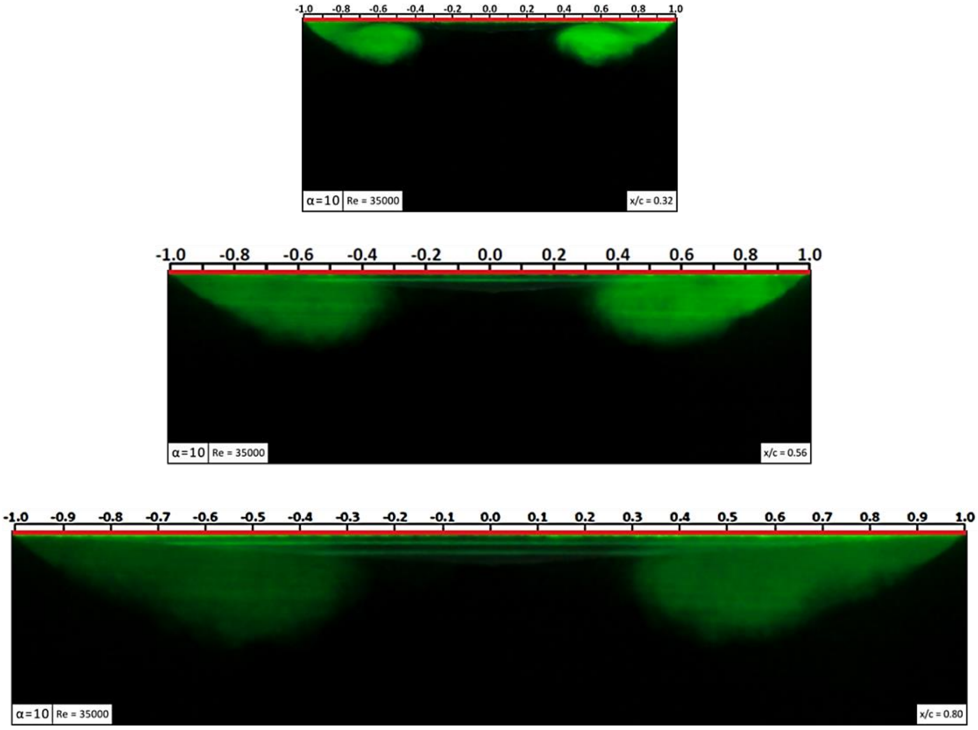

Figure 4.17 Crossflow visualization at 10-degree angle of attack and $Re = 35000$ in end-view planes at x/c = 0.32, x/c = 0.56 and x/c = 0.80

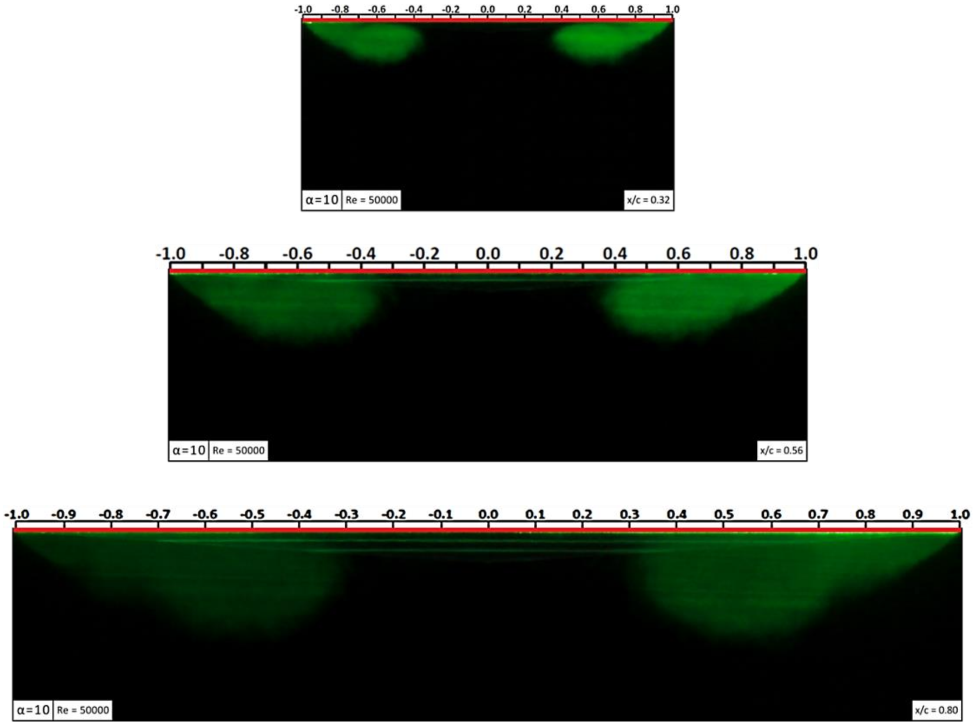

Figure 4.18 Crossflow visualization at 10-degree angle of attack and $Re = 50000$ in end-view planes at x/c = 0.32, x/c = 0.56 and x/c = 0.80

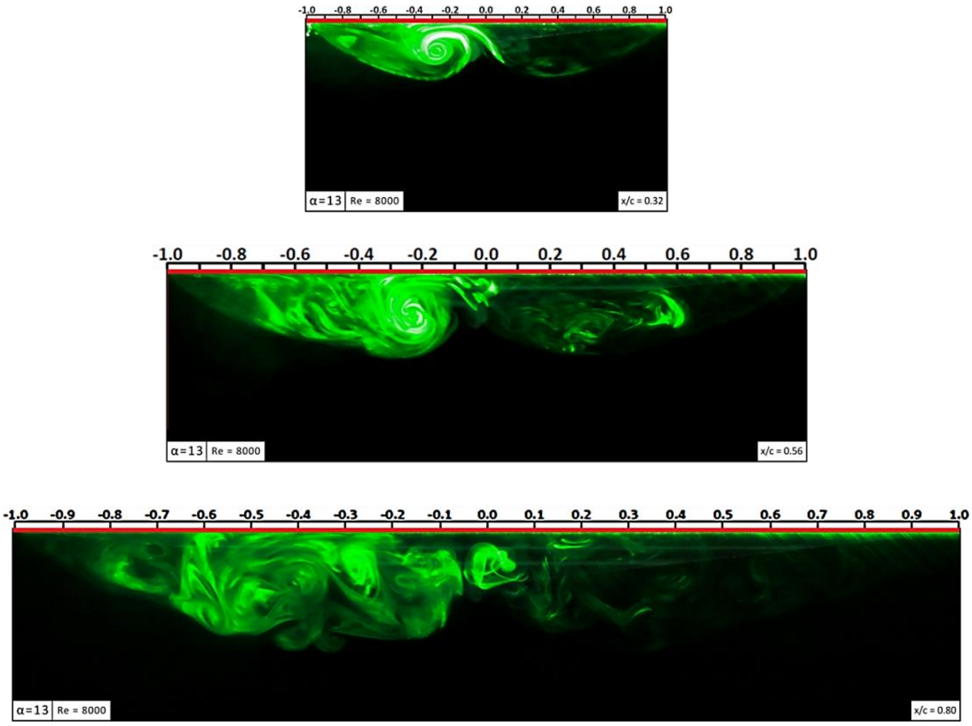

Figure 4.19 Crossflow visualization at 13-degree angle of attack and $Re = 80000$ in end-view planes at x/c = 0.32, x/c = 0.56 and x/c = 0.80

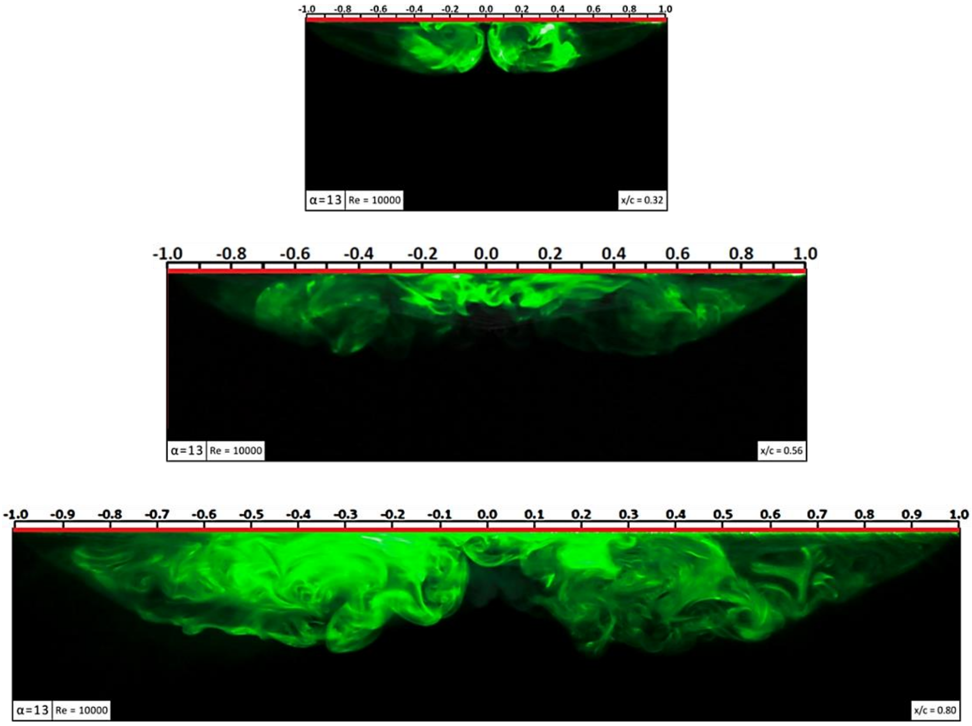

Figure 4.20 Crossflow visualization at 13-degree angle of attack and $Re = 10000$ in end-view planes at x/c = 0.32, x/c = 0.56 and x/c = 0.80

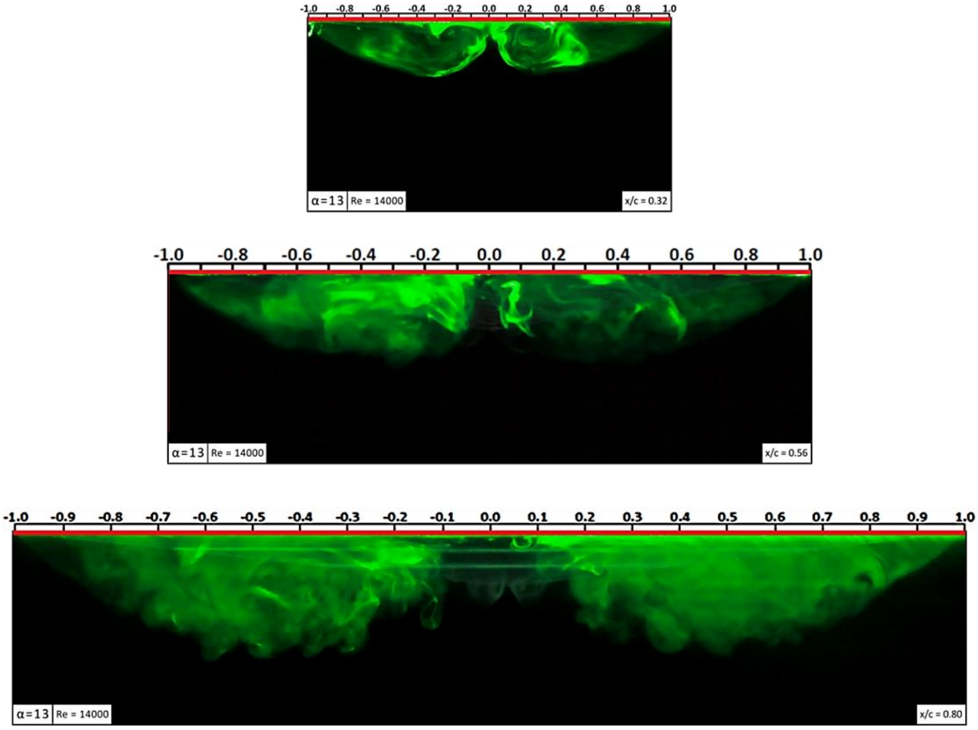

Figure 4.21 Crossflow visualization at 13-degree angle of attack and $Re = 14000$ in end-view planes at x/c = 0.32, x/c = 0.56 and x/c = 0.80

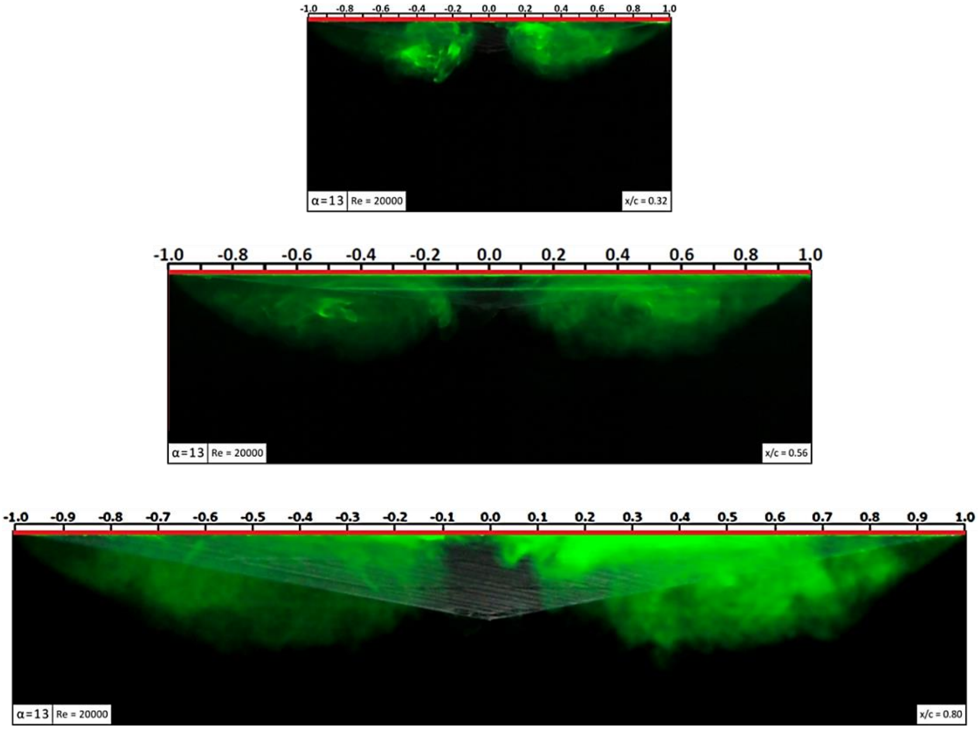

Figure 4.22 Crossflow visualization at 13-degree angle of attack and $Re = 20000$ in end-view planes at x/c = 0.32, x/c = 0.56 and x/c = 0.80

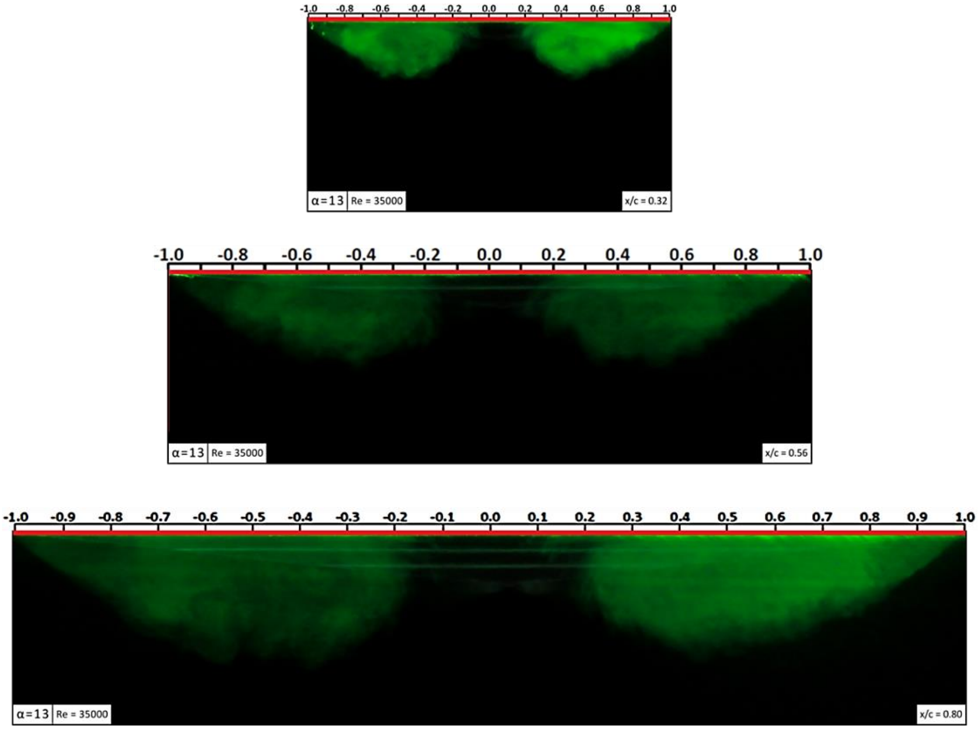

Figure 4.23 Crossflow visualization at 13-degree angle of attack and $Re = 35000$ in end-view planes at x/c = 0.32, x/c = 0.56 and x/c = 0.80

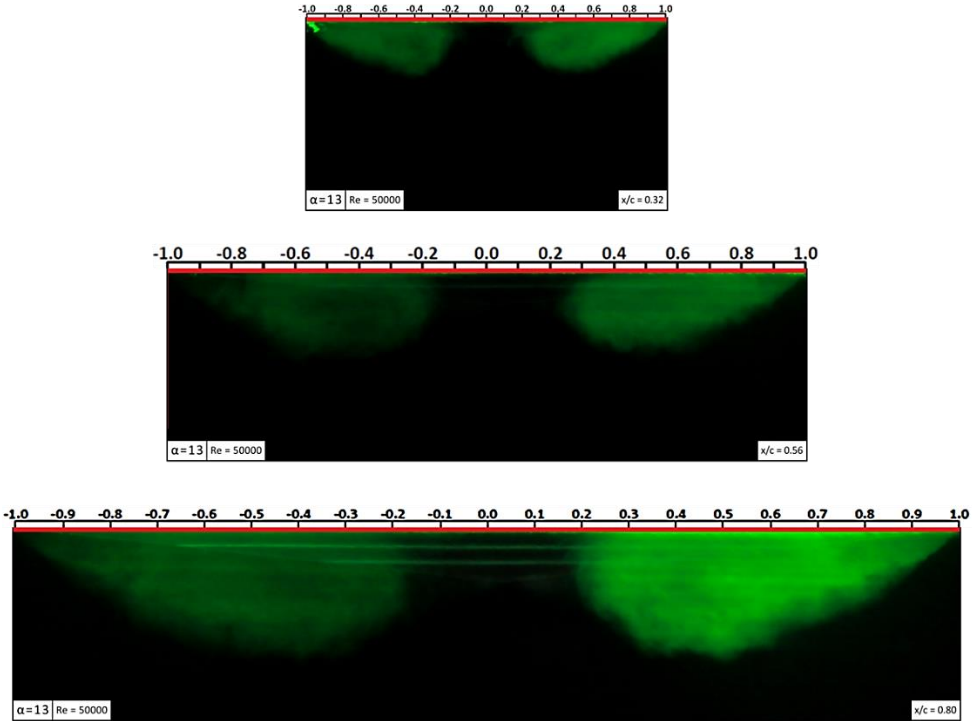

Figure 4.24 Crossflow visualization at 13-degree angle of attack and $Re = 50000$ in end-view planes at x/c = 0.32, x/c = 0.56 and x/c = 0.80

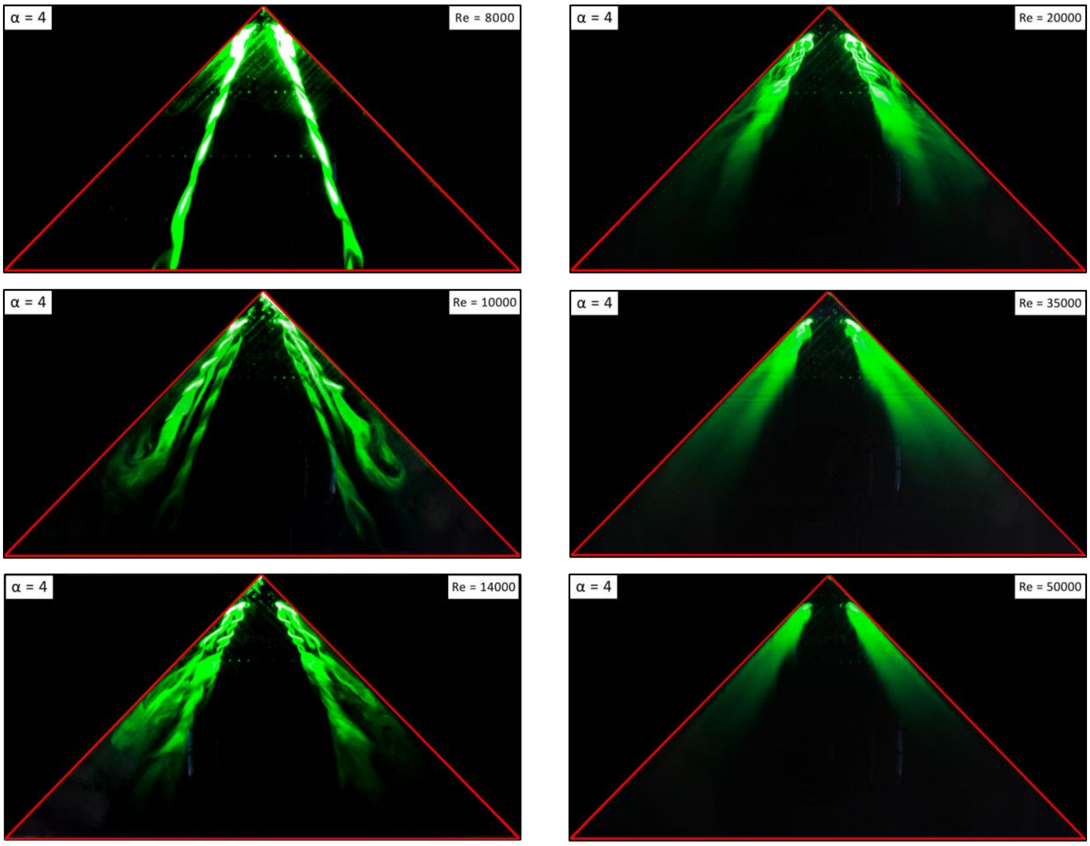

Figure 4.25 Flow visualization images taken at plan-view at different Reynolds numbers where the angle of attack was $\alpha = 4°$

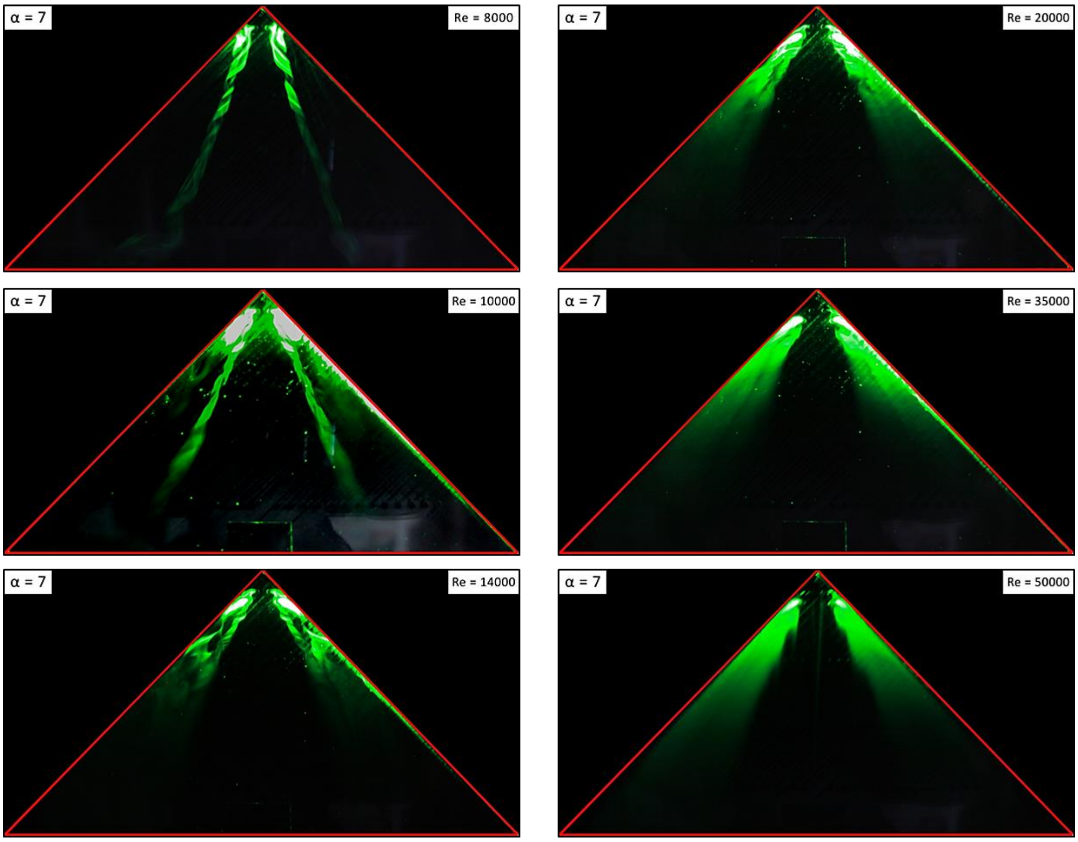

Figure 4.26 Flow visualization images taken at plan-view at different Reynolds numbers where the angle of attack was $\alpha = 7°$

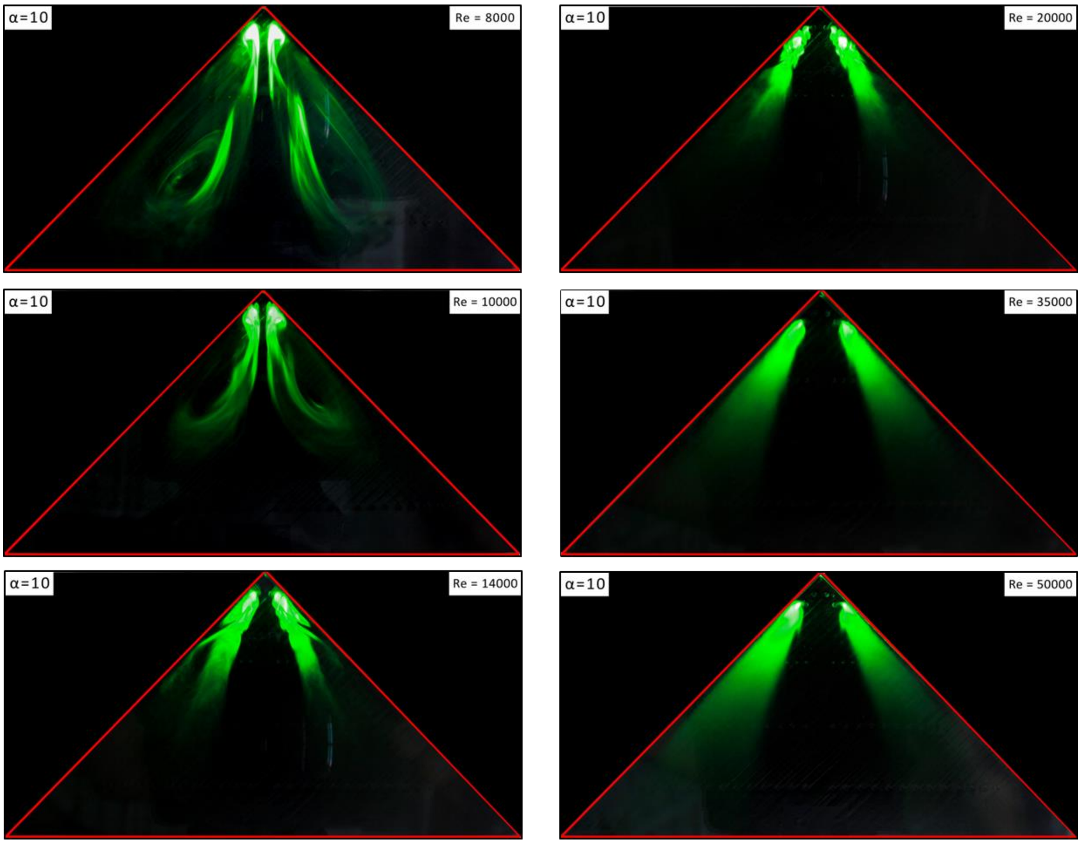

Figure 4.27 Flow visualization images taken at plan-view at different Reynolds numbers where the angle of attack was $\alpha = 10°$

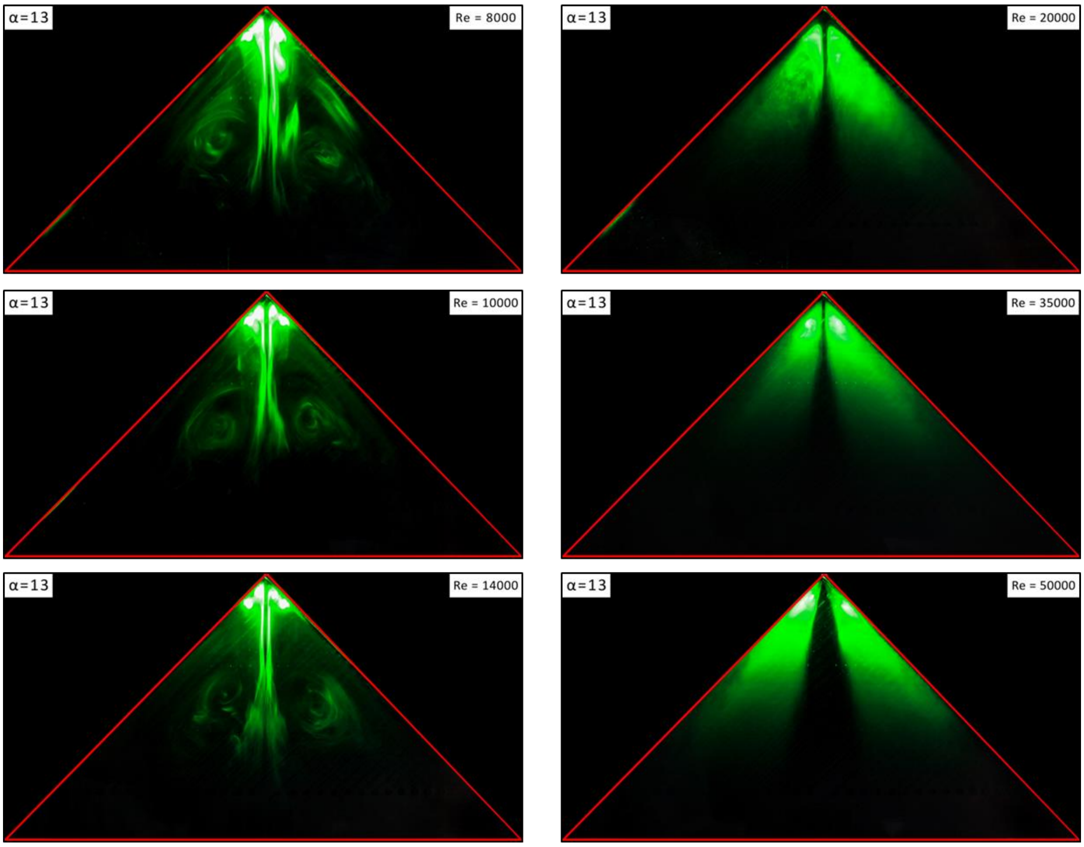

Figure 4.28 Flow visualization images taken at plan-view at different Reynolds numbers where the angle of attack was $\alpha = 13°$

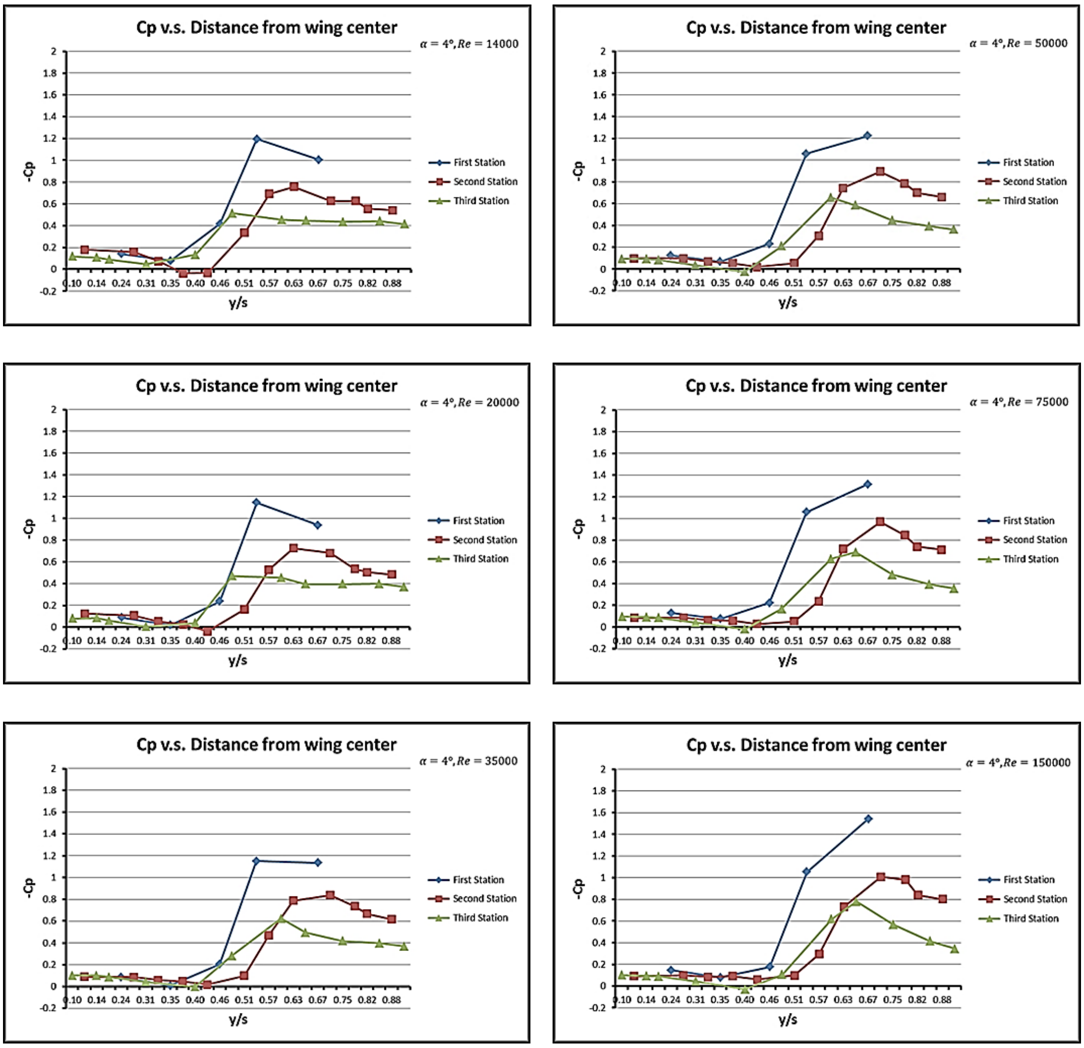

Figure 4.29 Spanwise variation of steady pressure distribution at three different chordwise stations corresponding to x/c = 0.32, x/c = 0.56 and x/c = 0.80 at 4-degree angle of attack for different Reynolds numbers

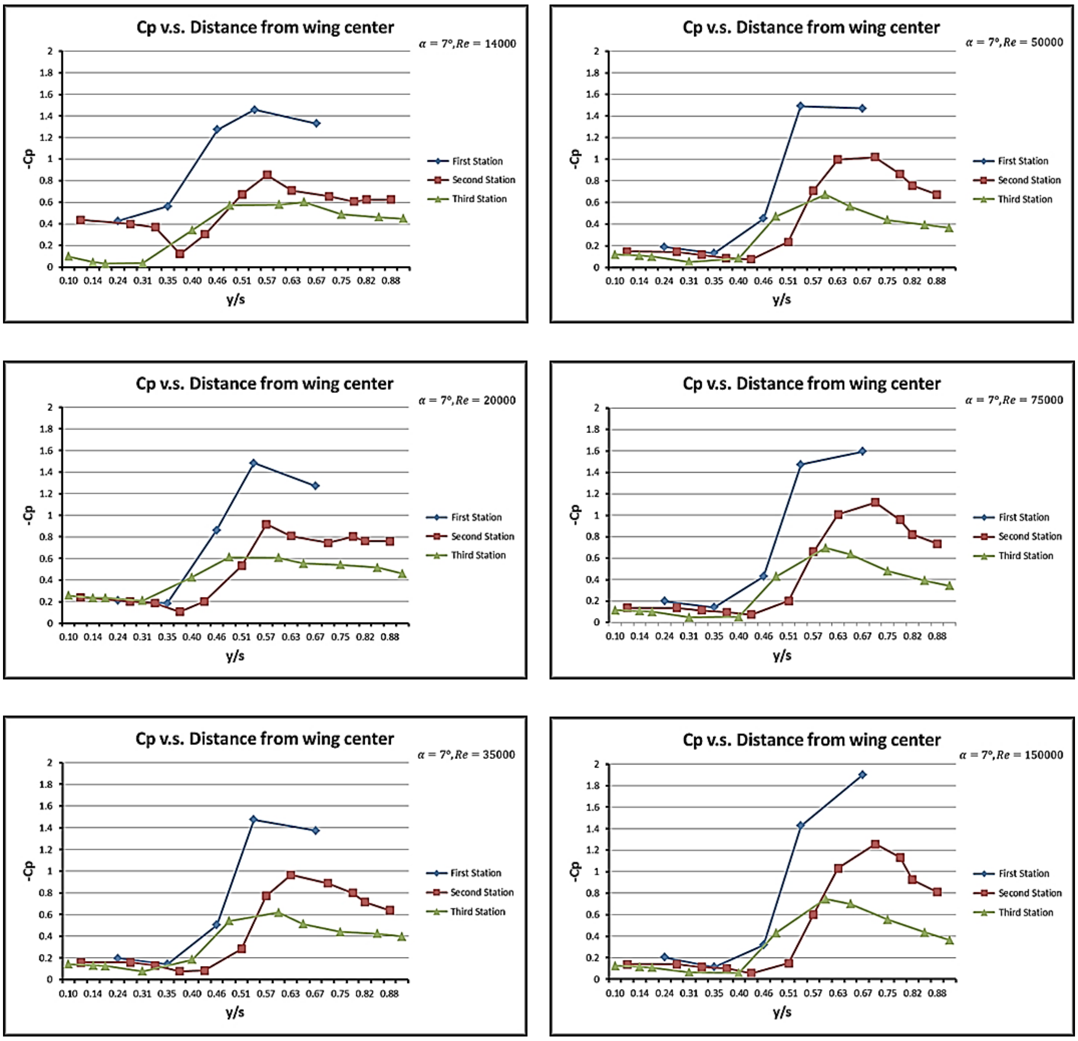

Figure 4.30 Spanwise variation of steady pressure distribution at three different chordwise stations corresponding to x/c = 0.32, x/c = 0.56 and x/c = 0.80 at 7-degree angle of attack for different Reynolds numbers

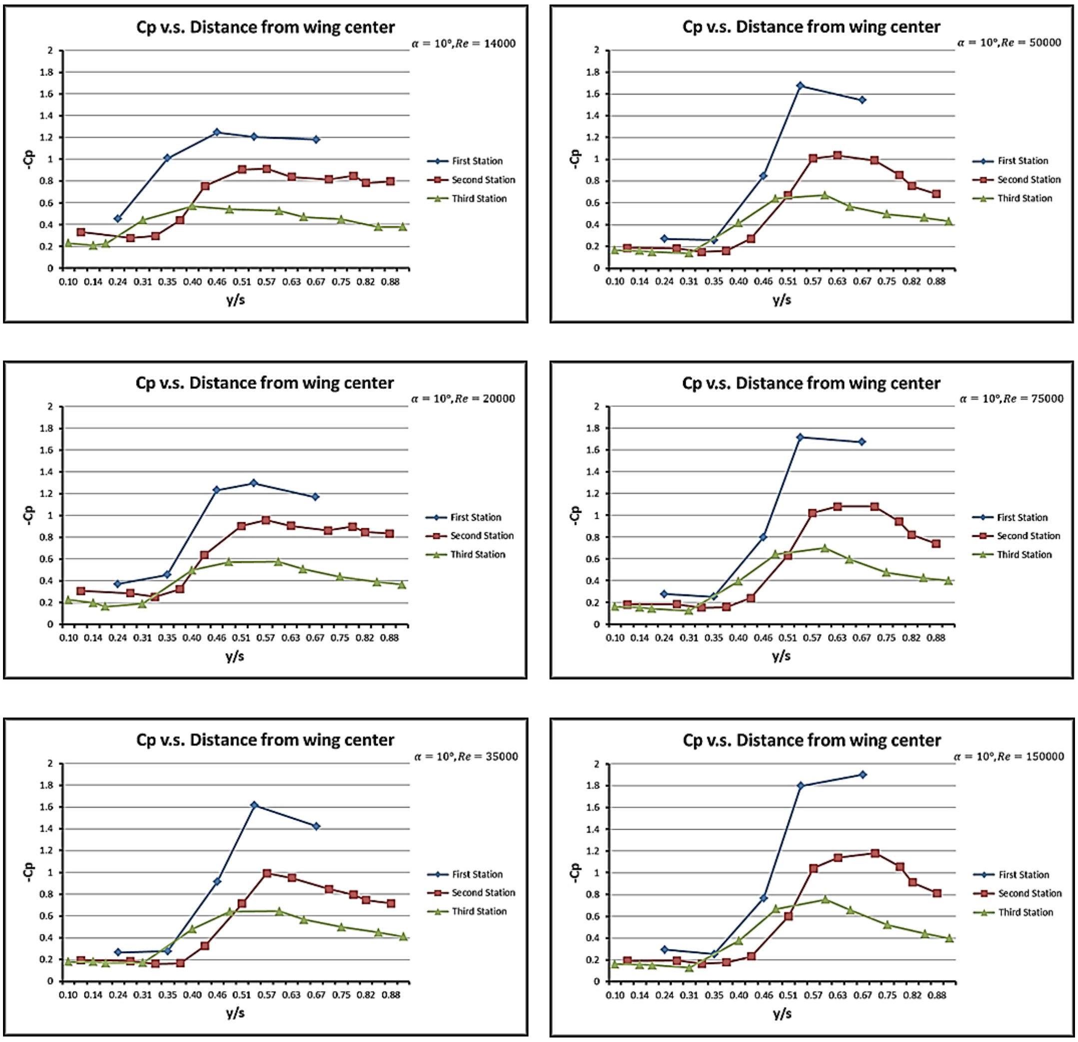

Figure 4.31 Spanwise variation of steady pressure distribution at three different chordwise stations corresponding to x/c = 0.32, x/c = 0.56 and x/c = 0.80 at 10-degree angle of attack for different Reynolds numbers

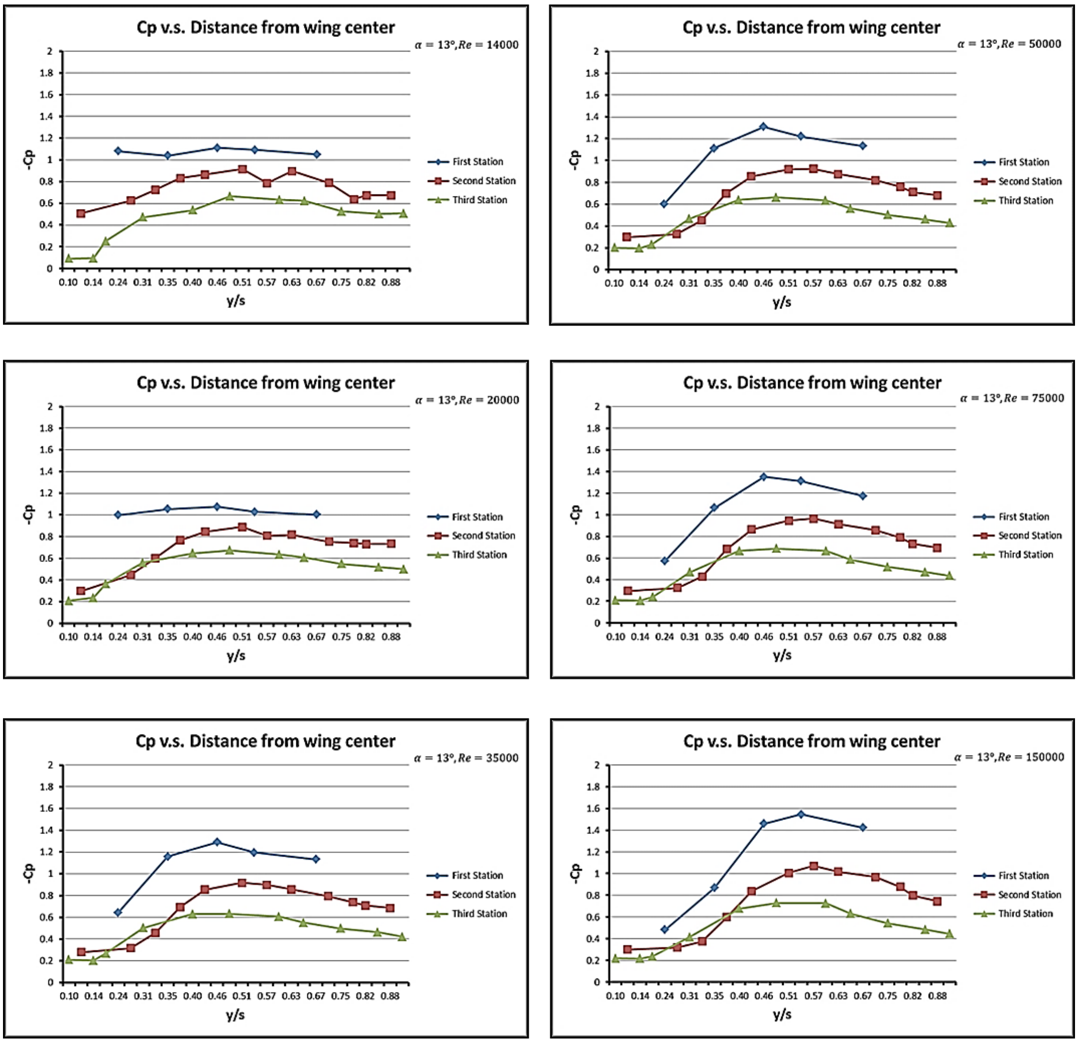

Figure 4.32 Spanwise variation of steady pressure distribution at three different chordwise stations corresponding to x/c = 0.32, x/c = 0.56 and x/c = 0.80 at 13-degree angle of attack for different Reynolds numbers

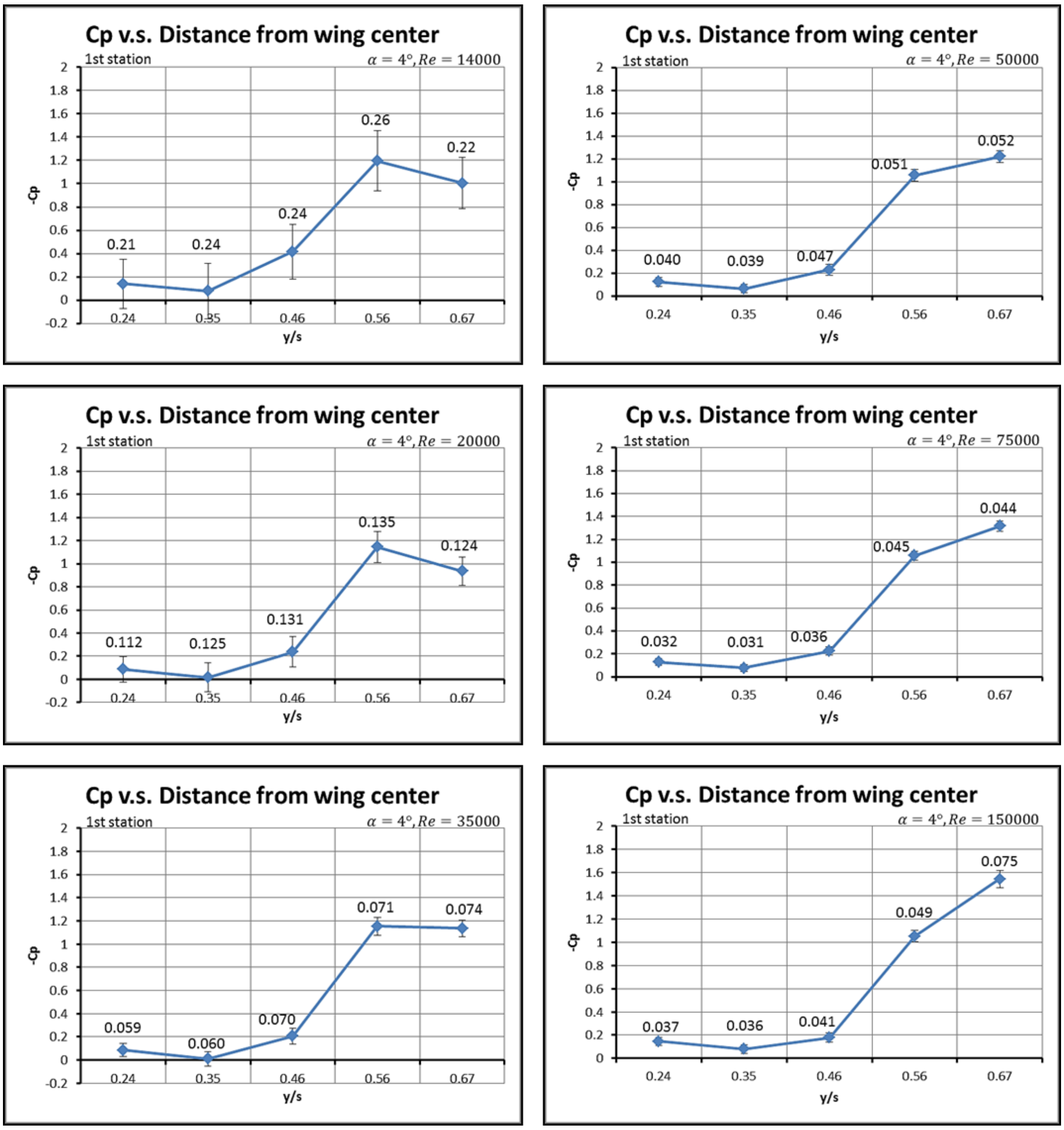

Figure 4.33 RMS of pressure measurements on a chordwise station located at x/c = 0.32 at 4-degree angle of attack and at different Reynolds numbers

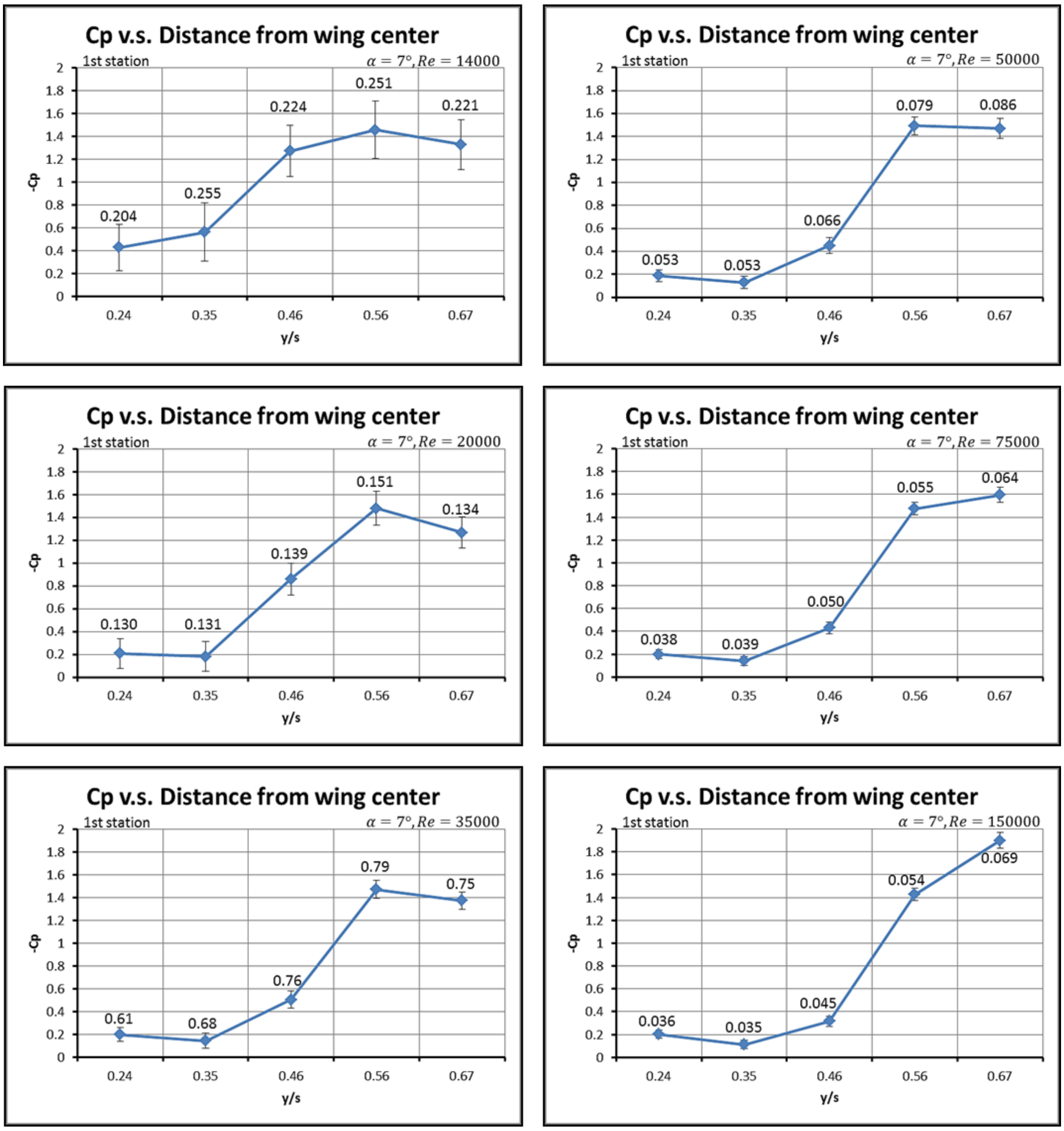

Figure 4.34 RMS of pressure measurements on a chordwise station located at x/c = 0.32 at 7-degree angle of attack and at different Reynolds numbers

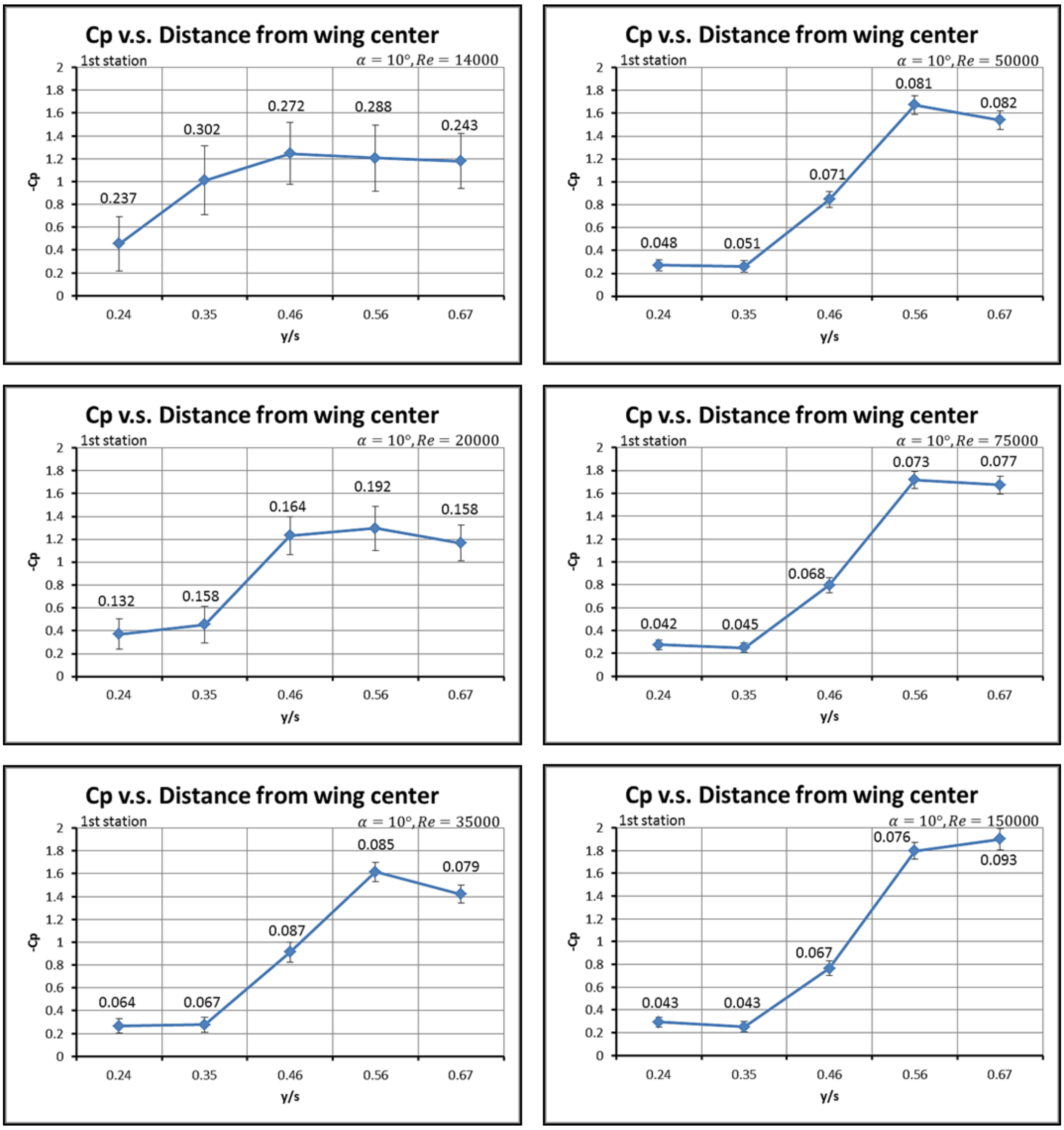

Figure 4.35 RMS of pressure measurements on a chordwise station located at x/c = 0.32 at 10-degree angle of attack and at different Reynolds numbers

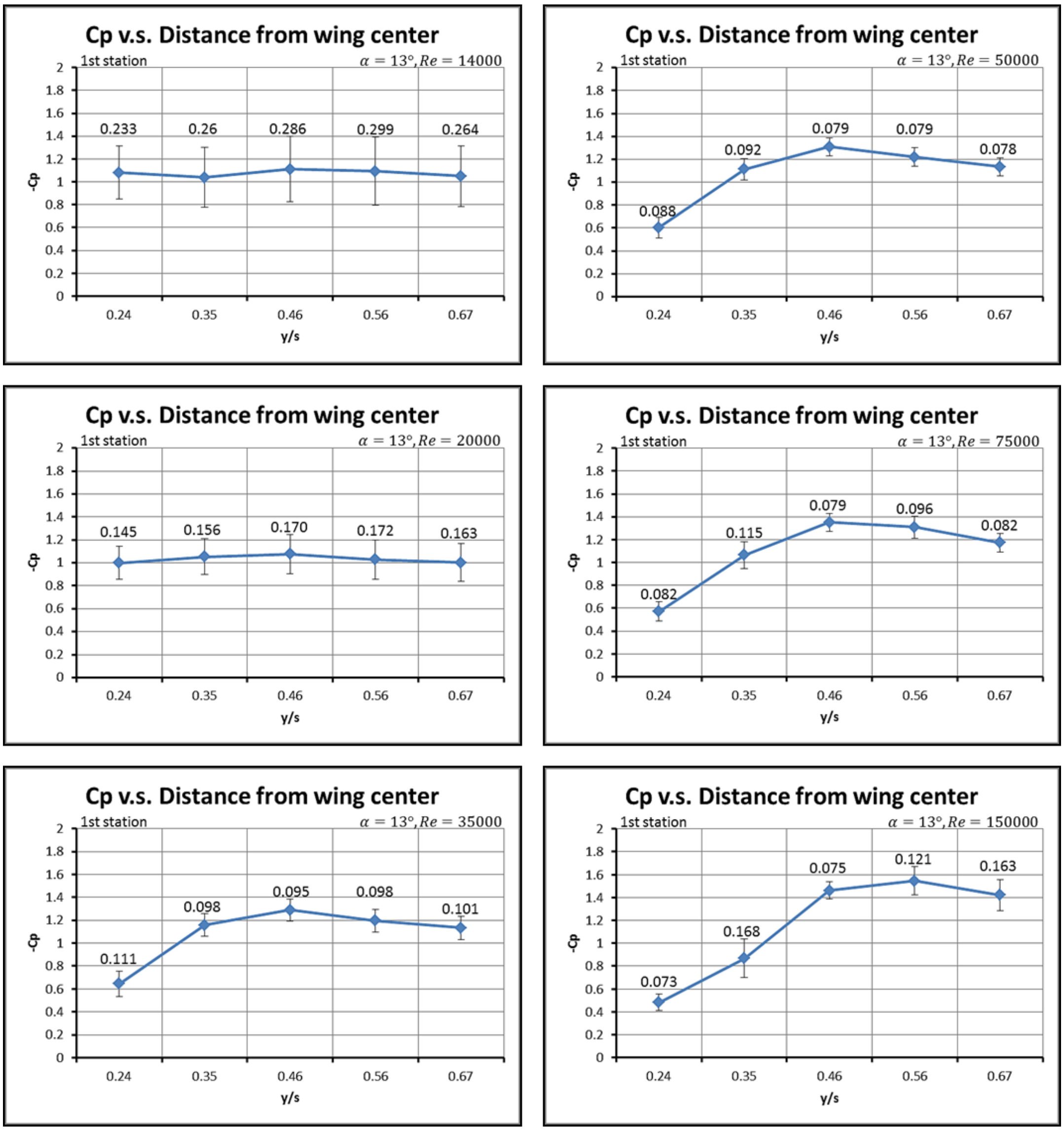

Figure 4.36 RMS of pressure measurements on a chordwise station located at x/c = 0.32 at 13-degree angle of attack and at different Reynolds numbers

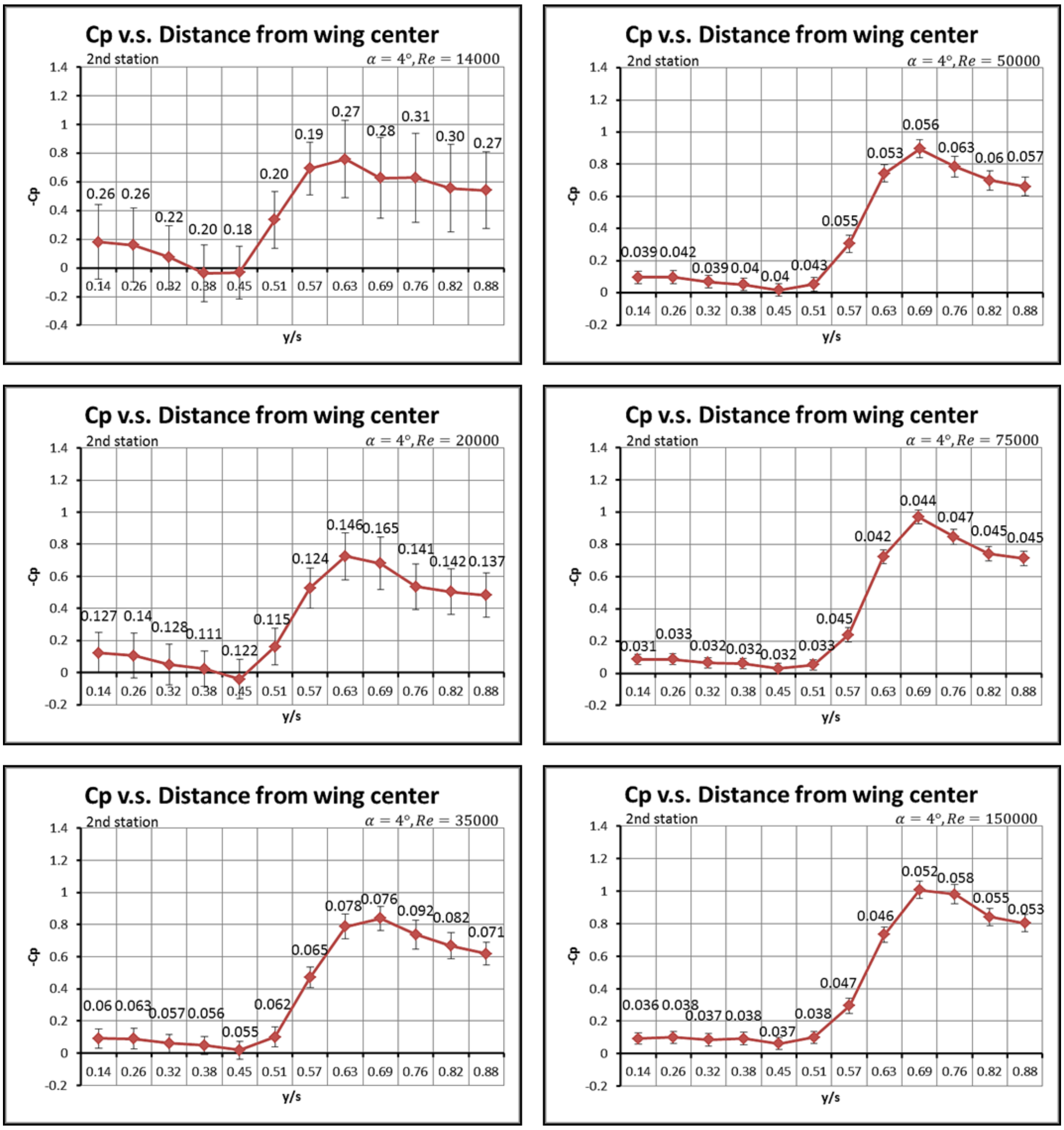

Figure 4.37 RMS of pressure measurements on a chordwise station located at x/c = 0.56 at 4-degree angle of attack and at different Reynolds numbers

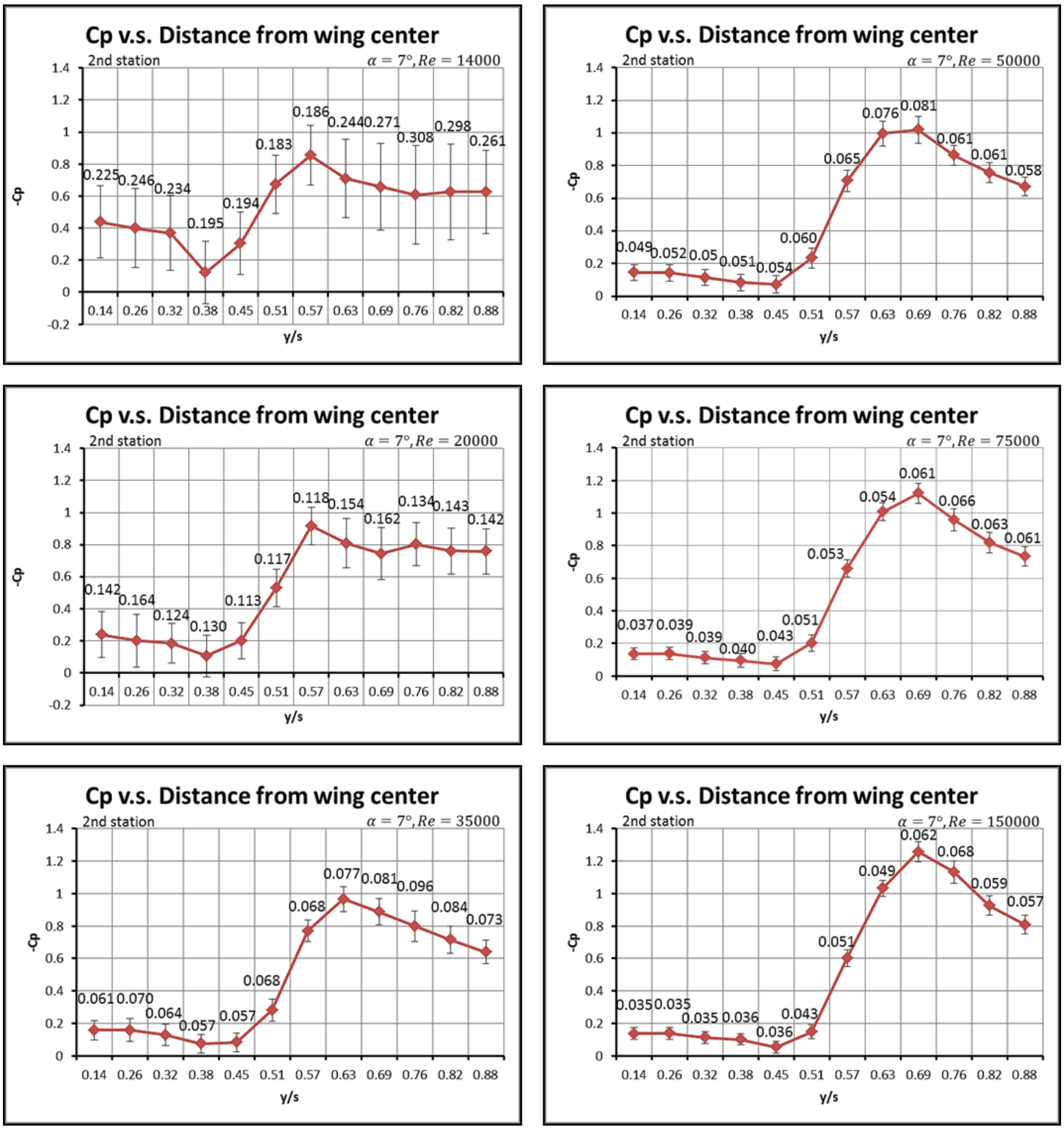

Figure 4.38 RMS of pressure measurements on a chordwise station located at x/c = 0.56 at 7-degree angle of attack and at different Reynolds numbers

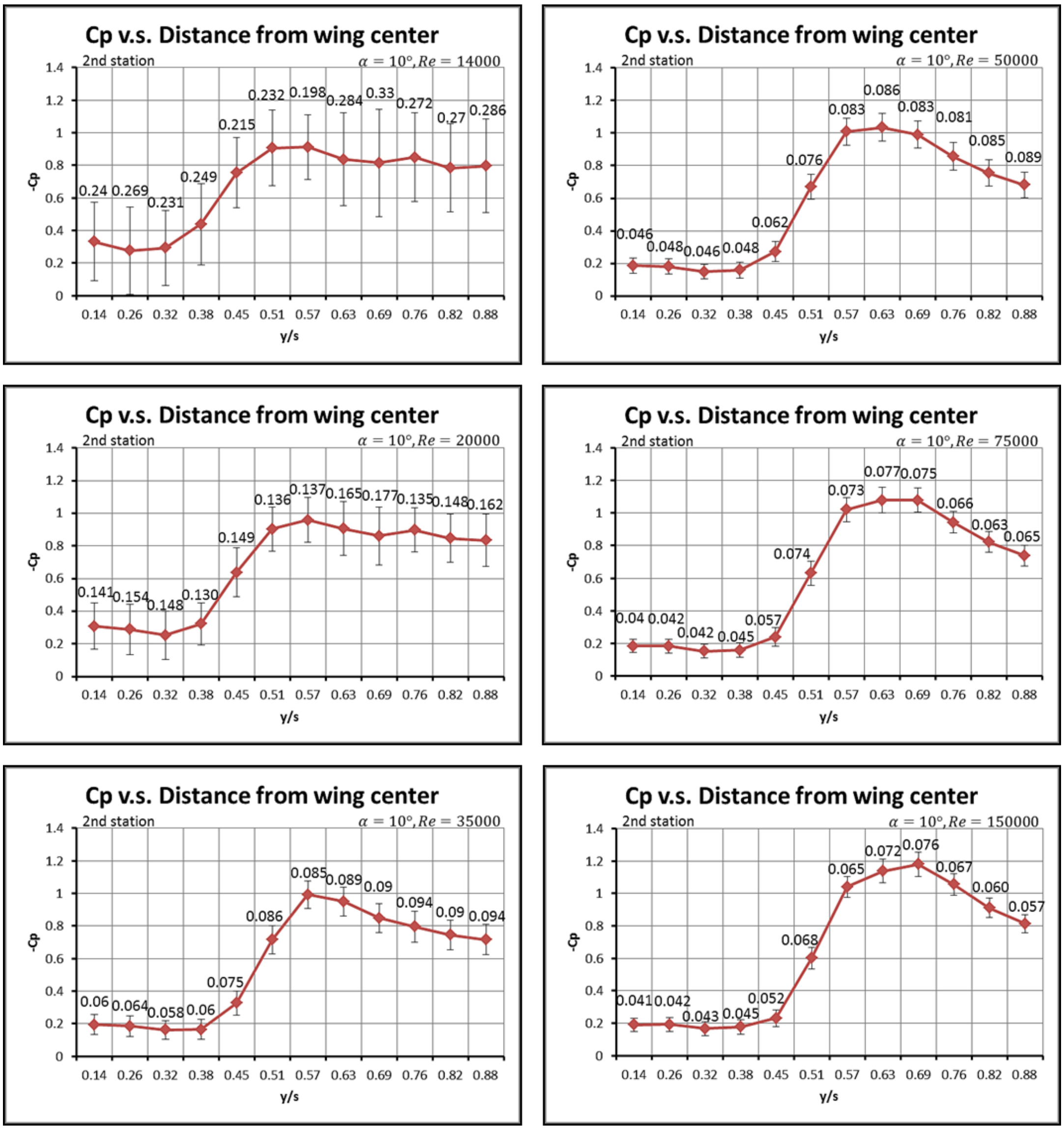

Figure 4.39 RMS of pressure measurements on a chordwise station located at x/c = 0.56 at 10-degree angle of attack and at different Reynolds numbers

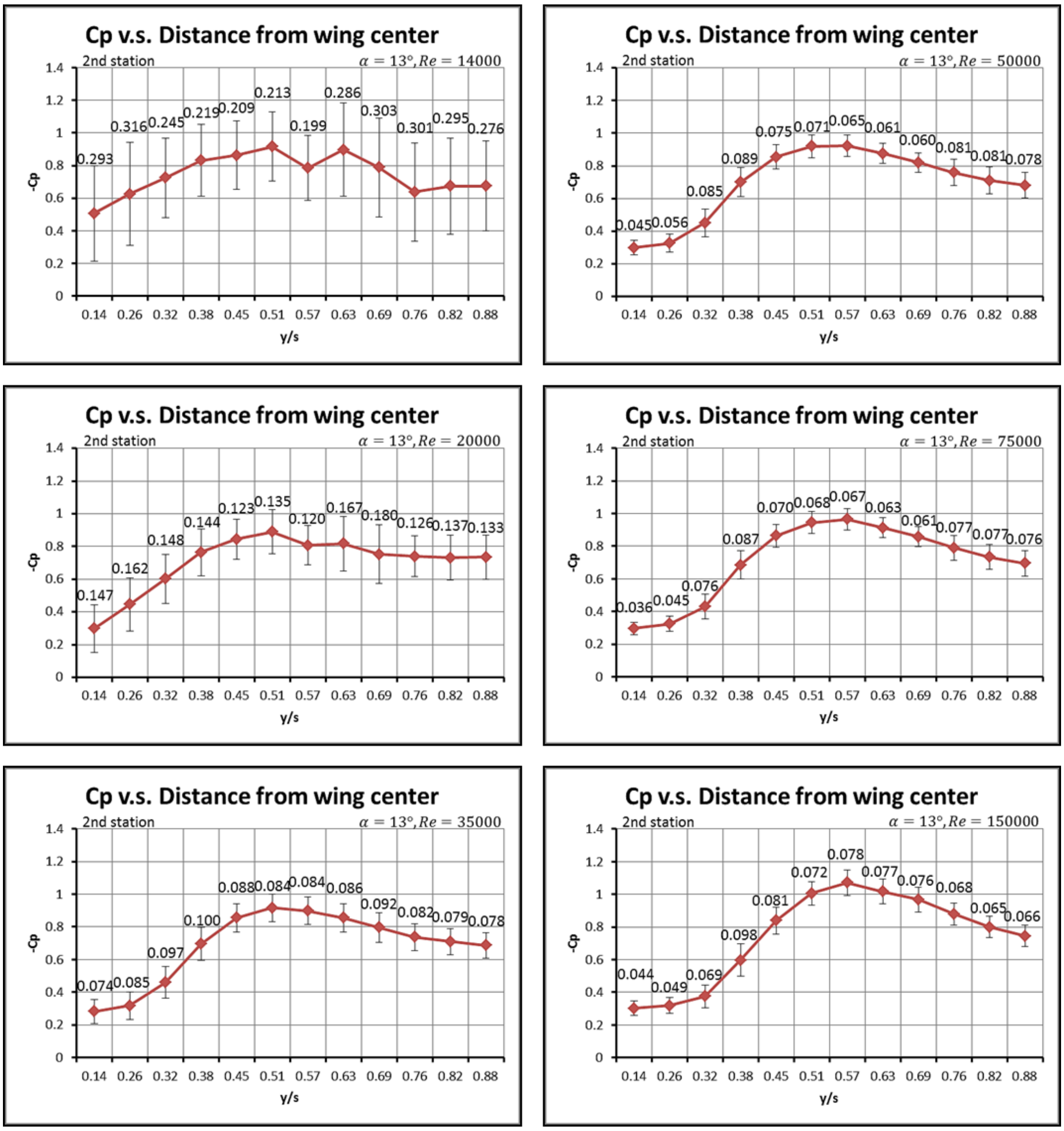

Figure 4.40 RMS of pressure measurements on a chordwise station located at x/c = 0.56 at 13-degree angle of attack and at different Reynolds numbers

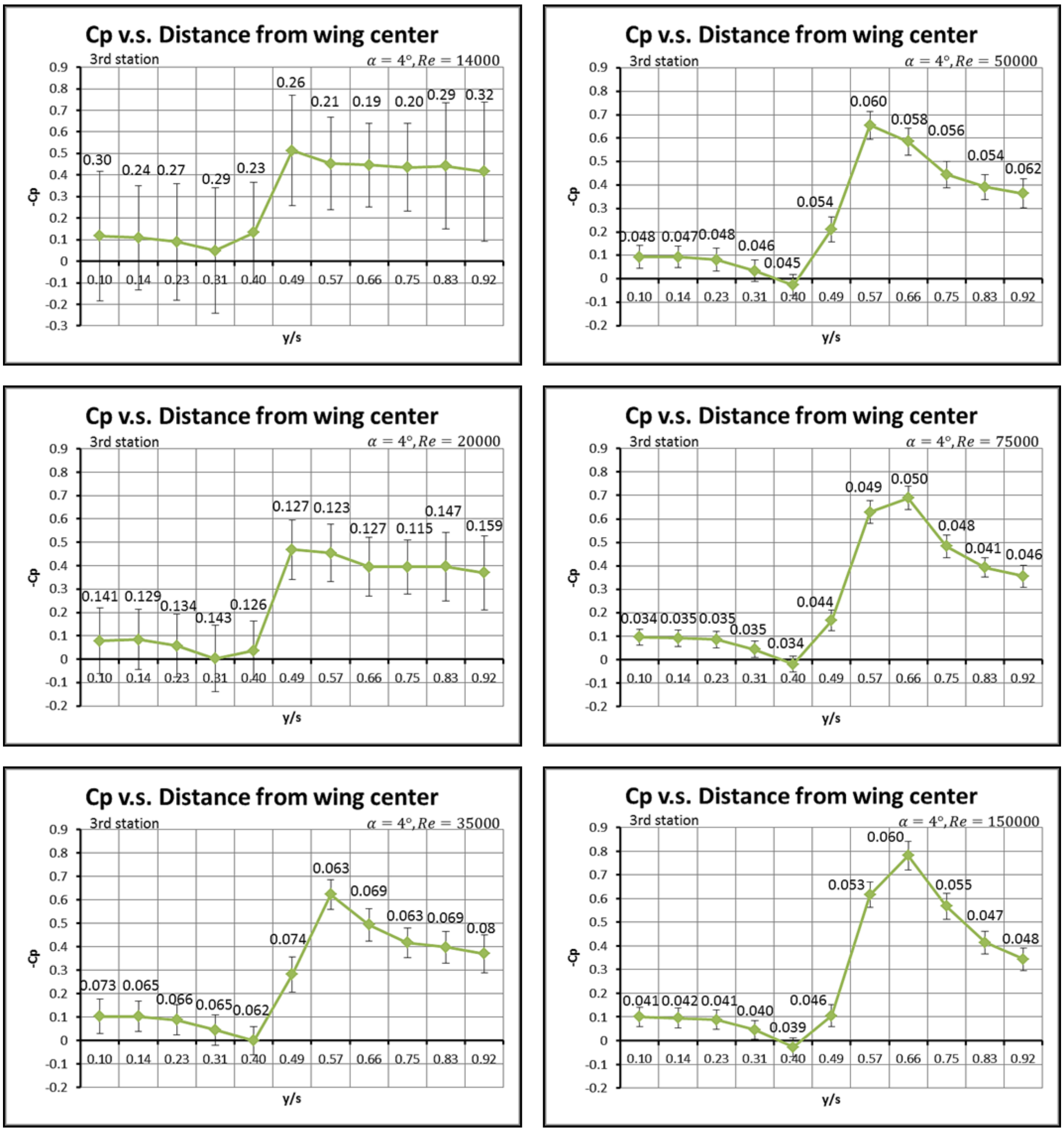

Figure 4.41 RMS of pressure measurements on a chordwise station located at x/c = 0.80 at 4-degree angle of attack and at different Reynolds numbers

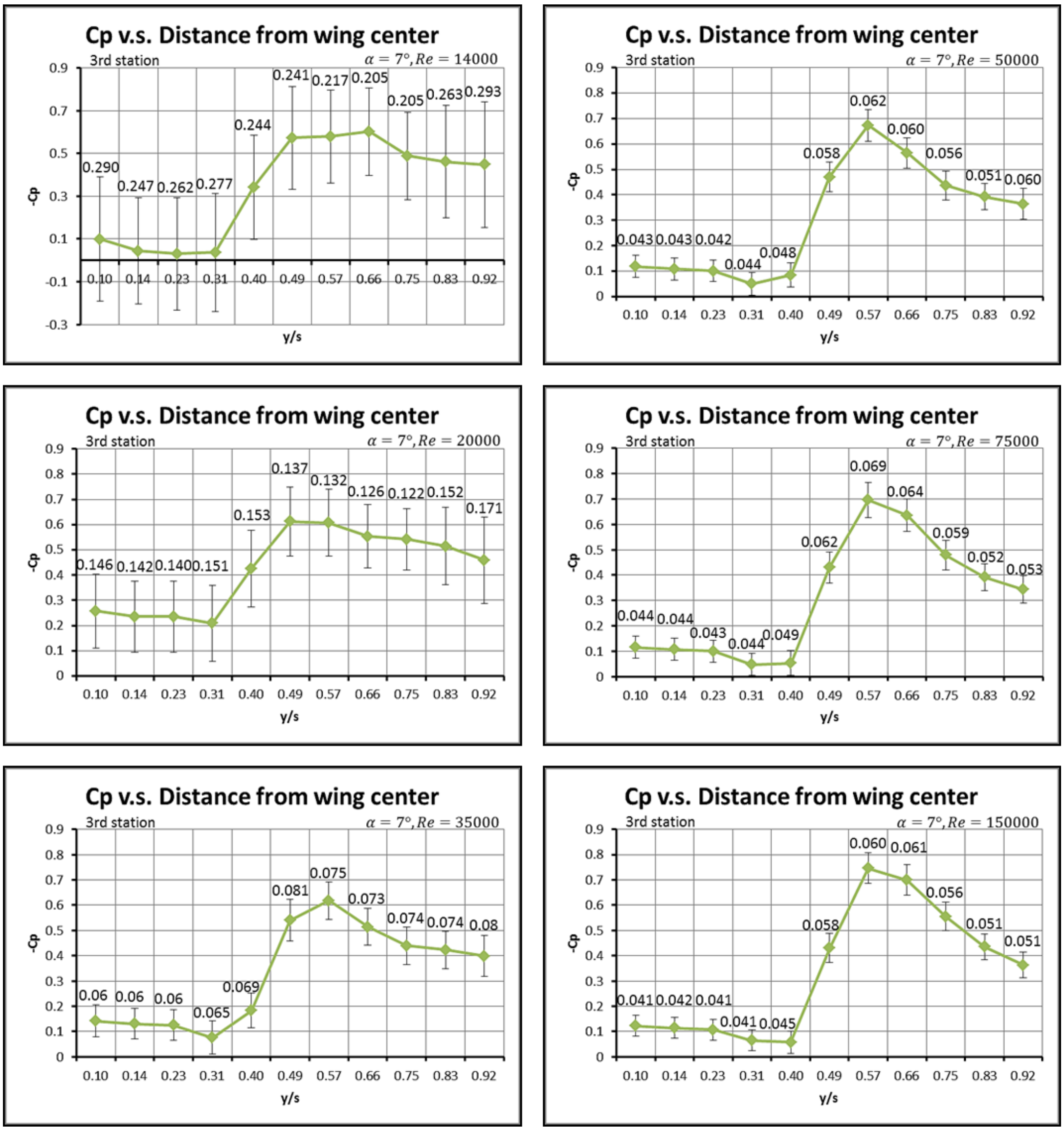

Figure 4.42 RMS of pressure measurements on a chordwise station located at x/c = 0.80 at 7-degree angle of attack and at different Reynolds numbers

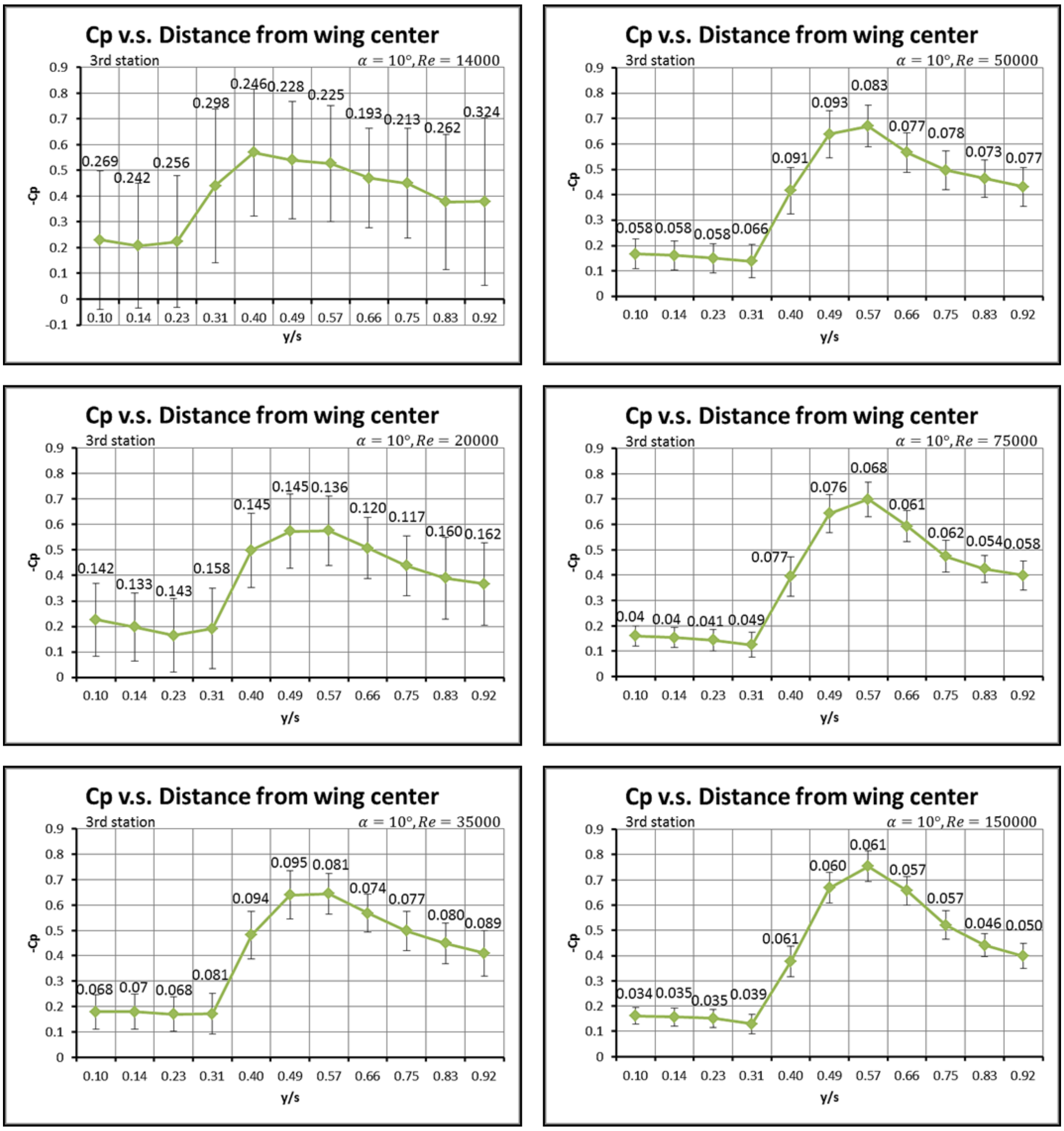

Figure 4.43 RMS of pressure measurements on a chordwise station located at x/c = 0.80 at 10-degree angle of attack and at different Reynolds numbers

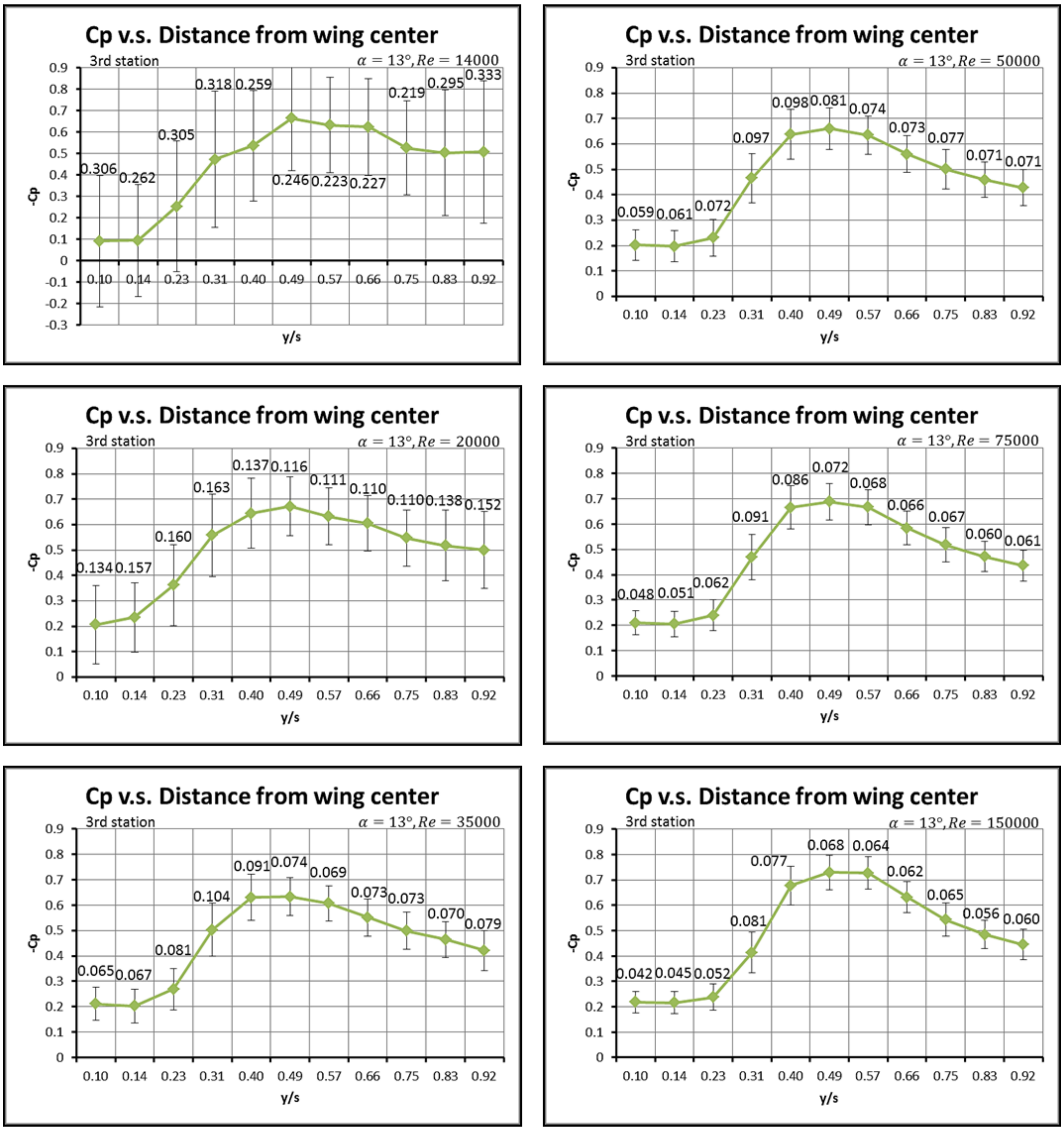

Figure 4.44 RMS of pressure measurements on a chordwise station located at x/c = 0.80 at 13-degree angle of attack and at different Reynolds numbers

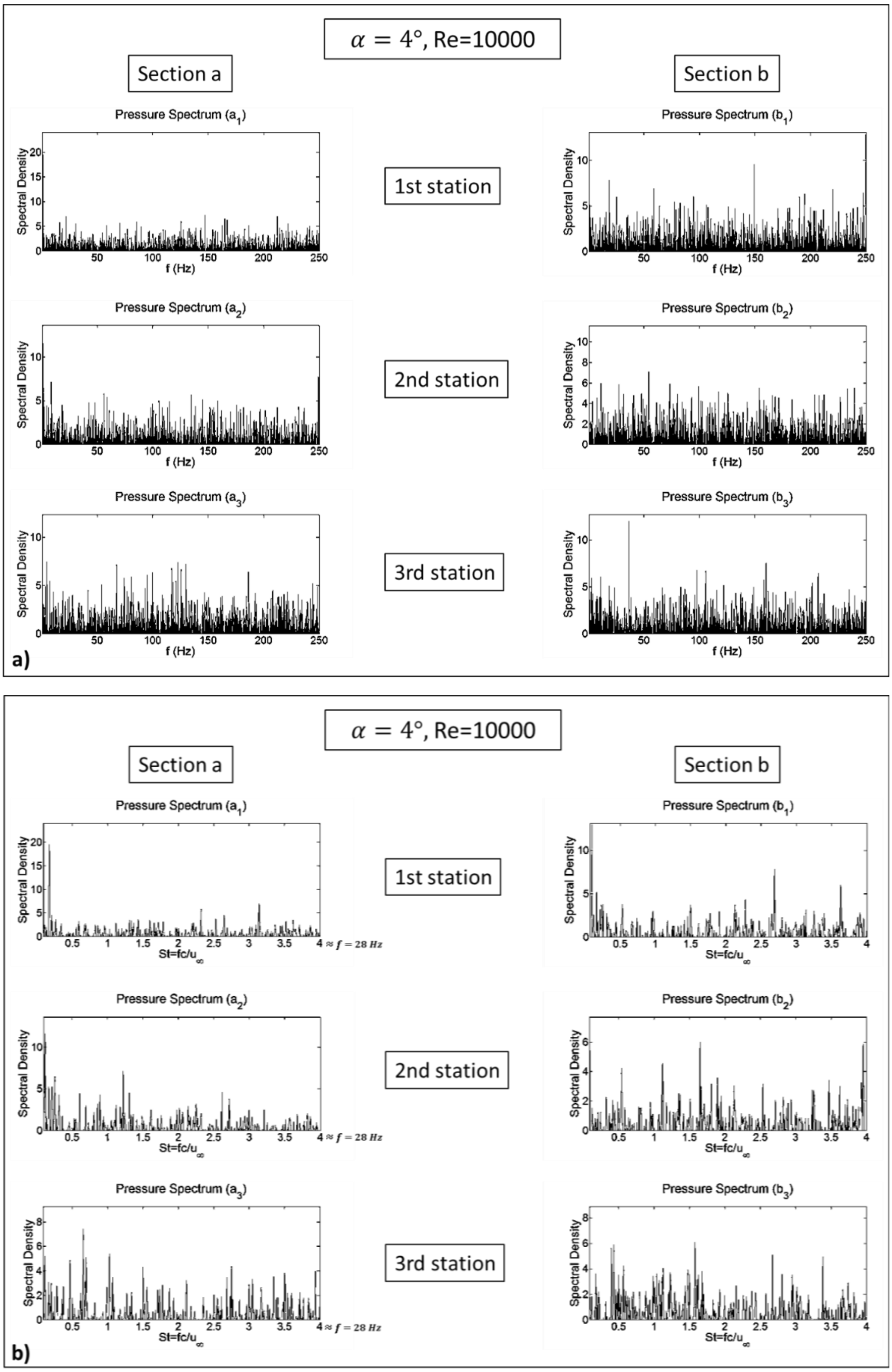

Figure 4.45 Power Spectral Densities of pressure measurements on wing surface for 4-degree angle of attack and *Re = 10.000* at two different taps in each three different chordwise stations corresponding to x/c = 0.32, x/c = 0.56 and x/c = 0.80. a) Spectral Densities as a function of frequency b) Spectral Densities as a function of Strouhal number for up to St = 4

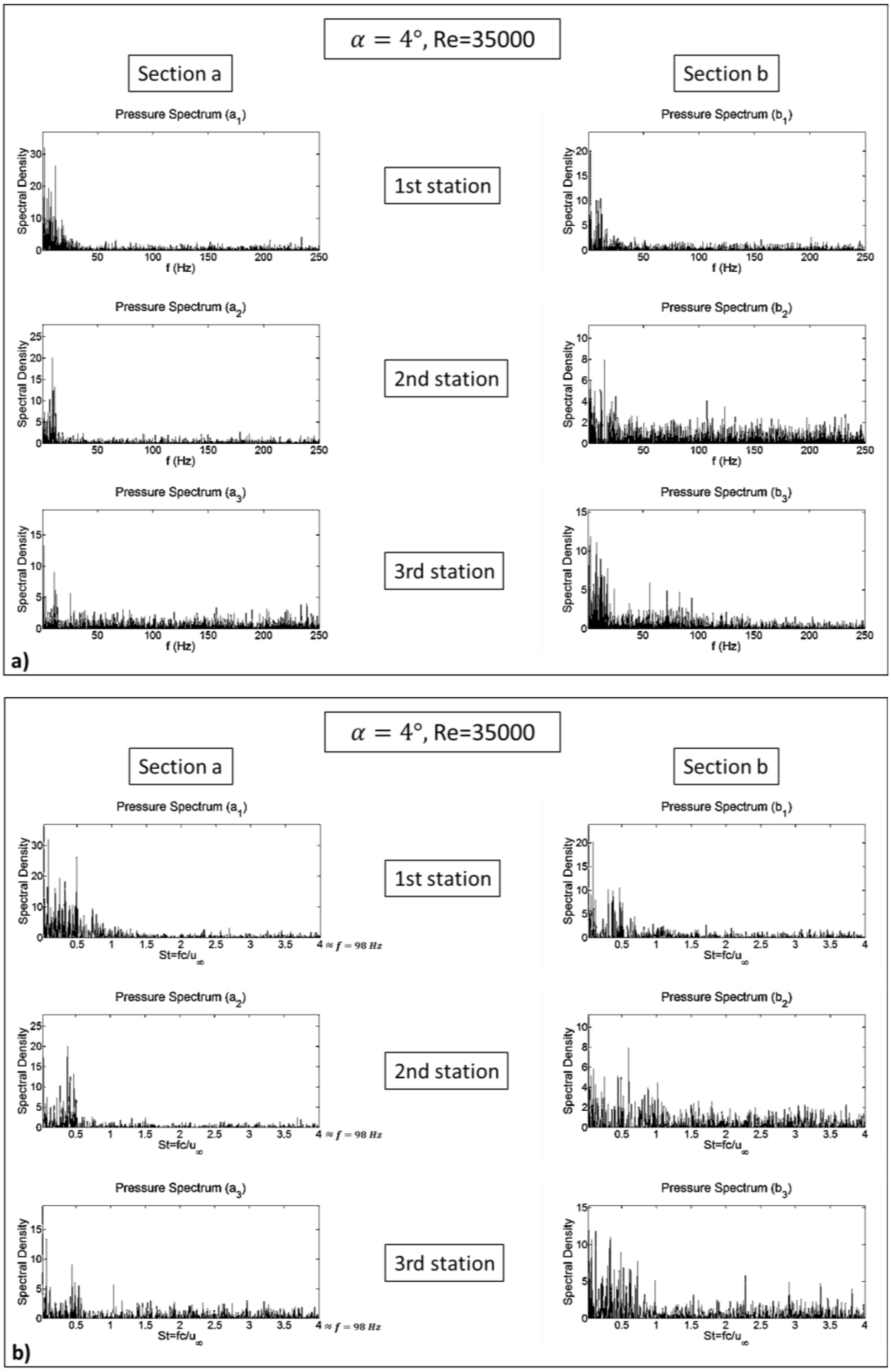

Figure 4.46 Power Spectral Densities of pressure measurements on wing surface for 4-degree angle of attack and *Re = 35.000* at two different taps in each three different chordwise stations corresponding to x/c = 0.32, x/c = 0.56 and x/c = 0.80. a) Spectral Densities as a function of frequency b) Spectral Densities as a function of Strouhal number for up to St = 4

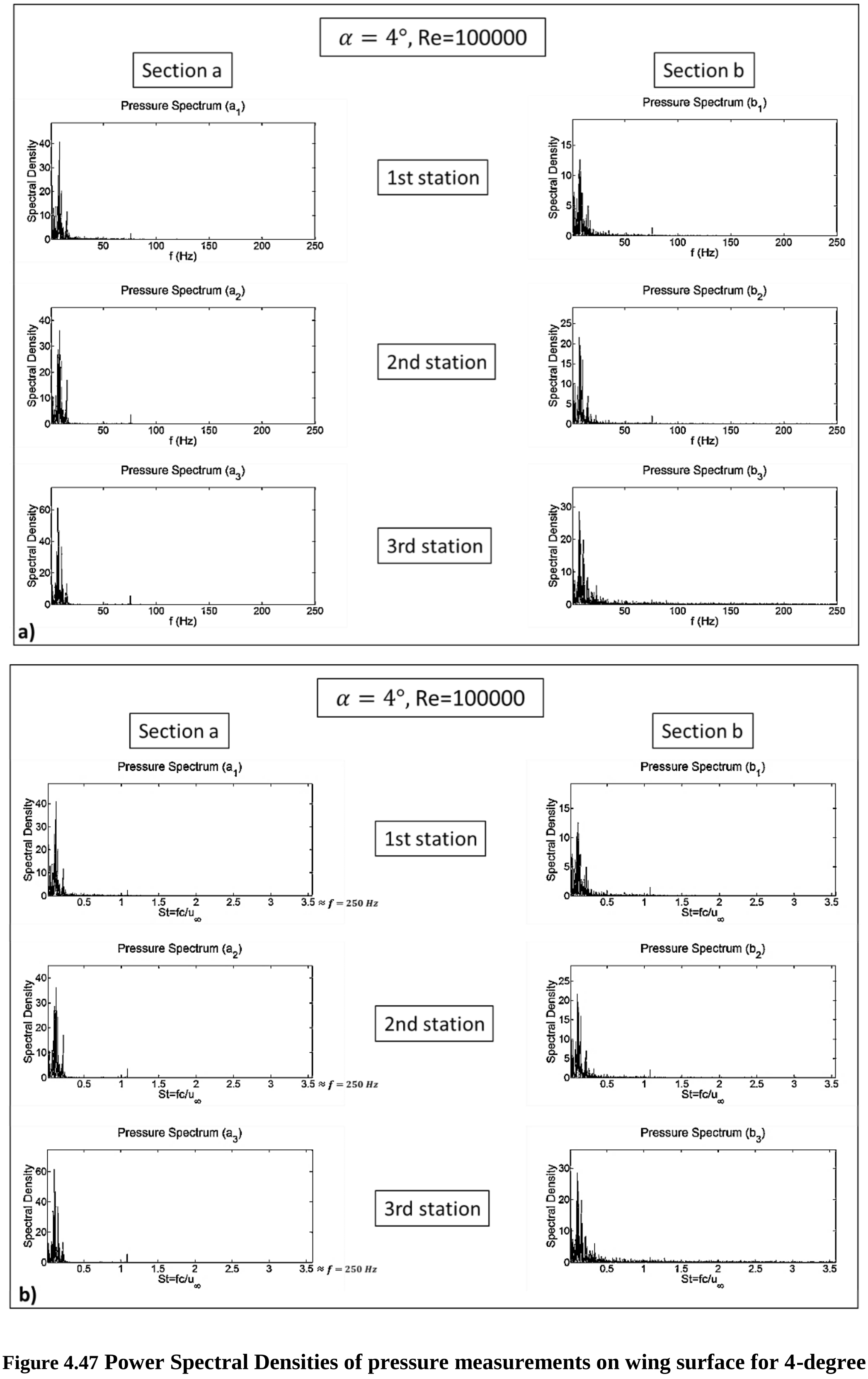

Figure 4.47 Power Spectral Densities of pressure measurements on wing surface for 4-degree angle of attack and *Re = 100.000* at two different taps in each three different chordwise stations corresponding to x/c = 0.32, x/c = 0.56 and x/c = 0.80. a) Spectral Densities as a function of frequency b) Spectral Densities as a function of Strouhal number for up to St = 3.56

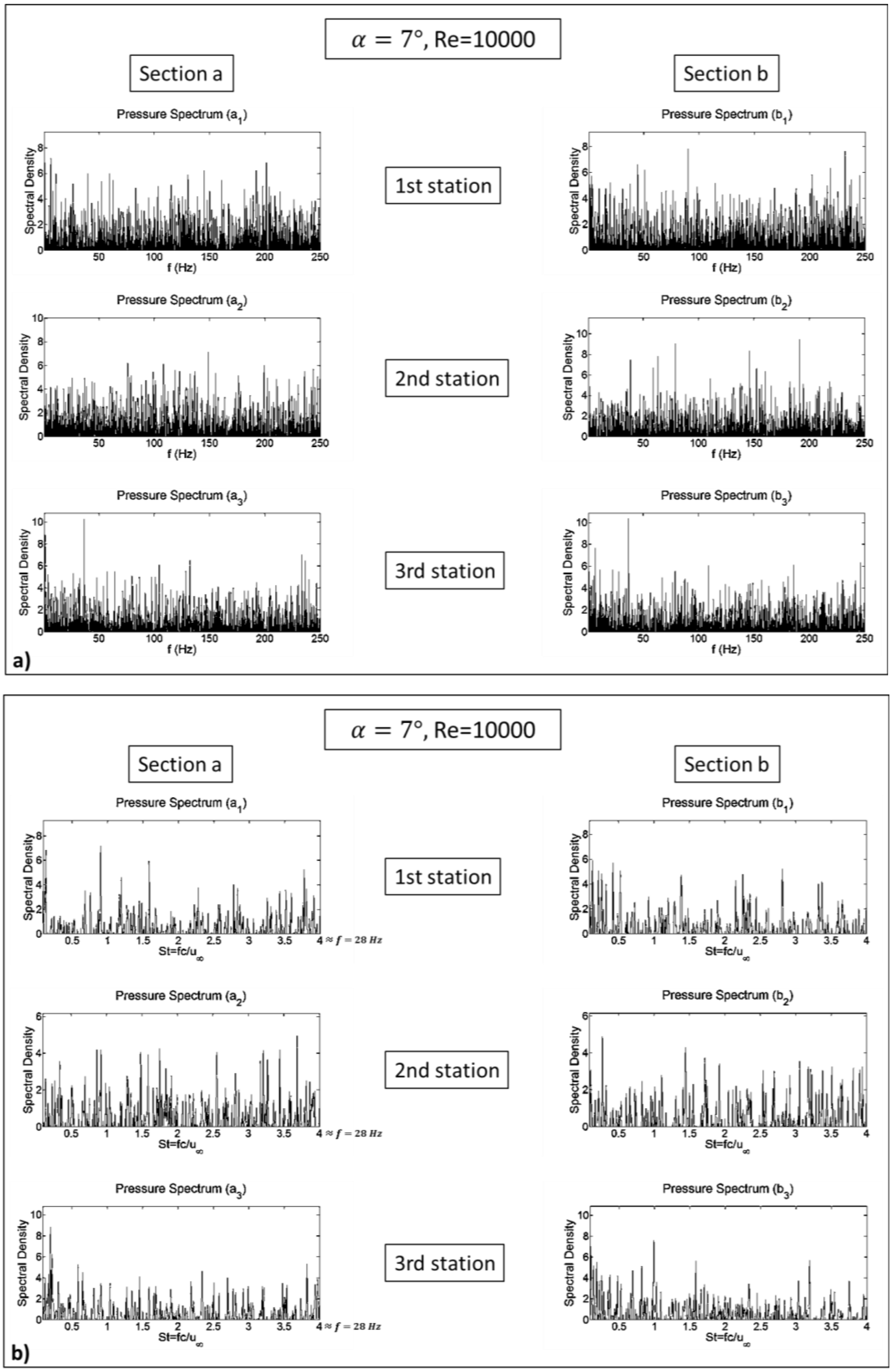

Figure 4.48 **Power Spectral Densities of pressure measurements on wing surface for 7-degree angle of attack and *Re = 10.000* at two different taps in each three different chordwise stations corresponding to x/c = 0.32, x/c = 0.56 and x/c = 0.80. a) Spectral Densities as a function of frequency b) Spectral Densities as a function of Strouhal number for up to St = 4**

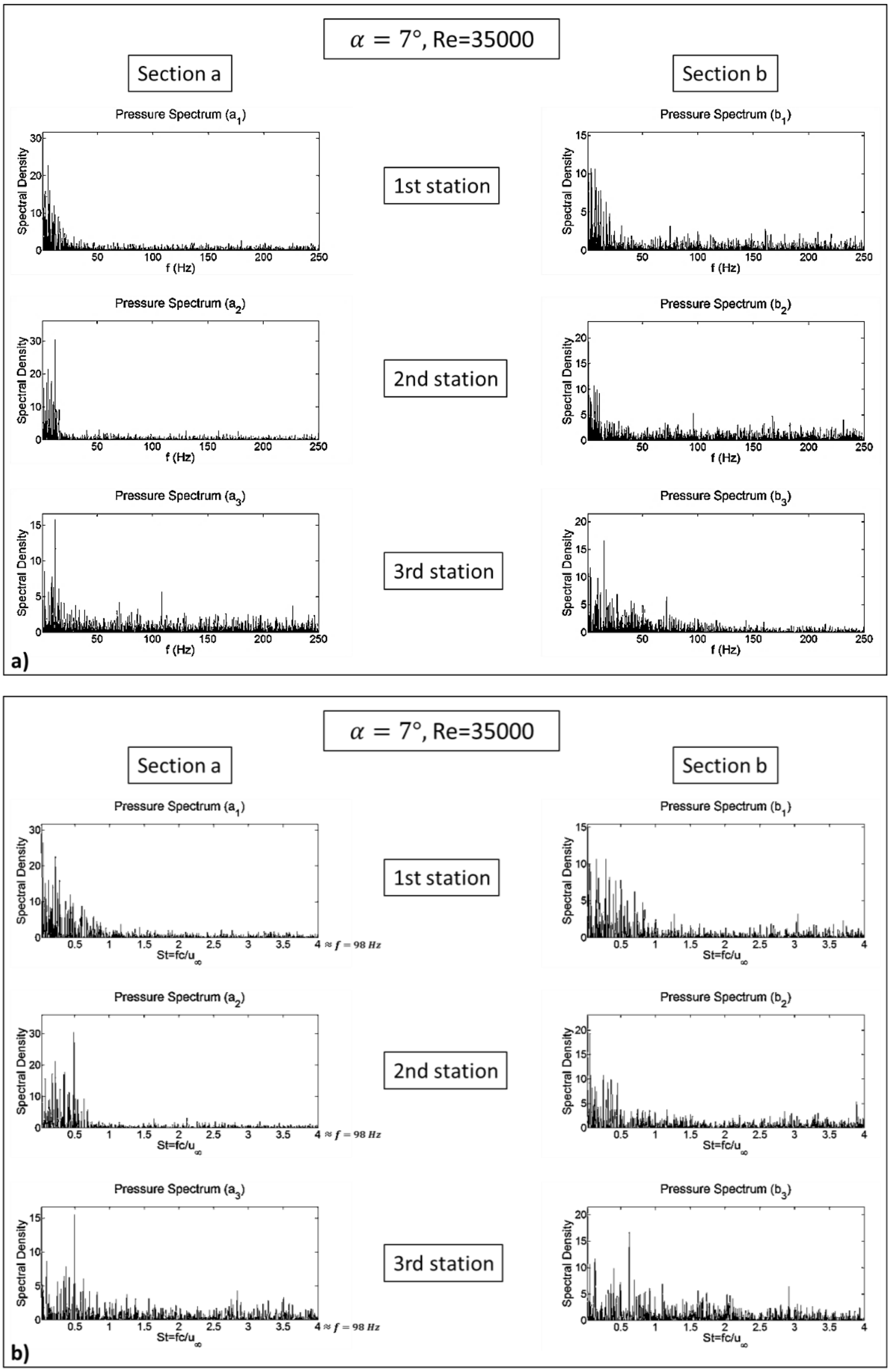

Figure 4.49 Power Spectral Densities of pressure measurements on wing surface for 7-degree angle of attack and *Re = 35.000* at two different taps in each three different chordwise stations corresponding to x/c = 0.32, x/c = 0.56 and x/c = 0.80. a) Spectral Densities as a function of frequency b) Spectral Densities as a function of Strouhal number for up to St = 4

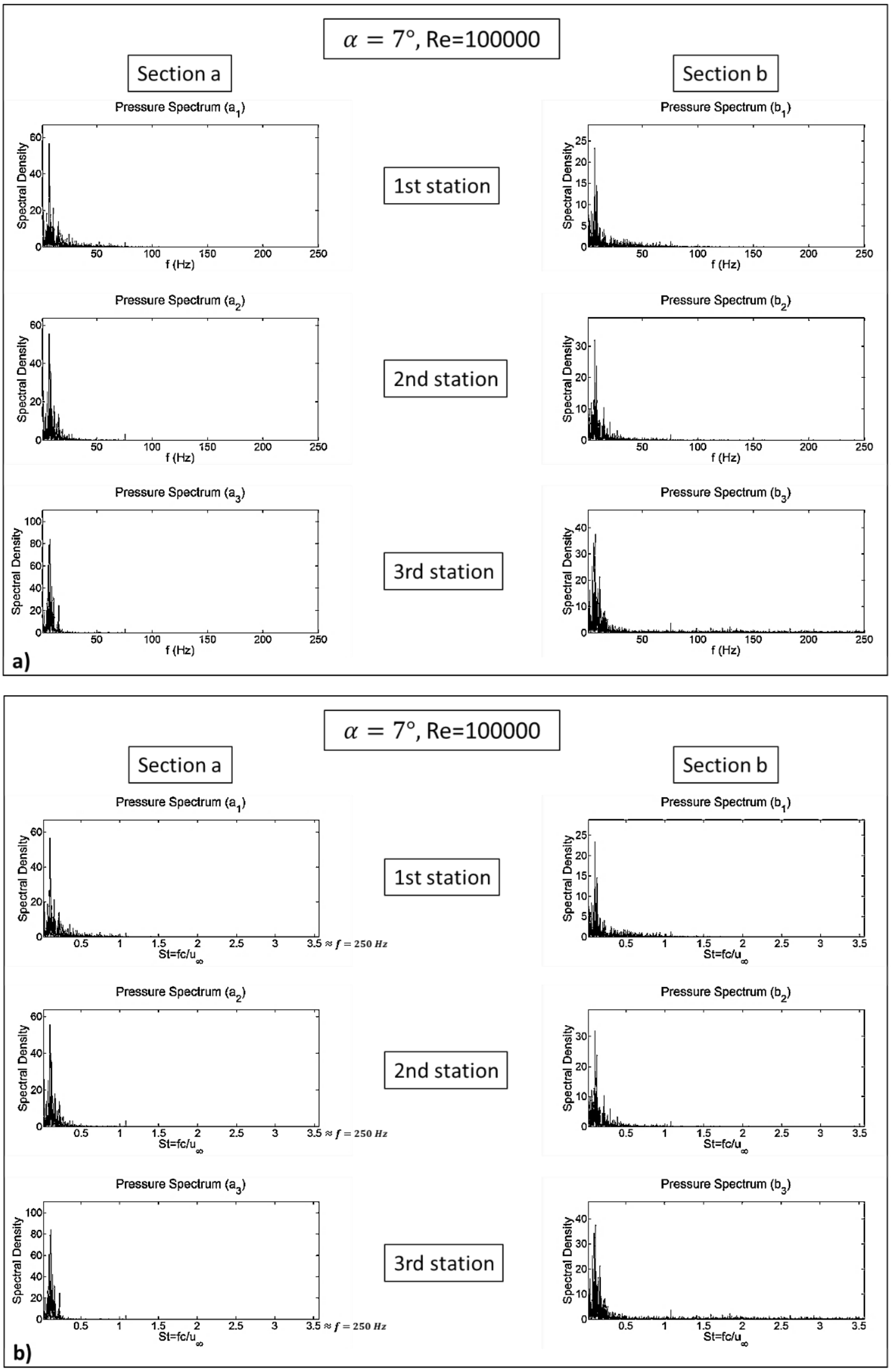

Figure 4.50 Power Spectral Densities of pressure measurements on wing surface for 7-degree angle of attack and *Re = 100.000* at two different taps in each three different chordwise stations corresponding to x/c = 0.32, x/c = 0.56 and x/c = 0.80. a) Spectral Densities as a function of frequency b) Spectral Densities as a function of Strouhal number for up to St = 3.56

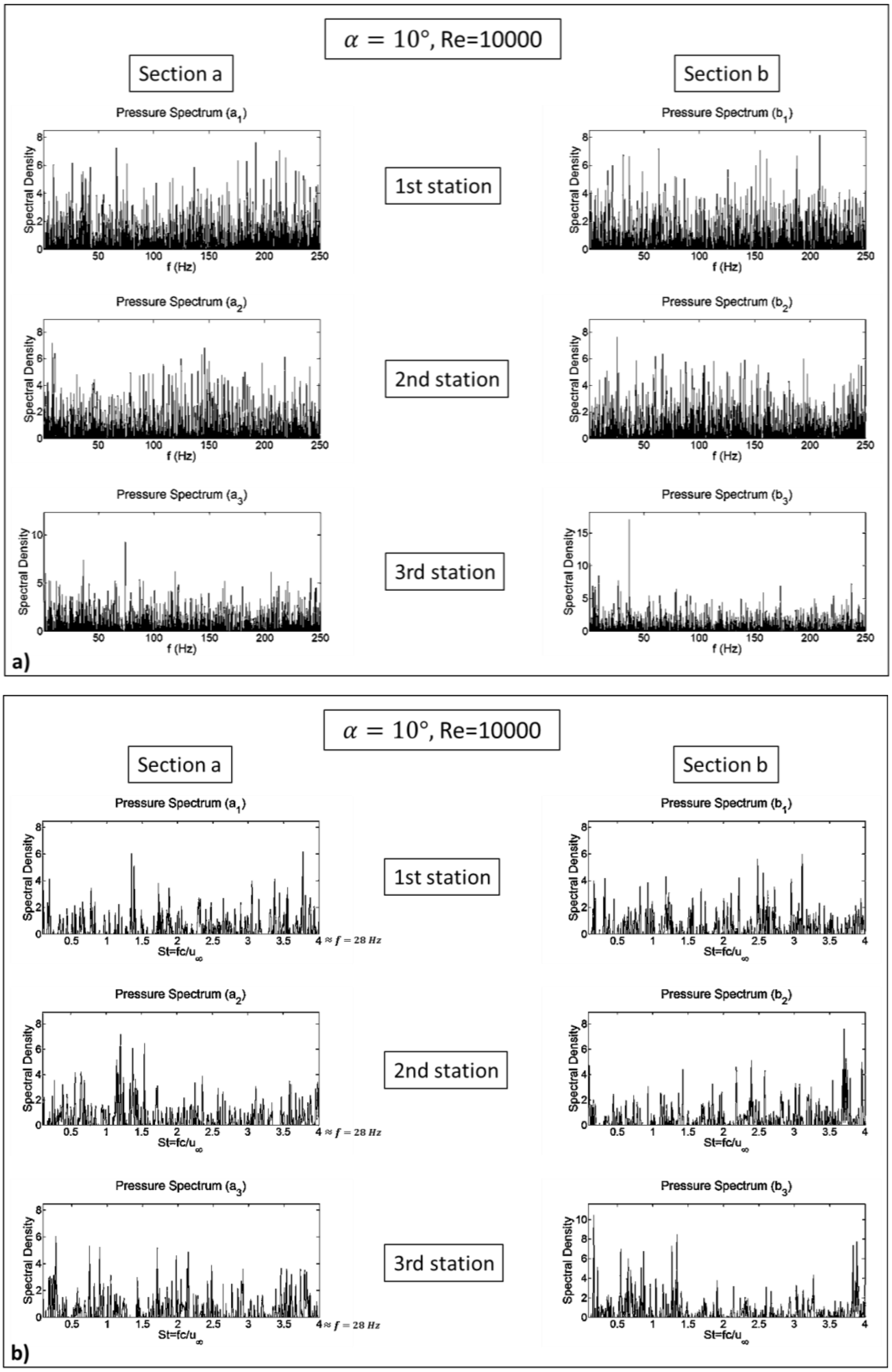

Figure 4.51 Power Spectral Densities of pressure measurements on wing surface for 10-degree angle of attack and *Re = 10.000* at two different taps in each three different chordwise stations corresponding to x/c = 0.32, x/c = 0.56 and x/c = 0.80. a) Spectral Densities as a function of frequency b) Spectral Densities as a function of Strouhal number for up to St = 4

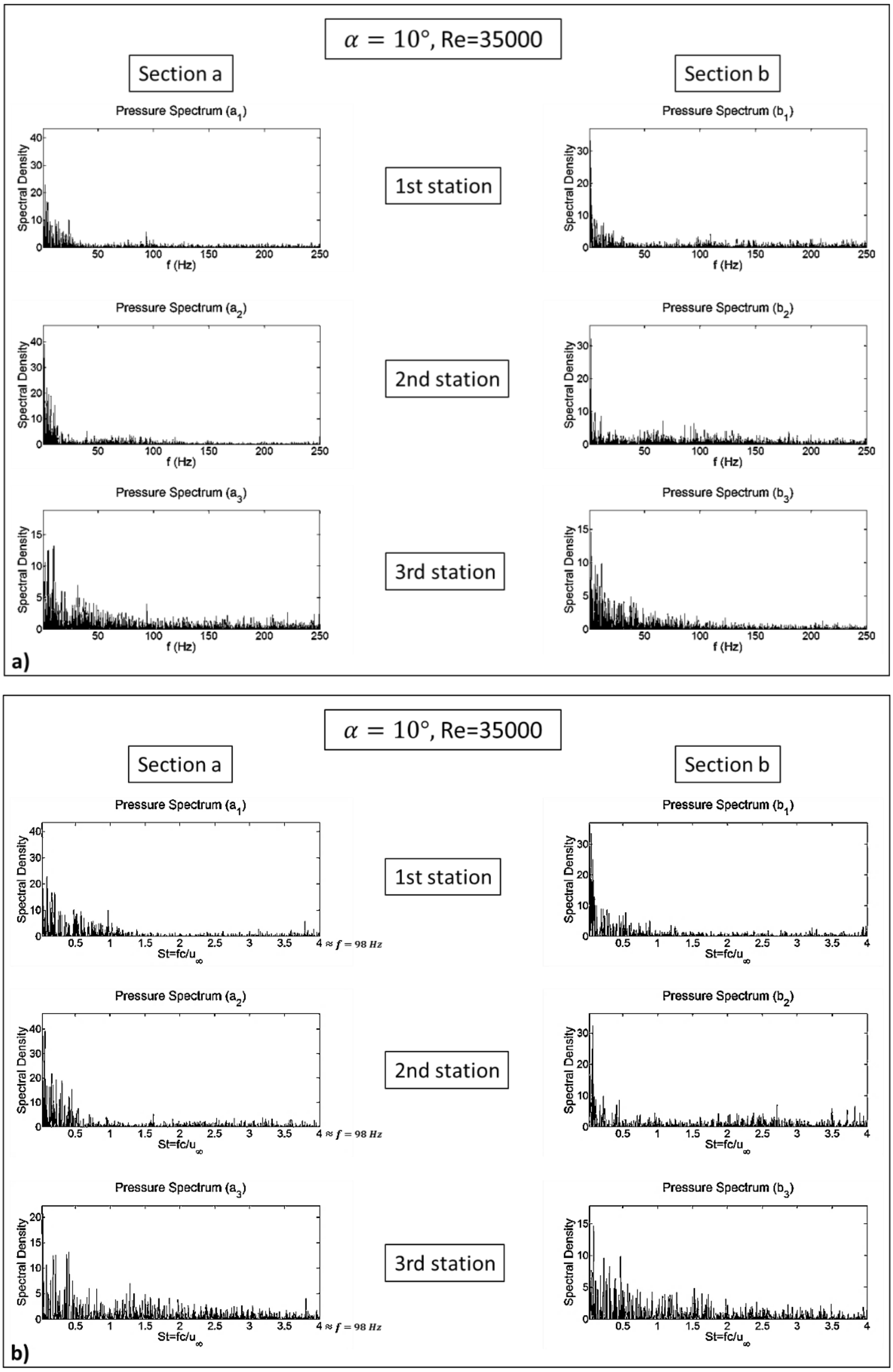

Figure 4.52 **Power Spectral Densities of pressure measurements on wing surface for 10-degree angle of attack and *Re = 35.000* at two different taps in each three different chordwise stations corresponding to x/c = 0.32, x/c = 0.56 and x/c = 0.80. a) Spectral Densities as a function of frequency b) Spectral Densities as a function of Strouhal number for up to St = 4**

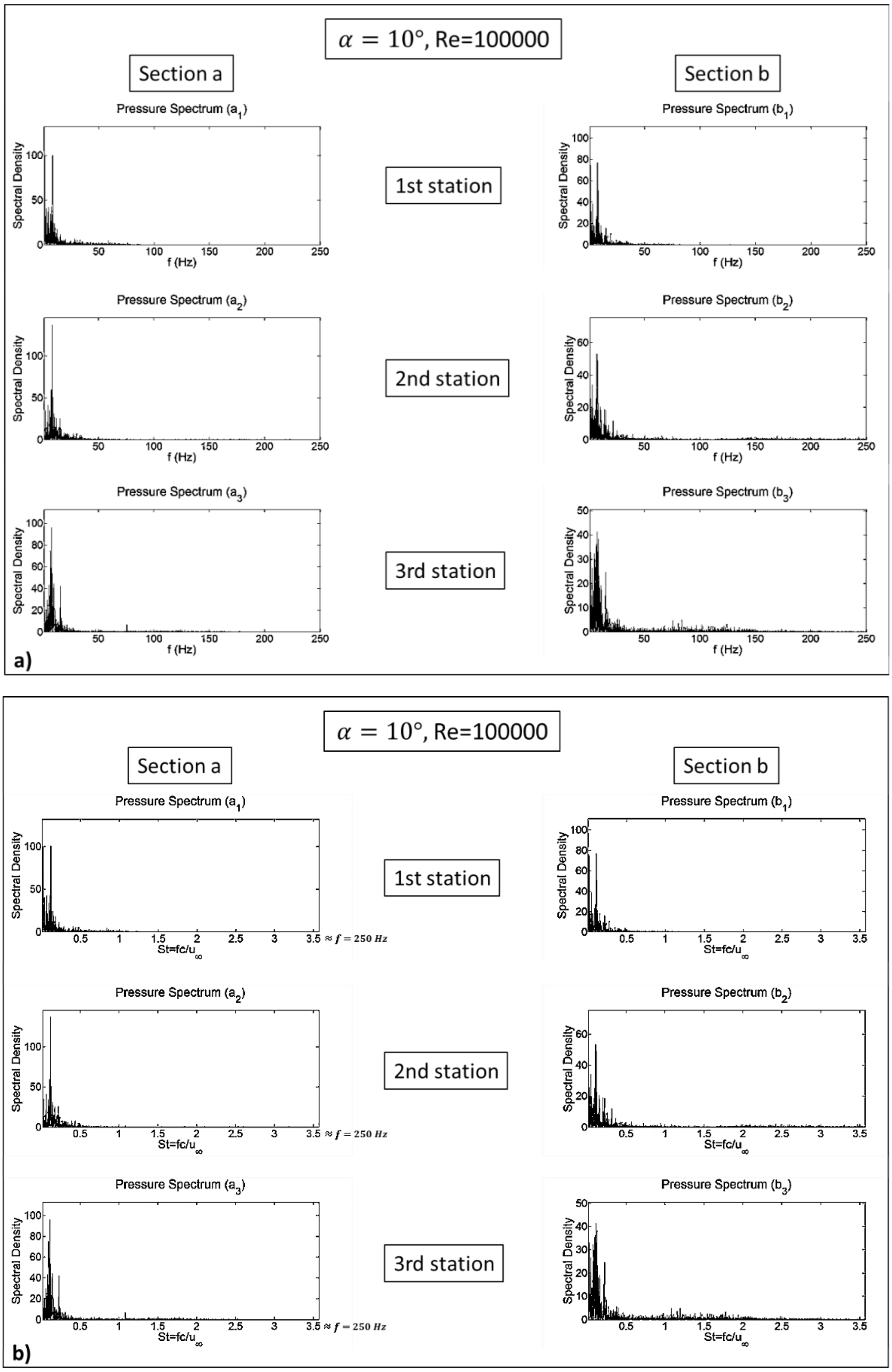

Figure 4.53 Power Spectral Densities of pressure measurements on wing surface for 10-degree angle of attack and *Re = 100.000* at two different taps in each three different chordwise stations corresponding to x/c = 0.32, x/c = 0.56 and x/c = 0.80. a) Spectral Densities as a function of frequency b) Spectral Densities as a function of Strouhal number for up to St = 3.56

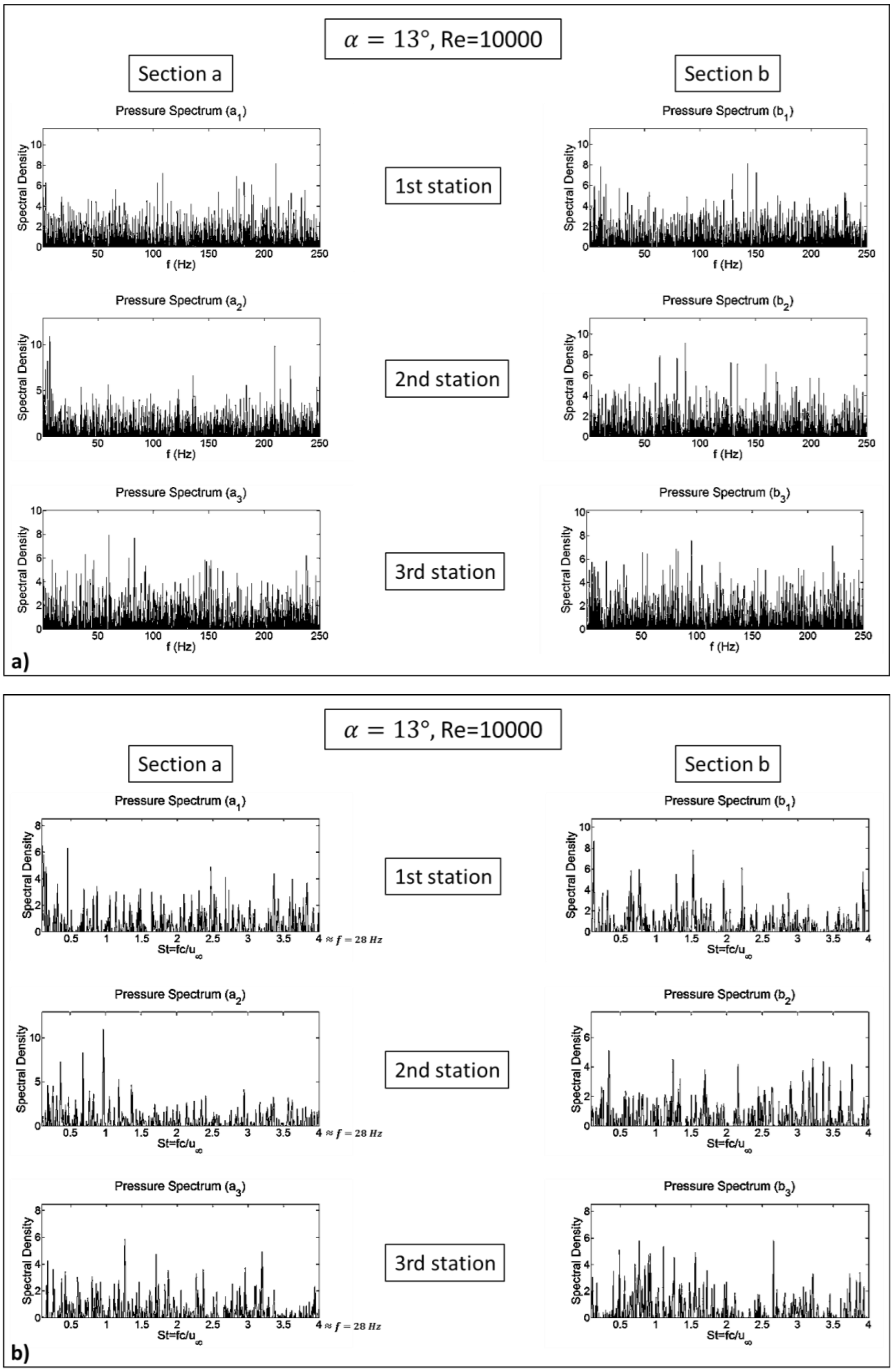

Figure 4.54 Power Spectral Densities of pressure measurements on wing surface for 13-degree angle of attack and ***Re = 10.000*** at two different taps in each three different chordwise stations corresponding to x/c = 0.32, x/c = 0.56 and x/c = 0.80. a) Spectral Densities as a function of frequency b) Spectral Densities as a function of Strouhal number for up to St = 4

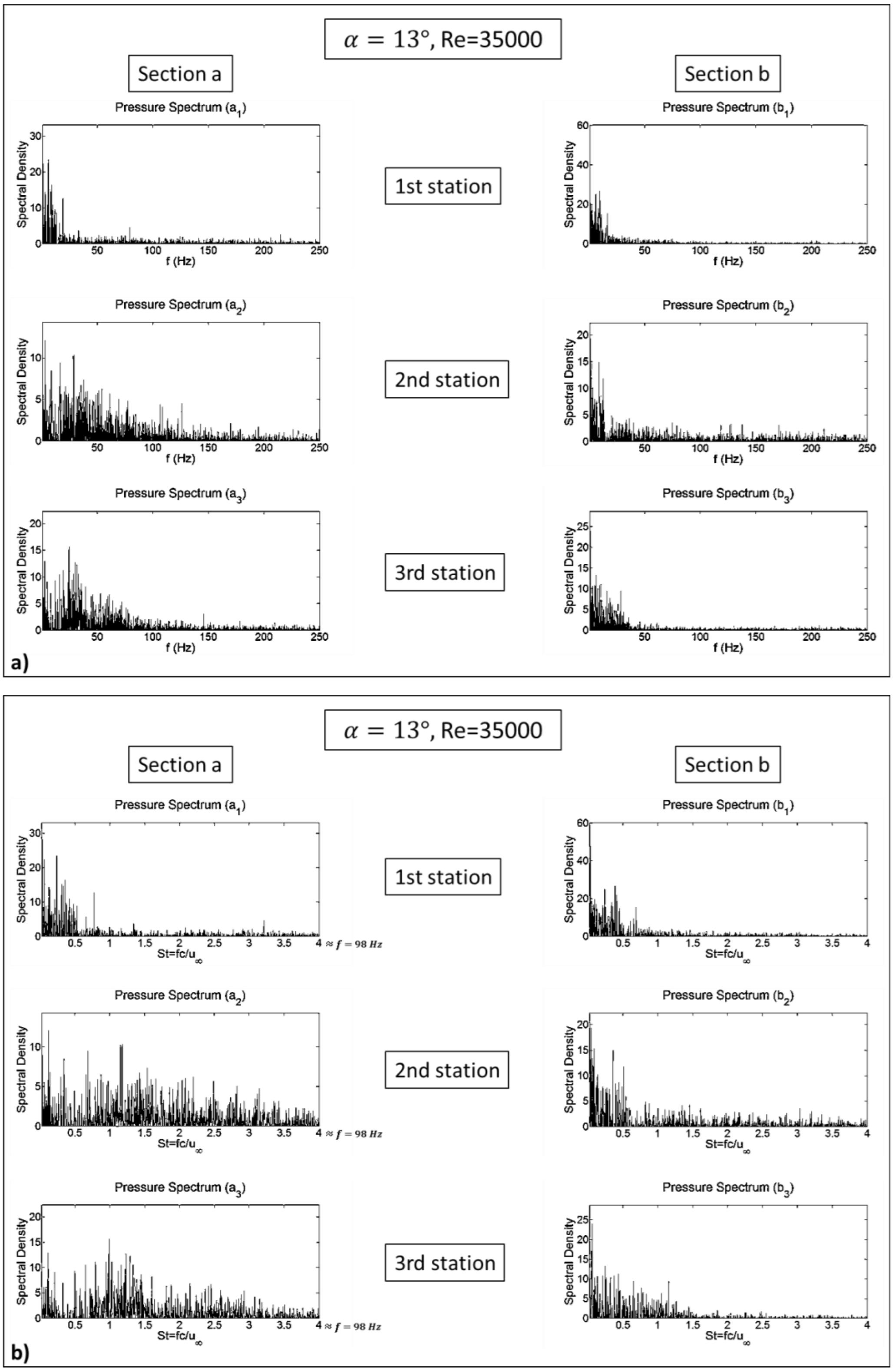

Figure 4.55 Power Spectral Densities of pressure measurements on wing surface for 13-degree angle of attack and *Re = 35.000* at two different taps in each three different chordwise stations corresponding to x/c = 0.32, x/c = 0.56 and x/c = 0.80. a) Spectral Densities as a function of frequency b) Spectral Densities as a function of Strouhal number for up to St = 4

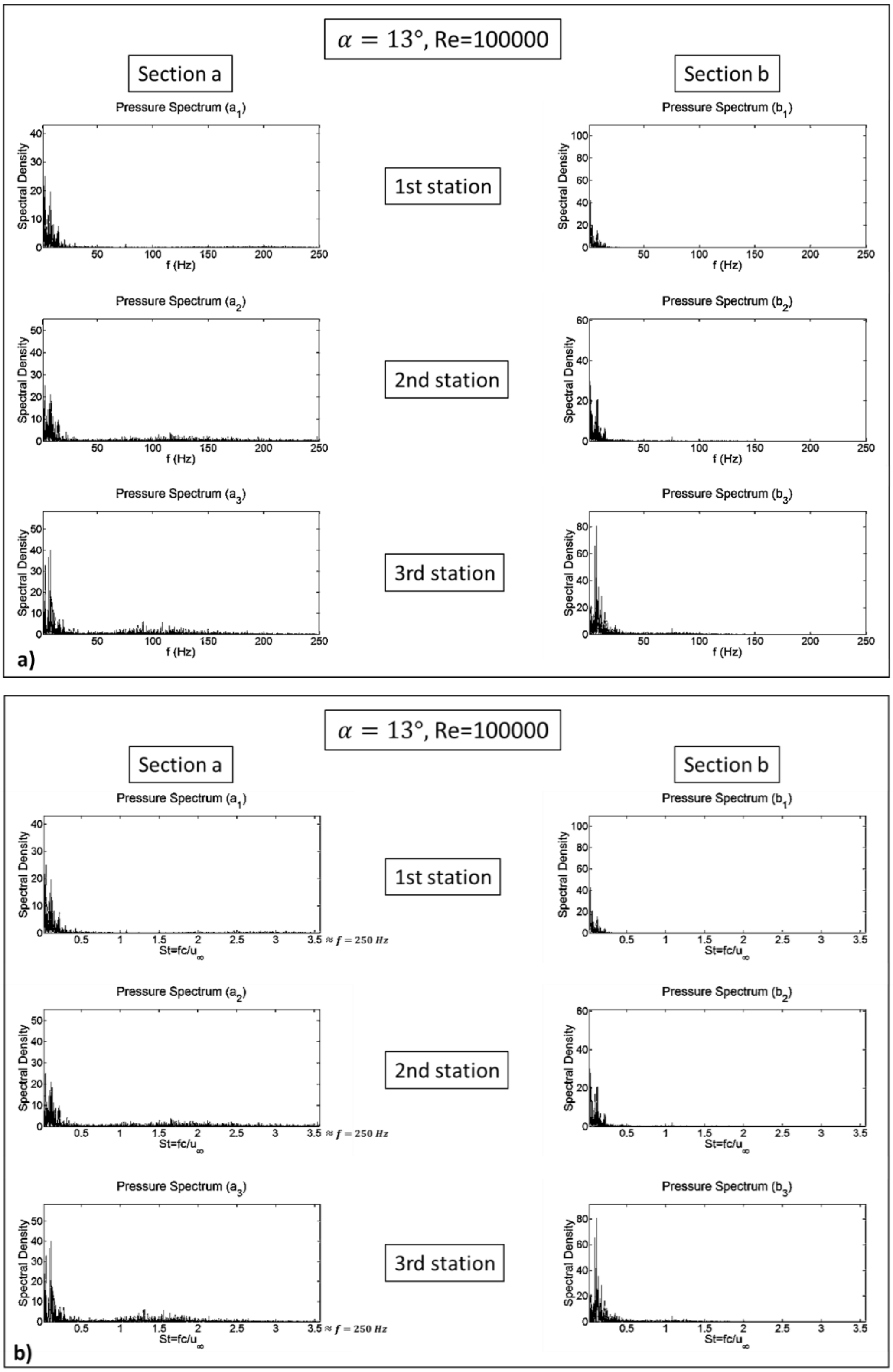

Figure 4.56 Power Spectral Densities of pressure measurements on wing surface for 10-degree angle of attack and *Re = 100.000* at two different taps in each three different chordwise stations corresponding to x/c = 0.32, x/c = 0.56 and x/c = 0.80. a) Spectral Densities as a function of frequency b) Spectral Densities as a function of Strouhal number for up to St = 3.56

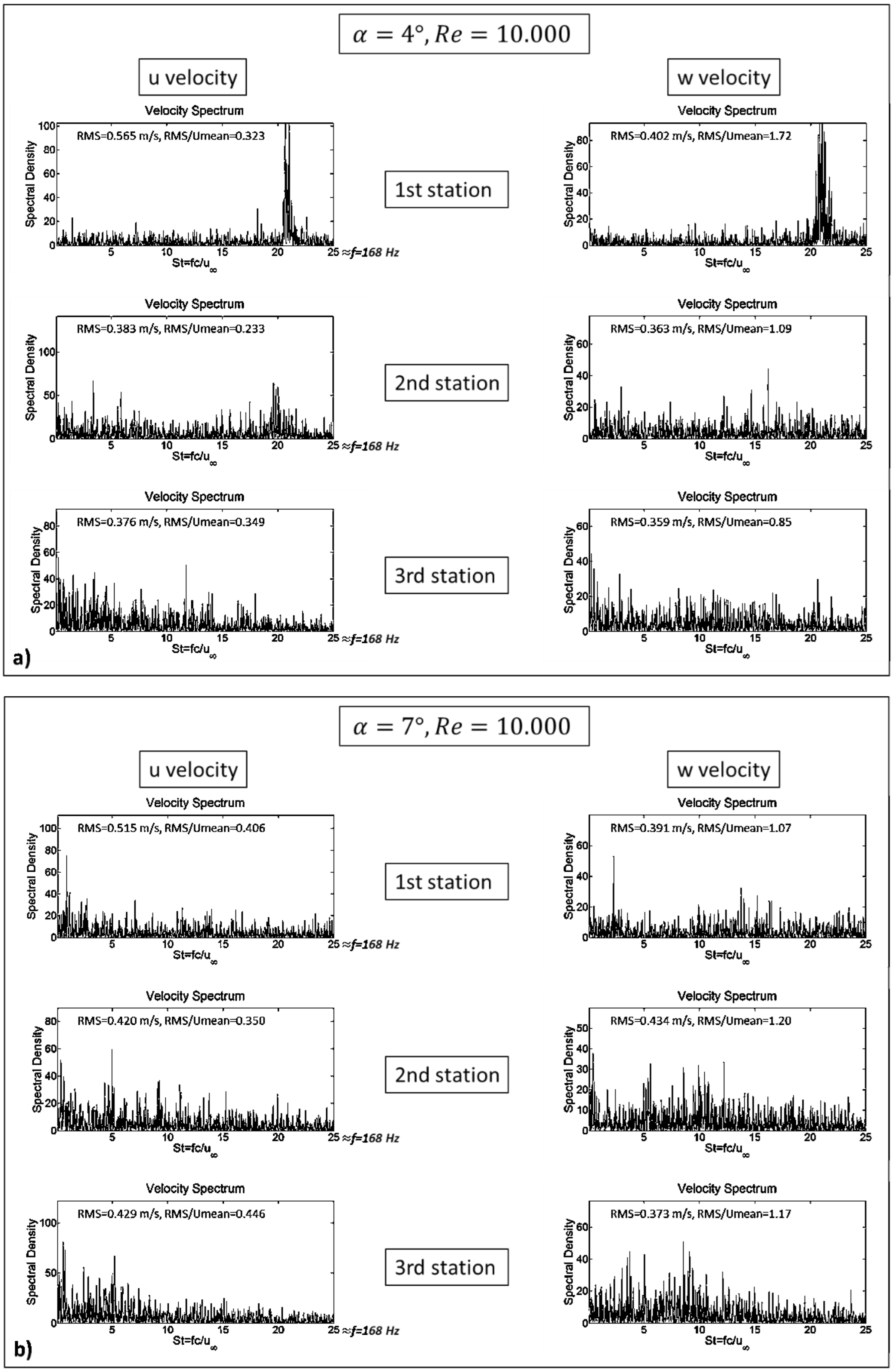

Figure 4.57 Power Spectral Densities of 2-components velocity measurements using LDA at leading edge vortex core at *Re = 10.000* at three different chordwise stations corresponding to x/c = 0.32, x/c = 0.56 and x/c = 0.80. a) Spectral Densities of velocity measurements at $\alpha = 4°$ b) Spectral Densities of velocity measurements at $\alpha = 7°$

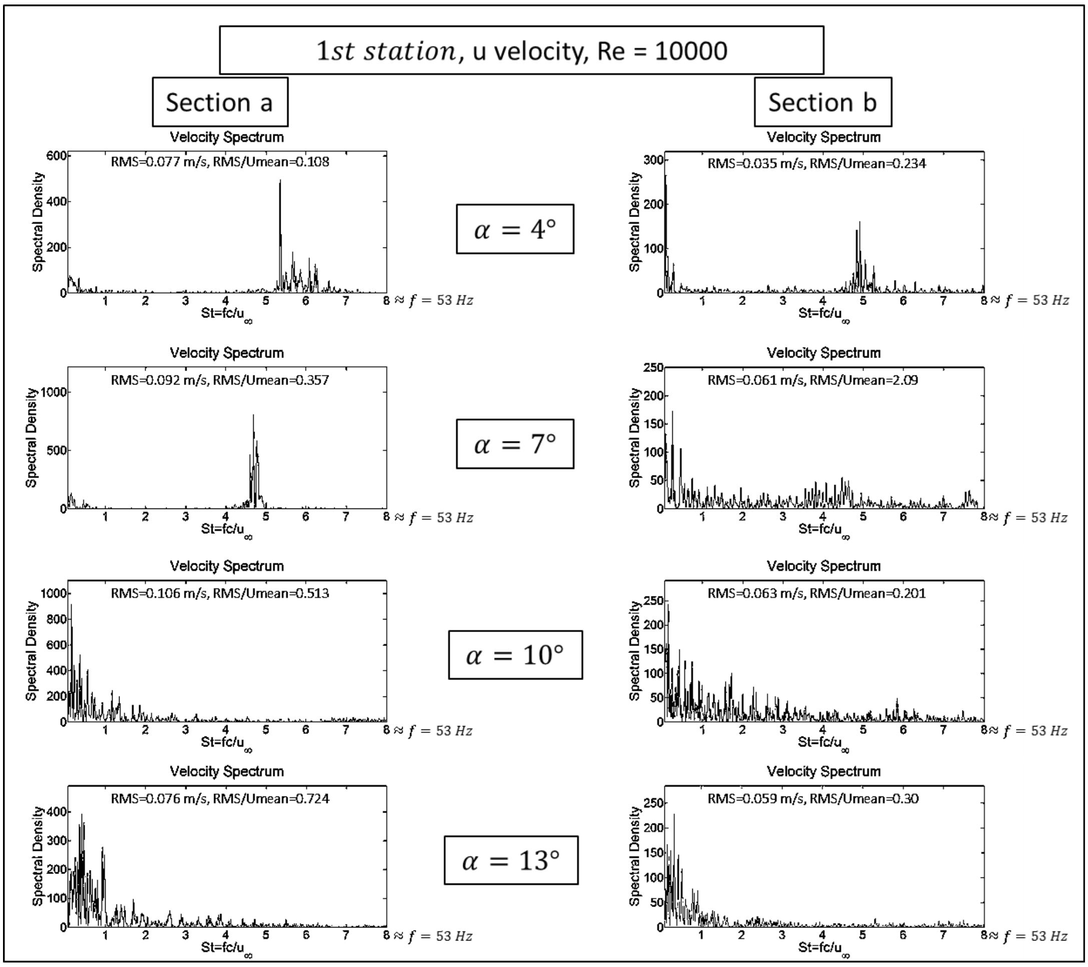

Figure 4.58 Power Spectral Densities of u component of velocities measured using LDA at $Re = 10.000$ at different angles of attack. Measurement points are located 5 mm close to the wing surface and beneath the first pressure measurement section where lines of sections a and b pass

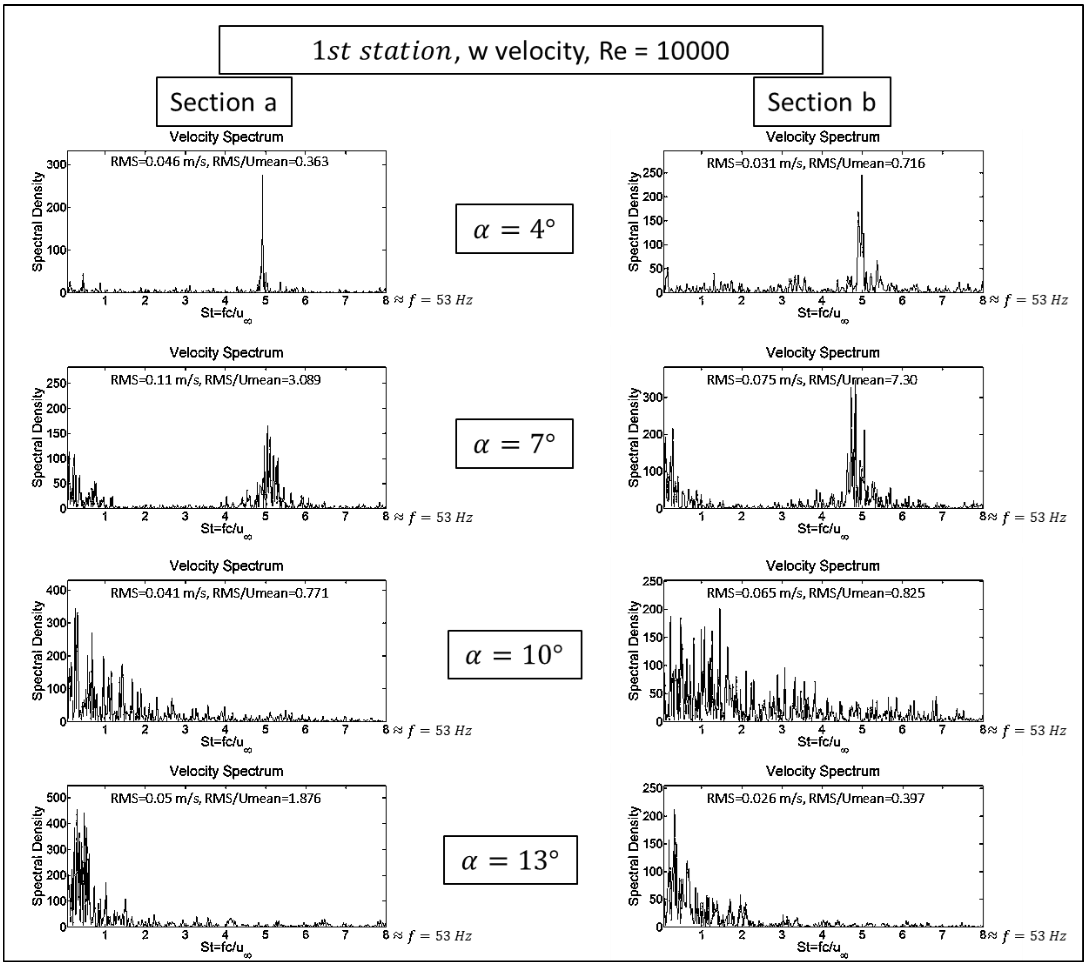

Figure 4.59 Power Spectral Densities of ω component of velocities measured using LDA at $Re = 10.000$ at different angles of attack. Measurement points are located 5 mm close to the wing surface and beneath the first pressure measurement section where lines of sections a and b pass

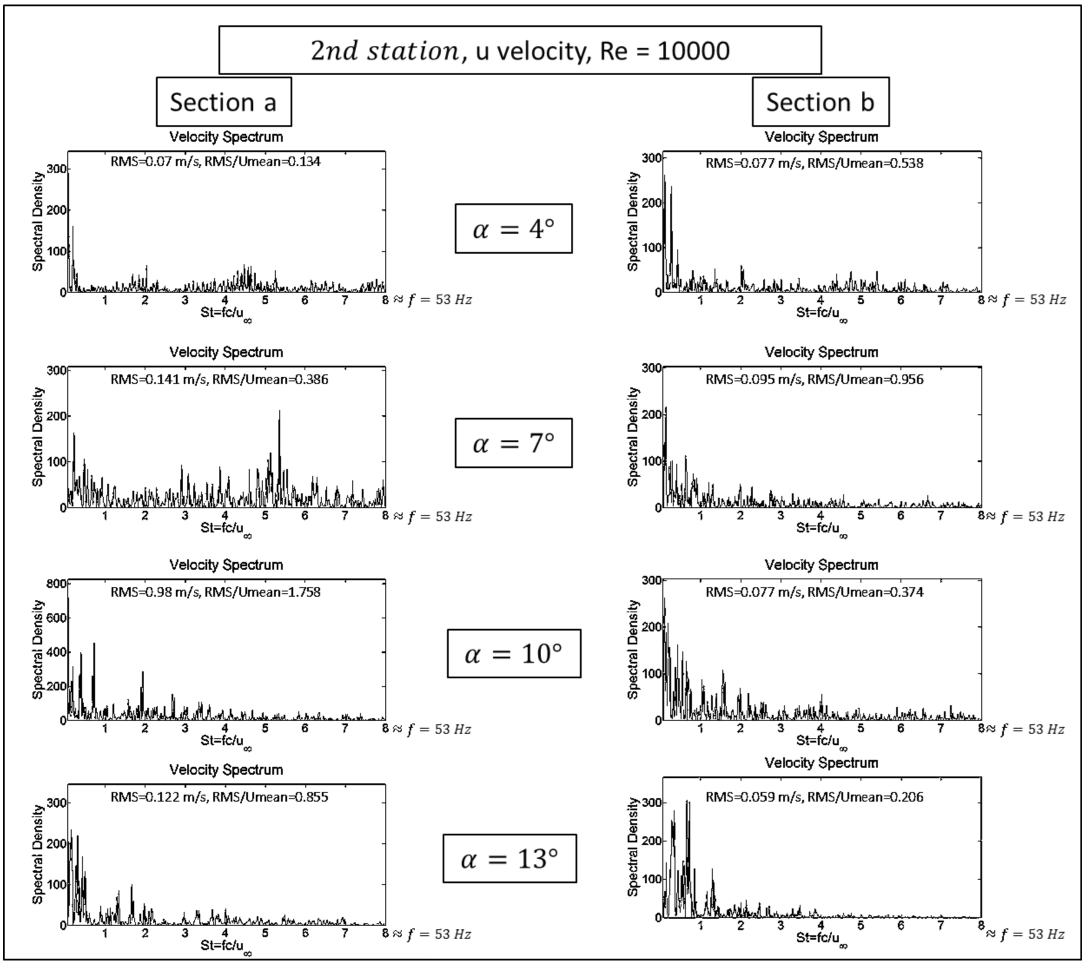

Figure 4.60 Power Spectral Densities of u component of velocities measured using LDA at $Re = 10.000$ at different angles of attack. Measurement points are located 5 mm close to the wing surface and beneath the second pressure measurement section where lines of sections a and b pass

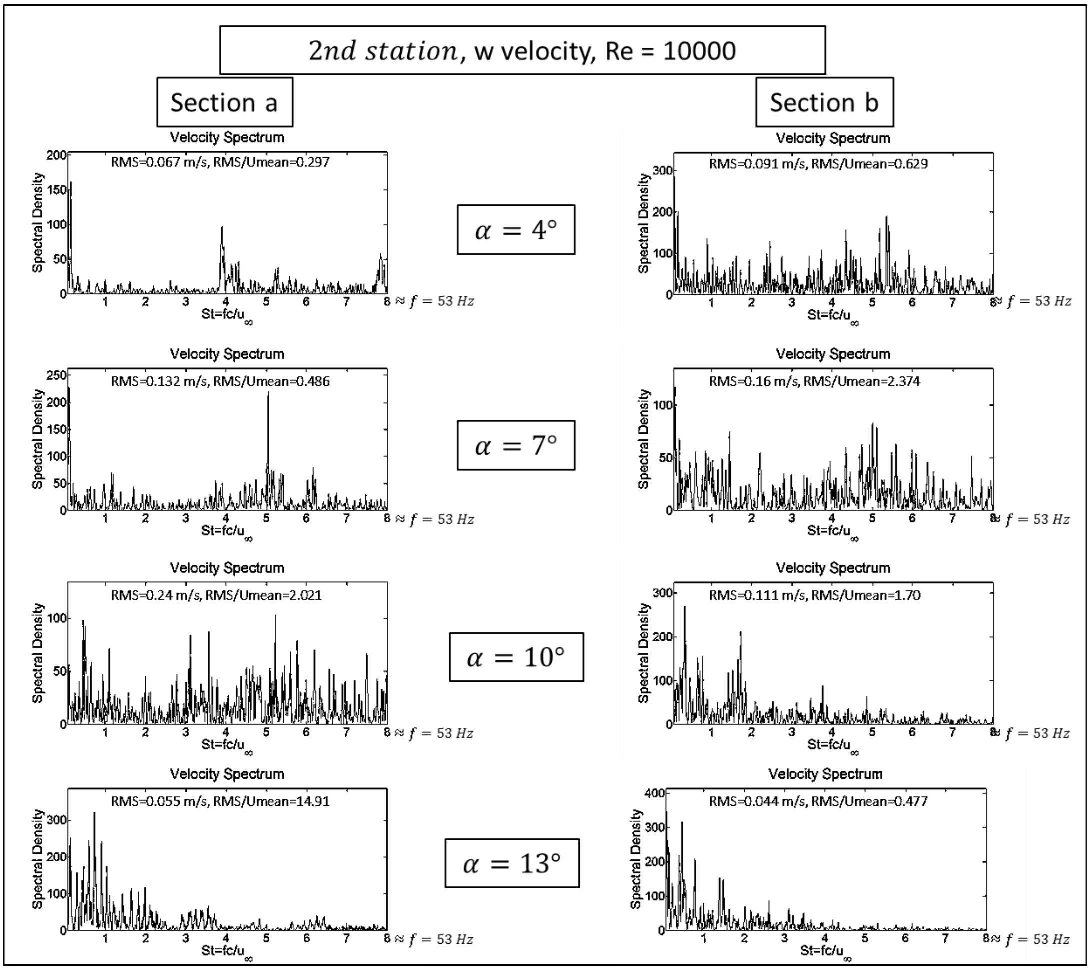

Figure 4.61 Power Spectral Densities of ω component of velocities measured using LDA at $Re = 10.000$ at different angles of attack. Measurement points are located 5 mm close to the wing surface and beneath the second pressure measurement section where lines of sections a and b pass

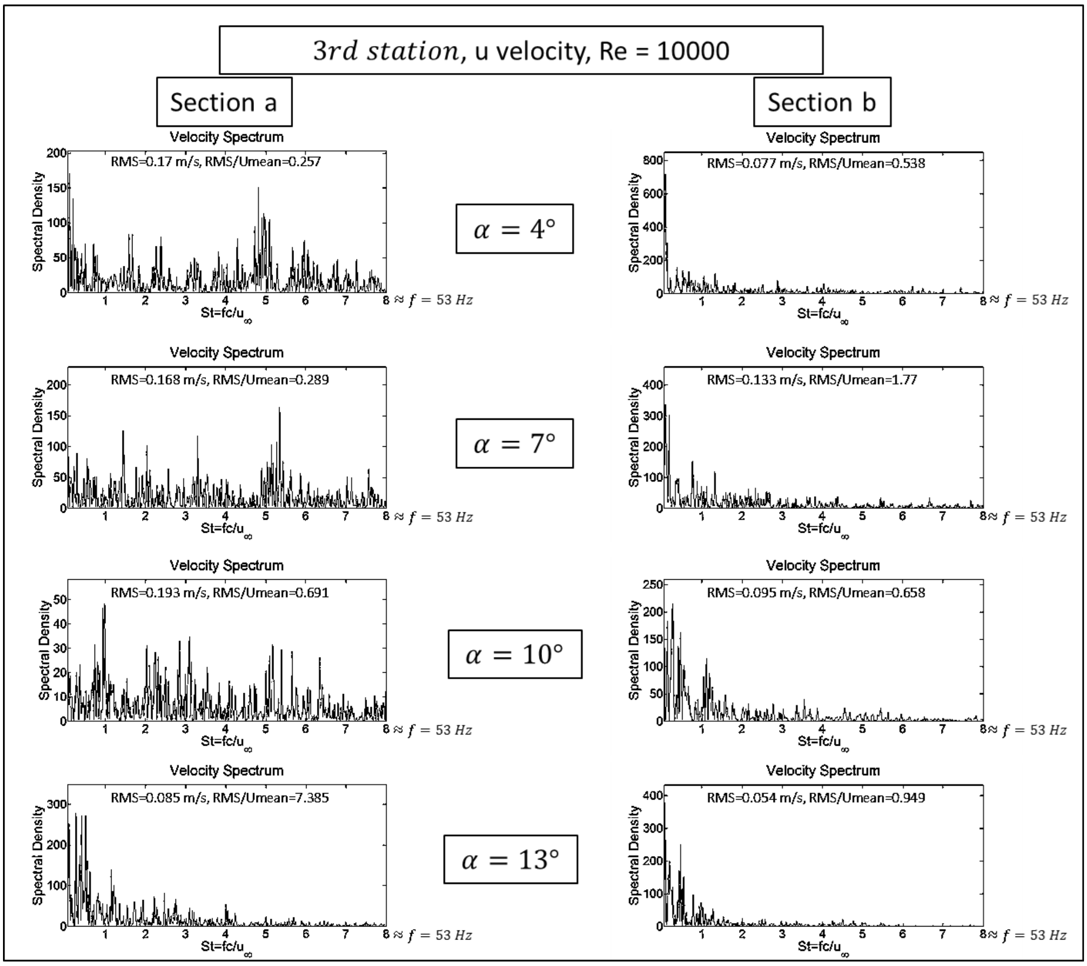

Figure 4.62 Power Spectral Densities of u component of velocities measured using LDA at $Re = 10.000$ at different angles of attack. Measurement points are located 5 mm close to the wing surface and beneath the third pressure measurement section where lines of sections a and b pass

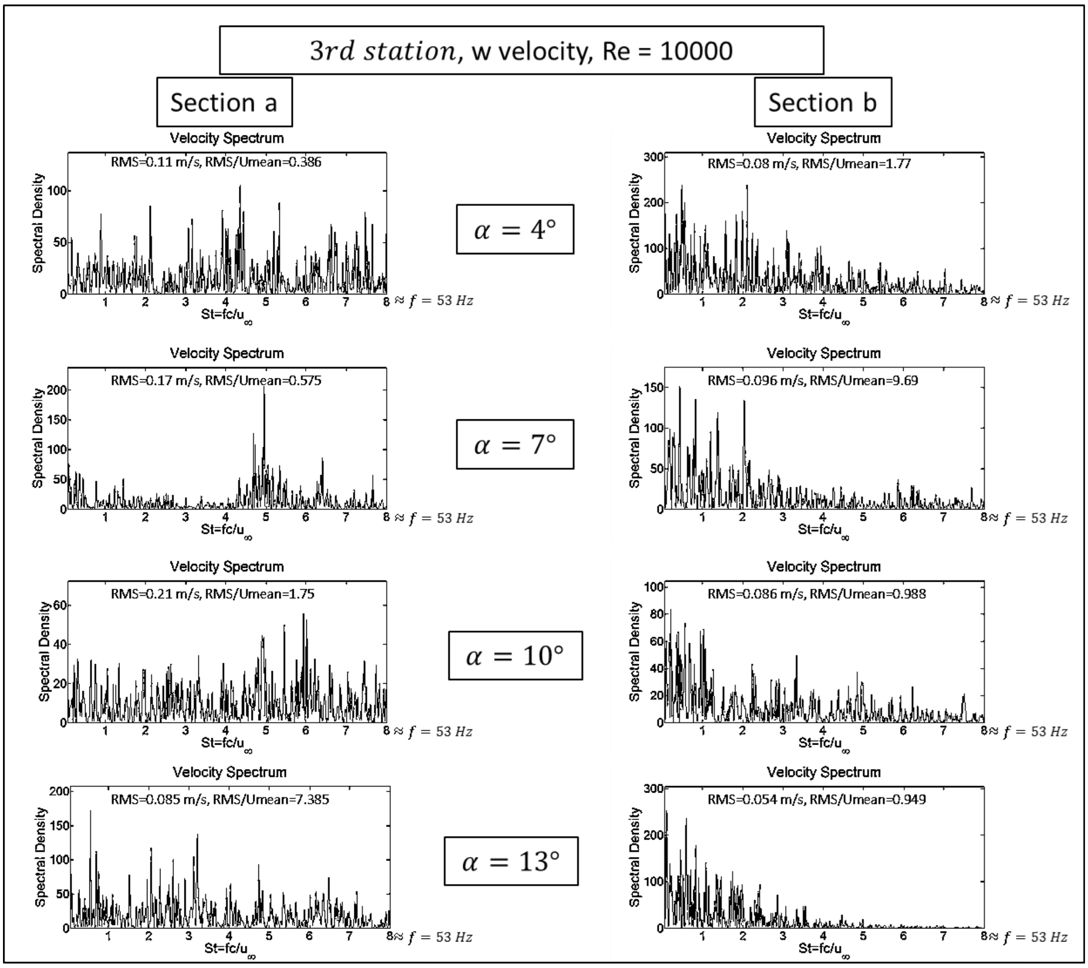

Figure 4.63 Power Spectral Densities of ω component of velocities measured using LDA at $Re = 10.000$ at different angles of attack. Measurement points are located 5 mm close to the wing surface and beneath the third pressure measurement section where lines of sections a and b pass

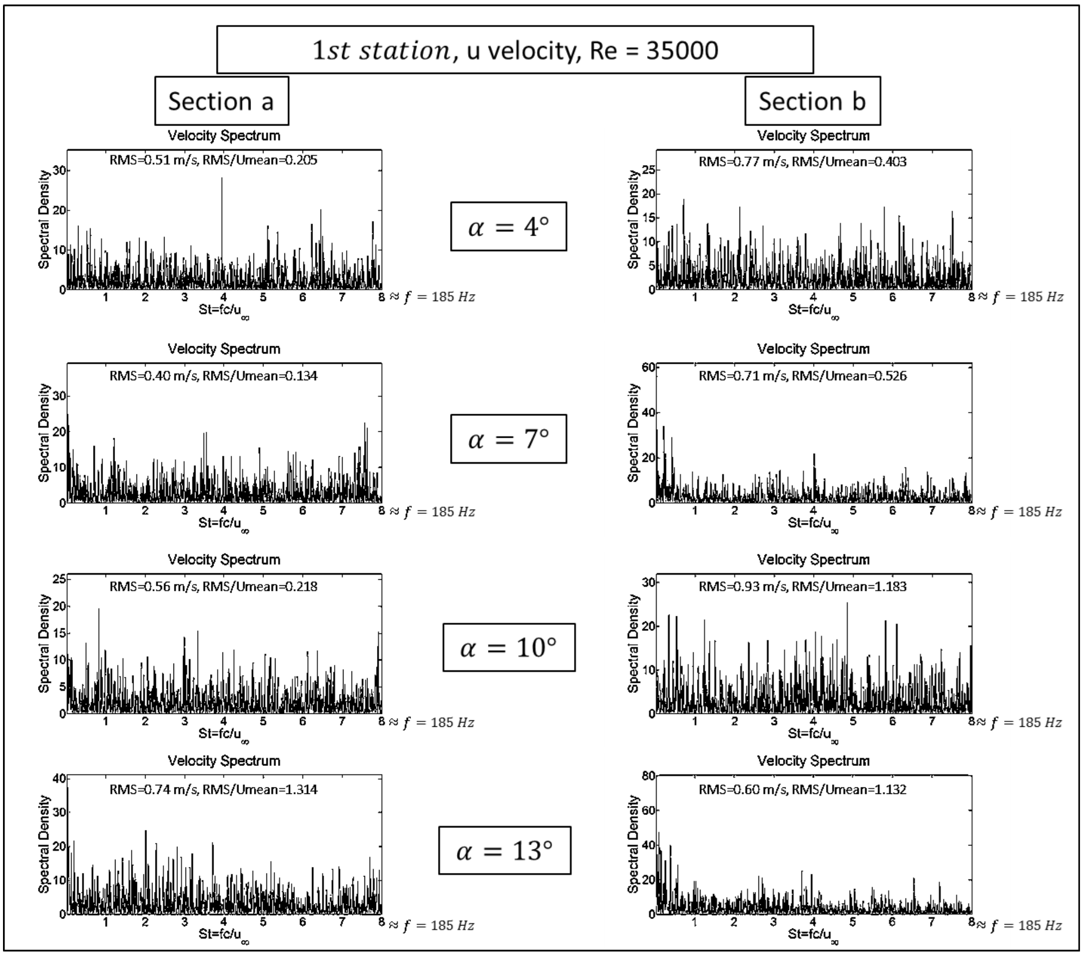

Figure 4.64 Power Spectral Densities of u component of velocities measured using LDA at $Re = 35.000$ at different angles of attack. Measurement points are located 5 mm close to the wing surface and beneath the first pressure measurement section where lines of sections a and b pass

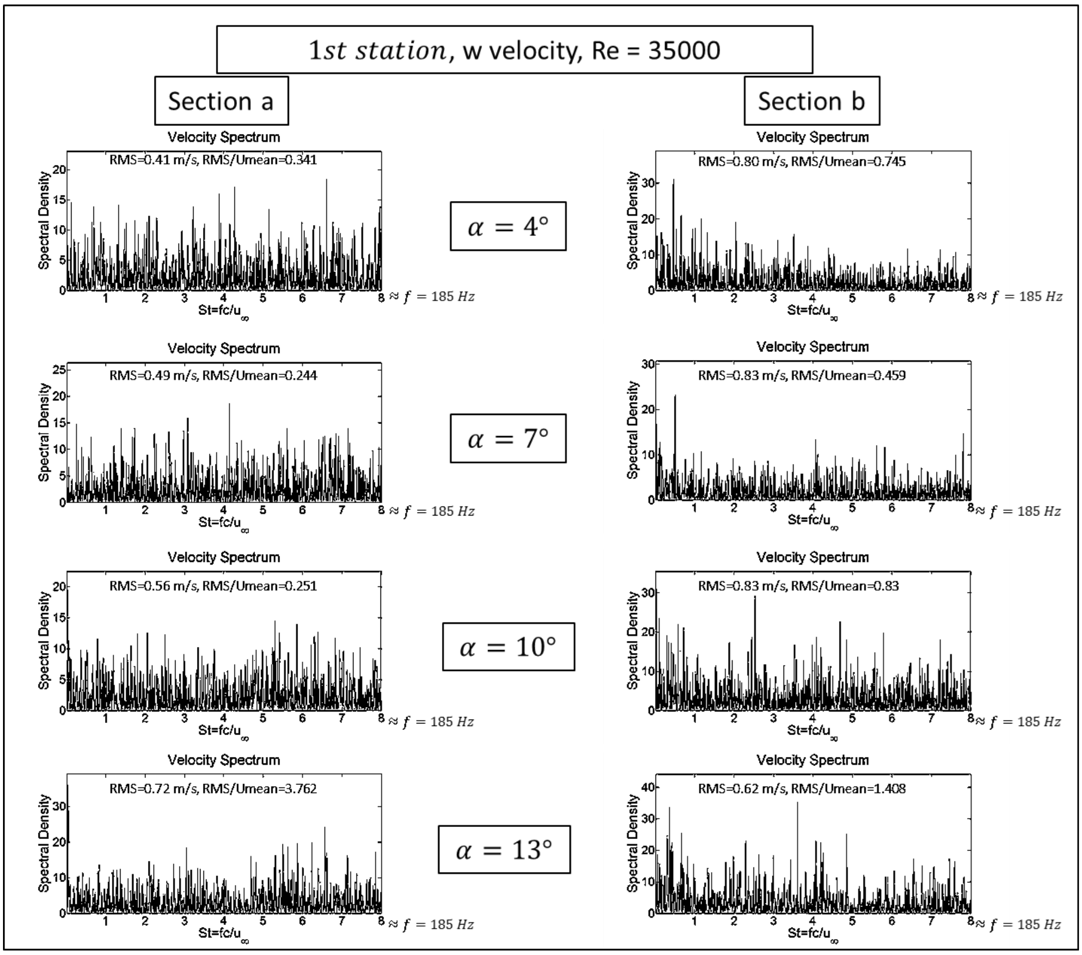

Figure 4.65 Power Spectral Densities of ω component of velocities measured using LDA at $Re = 35.000$ at different angles of attack. Measurement points are located 5 mm close to the wing surface and beneath the first pressure measurement section where lines of sections a and b pass

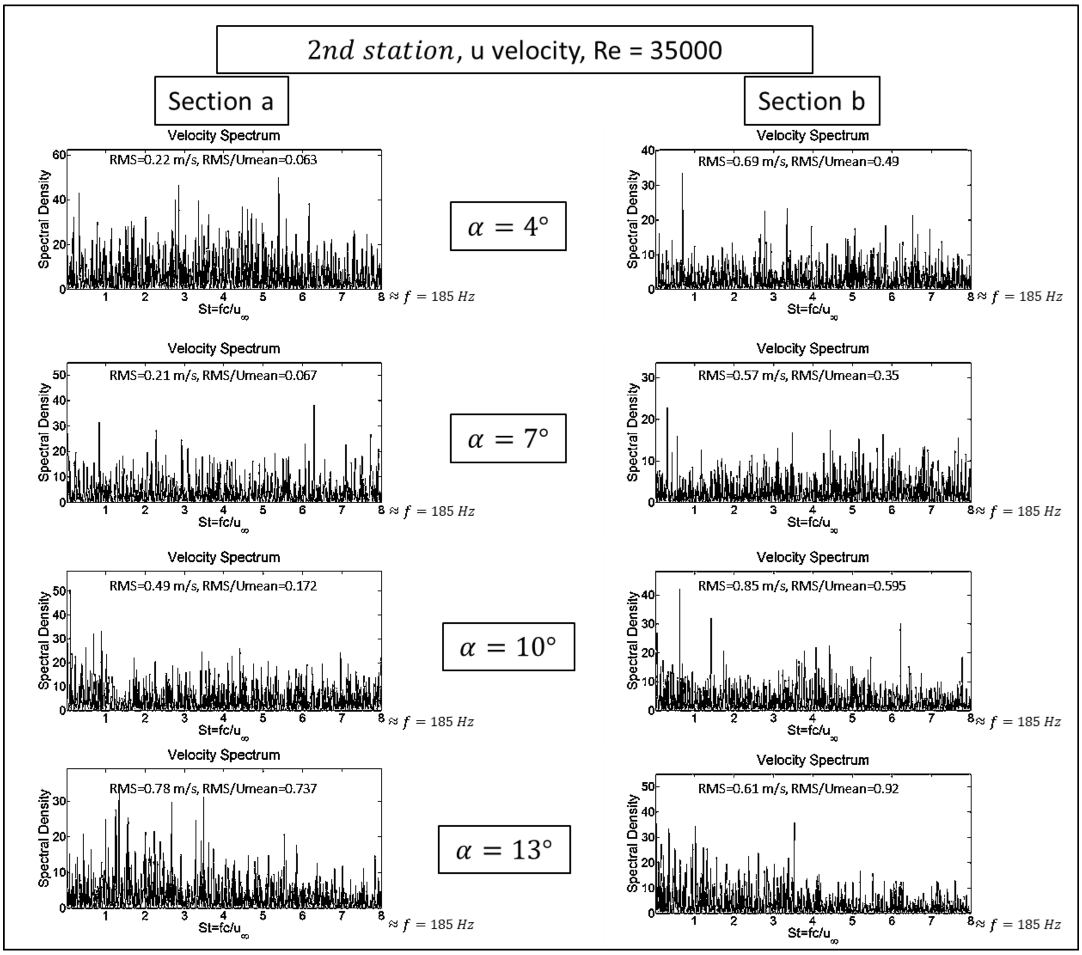

Figure 4.66 Power Spectral Densities of u component of velocities measured using LDA at $Re = 35.000$ at different angles of attack. Measurement points are located 5 mm close to the wing surface and beneath the second pressure measurement section where lines of sections a and b pass

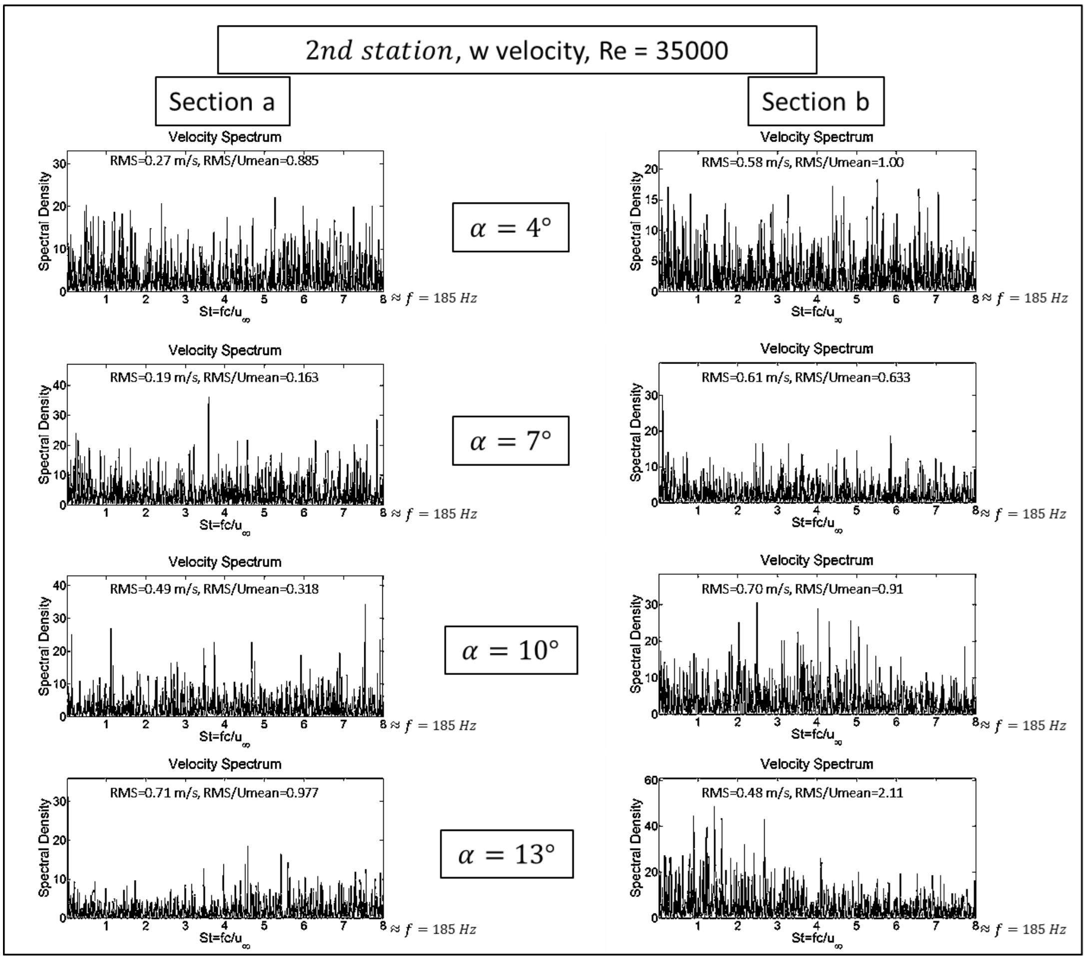

Figure 4.67 Power Spectral Densities of ω component of velocities measured using LDA at $Re = 35.000$ at different angles of attack. Measurement points are located 5 mm close to the wing surface and beneath the second pressure measurement section where lines of sections a and b pass

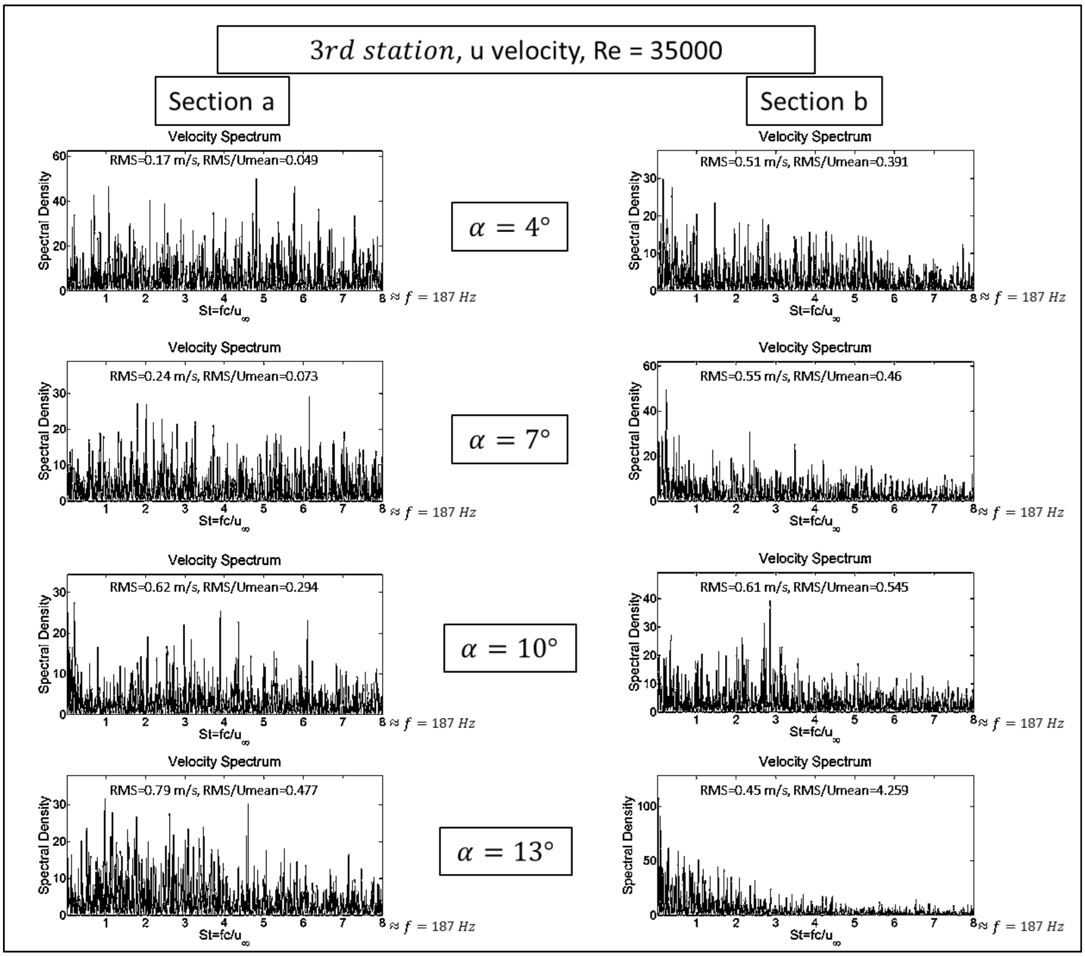

Figure 4.68 Power Spectral Densities of u component of velocities measured using LDA at $Re = 35.000$ at different angles of attack. Measurement points are located 5 mm close to the wing surface and beneath the third pressure measurement section where lines of sections a and b pass

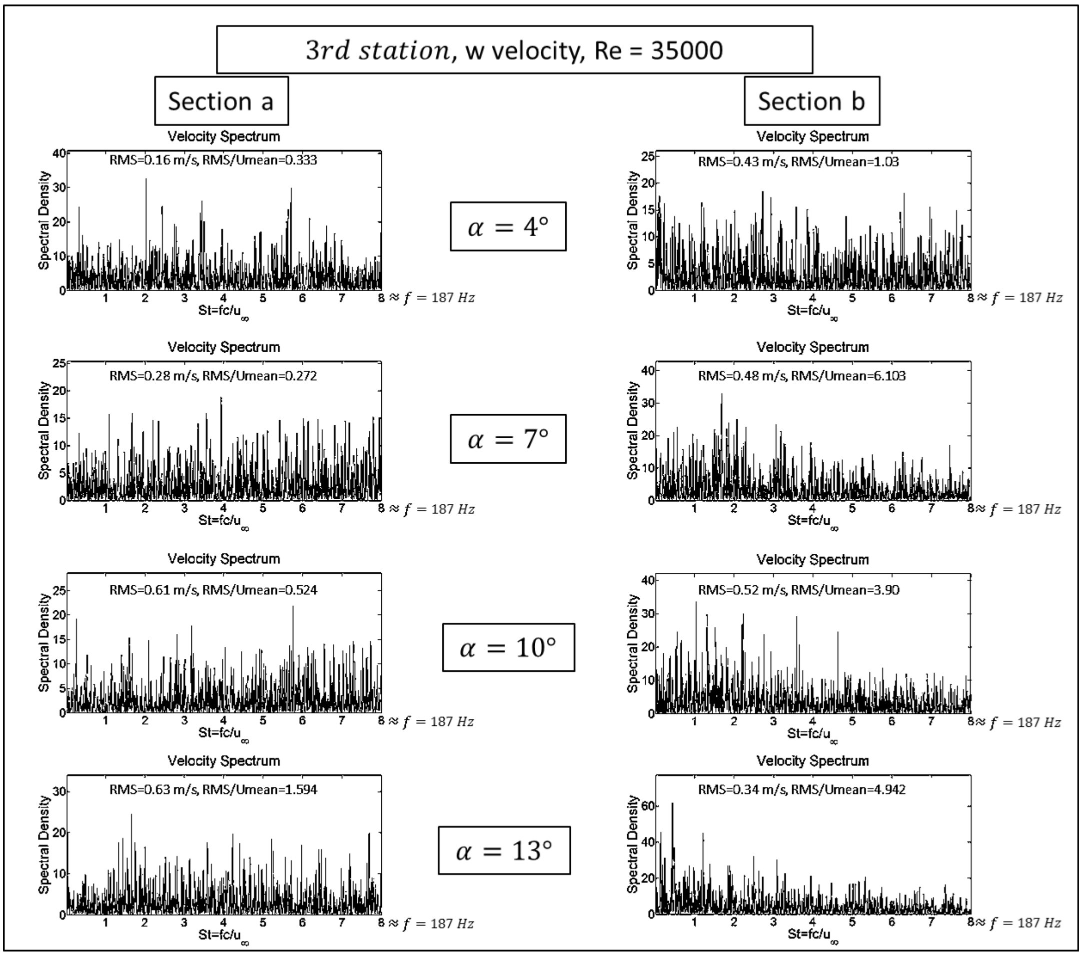

Figure 4.69 **Power Spectral Densities of ω component of velocities measured using LDA at $Re = 35.000$ at different angles of attack. Measurement points are located 5 mm close to the wing surface and beneath the third pressure measurement section where lines of sections a and b pass**

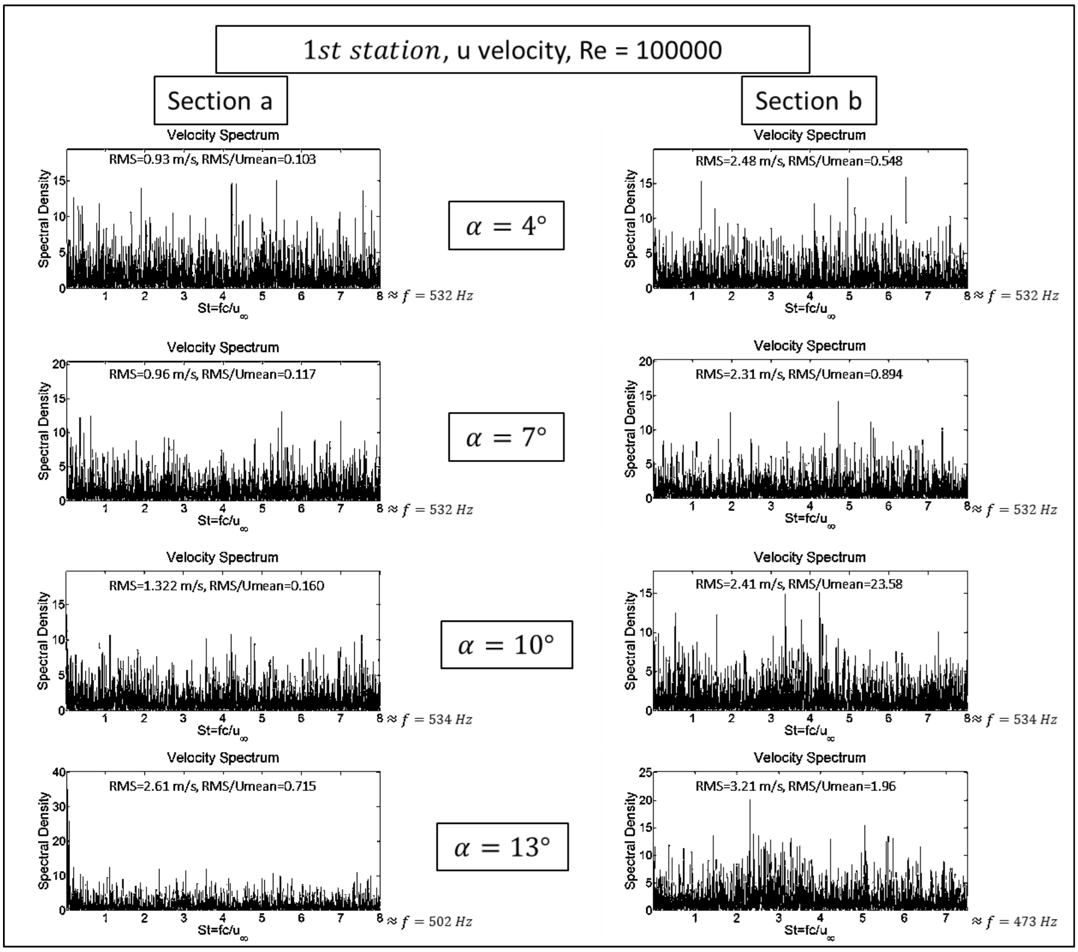

Figure 4.70 Power Spectral Densities of u component of velocities measured using LDA at $Re = 100.000$ at different angles of attack. Measurement points are located 5 mm close to the wing surface and beneath the first pressure measurement section where lines of sections a and b pass

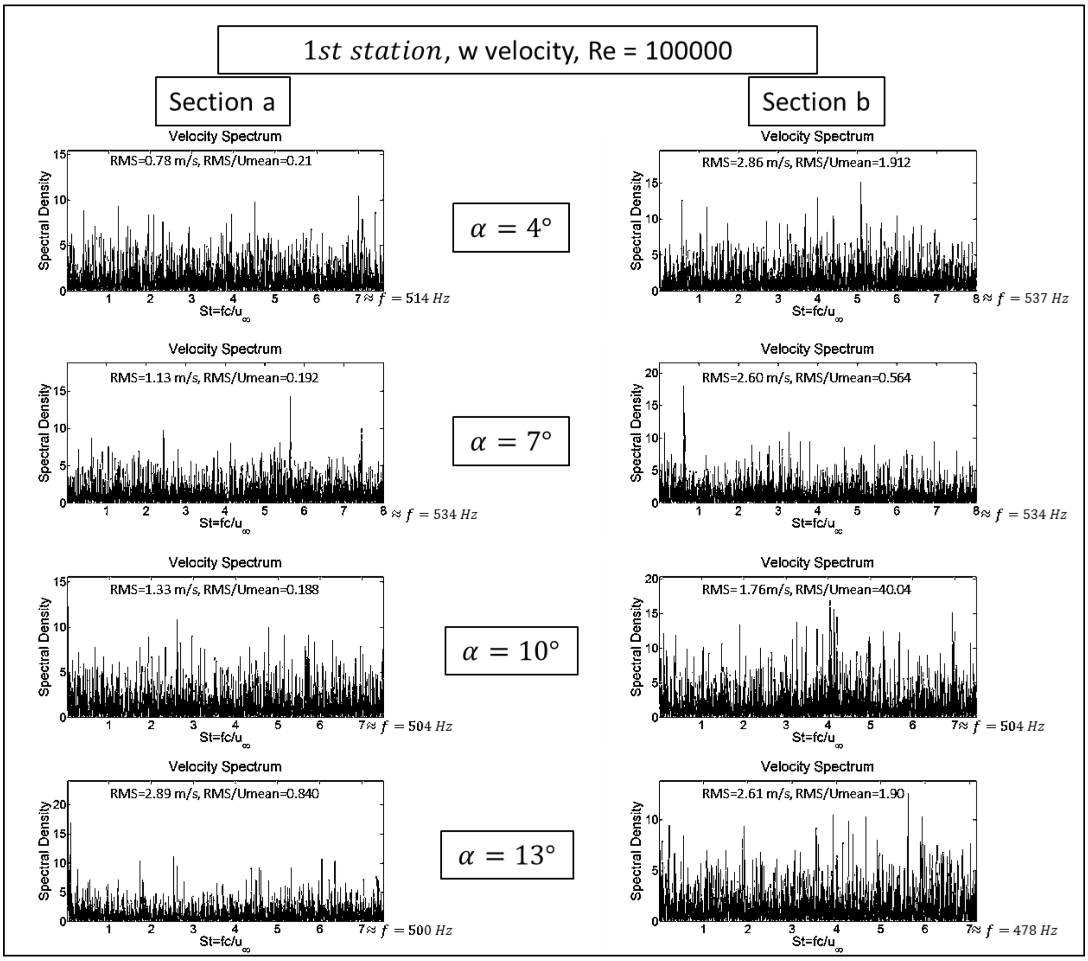

Figure 4.71 Power Spectral Densities of ω component of velocities measured using LDA at $Re = 100.000$ at different angles of attack. Measurement points are located 5 mm close to the wing surface and beneath the first pressure measurement section where lines of sections a and b pass

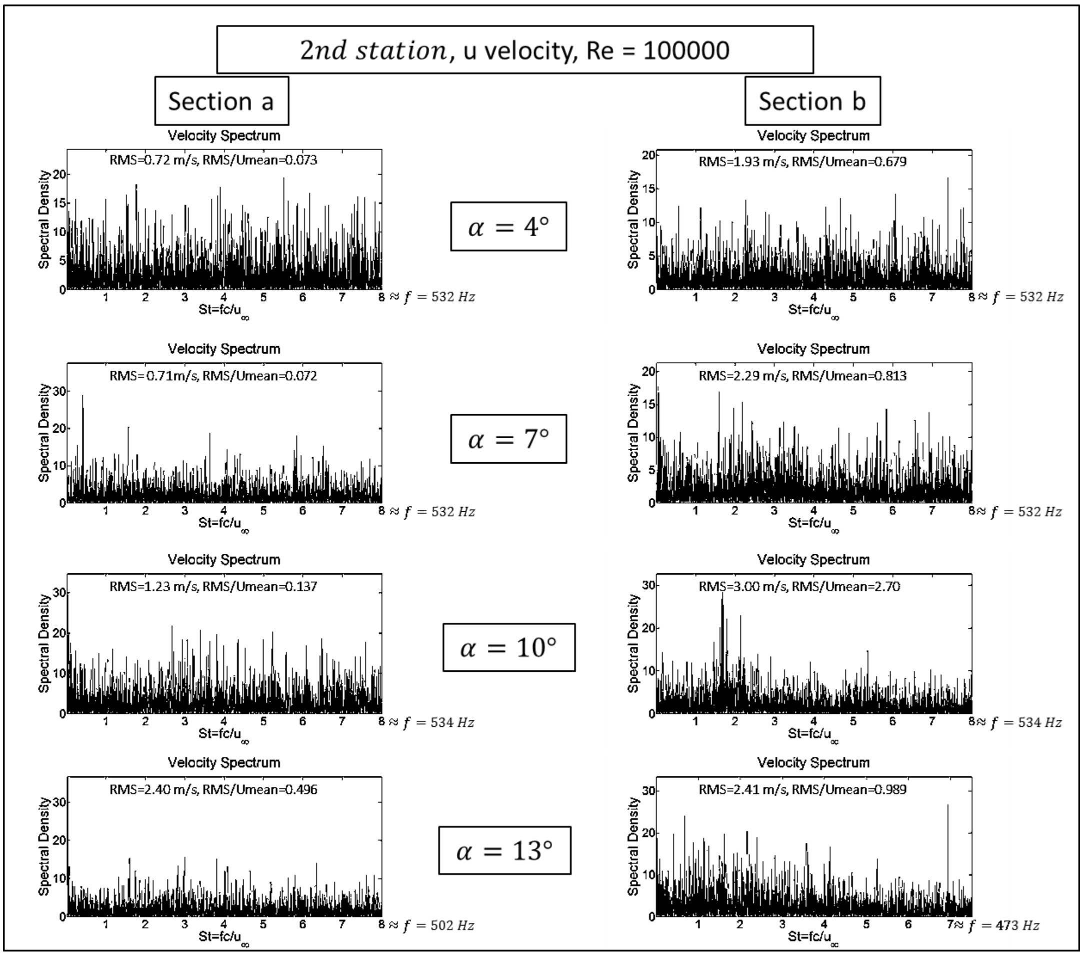

Figure 4.72 Power Spectral Densities of u component of velocities measured using LDA at $Re = 100.000$ at different angles of attack. Measurement points are located 5 mm close to the wing surface and beneath the second pressure measurement section where lines of sections a and b pass

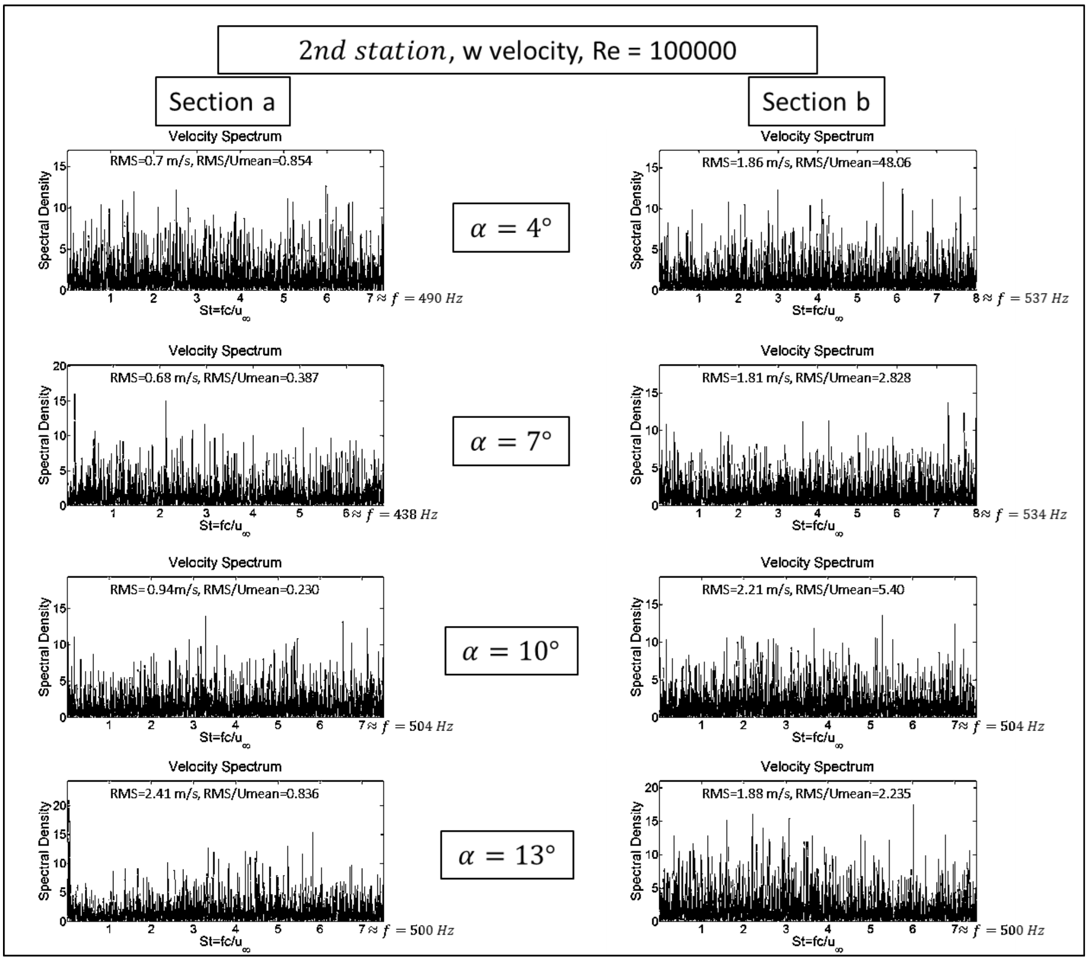

Figure 4.73 Power Spectral Densities of ω component of velocities measured using LDA at $Re = 100.000$ at different angles of attack. Measurement points are located 5 mm close to the wing surface and beneath the second pressure measurement section where lines of sections a and b pass

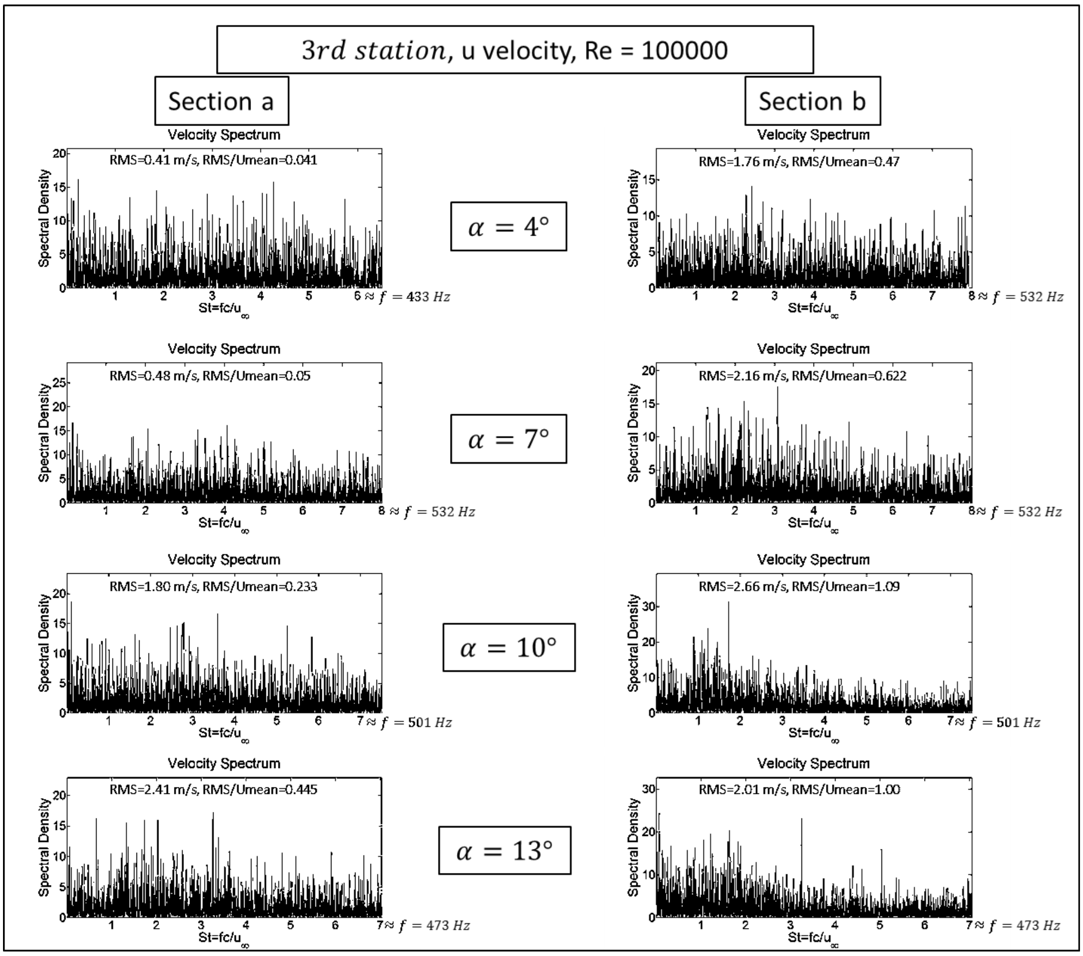

Figure 4.74 Power Spectral Densities of u component of velocities measured using LDA at $Re = 100.000$ at different angles of attack. Measurement points are located 5 mm close to the wing surface and beneath the third pressure measurement section where lines of sections a and b pass

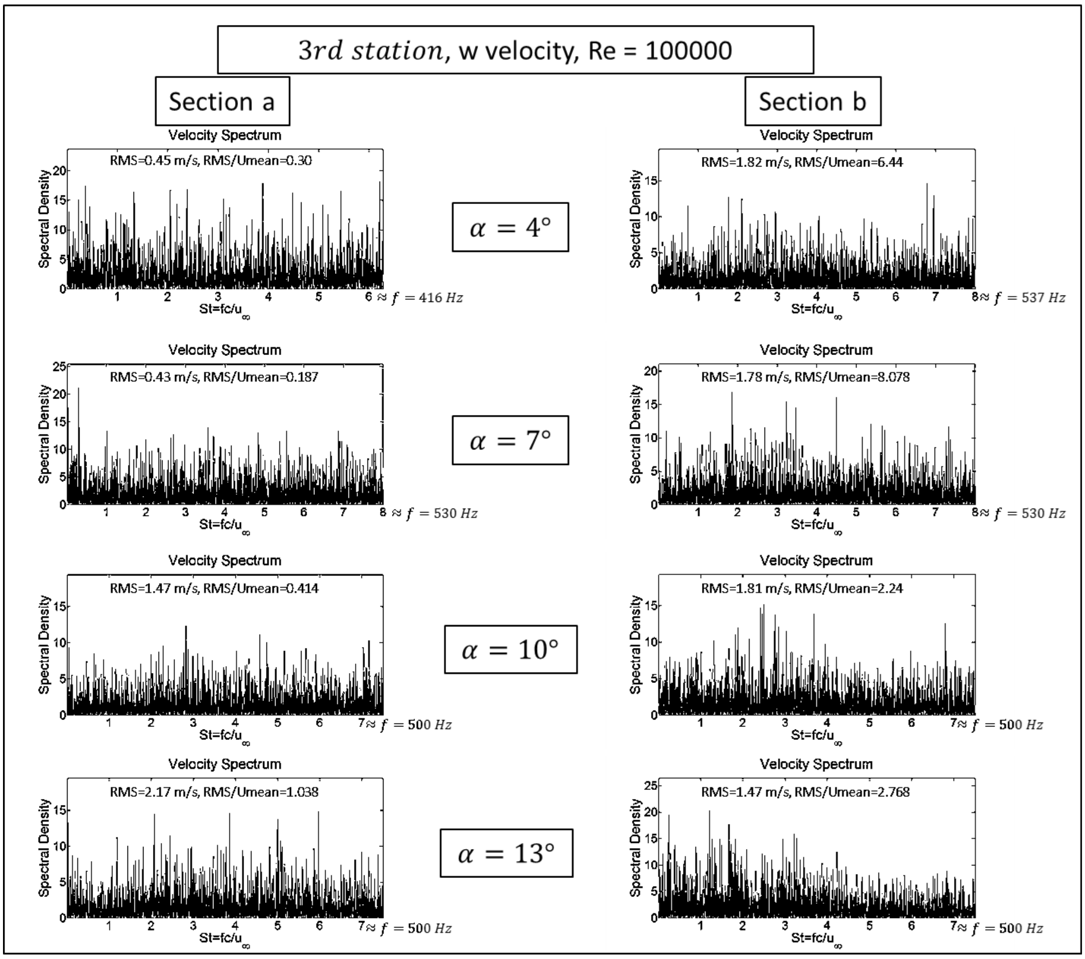

Figure 4.75 Power Spectral Densities of ω component of velocities measured using LDA at $Re = 100.000$ at different angles of attack. Measurement points are located 5 mm close to the wing surface and beneath the third pressure measurement section where lines of sections a and b pass

CHAPTER 5

1. DISCUSSION AND CONCLUSION

5.1 Conclusion

An experimental study is conducted in the present study so as to investigate the flow structure on a moderate sweep delta wing with $\Lambda = 45°$ leading-edge sweep. Formation of leading-edge vortices and their breakdown, and three-dimensional separation from the surface of the wing is investigated at an angle of attack range from $4°$ to $13°$ and for Reynolds numbers from $Re = 8x10^3 to\ Re = 1.5x10^5$ both qualitatively and quantitatively using laser illuminated smoke visualization, surface pressure measurements and Laser Doppler Anemometry (LDA) technique. Smoke visualization experiments were performed at three different crossflow planes which correspond to the pressure measurement stations, and at a plane which passes through the core of leading edge vortices. The mean and unsteady pressure measurements were taken from pressure taps that are located in three spanwise stations on the surface of the wing. The mean and unsteady velocity measurements are performed at the leading edge vortex core and at particular points on a plane which is 5 mm close to the wing surface. The power spectral densities of pressure and velocity measurements were also calculated along with the statistical analysis in order to understand the unsteady behavior of the flow structure. As a result of the present investigation, the following are concluded:

- Increase in attack angle moves the vortex structure inboard towards the wing centerline, whereas an increase in Reynolds number causes a contrary effect in the flow and moves the vortex structure outboard towards the leading edge.

- Considering prestall and stall conditions, increase in attack angle significantly change the flow structure at low Reynolds numbers, however its influence is quite limited at high Reynolds numbers.
- Vortex breakdown location moves upstream towards the apex of the wing with increasing Reynolds number.
- The flow reaches to an asymptotic state after a certain Reynolds number and thus further increase in Reynolds number does not cause a noticeable change in the flow. This finding is quite in line with Taylor and Gursul's [4] study which was conducted on a 50-degree sweep wing and was observed that the flow reaches to an asymptotic state at Reynolds number $Re = 3x10^4$.
- The suction pressure peaks, which also indicate the core of the leading edge vortex, reduce in downstream direction. At locations downstream of vortex breakdown significant reductions in suction effects are detected. For the prestall regime, the suction peaks increase with increasing Reynolds number and angle of attack.
- The highest pressure fluctuations take place between the reattachment region and the vortex core for relatively high angle of attack condition. For the prestall regimes, the highest pressure fluctuations are detected at regions close to the vortex core.

- The pressure spectrums for Reynolds number $Re = 10^4$ do not have any discernable spectral peak which is common at all measurement locations and conditions. Instead, there are wide range of spectral peaks scattered in broad spectra. However, increase in Reynolds number to $Re = 3.5x10^4$ and $Re = 10^5$ causes dominant spectral peaks close to dimensionless frequency $St = 0$ in pressure spectra.
- Neither streamwise, nor vertical velocity measurements at the vortex core indicate a dominant spectral peak that is common at all the cases, instead there are wide range of spectral distributions with dominant peaks at different dimensionless frequencies. The highest mean axial velocity at vortex core is measured at 4-degree angle of attack at $x/c = 0.32$, and it is found to be 1.77 times greater than the freestream velocity.

- The spectra of near surface velocity measurements at Reynolds number $Re = 10^4$ indicate the existence of distinct dominant peaks for the regions under the influence of strong leading-edge vortex cores or three-dimensional separation from the surface. However, at Reynolds numbers $Re = 3.5x10^4$ and $Re = 10^5$, spectral peaks, which are scattered in broad dimensionless frequencies, exist in the spectra.
- Considering the attack angles of $\alpha = 4°,\ 7°$ and $10°$, the highest velocity fluctuations take place at the regions around the vortex core axis. These regions are close to the center of the wing at low Reynolds numbers, but increase in Reynolds number moves these regions towards the leading-edge of the wing by moving the vortex structure as it is mentioned before.
- The velocity fluctuations at locations close to the reattachment region at 13-degree angle of attack and high Reynolds numbers, when the vortex breakdown location reached to the apex of the wing, are higher than the ones measured at same locations at lower attack angles and same Reynolds numbers. However the fluctuations in ω-component of the velocity at locations outboard of the symmetry plane become minimum when the wing reaches to stall regime.

5.2 Recommendations for Future Work

The present study provides a detailed analysis of flow structure on 45-degree sweep delta wing considering a wide range of Reynolds numbers and attack angles. Both steady and unsteady nature of the flow structure is investigated in detail using qualitative and quantitative flow measurement techniques. In addition to the flow structure analysis, the following could be investigated to complement the present study:

- Current experimental set up requires significant amount of time for the laser probe alignment and tracing different points in the flow field. Due to this limitation, LDA measurement points are limited in the present study. With computer controlled traverse mechanism, more points can be traced in the flow field and more information regarding velocity fluctuations can be obtained. Similarly, for the pressure measurements, using more pressure tap stations and pressure taps, more information regarding pressure fluctuations can be obtained.

- Due to the limitation of the LDA measurement system used in the present study, limited information regarding the relationship of the fluctuation behavior for different velocity components can be obtained. 3-D LDA measurements can be performed and thus, correlations between velocity fluctuations can be understood.
- Force-balance measurements can be employed on the planform to confirm the aerodynamic characteristics of the wing inferred from the flow field measurements performed in the present study.
- Stall is an undesired phenomenon since it causes a dramatic drop in aerodynamic performance of the wings. It can be very useful to study how to eliminate or delay the stall on this planform by using one of the various active or passive flow control techniques or investigating a method that combines more than one flow control techniques so as to increase the aerodynamic performance and stability of the present wing.

REFERENCES

[1] Gursul, I., "*Vortex Flows on UAVs: Issues and Challenges"*, The Aeronautical Journal, vol. 108, No. 1090, December 2004, pp. 597-610.

[2] "*Workshop on Aerodynamic Issues of Unmanned Air Vehicles*", 4-5 November 2002, University of Bath, UK.

[3] Gursul, I., Gordnier, R. and Visbal, M., "*Unsteady Aerodynamics of Nonslender Delta Wings*", Progress in Aerospace Sciences 41, pp. 515–557 2005.

[4] Taylor, G. S., and Gursul, I., "*Buffeting Flows over a Low-Sweep Delta Wing*", AIAA Journal, Vol. 42, No. 9, 2004, pp. 1737–1745. doi:10.2514/1.5391.

[5] Yavuz, M. M., "*Origin and Control of the Flow Structure and Topology on Delta Wings*", The Departmant of Mechanical Engineering and Mechanics Lehigh University, U.S.A., January 2006.

[6] Yayla, S., "*Flow Characteristics of Diamond and Lambda Wings at Different Flight Conditions*", Cukurova University, Turkey, 2009.

[7] Doligalski, T. L., Smith, C. R., and Walker, J. D., "*Vortex Interactions with Walls*", Annual Review of FluidMechanics,Vol.26, 1994, pp. 573-616.

[8] Andreopoulos, J., and Agui, J., "*Wall Vorticity Flux Dynamics in a Two dimensional Boundary Layer*", Journal of Fluid Mechanics, Vol. 309, 1996, pp. 45-84.

[9] Ol, M., Gharib, M., "*Leading Edge Vortex Structures of Non-slender Delta Wings at Low Reynolds Numbers*", AIAA Journal, Vol.41, No. 1 January 2003, pp. 16-26.

[10] Earnshaw, P. B. and Lawford, J. A., "*Low-Speed Wind-Tunnel Experiments on a Series of Sharp-Edged Delta Wings*", ARC Reports and Memoranda No. 3424, March 1964.

[11] Werle, H., “*Quelques résultats expérimentaux sur les ailes en flèches, aux faibles vitesses, obtenus en tunnel hydrodynamique*”, Rech. Aeronautique 41, 23 1954.

[12] Williams, N. M., “*Active Flow control on a Nonslender Delta Wing*”, Doctor of Philosophy Thesis, Department of Mechanical Engineering University of Bath, UK, March 2009.

[13] Delery, J. M., Robert Legendre and Henry Werle, “*Toward the elucidation of three dimensional separation*”, Annual Review of Fluid Dynamics, Vol. 33, pp. 129-154, 2001.

[14] Breitsamter, C.,”*Unsteady flow phenomena associated with leading-edge vortices*”, Progress in Aerospace Sciences, Vol.44, pp.48–65, 2008.

[15] Gordnier, R. E. and Visbal, M. R., “*Higher-Order Compact Difference Scheme Applied to the Simulation of a Low Sweep Delta Wing Flow*”, AIAA 2003-0620, 41st AIAA Aerospace Sciences Meeting and Exhibit, 6-9 January 2003, Reno, NV.

[16] Wang, J. J., Zhang, W., “*Experimental Investigations on Leading-Edge Vortex Structures for Flow Over Non-Slender Delta Wings*”, Chin.Phys.Lett., Vol. 25, No:7, 2008.

[17] Gursul, I., Vardaki, E., Margaris, P., Wang, Z., “*Control of Wing Vortices*”, Active Flow Control", NNFM 95, pp. 137-151, 2007.

[18] Wentz W. H., Kohlman D. L., *“Vortex breakdown on slender sharp-edged wings”,* J Aircr, 1971, 8(3):156–61.

[19] Erickson G.E., “*Water tunnel studies of leading edge vortices*”, J Aircr, 1982, 19(6):442–8.

[20] Bartlett G. E., Vidal R. J., “*Experimental investigation of influence of edge shape on the aerodynamic characteristics of low aspect ratio wings at low speeds*”, J Aeronaut Sci, 1955, 22(8):517–33.

[21] Benjamin, T. B., “*Theory of the vortex breakdown phenomenon*”, Journal of Fluid Mechanics, 1962, 14:593-629.

[22] Benjamin, T. B., "*Some developments in the theory of vortex breakdown*", Journal of Fluid Mechanics, 1967, 28(1):65-848.

[23] Sarpkaya, T., "*On Stationary and Traveling Vortex Breakdown*", Journal of Fluid Mechanics, Vol. 45, No. 3, 1971, pp. 545-559.

[24] Sarpkaya, T., "*Vortex Breakdown on Swirling Conical Flows*", AIAA Journal, Vol. 9, 1971, pp. 1792-1799.

[25] Sarpkaya, T., "*Effect of Average Pressure Gradient on Vortex Breakdown*", AIAA Journal, Vol. 12, 1974, pp. 602-607.

[26] Leibovich, S., "*Structure of Vortex Breakdown*", Annual Review of Fluid Mechanics, Vol. 10, 1978, pp. 221-246.

[27] Leibovich, S., "*Vortex Stability and Breakdown: Survey and Extension*", AIAA Journal, Vol. 22, 1984, pp. 1192-1206.

[28] Wedemayer, E., "*Vortex Breakdown*", High Angle-of-Attack Aerodynamics, AGARD 121, March 1982.

[29] Polhamus E. C., "*Predictions of vortex-lift characteristics by a leading-edge suction analogy*", J Aircr, 1971, 8(4):193–9.

[30] Escuider, M., "*Vortex breakdown: Observations and Explanations*", Progress in Aerospace Science, Vol. 25, 1988, pp. 189-229.

[31] Lee M., and Ho C., "*Lift force of delta wings*", Appl Mech Rev., 1990, 43(9):209–21.

[32] Brown, G. L. and Lopez, J. M., "*Asymmetric Vortex Breakdown. Part II. Physical Mechanisms*", Journal of Fluid Mechanics, Vol. 221, 1990, pp. 553-76.

[33] Delery, J. M., "*Aspects of vortex breakdown*", Progress in Aerospace Sciences, Vol. 30, 1994, pp. 1-59.

[34] Rockwell, D., "*Three-dimensional flow structure on delta wings at high angle-of-attack: experimental concepts and issues*", AIAA 93-0050, 31st AIAA Aerospace Sciences Meeting & Exhibit, 11–14 January 1993, Reno, NV.

[35] Gordnier, R. E., and Visbal, M. R., "*Unsteady vortex structure over a delta wing*", J Aircr, 1994, 31(1):243–8.

[36] Menke, M., Yang, H. and Gursul, I., "*Experiments on the unsteady nature of vortex breakdown over delta wings*", Exp Fluids, 1999, 27:262–72.

[37] Ashley, H., Katz, J. and Jarrah, M. A., Vaneck, T., "*Survey of Research on Unsteady Aerodynamic Loading of Delta Wing*", Journal of Fluids and Structures, Vol. 5, 1991, pp. 363-390.

[38] Gursul, I., "*Review of unsteady vortex flows over delta wings*", AIAA-2003-3942, AIAA Applied Aerodynamics Conference, 26-26 June, Orlando FL.

[39] Gursul, I., "*Review of unsteady vortex flows over slender delta wings*", Journal of Aircraft, 2005, 42(2), 299-319.

[40] Gursul, I., "*Unsteady flow phenomena over delta wings at high angle-of-attack*", AIAA Journal, 1994, 32(2):225–31.

[41] Lowson, M. V., "*Some Experiments with Vortex Breakdown*," Journal of the Royal Aeronautical Society, Vol. 68, 1964, p. 343.

[42] Rediniotis O. K., Stapountzis, H., Telionis, D. P., "*Periodic vortex shedding over delta wings*", AIAA Journal, 1993, 31(9):1555–61.

[43] Menke, M., Gursul, I., "*Unsteady nature of leading edge vortices*", Phys Fluids, 1997, 9(10):2960–6.

[44] Gursul, I., Xie, W., "*Buffeting flows over delta wings*", AIAA Journal, 1999, 37(1):58–65.

[45] Fisher, D. F., Del Frate, J. H., and Richwine, D. M., "*In Flight Flow Visualization Characteristics of the NASA F-18 High Alpha Research Vehicle at High Angles of Attack*," NASA TM 4193, May 1990.

[46] Ayoub, A., and McLachlan, B. G., "*Slender Delta Wing at High Angles of Attack—A Flow Visualization Study*," AIAA Paper 87-1230, 1987.

[47] Menke, M., and Gursul, I. "*Self-Excited Oscillations of Vortex Breakdown Location over Delta Wings*", AIAA Paper 97-0744, Jan. 1997.

[48] Gursul, I., and Yang, H., "*On Fluctuations of Vortex Breakdown Location*," *Physics of Fluids*, Vol. 7, No. 1, 1995, pp. 229–231.

[49] Portnoy, H., "*Unsteady Motion of Vortex Breakdown Positions on Delta Wings*", International Council of the Aeronautical Science, A89-13501, ICAS, Jerusalem, Aug.–Sept. 1988.

[50] Menke, M., and Gursul, I., "*Nonlinear Response of Vortex Breakdown over a Pitching Delta Wing*", *Journal of Aircraft*, Vol. 36, No. 3, 1999, pp. 496–500.

[51] Rediniotis, O. K., Stapountzis, H., and Telionis, D. P., "*Vortex Shedding over Delta Wings*," AIAA Journal, Vol. 28, No. 5, 1990, pp. 944–946.

[52] Gursul, I., and Xie, W., "*Origin of Vortex Wandering over Delta Wings*", Journal of Aircraft, Vol. 37, No. 2, 2000, pp. 348–350.

[53] Schmucker, A., and Gersten, K., "*Vortex Breakdown and its Control on Delta Wings*", Fluid Dynamics Research, Vol. 3, 1988, pp. 268–272.

[54] Degani, D., and Zilliac, G. G., "*Experimental Study of Nonsteady Asymmetric Flow Around an Ogive-Cylinder at Incidence*," AIAA Journal, Vol. 28, No. 4, 1990, pp. 642–649.

[55] Kommallein, S., and Hummel, D., "*LDA Investigations of the Separated Flow Over Slender Wings*", Physics of Separated Flows—Numerical, Experimental, and Theoretical Aspects, edited by K. Gersten, Vieweg, Brunswick, Germany, 1993, pp. 275–282.

[56] Cornelius, K. C., "*Analysis of Vortex Bursting Utilizing Three-Dimensional Laser Measurements*", Journal of Aircraft, Vol. 32, No. 2, 1995, pp. 297–306.

[57] Cassidy J. J., and Falvey, H. T., "*Observations of unsteady flow arising after vortex breakdown*", Journal of Fluid Mechanics, 1970, 41, pp 727-736 doi:10.1017/S0022112070000873

[58] Lee, B. H. K., and Tang, F. C., "*Characteristics of the Surface Pressures on an F/A-18 Vertical Fin Due to Buffet*", Journal of Aircraft, Vol. 31, No. 1, 1994, pp. 228–235.

[59] Klute, S. M., and Telionis, D. P., "*The Unsteady Characteristics of the Flow Over an F/A 18 at High Alpha*", AIAA Paper 96-0824, 1996.

[60] Gad-el-Hak, M., and Blackwelder, R. F., "*The Discrete Vortices from a Delta wing*", AIAA Journal, Vol. 23, No. 6, 1985, pp. 961–962.

[61] Riley, A. J., and Lowson, M. V., "*Development of a Three-Dimensional Free Shear Layer*", Journal of Fluid Mechanics, Vol. 369, 1998, pp. 49–89.

[62] Payne, F. M., Ng, T. T., Nelson, R. C., and Schiff, L. B., "*Visualization and Wake Surveys of Vortical Flow over a Delta Wing*", AIAA Journal, Vol. 26, No. 2, 1988, pp. 137-141.

[63] Lowson, M. V., "*The Three Dimensional Vortex Sheet Structure on Delta Wings*", Fluid Dynamics of Three-Dimensional Turbulent Shear Flows and Transition, CP-438, AGARD, 1988, pp. 11.1–11.16.

[64] Gordnier, R. E., "*Computation of Kelvin-Helmholtz Instability for Delta Wing Vortex Flows*", Flight Dynamics Directorate, Wright Lab, WL-TR-91-3098, Wright-Patterson AFB, OH, Nov. 1991.

[65] Reynolds, G., and Abtahi, A. A., "*Three dimensional Vortex Development, Breakdown and Control*", AIAA Paper 89-0998, March 1989.

[66] Ng, T. T., and Oliver D. R., "*Leading-Edge Vortex and Shear Layer Instabilities*", AIAA Paper 98-0313, Jan. 1998.

[67] Visbal, M. R., Gordnier, R. E., "*Origin of the computed unsteadiness in the shear layer of delta wings*", J Aircraft, 1995, 32(5):1146–8.

[68] Visbal, M. R., Gordnier, R. E., "*On the structure of the shear layer emanating from a swept leading edge at angle of attack*", AIAA-2003-4016, 33rd Fluid Dynamics Conference and Exhibit, June 2003, Orlando, FL.

[69] Squire, L. C., "*The motion of a thin oil sheet under the steady boundary layer on a body*", Journal of Fluid Mechanics, Vol. 11, 1961, pp. 161-179.

[70] Verhagen, N. G., Meeder, J. P., and Verhelst, J. M., "*Boundary Layer Effects of the Flow of a Leading-Edge Vortex*", AIAA Paper 93-3463, Aug. 1993.

[71] Washburn, A. E., and Visser,K. D., "*Evolution of the Vortical Structures in the Shear Layer of Delta Wings*", AIAA Paper 94–2317, 1994.

[72] Mitchell, A. M., and Molton, P., "*Vortical Substructures in the Shear Layers Forming Leading-Edge Vortices*", AIAA Journal, Vol. 40, No. 8, 2002, pp. 1689–1692.

[73] S., Morton., "*High resolution computational unsteady aerodynamic techniques applied to maneuvering unmanned combat aircraft*", Workshop on Aerodynamic Issues of Unmanned Air Vehicles, University of Bath, UK, November 2002.

[74] Newsome, R.W., "*Euler and Navier–Stokes solutions for flow over a conical delta wing*", AIAA J. 24 (2) (1986).

[75] Gursul, I., Allan, M. R., and Badcock K. J., "*Opportunities for the integrated use of measurements and computations for the understanding of delta wing aerodynamics",* Aerospace Science and Technology, Volume 9, Issue 3, April 2005, pp. 181-189.

[76] Yaniktepe, B., Rockwell, D., "*Flow structure on a delta wing of low sweep angle*", AIAA J, 2004, 42(3):513–23.

[77] Canpolat, C., "*Vortex Formation over a Nonslender Delta Wing", Department of Mechanical Engineering*, M.Sc. Thesis, Cukurova University, Turkey, 2008.

[78] Ol, M. V., "*An experimental investigation of leading edge vortices and passage to stall of nonslender delta wings*", Symposium on Advanced Flow Management, RTO AVT-072, May 2001, Paper 2.

[79] Ol, M. V., Gharib, M., "*The passage toward stall of nonslender delta wings at low Reynolds number*", AIAA Paper 2001-2843, 31st AIAA Fluid Dynamics Conference and Exhibit, 11–14 June 2001, Anaheim, CA.

[80] Taylor, G. S., Schnorbus, T., and Gursul, I., "*An Investigation of Vortex Flows over Low Sweep Delta Wings*", AIAA-2003-4021, AIAA Fluid Dynamics Conference, 26-26 June 2003, Orlando, FL.

[81] Honkan, A., Andreopoulos, J., "*Instantaneous three-dimensional vorticity measurements in vortical flow over a delta wing*", AIAA J, 1997, 35(10):1612–20.

[82] Yavuz, M. M., Elkhoury, M., Rockwell, D., "*Near-surface topology and flow structure on a delta wing*", AIAA J, 2004, 42(2):332–40.

[83] Miau, J. J., Kuo, K. T., Liu, W. H., Hsieh, S. J., Chou, J. H., and Lin, C.K., "*Flow developments above 50-degree sweep delta wings with different leading-edge profiles*", J Aircraft, 1995, 32(4):787–94.

[84] McClain, A., "*Aerodynamics of nonslender delta wings*", Master of Phil. Thesis, University of Bath, Department of Mechanical Engineering, March 2004.

[85] Kawazoe, H., Nakamura, Y., Ono, T., Ushimaru, Y., "*Static and total pressure distributions around a thick delta wing with rounded leading-edge*", AIAA-94-2321, 25th AIAA Plasmadynamics and Lasers Conference, 20–23 June 1994, Colorado Springs, CO.

[86] Kegelman, J. T., Roos, F. W., "*Effects of leading-edge shape and vortex burst on the flowfield of a* 70° *sweep delta wing*", AIAA Paper No. 89-0086, AIAA 27th Aerospace Sciences Meeting, Reno, NV, January 1989.

[87] Verhaagen, N. G., "*Leading-Edge Radius Effects on Aerodynamic Characteristics of 50-degreeree Delta Wing*", Journal of Aircraft, Vol. 49, No. 2, March-April 2012.

[88] Canpolat, C., Yayla, S., Sahin, B., and Akilli, H., "*Dye Visualization of the Flow Structure over a Yawed Nonslender Delta Wing*", Journal of Aircraft, Vol 46, No. 5, September-October 2009.

[89] Yayla, S., “*Flow Characteristics of Diamond and Lambda Wings at Different Flight Conditions*”, Ph.D. Thesis, Department of Mechanical Engineering, Cukurova University, Turkey, 2009.

[90] Elkhoury, M., and Rockwell, D., “*Visualized Vortices on UCAV Planform: Effect of Reynolds Number*”, Journal of Aircraft, Vol. 41, No. 5, 2004, pp. 1244–1247.

[91] Elkhoury, M., Yavuz, M. M., and Rockwell, D., “*Near-Surface Topology of Unmanned Combat Air Vehicle Planform: Reynolds Number Dependence*”, Journal of Aircraft, Vol. 42, No. 5, September-October 2005.

[92] Mitchell, A.M., Delery, J., “*Research into vortex breakdown control”,* Progress in Aerospace Sciences, Vol. 37, No. 4, 2001, pp. 385-418.

[93] Taylor, G., Kroker, A., and Gursul, I., “*Passive Flow Control over Flexible Nonslender Delta Wings*”, AIAA 43rd Aerospace Sciences Meeting and Exhibit Conference, Reno, NV, AIAA-05-0865, January 2005.

[94] Taylor, G., Wang, Z., Vardaki, E., and Gursul, I., “*Lift Enhancement over Flexible Delta Wings”,* AIAA Journal, Vol. 45, No. 12, December 2007.

[95] Vardaki, E., Gursul, I., and Taylor, G., “*Physical Mechanisms of Lift Enhancement for Flexible Delta Wings*”, AIAA-2005-0867, 43rd Aerospace Sciences Meeting and Exhibit, 10-13 January 2005, Reno, NV.

[96] Myose, R. Y., Hayashibara, S., Yeong, P. C., Miller, L.S., “*Effects of canards on delta wing vortex breakdown during dynamic pitching*”, J Aircraft, 1997, 34(2):168–73.

[97] Spedding, G.R., Maxworthy, T., Rignot, E., “*Unsteady vortex flows over delta wings*”, Proceedings of the second AFOSR workshop on unsteady and separated flows, Colorado Springs, CO: US Air Force Academy; 1987, pp. 283–287.

[98] Lamar, J. E., and Campbell, J. F., “*Vortex Flaps – Advanced Control Devices for Supercruise Fighters*”, Aerospace America, January 1984, pp. 95-99.

[99] Klute, S. M., Rediniotis, O. K., Telionis, D.P., *"Flow control over delta wings at high angles of attack",* 11th AIAA Applied Aerodynamics Conference, AIAA-93-3494, August 1993.

[100] Bucholz, M.D., Tso J., *"Lift Augmentation on Delta Wing with Leading-Edge Fences and Gurney Flap"*, Journal of Aircraft, Vol. 37, No. 6, November–December 2000.

[101] Wood, N. J., Roberts, L., and Celik, Z., *"Control of Asymmetric Vortical Flow over Delta Wings at High Angles of Attack*", Journal of Aircraft, vol.27, no. 5, May 1990, pp.429-435.

[102] Greenwell, D. I., Wood, N.J., "*Roll Moment Characteristics of Asymmetric Tangential Leading-Edge Blowing on a Delta Wing*", Journal of Aircraft, Vol.31, No.1, Jan-Feb 1994.

[103] Bean, D. E., Wood, N.J., "*Experimental Investigation of Twin-Fin Buffeting and Suppression*", Journal of Aircraft, Vol.33, No.4, July-August 1996.

[104] McCormick, S., and Gursul, I., *"Effect of Shear Layer Control on Leading Edge Vortices"*, Journal of Aircraft, vol.33, no.6, November-December 1996, pp.1087-1093.

[105] Gad-El-Hak, M., and Blackwelder, R. F., "*Control of the Discrete Vortices from a Delta Wing*", AIAA Journal, Vol. 25, No. 8, 1987, pp.1042-9.

[106] Gu, W., Robinson, O., and Rockwell, D., "*Control of Vortices on a Delta Wing by Leading-Edge Injection*", AIAA Journal, vol. 31, no.7, July 1993, pp.1177-1186.

[107] Ferman, M. A., Huttsell, L. J., and Turner, E. W., "*Experiments with Tangential Blowing to Reduce Buffet Response on an F-15 Model*", Journal of Aircraft, Vol. 41, No. 4, July–August 2004.

[108] Cui, Y. D., Lim, T. T., and Tsai H. M., "*Control of Vortex Breakdown Over a Delta Wing Using Forebody Slot Blowing*", AIAA Journal, Vol. 45, No. 1, 2007, pp. 110–117.
doi:10.2514/1.22575

[109] Cui, Y. D., Lim, T. T., and Tsai H. M., "*Forebody Slot Blowing on Vortex Breakdown and Load Over a Delta Wing*", AIAA Journal, Vol. 46, No. 3, March 2008.

[110] Vorobieff, P., Rockwell, D., "*Vortex Breakdown on Pitching Delta Wing: Control by Intermittent Trailing Edge Blowing*", AIAA Journal, Vol. 36, No. 4, 1998, pp. 585-589.

[111] Johari, H., Olinger, D.J. and Fitzpatric, K.C., "*Delta Wing Vortex Control via Recessed Angled Spanwise Blowing*", Journal of Aircraft, vol.32, no.4, 1995, pp.804-810.

[112] Johari, H., and Moreira, J., "*Delta Wing Vortex Manipulation Using Pulsed and Steady Blowing During Ramp-Pitching",* Journal of Aircraft, Vol. 33, No. 2, March-April 1996.

[113] Maines B.H., Moeller, B. and Redinitiois O.K., "*The Effects of Leading Edge Suction on Delta Wing Vortex Breakdown.*" 37th AIAA Aerospace Sciences Meeting and Exhibit, Reno, NV, AIAA-99-0128, January 11-14, 1999.

[114] Badran, B., McCormick, S., and Gursul, I., "*Control of Leading-Edge Vortices with Suction*", J Aircraft, 1997, Vol. 35, No. 1, pp. 163-165.

[115] Hummel, D., "*Zur umstronmung scharfkantiger schlanker deltaflugel bei grossen anstellwinkeln*." Z. Flugwiss 1967; 15(10): 367-85.

[116] Owens, D. B., and Perkins, J., "*Vortex Suppression on Highly Swept Wings by Suction Boundary Layer Contro*", 33rd AIAA Aerospace Sciences Meeting and Exhibit, Reno, NV, AIAA-95-0683, January 1995.

[117] Helin, H., and Watry, C. W., "*Effects of Trailing-Edge Jet Entrainment on Delta Wing Vortices*", AIAA Journal, Vol. 32, No. 4, 1994, pp. 802–804.

[118] Shih, C., and Ding, Z., "*Trailing-Edge Jet Control of Leading Edge Vortices of a Delta Wing*", AIAA Journal, Vol. 34, No. 7, 1996, pp. 1447–1456.

[119] Mitchell, A. M., Molton, P., Barberis, D., and Délery, J., "*Control of Leading-Edge Vortex Breakdown by Trailing-Edge Injection*", Journal of Aircraft, Vol. 39, No. 2, 2002, pp. 221–226.

[120] Phillips, S., Lambert, C., and Gursul, I., *“Effect of a Trailing-Edge Jet on Fin Buffeting”* Journal of Aircraft, Vol. 40 No.3 pp. 590 – 599, 2003.

[121] Nawrocki, D., “*Differential and Vectored Trailing-Edge Jet Control of Delta Wing Vortices*”, AIAA Paper 95-0008, Jan. 1995.

[122] Wang, J. J., Li, Q. S., and Liu, J. Y., *“Effects of Vectored Trailing Edge Jet on Delta Wing Vortex Breakdown”,* Experiments in Fluids, Vol. 34, 2003, pp. 651-654.

[123] Deng, Q., Gursul, I., “*Vortex breakdown over a delta wing with oscillating leading-edge flaps*”, Exp Fluids, 1997, 23:347–52.

[124] Yavuz, M. M. and Rockwell, D., 2006, “*Control of Flow Structure on Delta Wing with Steady Trailing Edge Blowing”*, AIAA Journal, Vol. 44, No.3, March 2006, pp. 493-501.

[125] Yavuz, M. M. and Rockwell, D., 2006, *“Identification and Control of Three-Dimensional Separation on Low Swept Delta Wing”* AIAA Journal, Vol. 44, Nov 2006, pp. 2805-2811.

[126] Williams, N.M., Wang, Z. and Gursul, I. *“Active Flow Control on a Nonslender Delta Wing”* AIAA Journal of Aircraft, Vol. 45, No. 6, November - December 2008.

[127] Wang, Z., Jiang, P. and Gursul, I. “*Effect of Thrust-Vectoring Jets on Delta Wing Aerodynamics*”, AIAA Journal of Aircraft, Vol. 44, No. 6, November-December 2007.

[128] Jiang, P., Wang, Z., and Gursul, I., “*Effects of Unsteady Trailing-Edge Blowing on Delta Wing Aerodynamics*” AIAA Journal of Aircraft, Vol. 47, No. 2, March-April 2010.

[129] Vardaki, E., Wang,Z., Gursul, I., “*Flow Reattachment and Vortex Re-formation on Oscillating Low-Aspect-Ratio Wings*” AIAA Journal, Vol.56, No.6, June 2008.

[130] Ozgoren, M., Sahin, B., Rockwell, D., “*Perturbations of a Delta Wing: Control of Vortex Breakdown and Buffeting*”, Journal of Aircraft, Vol. 43, No.6, November-December 2001.

[131] Yılmaz, T.O., Rockwell, D., “ *Flow structure on a three - dimesional wing subjected to small amplitude perturbations*” Exp Fluids, No.47, pp. 579-597, 2009.

[132] W. Merzkirch: “*Flow Visualization”*, Springer Handbook of Experimental Fluid Mechanics, 2007.

[133] Dantec Dynamics, *“Laser Optical Measurement Systems and Sensors”,* http://www.dantecdynamics.com/laser-doppler-anemometry, July 2013.

[134] C. Saragiotis, *“Lomb normalized periodogram”,* http://www.mathworks.com/matlabcentral/fileexchange/22215-lomb-normalized-periodogram, September 2013.

[135] W.H. Press, S.A. Teukolsky, W.T. Vetterling, and B.P. Flannery, *"Numerical recipes in Fortran 77: the art of scientific computing"*, 2nd ed., vol. 1, Cambridge University Press, NY, USA, 2001.

APPENDIX A

ADDITIONAL FLOW VISUALIZATION ILLUSTRATIONS

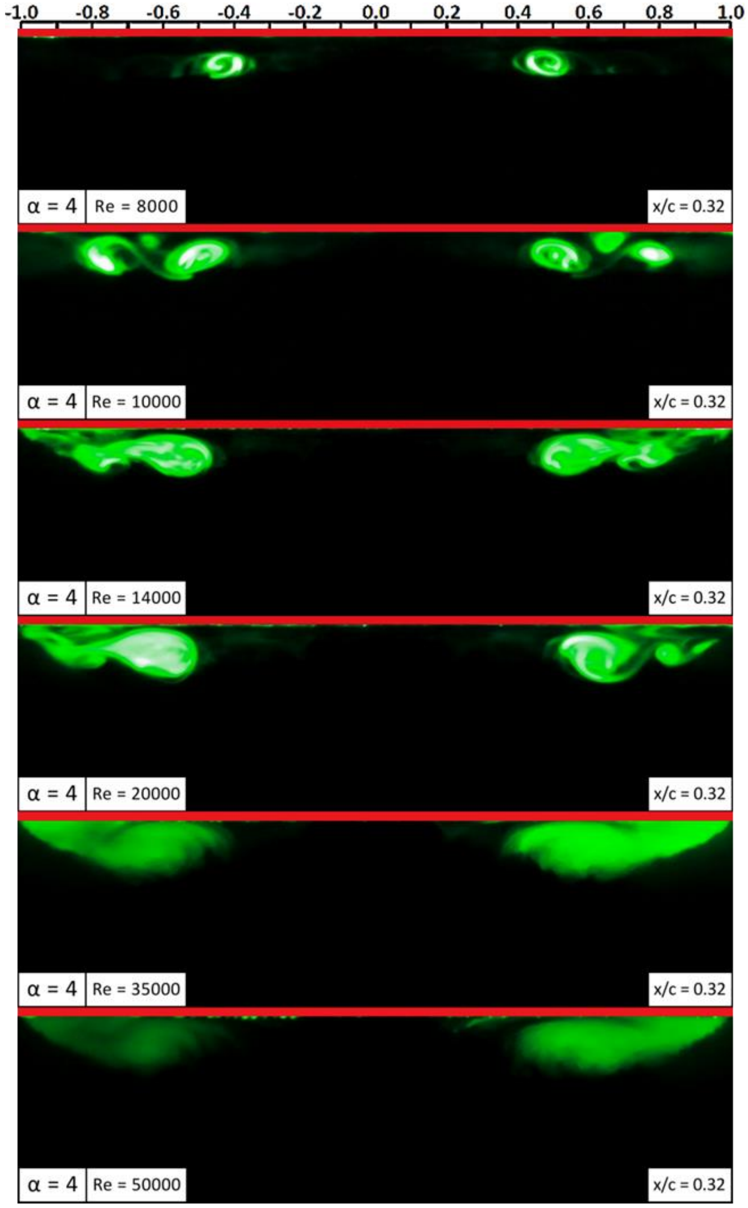

Figure A.1 Illustration of flow visualization images at a crossflow plane located at x/c = 0.32 for 4-degree angle of attack and at different Reynolds number

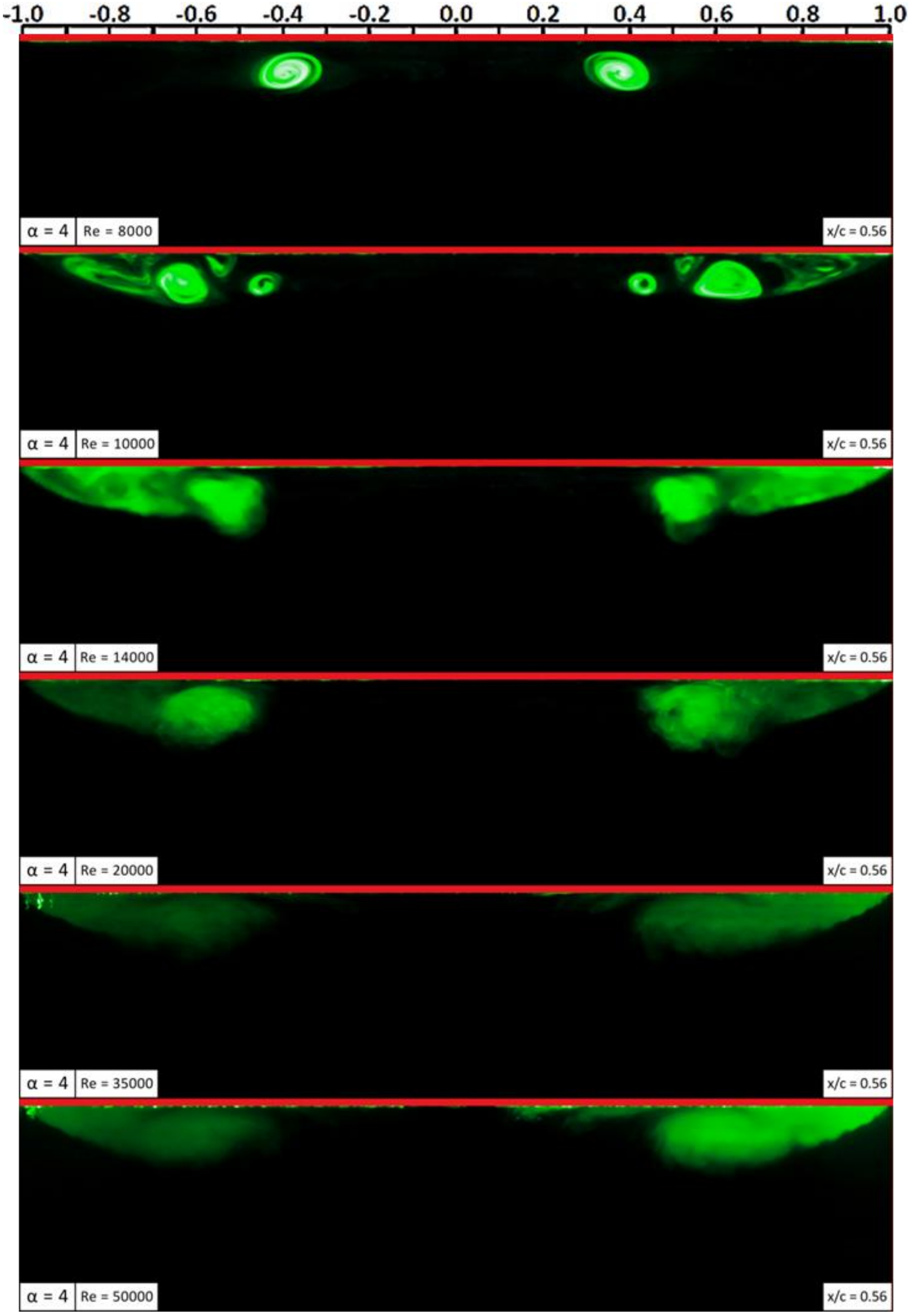

Figure A.2 Illustration of flow visualization images at a crossflow plane located at x/c = 0.56 for 4-degree angle of attack and at different Reynolds number

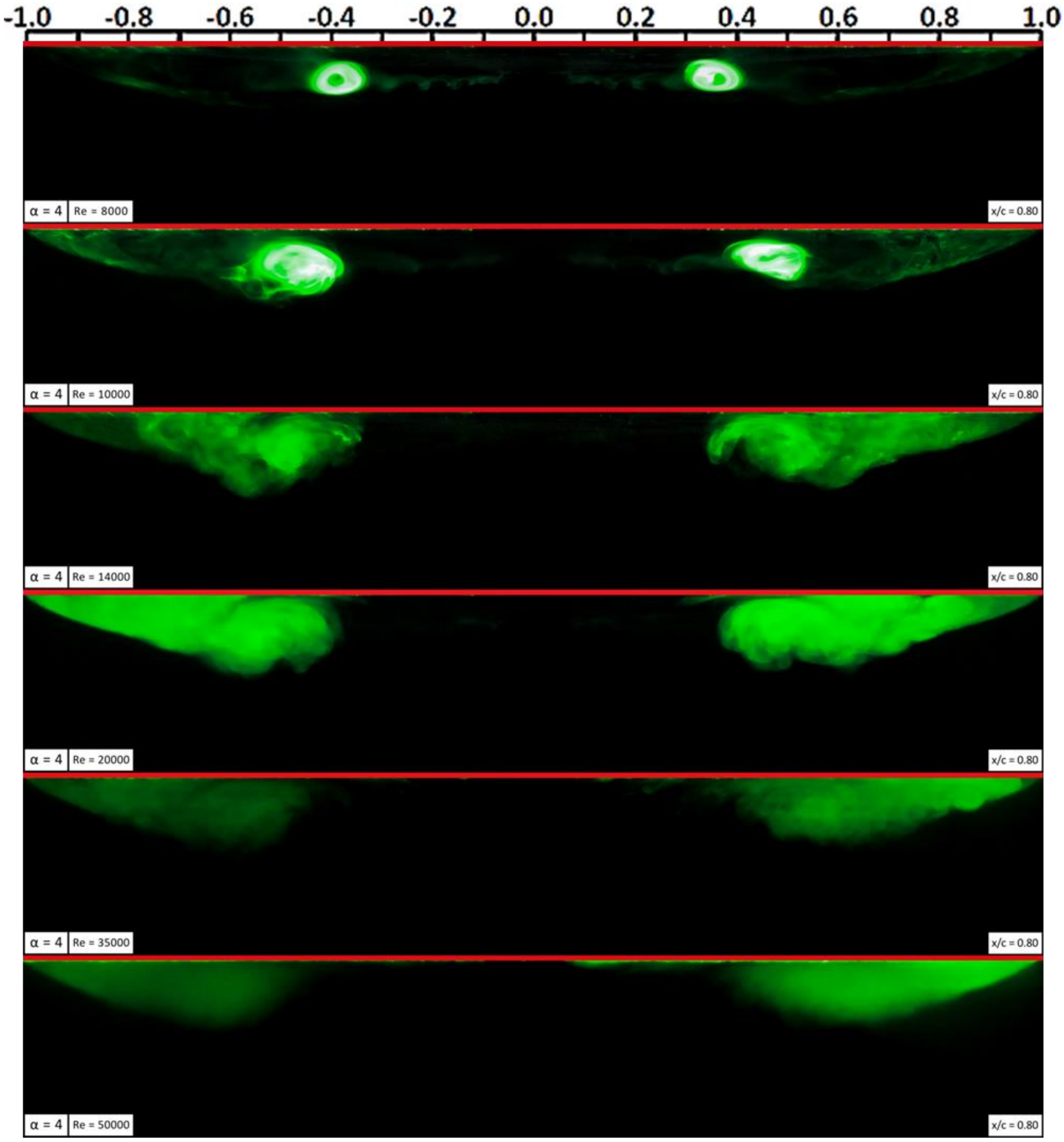

Figure A.3 Illustration of flow visualization images at a crossflow plane located at x/c = 0.80 for 4-degree angle of attack and at different Reynolds number

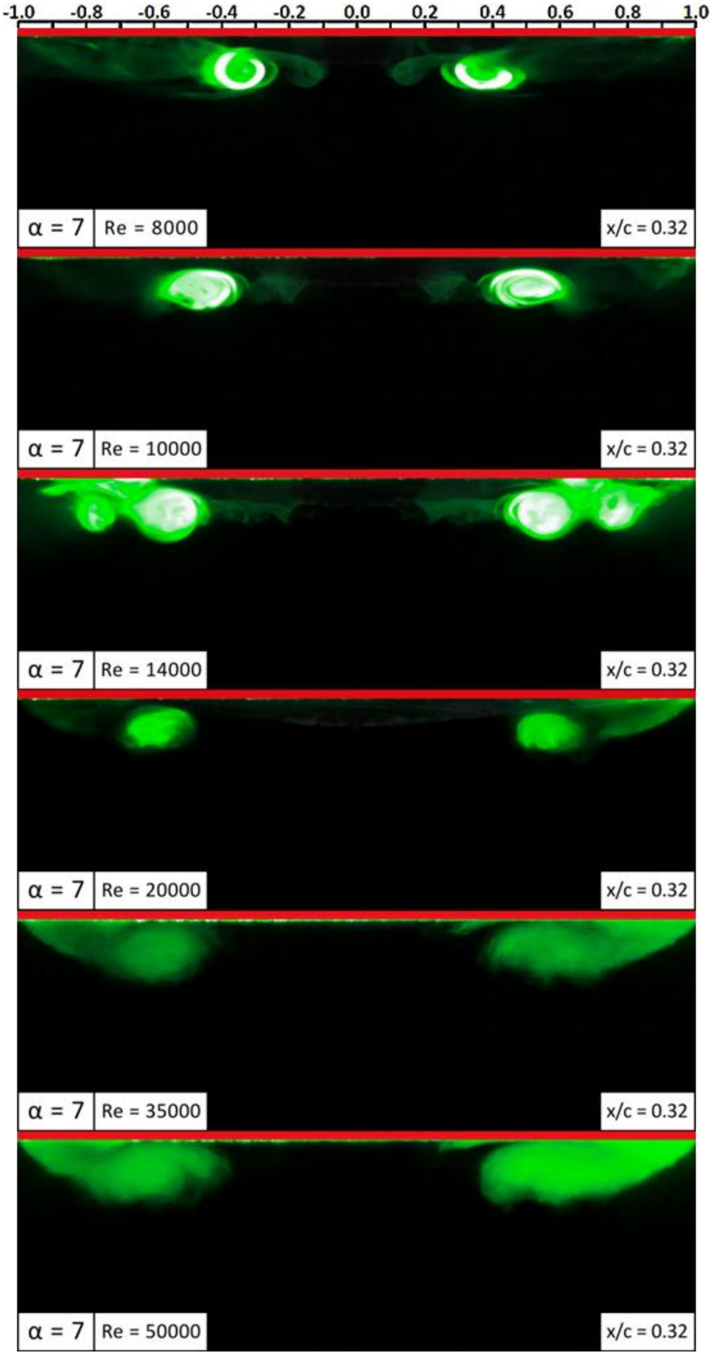

Figure A.4 Illustration of flow visualization images at a crossflow plane located at x/c = 0.32 for 7-degree angle of attack and at different Reynolds number

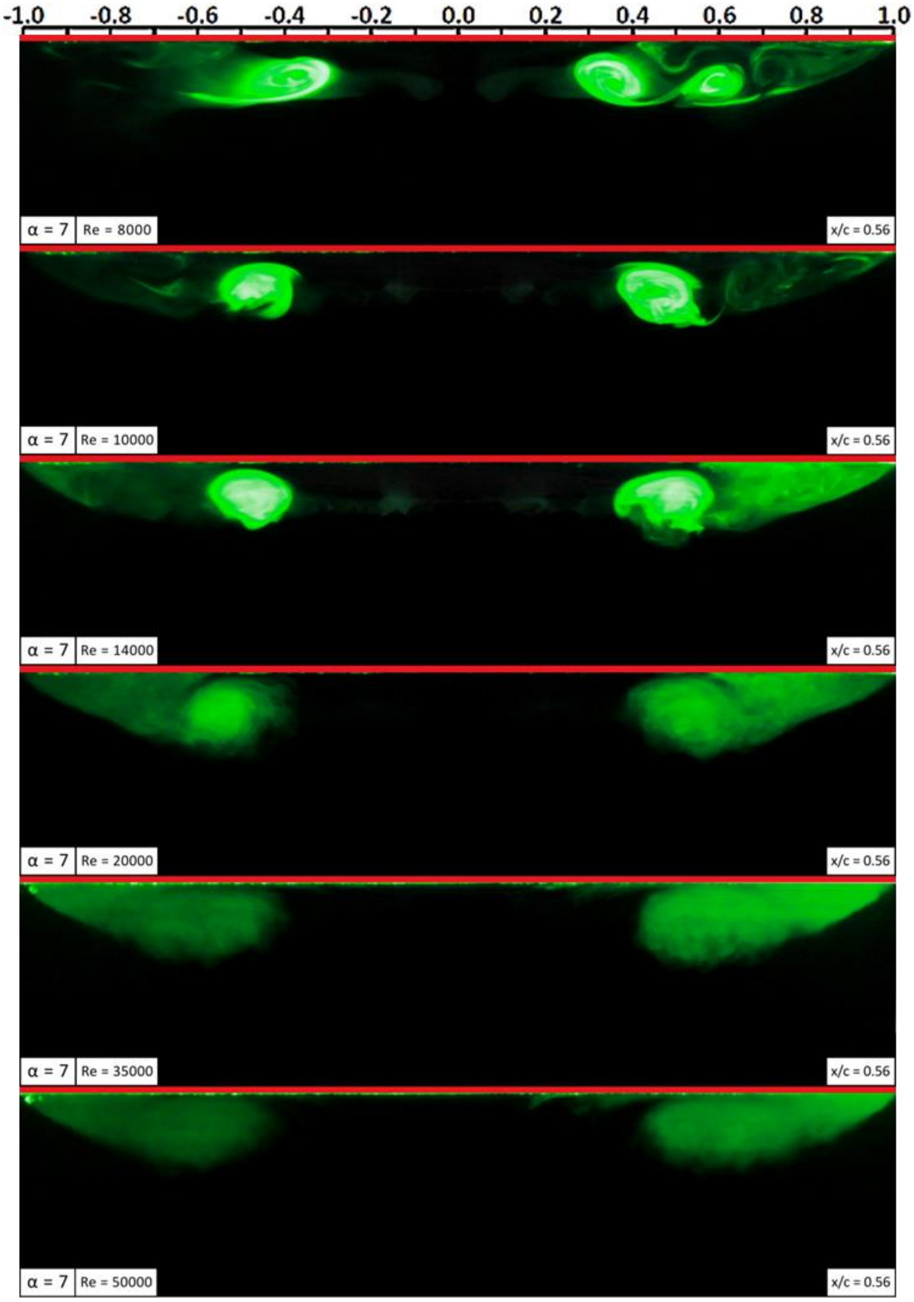

Figure A.5 Illustration of flow visualization images at a crossflow plane located at x/c = 0.56 for 7-degree angle of attack and at different Reynolds number

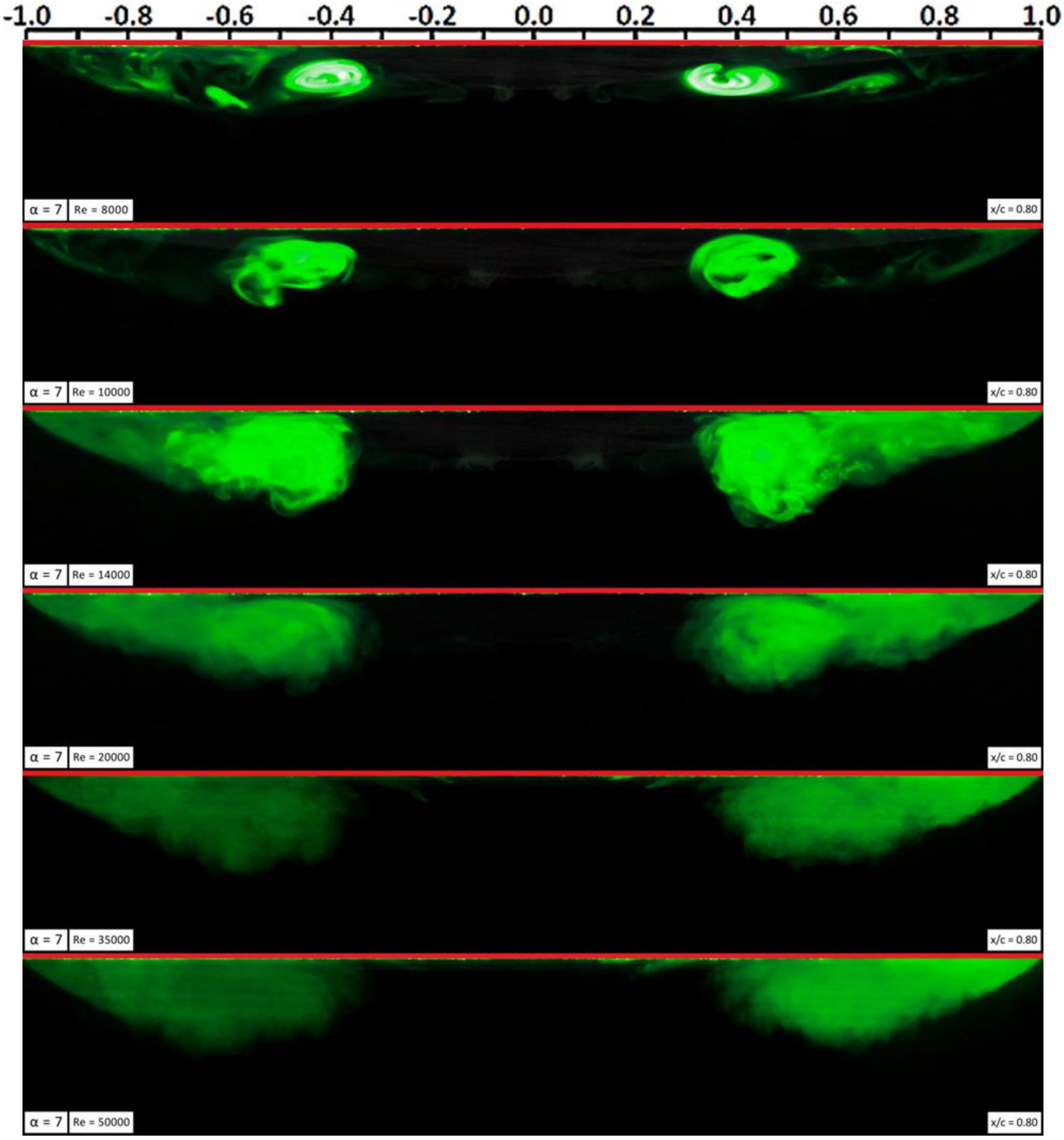

Figure A.6 Illustration of flow visualization images at a crossflow plane located at x/c = 0.80 for 7-degree angle of attack and at different Reynolds number

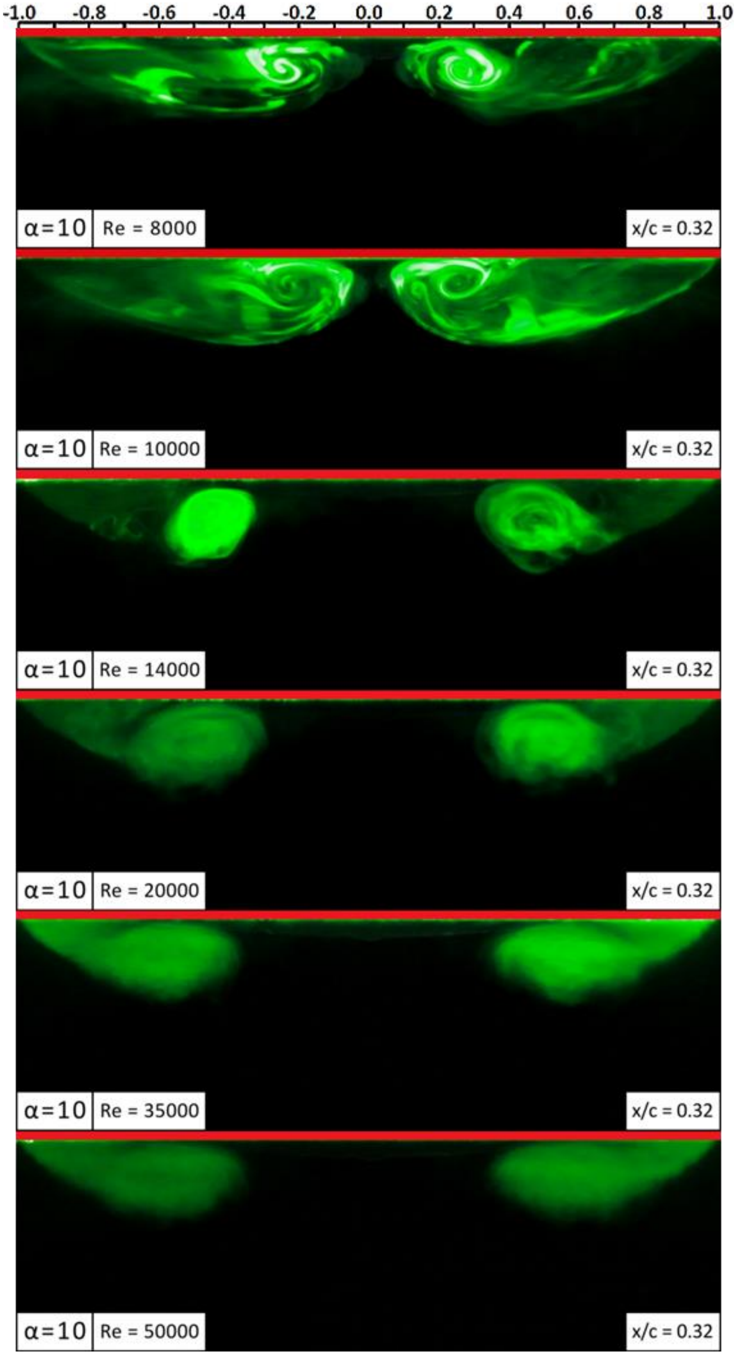

Figure A.7 Illustration of flow visualization images at a crossflow plane located at x/c = 0.32 for 10-degree angle of attack and at different Reynolds number

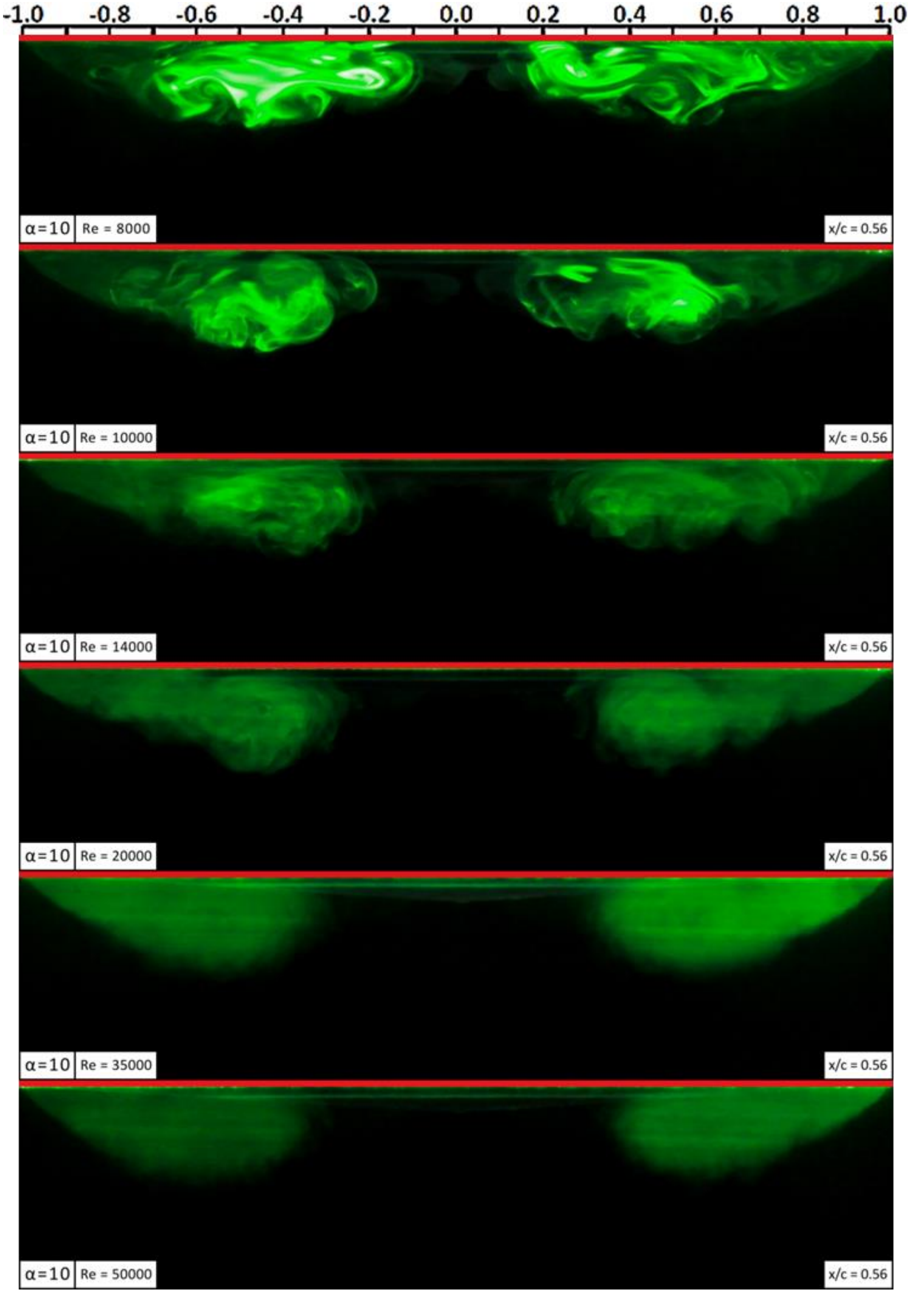

Figure A.8 Illustration of flow visualization images at a crossflow plane located at x/c = 0.56 for 10-degree angle of attack and at different Reynolds number

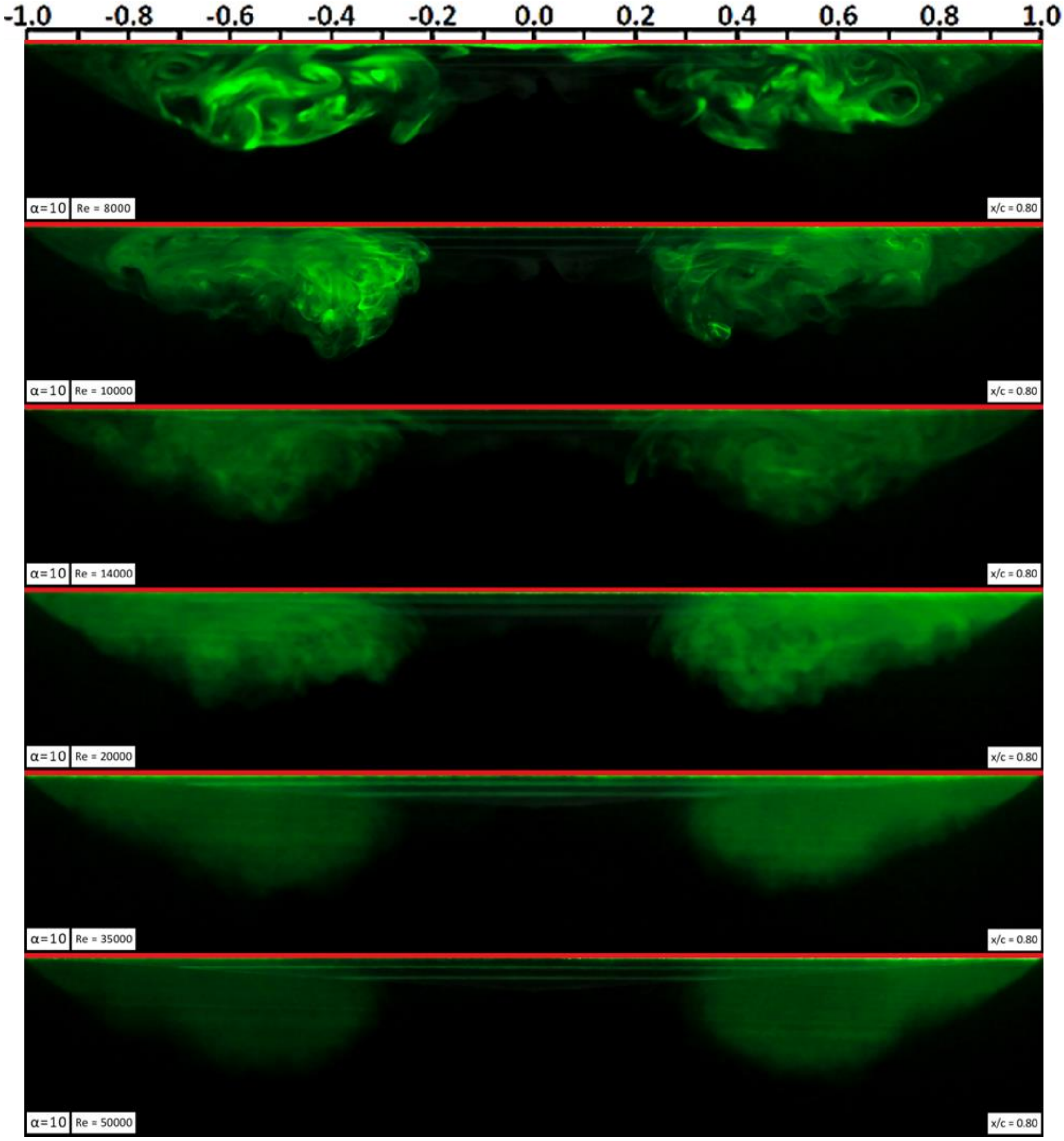

Figure A.9 Illustration of flow visualization images at a crossflow plane located at x/c = 0.80 for 10-degree angle of attack and at different Reynolds number

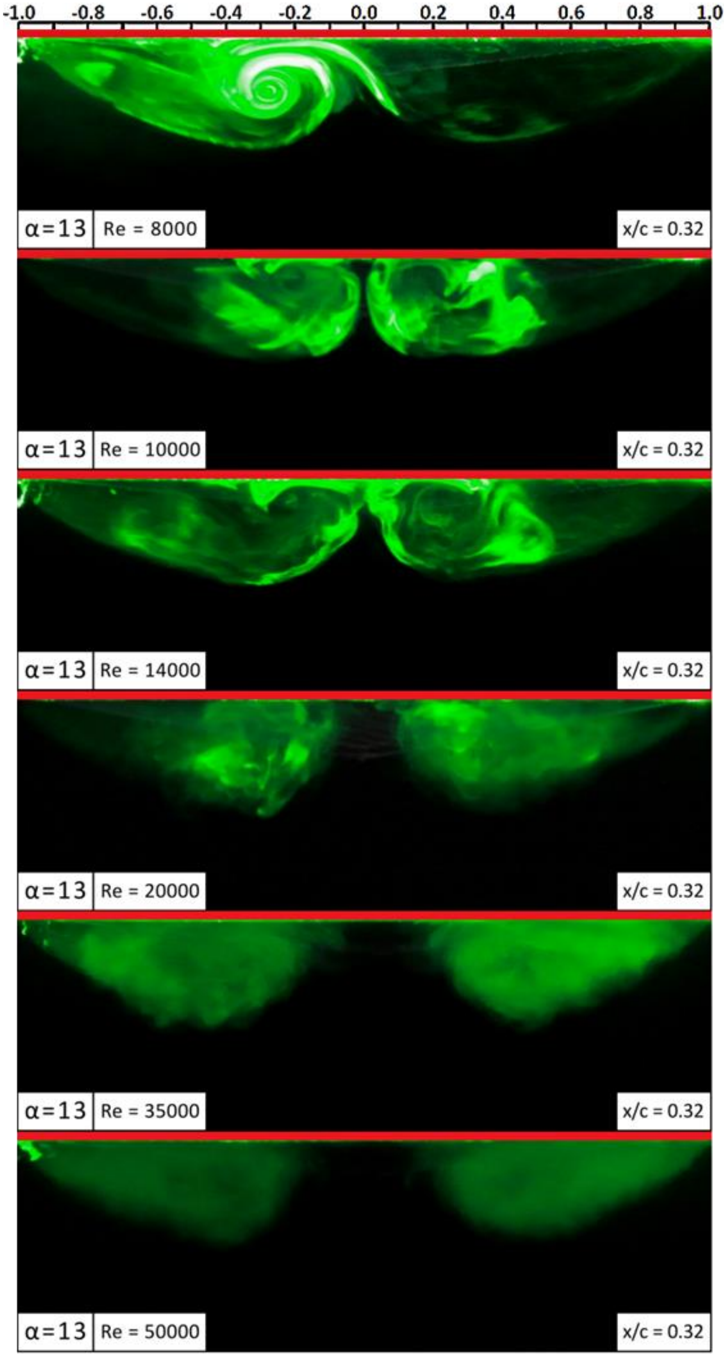

Figure A.10 Illustration of flow visualization images at a crossflow plane located at x/c = 0.32 for 13-degree angle of attack and at different Reynolds number

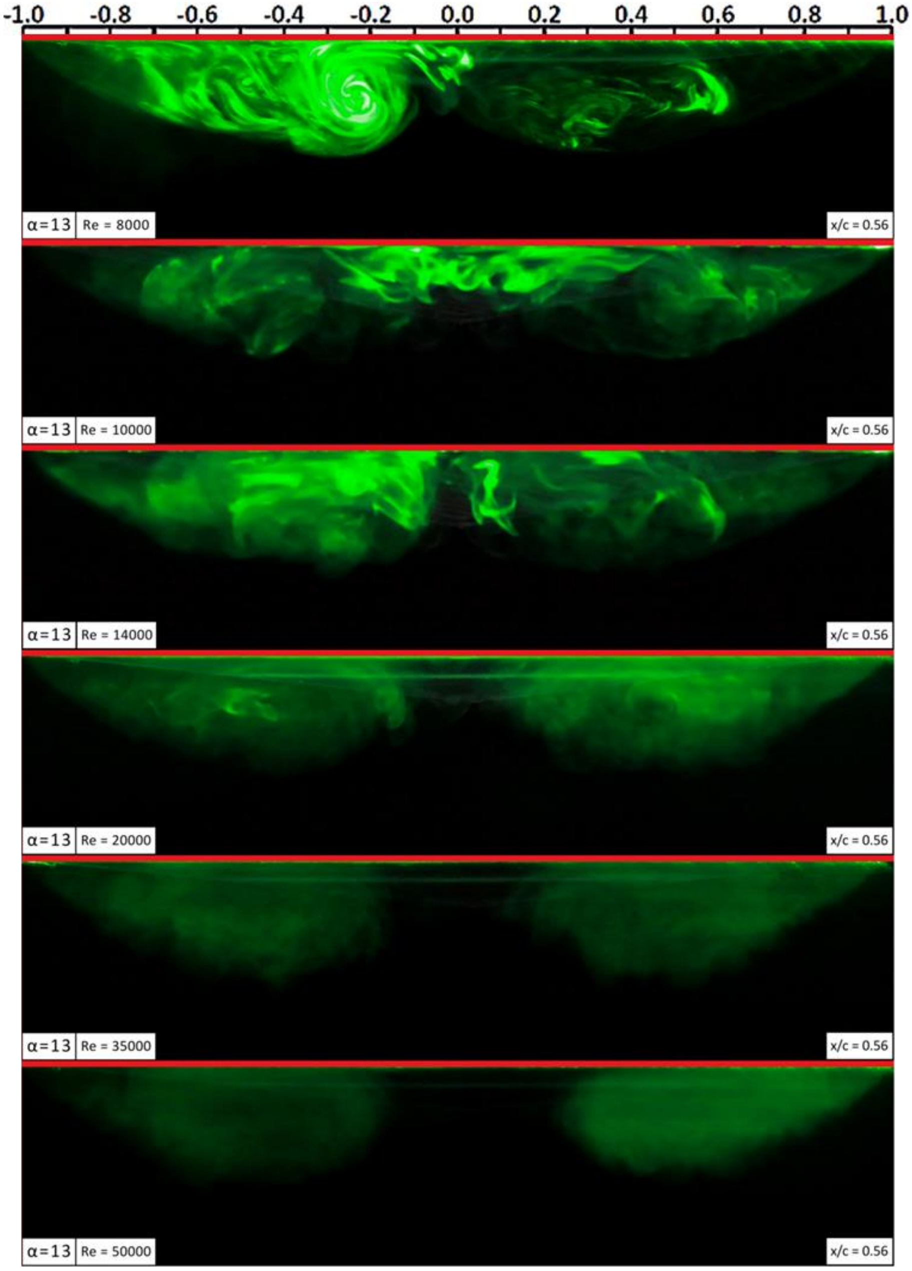

Figure A.11 Illustration of flow visualization images at a crossflow plane located at x/c = 0.56 for 13-degree angle of attack and at different Reynolds number

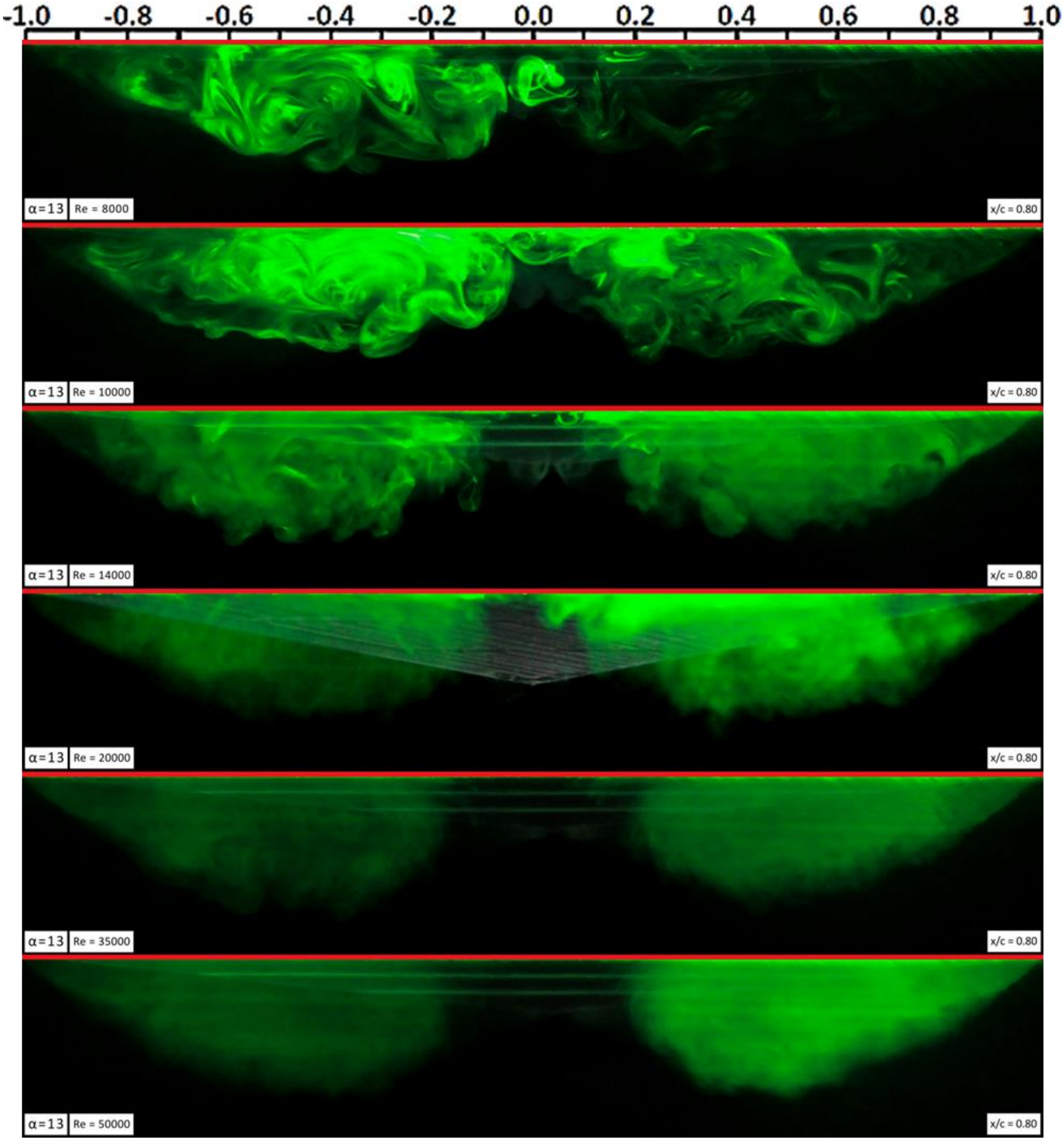

Figure A.12 Illustration of flow visualization images at a crossflow plane located at x/c = 0.80 for 13-degree angle of attack and at different Reynolds number

APPENDIX B

ADDITIONAL POWER SPECTRAL DENSITY ILLUSTRATIONS FOR PRESSURE DATA

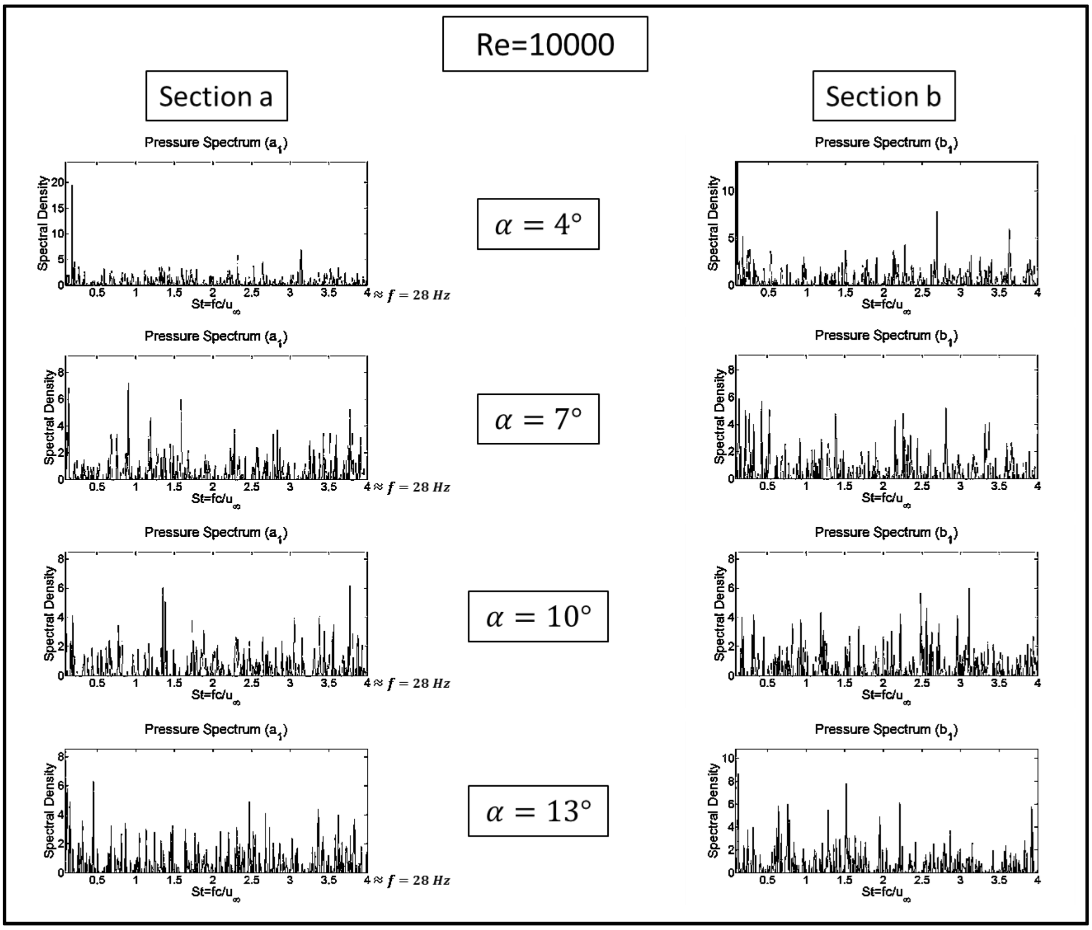

Figure B.1 Power Spectral Densities of pressure measurements at Re = 10.000 and at different angles of attack as a function of dimensionless frequency, $St = fc/U_\infty$. Measurements are taken at two different taps of first pressure measurement section where the lines of sections a and b pass

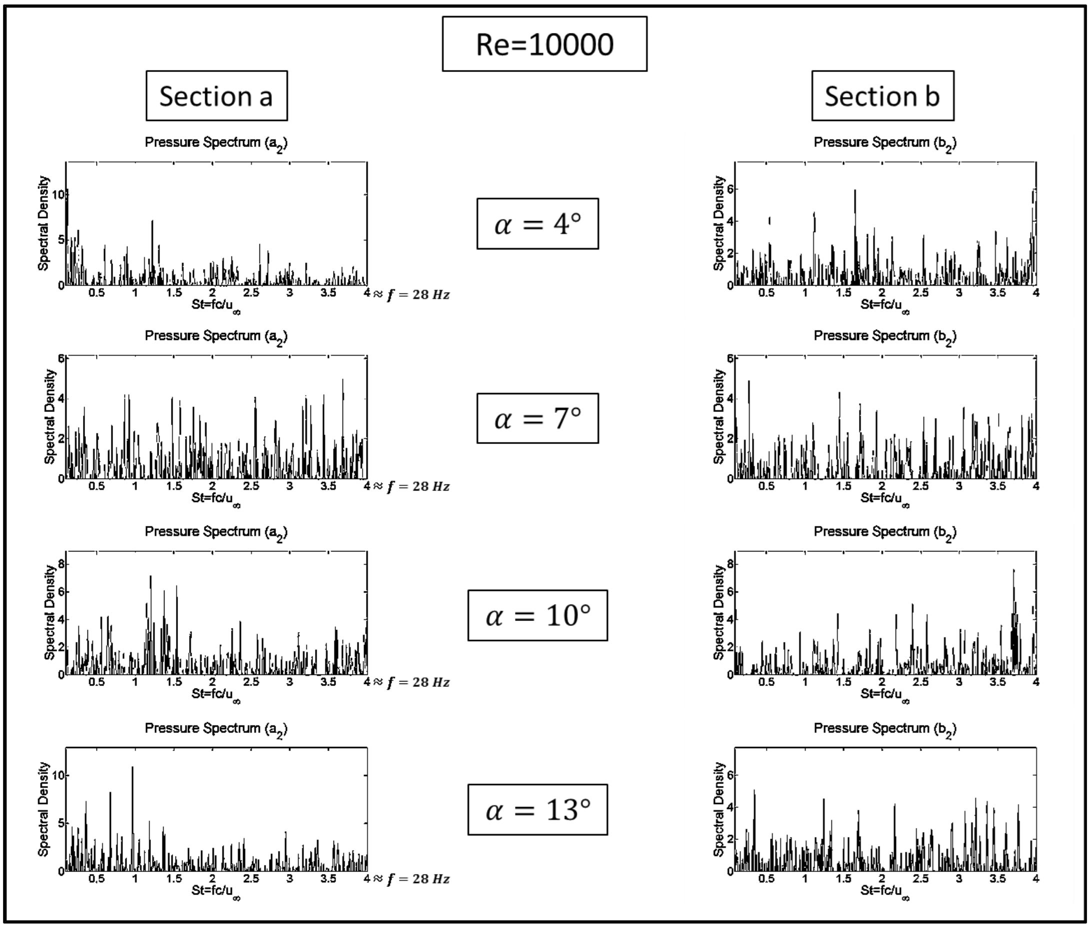

Figure B.2 Power Spectral Densities of pressure measurements at Re = 10.000 and at different angles of attack as a function of dimensionless frequency, $St = fc/U_\infty$. Measurements are taken at two different taps of second pressure measurement section where the lines of sections a and b pass

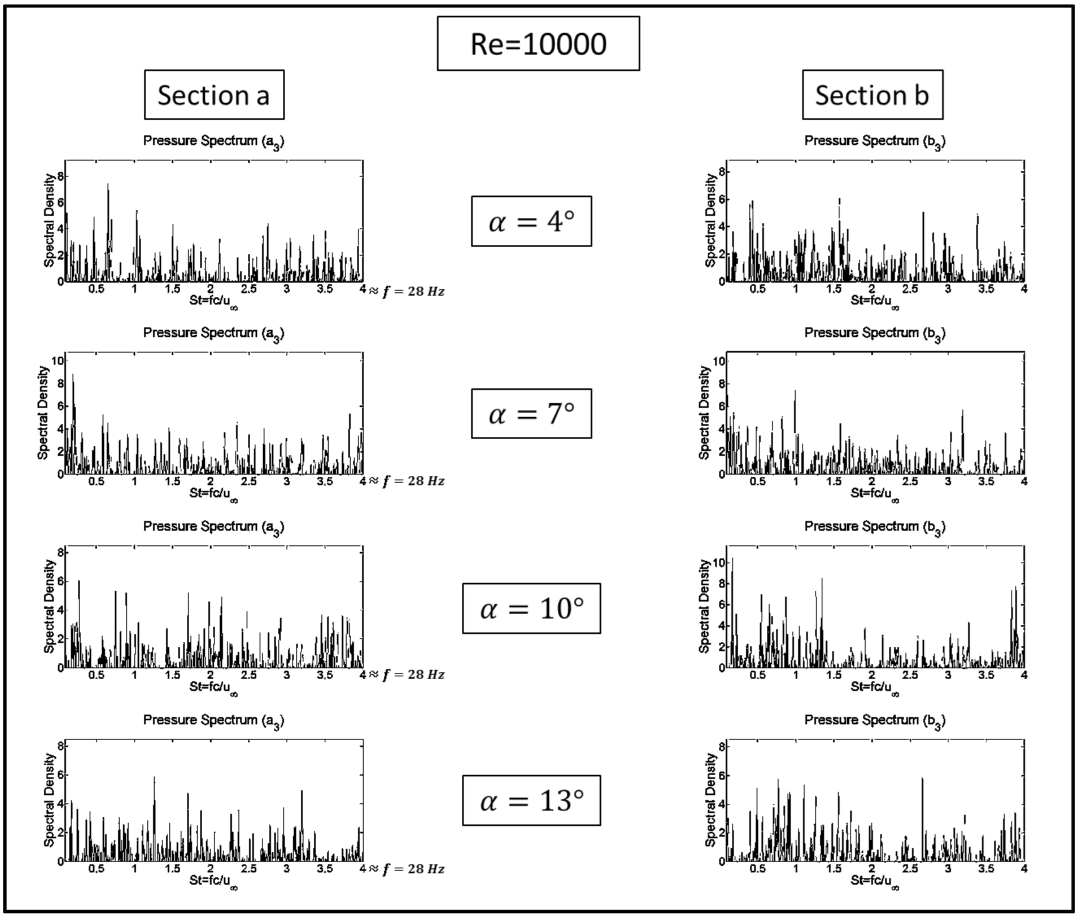

Figure B.3 Power Spectral Densities of pressure measurements at Re = 10.000 and at different angles of attack as a function of dimensionless frequency, $St = fc/U_\infty$. Measurements are taken at two different taps of third pressure measurement section where the lines of sections a and b pass

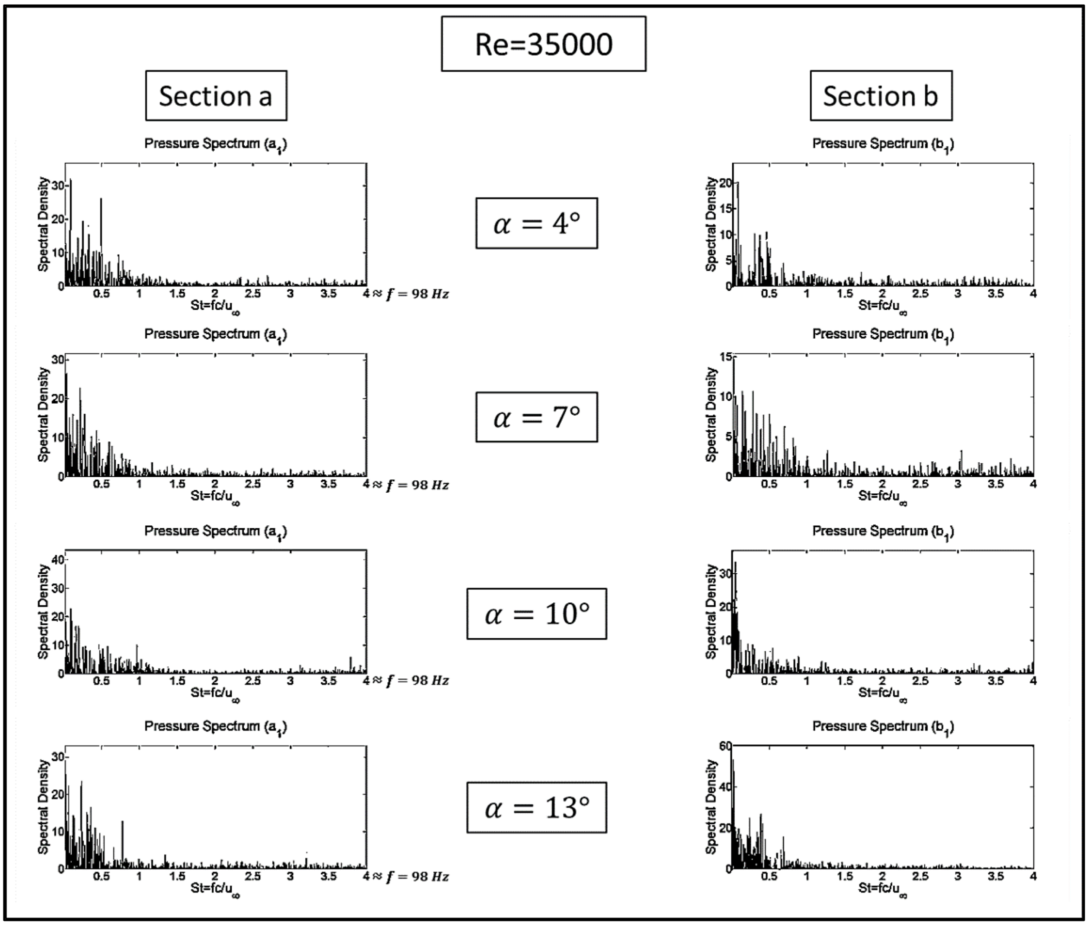

Figure B.4 Power Spectral Densities of pressure measurements at Re = 35.000 and at different angles of attack as a function of dimensionless frequency, $St = fc/U_\infty$. Measurements are taken at two different taps of first pressure measurement section where the lines of sections a and b pass

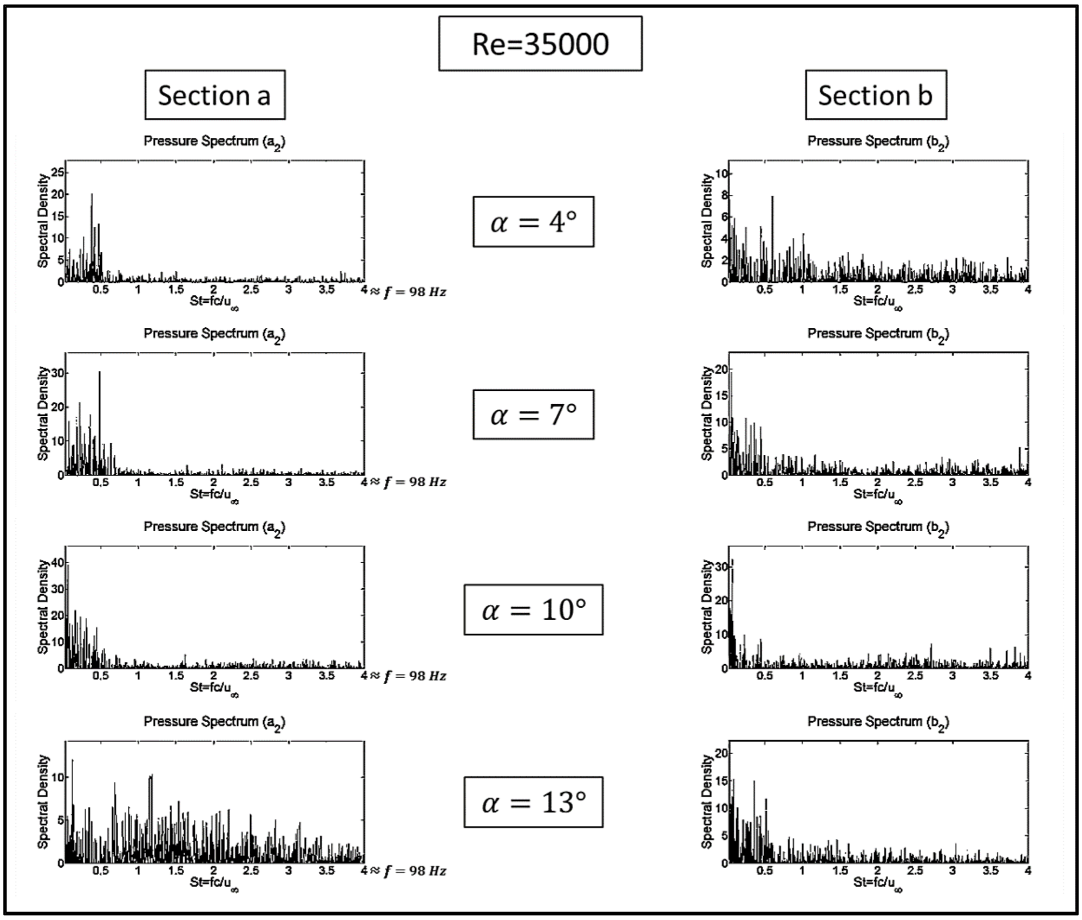

Figure B.5 Power Spectral Densities of pressure measurements at Re = 35.000 and at different angles of attack as a function of dimensionless frequency, $St = fc/U_{\infty}$. Measurements are taken at two different taps of second pressure measurement section where the lines of sections a and b pass

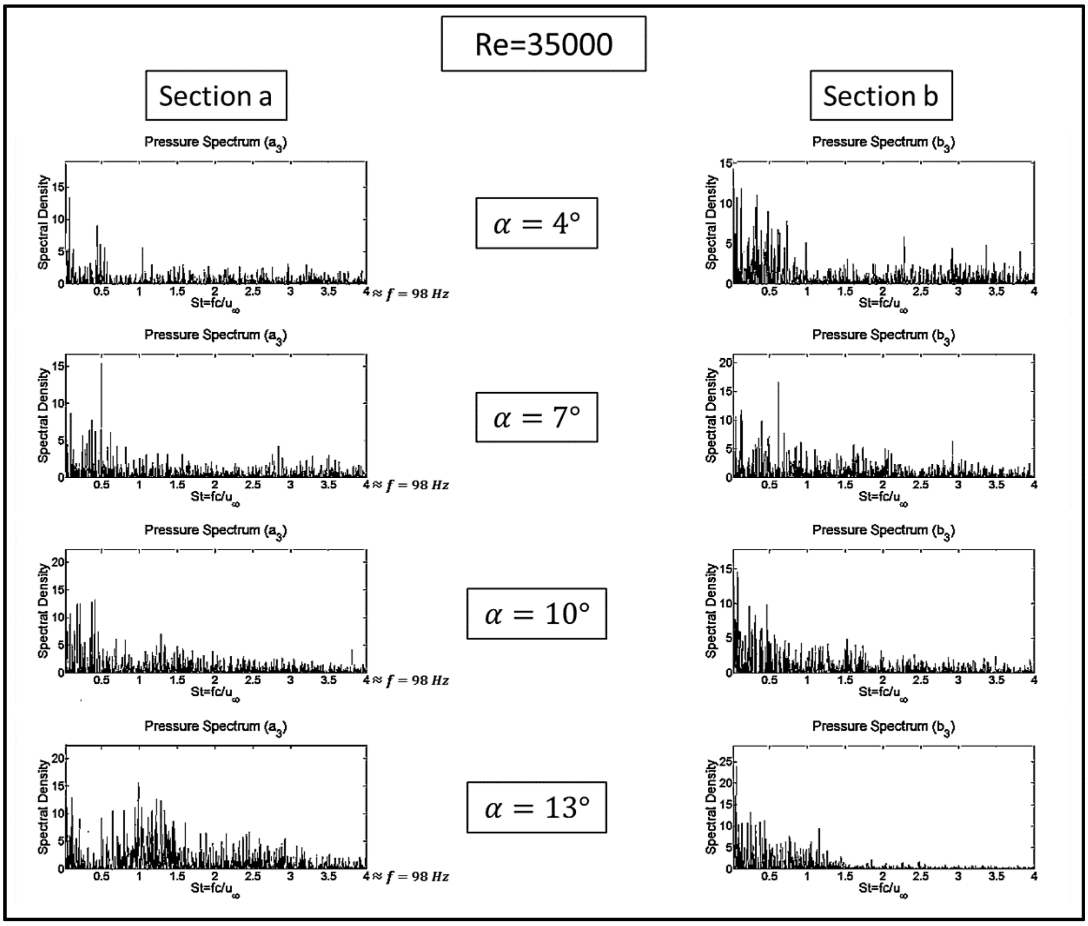

Figure B.6 Power Spectral Densities of pressure measurements at *Re* = 35.000 and at different angles of attack as a function of dimensionless frequency, $St = fc/U_\infty$. Measurements are taken at two different taps of third pressure measurement section where the lines of sections a and b pass

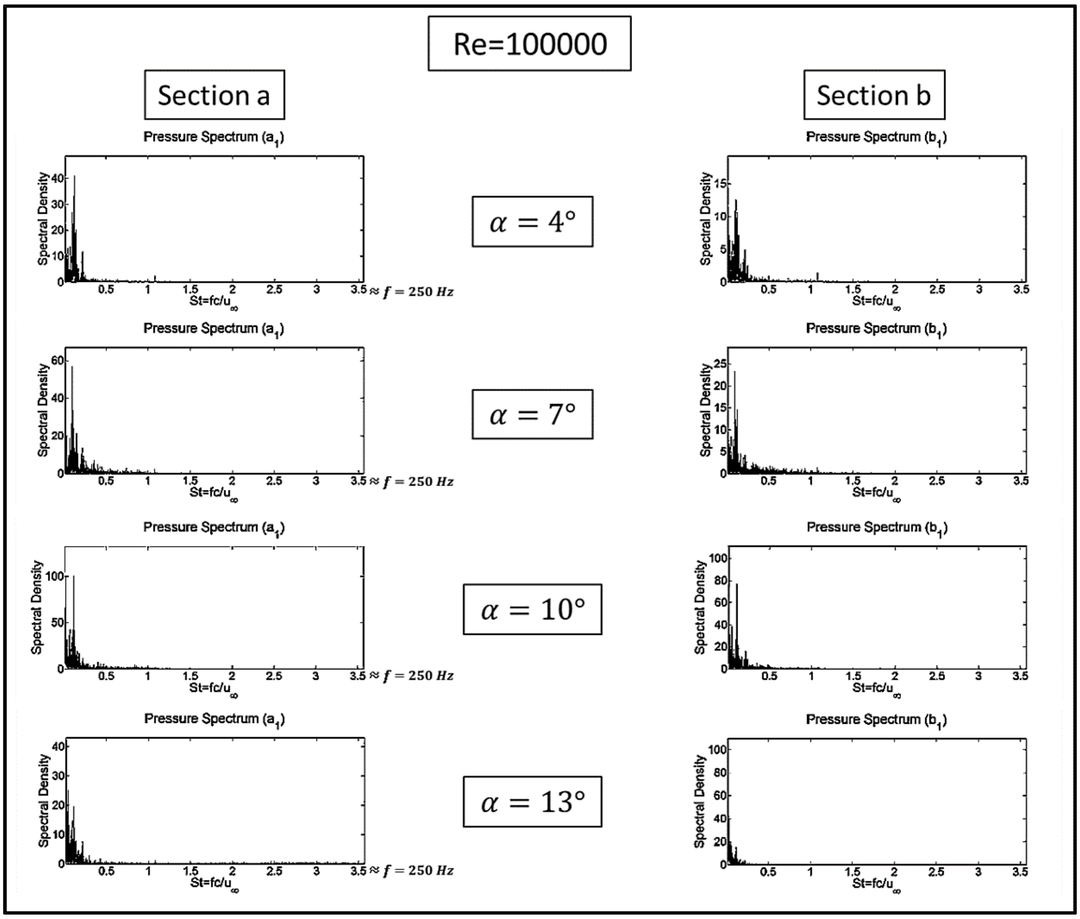

Figure B.7 Power Spectral Densities of pressure measurements at *Re* = 100.000 and at different angles of attack as a function of dimensionless frequency, $St = fc/U_\infty$. Measurements are taken at two different taps of first pressure measurement section where the lines of sections a and b pass

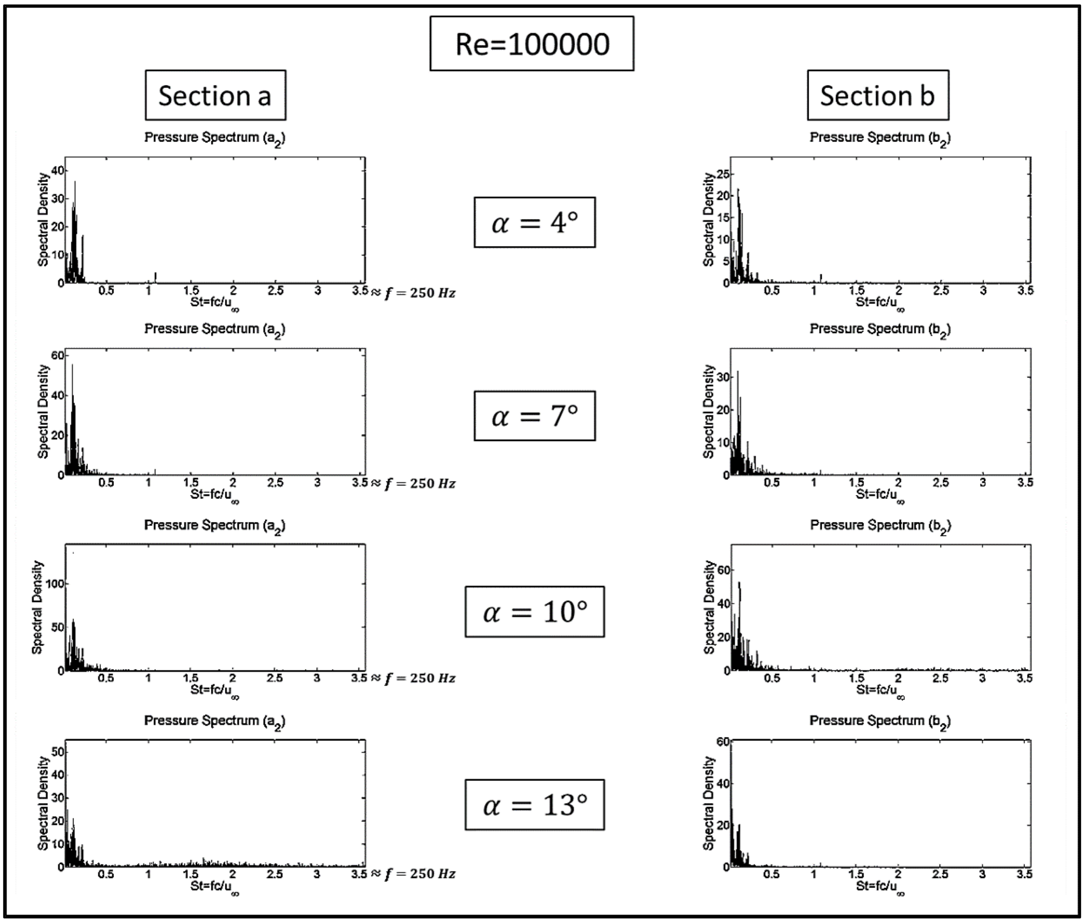

Figure B.8 Power Spectral Densities of pressure measurements at Re = 100.000 and at different angles of attack as a function of dimensionless frequency, $St = fc/U_{\infty}$. Measurements are taken at two different taps of second pressure measurement section where the lines of sections a and b pass

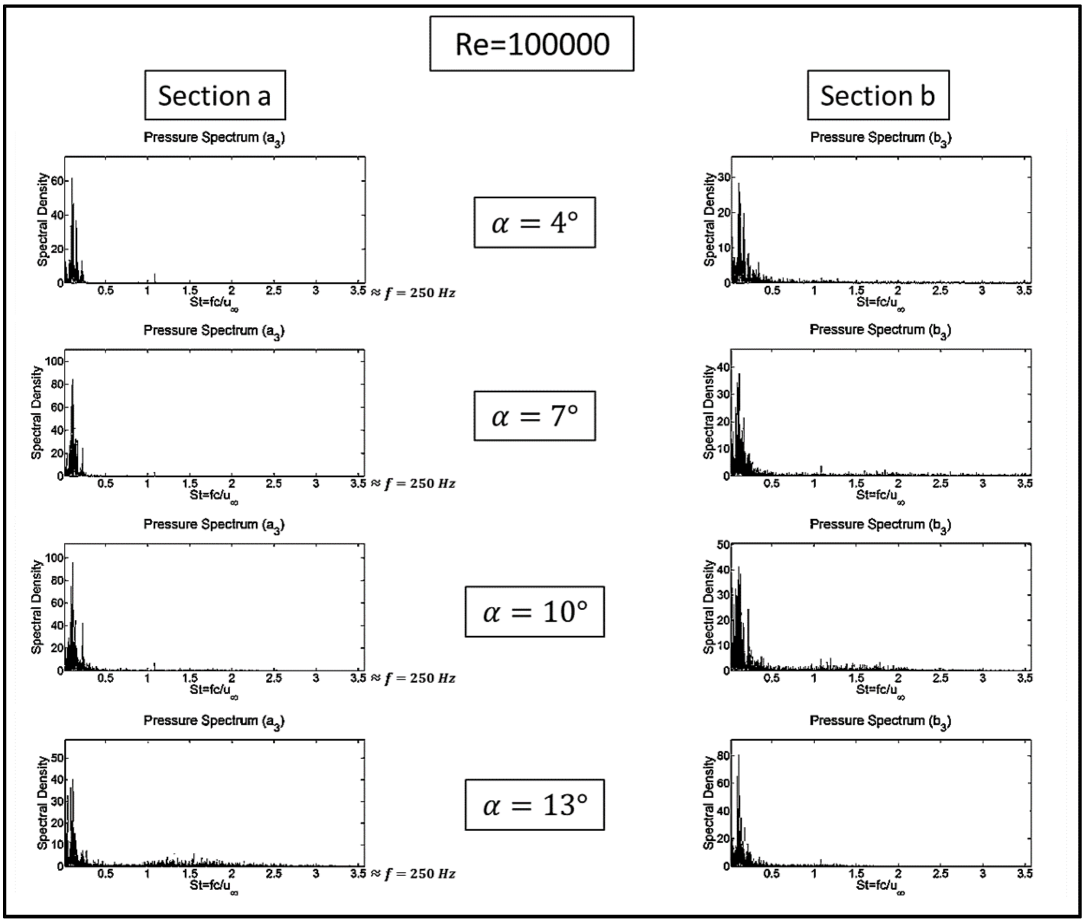

Figure B.9 Power Spectral Densities of pressure measurements at Re = 100.000 and at different angles of attack as a function of dimensionless frequency, $St = fc/U_\infty$. Measurements are taken at two different taps of third pressure measurement section where the lines of sections a and b pass

APPENDIX C

SAMPLE LDA MEASUREMENT CHARTS

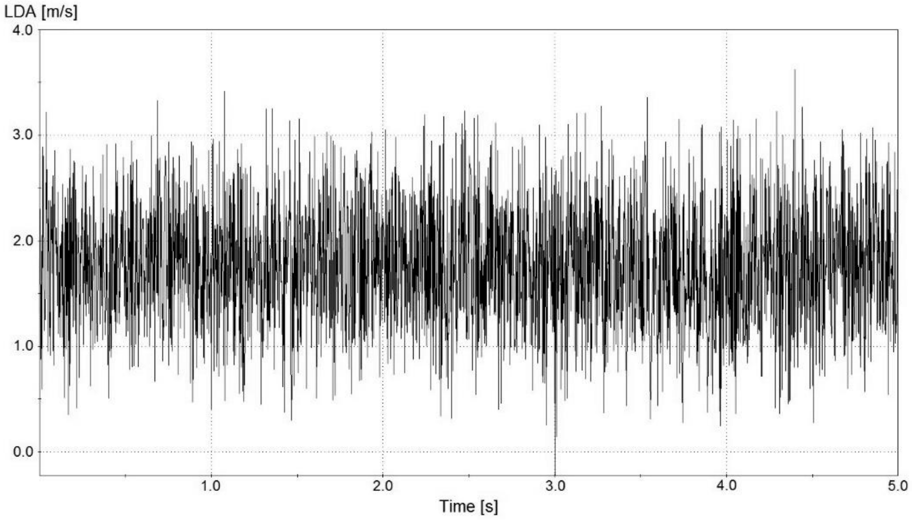

Figure C.1 Velocity measurement at vortex core on a chordwise location located at $x/c = 0.32$ in u-direction using LDA at 4 degree angle of attack and Reynolds number $Re = 10^4$

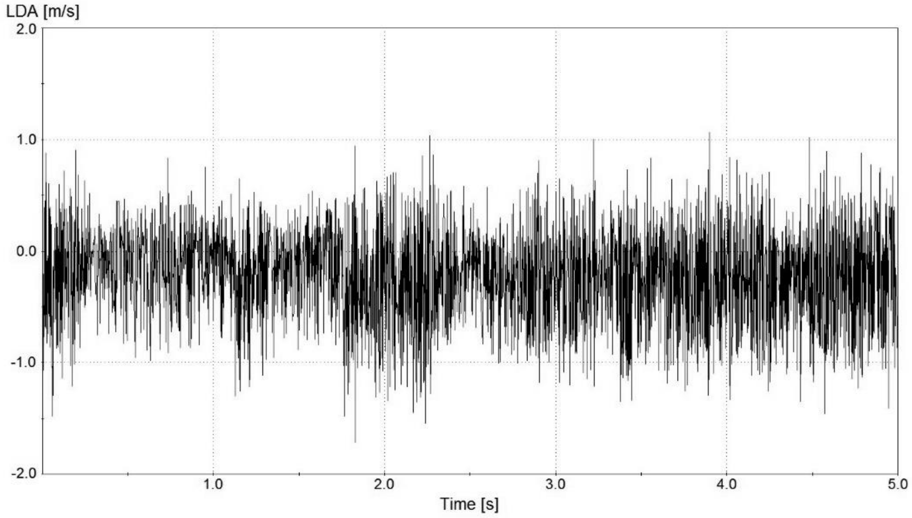

Figure C.2 Velocity measurement at vortex core on a chordwise location located at $x/c = 0.32$ in ω-direction using LDA at 4 degree angle of attack and Reynolds number $Re = 10^4$

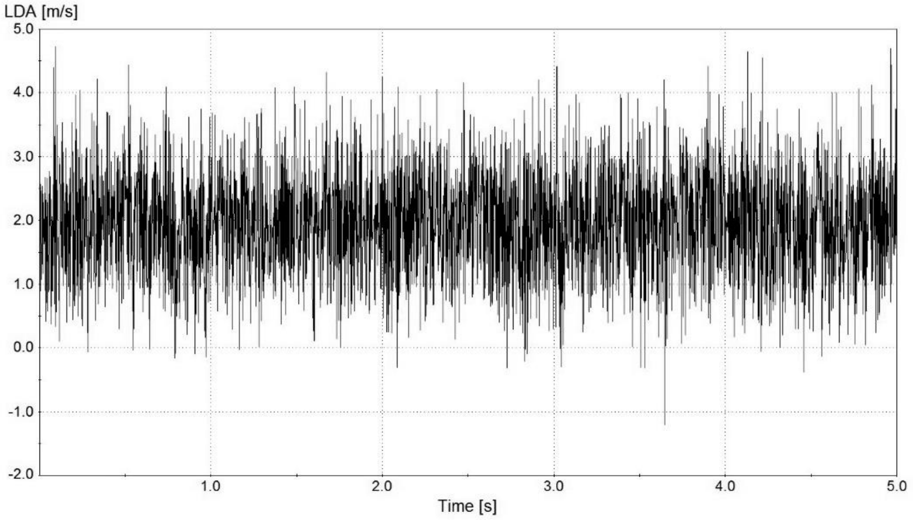

Figure C.3 Near surface velocity measurement at point b_2 on a chordwise distance located at $x/c = 0.56$ in u-direction using LDA at 4 degree angle of attack and Reynolds number $Re = 3.5x10^4$

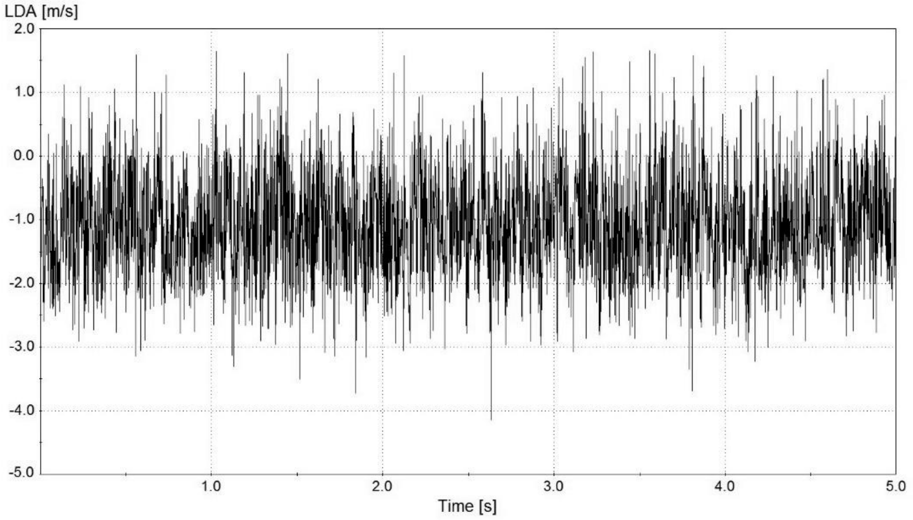

Figure C.4 Near surface velocity measurement at point b_2 on a chordwise distance located at $x/c = 0.56$ in ω-direction using LDA at 4 degree angle of attack and Reynolds number $Re = 3.5x10^4$

APPENDIX D

SOURCE CODES

Source Code of the Lomb-Scargle Normalized Periodogram [134]*:*

```
clear all
close all
clc

filename= input('Please write the filename of the
measurement data:\neg: 4_1_10000_w_p\n\n','s');
excel='.xlsx';
fileway=strcat(filename,excel);
A = xlsread(fileway);
t_d = A(:,1);
t(:,1)=t_d(:,1)/1000; %acquisition time as seconds
p = A(:,3);           %measurement data
Lomb_Data(p,t,1,1,4);


function [P,f,alpha] = Lomb_Data (x,t,varargin)

% LOMB caculates the Lomb normalized periodogram (aka
Lomb-Scargle, Gauss-Vanicek or Least-Squares spectrum) of
a vector x with coordinates in t.
%
% SYNTAX
%   [P,f,alpha] = lomb(x,t,fig,hifac,ofac,a);
%   [P,f,alpha] = lomb(x,t,fig,hifac,ofac);
%   [P,f,alpha] = lomb(x,t,fig,hifac);
%   [P,f,alpha] = lomb(x,t,fig);
%   [P,f,alpha] = lomb(x,t);
%
% INPUTS
%   x:     the vector whose spectrum is wanted.
%   t:     coord. of x (should have the same length).
%   fig:   if 0 (default), no figure is created.
```

```
%   hifac: the maximum frequency returned is
%   hifac) x (average Nyquist frequency). Default is 1
%   i.e. max frequency is the Nyquist frequency)
%   ofac:  oversampling factor. Typically it should be 4
or larger. Default is 4.
%   a:     additional significance levels to be drawn on
the %figure.
%


% OUTPUTS
%   P:     the Lomb normalized periodogram
%   f:     respective frequencies
%   alpha: statistical significance for each value of P


% NOTES
%%% INTERPRETATION AND SELECTION OF THE ofac PARAMETER
[135]
%    “The lowest independent frequency f to be examined
is the inverse of the span of the input data,
%               1/(tmax-tmin)=1/T.
%    This is the frequency such that the data can include
%one complete cycle. In an FFT method, higher independent
%frequencies would be integer multiples of 1/T. This
%oversampling parameter is the ofac. A value ofac >~4
%might be %typical in use”.
%
%%% THE hifac PARAMETER [135]
%    “Let fhi be the highest frequency of interest. One
way to %choose fhi is to compare it with the Nyquist
frequency, fc, %which we would obtain, if the N data
points were evenly spaced %over the same span T, that is
%               fc = N/(2T).
%    The input parameter hifac, is defined as fhi/fc. In
other words, hifac shows how higher (or lower) that the
fc we want to go”.


%% Inputs check and initialization
filename= input('Please write the filename for  saving:
\neg: 4_20000_2_P \n\n','s');
chord = 0.15; %chord length of the wing
vel = 3.484;  %freestream velocity (m/s)
y_scale = 1;  %scaling for y axis
St_set = 8;   %Desired Strouhal number for plotting
suffix1='_Lomb';
suffix2='_Lomb-St';
```

```
if nargin < 2, error('%s: there must be at least 2
inputs.',mfilename); end

[x,t,hifac,ofac,a_usr,f,fig] = init(x,t,varargin{:});

nf = length(f);

mx = mean(x);
x  = x-mx;
vx = var(x);
if vx==0, error('%s: x has zero
variance',upper(mfilename)); end


%% Main

P = zeros(nf,1);
for i=1:nf
    wt  = 2*pi*f(i)*t;  % \omega t
    swt = sin(wt);
    cwt = cos(wt);

    %% Calculate \omega\tau and related quantities
    % I use some trigonometric identities to reduce the
computations
    Ss2wt = 2*cwt.'*swt;        % \sum_t\sin(2\omega\t)
    Sc2wt = (cwt-swt).'*(cwt+swt);
                                % \sum_t\cos(2\omega\t)
    wtau  = 0.5*atan2(Ss2wt,Sc2wt);         %\omega\tau

    swtau = sin(wtau);
    cwtau = cos(wtau);

    % Some trigonometric identities to reduce the
computations
    swttau = swt*cwtau - cwt*swtau;  % \sin\omega(t-
\tau))
    cwttau = cwt*cwtau + swt*swtau;  % \cos\omega(t-
\tau))

    P(i) = ((x.'*cwttau)^2)/(cwttau.'*cwttau) +
((x.'*swttau)^2)/(swttau.'*swttau);
end
P = P/(2*vx);

%% Significance
M = 2*nf/ofac;
alpha = 1 - (1-exp(-P)).^M;   % statistical significance
alpha(alpha<0.1) = M*exp(-P(alpha<0.1)); % (to avoid
round-off errors)
```

```
%% Figure
if fig
%     figure
%     styles = {':','-.','--'};

    a = [0.001 0.005 0.01 0.05 0.1 0.5];
    La = length(a);
    z = -log(1-(1-a).^(1/M));
%     hold on;
%     for i=1:La
%
line([f(1),0.87*f(end)],[z(i),z(i)],'Color','k','LineStyl
e',styles{ceil(i*3/La)});
%         text(0.9*f(end),z(i),strcat('\alpha =
',num2str(a(i))),'fontsize',8);
% lgd{i}=strcat('\alpha=',num2str(a(i)));
%     end
    if ~isempty(a_usr)
        [tmp,ind] = intersect(a_usr,a);
        a_usr(ind)=[];
        La_usr = length(a_usr);
        z_usr  = -log(1-(1-a_usr).^(1/M));
%         for i = 1:La_usr
%
line([f(1),0.87*f(end)],[z_usr(i),z_usr(i)],'Color','r','
LineStyle',styles{ceil(i*3/La_usr)});
%             text(0.9*f(end),z_usr(i),strcat('\alpha =
',num2str(a_usr(i))),'fontsize',8);
%     %
lgd{La+i}=strcat('\alpha=',num2str(a_usr(i)));
%         end
    z = [z z_usr];
    end
%     legend(lgd);



    fig = figure;
    set(fig,'units','normalized','outerposition',[0 0 1
1]);
    f1=plot(f,P);
    set(gca,'FontSize',30)
    title('Velocity Spectrum','FontSize',35)
    xlabel('f (Hz)','FontSize',34);
    ylabel('Spectral Density','FontSize',34)
    %xlim([0 f(end)]);
    ylim([0,y_scale*max([z'; P])]);
    xlim([0 St_set/(chord/vel)]);
    saveas(f1,strcat(filename,suffix1),'bmp');
```

```
    fig = figure;
    set(fig,'units','normalized','outerposition',[0 0 1
1]);
    f4=plot(f*(chord/vel),P);
    set(gca,'FontSize',30)
    title('Velocity Spectrum','FontSize',35)
    xlabel('St=fc/u_{\infty}','FontSize',34)
    ylabel('Spectral Density','FontSize',34)
    %xlim([0 f(end)]);
    ylim([0,y_scale*max([z'; P])]);
    xlim([0 St_set]);
    saveas(f4,strcat(filename,suffix4),'bmp');


end

end


%% ### Local functions

%% init (initialize)
function [x,t,hifac,ofac,a,f,fig] = init(x,t,varargin)
    if nargin < 6, a = [];    % set default value for a
    else           a = sort(varargin{4});
                   a = a(:)';
    end
    if nargin < 5, ofac = 4;  % set default value for
ofac
    else           ofac = varargin{3};
    end
    if nargin < 4, hifac = 1; % set default value for
hifac
    else           hifac = varargin{2};
    end
    if nargin < 3, fig = 0;   % set default value for
hifac
    else           fig = varargin{1};
    end

    if isempty(ofac),  ofac  = 4; end
    if isempty(hifac), hifac = 1; end
    if isempty(fig),   fig   = 0; end

    if ~isvector(x) ||~isvector(t),
        error('%s: inputs x and t must be
vectors',mfilename);
    else
```

```
        x = x(:); t = t(:);
        nt = length(t);
        if length(x)~=nt
            error('%s: Inputs x and t must have the same
length',mfilename);
        end
    end

    [t,ind] = unique(t);    % discard double entries and
sort t
    x = x(ind);
    if length(x)~=nt, disp(sprintf('WARNING %s: Double
entries have been eliminated',mfilename)); end

    T = t(end) - t(1);
    nf = round(0.5*ofac*hifac*nt);
    f = (1:nf)'/(T*ofac);
end
```

Source code of the spectral analysis method that use MATLAB's built in FFT function

```
clear all
close all
clc
Sf = 1000;      % Sampling frequency
T = 1/Sf;       % Sample time
L = 5000;       % Length of signal
time = (0.001:1/Fs:5);   % Time vector
chord = 0.15;   % Chord length of the wing
u = 1.007;  % Free stream velocity of the corresponding
measurement
St_set = 8;     %Desired Strouhal number for plotting
y_scale = 0.5;  %Scale adjusting for y axis

filename= input('Please write the filename of the
measured data:\neg: File_Name (without _int)\n\n','s');
int_data='_int_data.xlsx';
suffix1='-5s-1000hz';
suffix2='-5s-1000hz-St';

NFFT = 2^nextpow2(L); % Next power of 2 from length of y
Z = fft(velocities_linearly_interpolated,NFFT)/L;
k = Sf/2*linspace(0,1,NFFT/2+1);
```

```
fig = figure;
set(fig,'units','normalized','outerposition',[0 0 1 1]);
f1=plot(k,2*abs(Z(1:NFFT/2+1)));
xlim([0 500])
ylim([0 y_scale])
set(gca,'FontSize',30)
title('Velocity Spectrum','FontSize',35)
xlabel('f (Hz)','FontSize',34);
ylabel('Spectral Density','FontSize',34)
saveas(f1,strcat(filename,suffix1),'bmp');

fig = figure;
set(fig,'units','normalized','outerposition',[0 0 1 1]);
f2=plot(k*(chord/u),(2*abs(Z(1:NFFT/2+1))));
xlim([0 St_set])
ylim([0 y_scale])
set(gca,'FontSize',30)
title('Velocity Spectrum','FontSize',35)
xlabel('St=fc/u_{\infty}','FontSize',34)
ylabel('Spectral Density','FontSize',34)
saveas(f2,strcat(filename,suffix2),'bmp');
```

Source code of the interpolation method that used for arranging the LDA data for MATLAB's FFT

```
clear all
close all
clc
Sf = 1000;      % Sampling frequency
T = 1/Sf;       % Sample time
L = 5000;       % Length of signal
time = (0.001:1/Sf:5);    % Time vector
filename= input('Please write the filename of the
velocity data:\neg: File_Name\n\n','s');
excel='.xlsx';
int_data='_int_data.xlsx';
fileway=strcat(filename,excel);
dummy_t_values_of_LDA=xlsread(fileway,'A7:A7507');
velocities_of_LDA=xlsread(fileway,'C7:C7507');
velocities_linearly_interpolated=zeros(5000,1);
delta_t_values=zeros(5000,1);
t=0;
a=length(dummy_t_values_of_LDA);
```

```
for i=1:5000
    delta_t_values(i,1)=t;
    t=t+1/1000;
end
k=1;
for k=1:a
    t_values_of_LDA(k,1)=dummy_t_values_of_LDA(k,1)/1000;
end



%%%%%   Linear interpolation part  %%%%%

for i = 1:5000
    for k = 1:a-1
        if delta_t_values(i,1) > t_values_of_LDA(k,1) &&
delta_t_values(i,1)< t_values_with_LDA(k+1,1)

velocities_linearly_interpolated(i,1)=velocities_of_LDA(k
,1)+(velocities_of_LDA(k+1,1)-
velocities_of_LDA(k,1))*(delta_t_values(i,1)-
t_values_of_LDA(k,1))/(t_values_of_LDA(k+1,1)-
t_values_of_LDA(k,1));
        end
    end
end

summation_of_velocities =
sum(velocities_linearly_interpolated);
elements_zero = 0;

for i = 1:5000
    if velocities_linearly_interpolated(i,1) == 0
        elements_zero = elements_zero + 1;
    end
end

average = summation_of_velocities/(5000-elements_zero);

for i = 1:5000
    if velocities_linearly_interpolated(i,1) == 0
        velocities_linearly_interpolated(i,1) = average;
    end
end

xlswrite(strcat(filename,int_data),velocities_linearly_in
terpolated(1:5000));
```